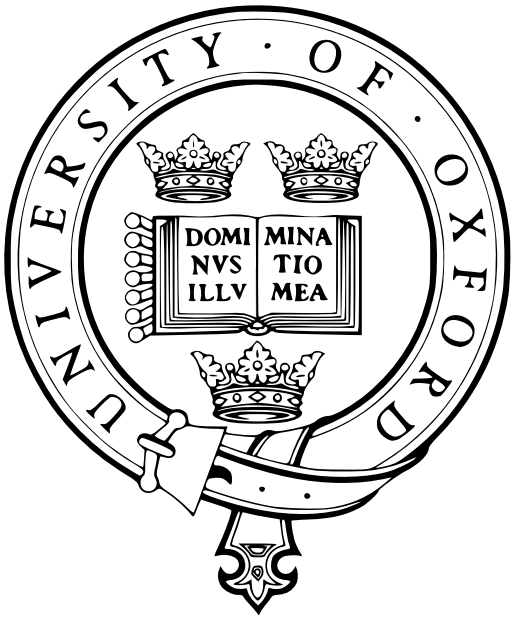


Structure and dynamics of two-dimensional binary colloidal polycrystals and fluids

Joseph D. Hutchinson

Lincoln College
University of Oxford

Supervisor: Prof. Roel P. A. Dullens

A thesis submitted for the degree of
Doctor of Philosophy

Trinity Term 2021

Abstract

The structural and dynamic behaviour of two-dimensional binary colloidal polycrystals and fluids are studied through optical microscopy and optical tweezing. Firstly, grain size evolution in an impurity doped polycrystalline monolayer is studied. A model is developed, combining crystallisation and curvature driven grain growth, which works well in describing grain size evolution at different impurity concentrations. The amount of dopant is found to affect the frustration of crystallisation and pinning of grain boundaries. Next studied is grain rotation in polycrystals. The rate of rotation for a single grain is well described by a model combining grain size and the grain boundary misorientation. The rate of rotation induced grain coalescence is placed in the context of grain size evolution and the trajectories of particles and dislocations are studied. To study the pinning forces of impurities in grain boundaries, active microrheology with optical tweezing is utilised. A model accounting for grain boundary deformation, contact angles between the impurity and grain boundary, and elastic response from the crystal is used to measure the pinning force on the impurity. An anomalously high depinning force is found, corresponding to the creation of a entity analogous to a dislocation. Next, the thermal fluctuations of a grain boundary between two pinned impurities are studied for different impurity spacings. The form of the fluctuations is dominated by the mode with a wavelength twice the impurity spacing. This spacing is also found to impact the mobility of the grain boundary and the mean-squared displacement. Finally, a binary system is placed on an angle to set up sedimentation-diffusion equilibrium. The particle sizes and materials are chosen to prevent fractionation. The structure of the system is found to be amorphous for all area fractions. The entire system for different tilt angles is found to be diffusive, with dynamics slowing down with a steeper tilt angle. The cause of the diffusive dynamics at all area fractions is found to be due to dynamic heterogeneities, which propagate from low to high densities, with higher tilt angles having a greater activation energy for this mechanism.

Declaration

This thesis is submitted for the degree of Doctor of Philosophy in Physical and Theoretical Chemistry at the University of Oxford. No part of this thesis has been accepted or is currently being submitted for any degree, diploma, certificate or other qualification in this University or elsewhere. This thesis is wholly my own work, except where indicated.

Contents

Abstract **i**

Declaration **iii**

1 Introduction **1**

1.1 Binary materials 2

1.2 Colloidal model systems 3

1.3 Scope of the thesis 5

2 Theoretical background and experimental methods **7**

2.1 Theoretical background 8

2.1.1 Colloidal model system 8

2.1.2 Hard spheres and disks 11

2.1.3 Binary colloidal hard disk systems 14

2.1.4 Crystals and grain boundaries 16

2.1.5 Glasses and supercooled fluids 21

2.2 Experimental methods 23

2.2.1 Colloidal model systems 23

2.2.2 Video microscopy 24

2.2.3 Optical Trapping 26

2.2.4 Image Analysis 28

2.3 Computer simulations 29

2.3.1 Brownian dynamics simulations 29
2.3.2 Monte Carlo simulations 30

3 Crystallisation and grain growth in impurity-doped colloidal monolayers 33

3.1 Introduction 34
3.2 Theory 35
3.2.1 Dynamic scaling 35
3.3 Methods 36
3.3.1 Experimental system and set-up 36
3.3.2 Key parameters 37
3.4 Results and discussion 39
3.4.1 Evolution of impurity-doped colloidal monolayers 39
3.4.2 Dynamic scaling 40
3.4.3 Crystallisation and grain growth 41
3.4.4 Grain boundary character distributions 43
3.4.5 Growth law 44
3.4.6 Crystallisation 47
3.4.7 Measuring grain growth 48
3.4.8 Grain evolution model 50
3.5 Conclusion 50

4 Grain rotation in two-dimensional colloidal polycrystals 53

4.1 Introduction 54
4.2 Theory 55
4.2.1 Angular velocity of rotating grains 55
4.2.2 Grain boundary sliding of circular grains 57
4.2.3 Dislocations in rotating grains 57
4.3 Experimental system and analysis 58

4.4 Results and discussion . . . 60
4.4.1 Quantifying rotational motion in a polycrystal . . . 60
4.4.2 Grain growth due to rotation driven coalescence . . . 64
4.4.3 Particle and dislocation dynamics during grain rotation . . . 66
4.5 Conclusion . . . 71

5 Active deformation and depinning of grain boundaries in colloidal polycrystals 73

5.1 Introduction . . . 74
5.2 Theory . . . 75
5.2.1 Microrheology of colloidal crystals using optical tweezers . . . 75
5.2.2 Elastic response of the crystal . . . 76
5.2.3 Dislocations and impurities . . . 77
5.2.4 Boundary pinning and deformation . . . 78
5.3 Experiment and simulations . . . 82
5.3.1 Experiment . . . 82
5.3.2 Methods of analysis . . . 84
5.3.3 Simulations . . . 86
5.4 Results and discussion . . . 87
5.4.1 The crystal's elastic response to probe drag . . . 87
5.4.2 Visualising the depinning and the trapping force . . . 89
5.4.3 Measuring the pinning force . . . 91
5.4.4 Depinning and dislocation formation . . . 93
5.5 Conclusion . . . 96

6 Grain boundary fluctuations between pinned impurities 99

6.1 Introduction . . . 100
6.2 Theory . . . 101

6.2.1 Capillary wave theory . . . 101
6.2.2 Grain boundary diffusion . . . 105
6.2.3 Motion and forces of the pinned grain boundary . . . 106
6.3 Experimental . . . 107
6.4 Results and discussion . . . 109
6.4.1 The unpinned grain boundary . . . 109
6.4.2 Spatial aspects of the pinned boundary . . . 110
6.4.3 The dynamic height-height correlation function of the pinned boundary . 112
6.4.4 Mean-squared displacements of pinned boundaries . . . 114
6.5 Conclusion . . . 116

7 Sedimentation-diffusion equilibrium of two-dimensional binary colloidal fluids 117

7.1 Introduction . . . 118
7.2 Theory . . . 119
7.2.1 Sedimentation-diffusion equilibrium . . . 119
7.2.2 The structure of glasses and supercooled fluids . . . 121
7.2.3 The dynamics of glasses and supercooled fluids . . . 123
7.3 Methods . . . 127
7.3.1 Experiments . . . 127
7.3.2 Colloidal particles . . . 128
7.3.3 Brownian dynamics simulations . . . 130
7.4 Results and discussion . . . 131
7.4.1 Density profiles . . . 131
7.4.2 Equation of state . . . 134
7.4.3 Structure . . . 135
7.4.4 Dynamics . . . 138
7.4.5 Dynamic heterogeneities and cooperative motion . . . 142

7.5 Conclusion 146

Appendix **149**

A Grain size evolution due to rotations 149

A.1 Theoretical grain size evolution 149

A.2 Measuring the rate of coalescence 150

B Measuring strain in colloidal crystals on a single particle resolution 151

C Dynamic Monte Carlo simulation of sedimentation-diffusion equilibrium for a binary hard disk system 155

C.1 Simulation set-up 155

C.2 Dynamic Monte Carlo sedimentation-diffusion profile 156

C.3 Simulation dynamics 157

Bibliography **159**

List of Publications **181**

Acknowledgements **183**

Chapter 1

Introduction

Looking backwards, the history of the Earth and its inhabitants can be traced by means of the properties and uses of materials. The Earth's structure itself has continuously evolved with tectonic plates forming domains shifting position and size [1], and rocks cycling through phases and structural configurations [2]: eroded by glaciers, in windswept deserts and stormy seas [3]; crushed and crystallised at extreme pressures under the crust [4]; and vitrified and hardened in dark trenches deep below the waves [5]. Prehistoric animals are preserved through permineralisation- the crystallisation and percolation of minerals in dinosaur bones [6]- or embalmed with amber- viscous tree resin envelops organisms and forms a solid glass, freezing the specimens in time [7]. The history of humanity can also be measured by way of the progression of materials understanding and processing: the transition between Stone and Bronze Ages is often discerned by the emergence of copper smelting [8]; ancient buildings are defined by their materials, resilient Roman concrete standing for millennia [9] or glazed ceramic Girih tiles adorning Islamic architecture in aperiodic patterns [10]; and archaeological dating of ceramic shard jigsaws and rusted metal coins [11]. Progress is also defined by jumps in technology: understanding alloys allowed for the mass refinement of steel through the removal of impurities [12], understanding the glass transition allowed for the mass production of flat window panes [13], and understanding the doping of semiconductors has allowed for the shrinking of transistors and the exponential growth of computing power [14].

Looking forwards, understanding the microstructure of materials is possible using the vast palette of established techniques, and will be vital for preparing the materials of the future for

prospective uses. The atomic structure of materials was only elucidated by X-ray crystallography around 100 years ago [15]. Since then, not only have experimental analytical techniques evolved, with direct measurement of the real space atomic arrangements arriving from scanning tunnelling microscopy [16] or high resolution atomic force microscopy [17] to dynamical analysis of glasses using nuclear magnetic resonance [18], but the increase in computing power has allowed computer simulations of materials to flourish [19]. The insight brought by these techniques is already applied to the macroscopic scale, in using ideal microscopic domain sizes to strengthen metals [20], single crystal jet-engine turbine blade casting [21], and hardening and toughening through alloying [22]. The latter case especially, proves the significance of how mastering the microscopic domain of binary materials allows for delicately calibrated material properties.

1.1 Binary materials

Atomic binary materials consist only of a mixture of two elements, but provide a wealth of structures and properties through their many arrangements and interactions [23]. In this thesis we are concerned with binary hard spheres, which exhibit structures ranging from doped crystals [24] to glasses lacking order [25].

Doping metals with secondary particles impedes the structural evolution relative to the undoped system [22]. The structure of a pure metal is typically polycrystalline, meaning the particles are arranged in domains called grains, in which all of the particles are orientated similarly [26, 27]. The one-dimensional interface between two grains is known as a grain boundary, the properties of which depend on the difference between the orientations of the grains, known as the misorientation [28]. The grain boundaries in the metal form a network, which evolves as a means to minimise the curvature of the lines, requiring particles in the grains to move and reorientate for assimilation into the new grain [29]. Alloying can be used to affect the structure of the pure metal, with the dopant sitting either in a grain or a grain boundary, having replaced the pure metal's particles [30]. When the dopant is in a grain boundary, it acts as an anchor, exerting a force on the grain boundary, holding it in place and preventing the network from evolving [31].

Binary glasses form in a variety of systems, the most ubiquitous of which being SiO_2 or window glass [32], with binary metallic glasses [33] also being common. In the case of the

latter, binary alloys form complex amorphous structures which cannot crystallise [34]. However other systems are typically more complex, such as polymer glasses [35], so binary systems are preferable to study. Glasses are also solids; their atoms move more slowly when compared to liquids, with no appreciable flow due to extremely large viscosities [36]. The structure however, completely lacks the periodicity, symmetry and long-range order that defines a crystal [37]. In this respect, there is little difference between the arrangement of particles in a solid glass and that of its liquid form, both are amorphous [38]. Herein lies the great interest in glasses [39]: what is the difference between the liquid and glass, and how does one transition to the other?

Experiments on these binary atomic materials are often challenging, owing to their length- and time-scales [40,41]. Therefore, either computational methods are employed [19,42], or model systems such as bubble-rafts [43, 44], granular materials [45, 46], dusty plasmas [47, 48], and colloidal particles [24, 49]. In this thesis we choose colloidal particles due to their experimental versatility and ease of manipulation.

1.2 Colloidal model systems

A colloidal suspension is a dispersion of solid particles, of sizes between 10 nm and 10 µm, in a liquid medium [50]. Common examples include red blood cells, soil particles in mud, and pigment particles in inks and paints. Owing to their sizes, colloidal particles were the key for Einstein [51] and Perrin [52] to convince the scientific community in the early twentieth century that atoms and molecules truly did exist. This is because the colloidal particles were light enough that the solvent molecules could impart momentum due to thermal fluctuations, which lead the particles to take a random walk, known as Brownian motion [51]. This property allows colloidal systems to thermally explore phase space, as atomic and molecular systems do, and therefore both exhibit similar phase behaviour [53]. In addition, colloidal particles can have finely tuned shapes and interactions. Regarding shapes, particles are typically spherical [54], but using rods [55], platelets [56], cubes [57] or dumbbells [58] or any other possible shape can lead to the exhibition of a wide array of different phase behaviours [59, 60]. The inter-particle interactions can also be adjusted, by changing the solvent, particle materials or surface functionalisation, or adding salt [61, 62]. Additional interactions can be created, via dipolar magnetic particles [63] or attractive depletion from polymers [64].

Regarding spherical particles, their interactions can be adjusted to resemble hard spheres [65]; these spheres cannot overlap, but otherwise have no inter-particle interactions. The phase behaviour of these colloidal particles is entirely controlled by the packing fraction, the total amount of space taken up by the particles divided by the total space available. At low packing fractions the system resembles a fluid, but increasing the packing fraction leads to crystallisation, or even a metastable glassy state [53]. This phase behaviour is well known for three-dimensional colloidal systems, but two-dimensional colloidal systems can also be made. Using particles with a greater mass density than the solvent leads to their sedimentation to the base of the container. By carefully adjusting the number of particles, a single layer of particles can form, known as a monolayer. These too show packing fraction related phase behaviour [66], with binary systems forming two-dimensional crystals [67] and glasses [68]. Two-dimensional colloidal crystals have been used to study grain growth [69, 70], grain boundary fluctuations [71], two-dimensional melting [63, 72] and the elastic properties of crystals [73, 74]. Glassy two-dimensional colloidal systems have been used to study local structures [68, 75], long-time dynamics [76, 77], dynamic heterogeneities [78, 79] and elastic properties of glasses [80, 81].

Finally, from an experimental point of view, colloidal particles provide both highly accessible and highly manipulable experiments for modelling atomic systems. The accessibility arises from the length-scales of micrometres and time-scales of seconds, which allows for the use of optical microscopy and standard-speed cameras to study their structure and dynamics. Conveniently, colloidal systems are also easily manipulated, often explained due to their 'soft' nature [50], referring to their Young's modulus, E, being many orders of magnitude lower than that of atomic systems [82]. For comparison, the typical energy in an atomic system is on the order of 1 eV, whereas for colloidal crystals this is on the order of k_BT. As the Young's modulus is the energy per unit volume, which for atomic and colloidal systems are on the order of Ångstrom cubed and micrometres cubed respectively, leading to $E \approx 10^{11}$ and $10^{-1}\,\mathrm{J\,m^{-3}}$ respectively. As a result, colloidal systems can easily be deformed using magnetic fields [83, 84], gravity [72, 85], or optical tweezing [86, 87]. Therefore, colloidal particle systems offer us a great experimental tool-set to model and manipulate crystals and glasses.

1.3 Scope of the thesis

In this thesis, we study the structure and dynamics of two-dimensional binary colloidal systems. We confine colloidal particles to a monolayer through gravity and image this via video microscopy. We use this to study polycrystals: how grain growth is affected by the inclusion of larger dopant particles, and how grains rotate due to torque from their grain boundaries. We next examine single grain boundary interactions with impurities: using optical tweezing to measure the forces of an impurity particle depinning from a grain boundary, and looking at the thermal grain boundary fluctuations in the region between two pinned impurities. Finally, we create an equal packing fraction mixture of small and large particles and place the system on a gravitational tilt to create a sedimentation-diffusion equilibrium, to examine the glass forming properties.

Firstly, in chapter 2, we discuss the theoretical background and the methods of the experiments and simulations. We introduce the physics of colloidal systems, the phase behaviour of hard disks and relevant parameters of binary colloidal systems. We then introduce two-dimensional crystals and supercooled fluids and glasses. We finally present the experimental methods of the colloidal system, sample preparation and microscopy set-ups, then introduce our simulation techniques.

In chapter 3, we investigate the effect of large particle doping on the grain growth of two-dimensional colloidal polycrystals. To this end, we examine the evolution of grain size and amount of crystallisation for different concentrations of dopants. We find an increased concentration increases grain boundary pinning and decreases the fraction of particles that crystallise. From this we establish a growth law based on the rate of crystallisation and rate of decrease in the grain boundary length to describe the evolution grain size for all impurity concentrations.

In chapter 4, we analyse grain rotations in polycrystals with different concentrations of dopants. We track the centres of the grains and follow their average orientations over time. We find good agreement of the angular velocities with a model linking the grain sizes and grain boundary energies. We contextualise the rotations within grain coalescence and curvature driven grain growth. Finally, we examine the dynamics of particles and dislocations during grain rotation.

In chapter 5, we use optical tweezing to depin a large impurity particle from a grain boundary and measure the forces acting on the impurity. We characterise the deformation in front of the impurity dragged through the crystal and measure the Young's modulus of the crystal. We use a model based on grain boundary deformation and contact angles between the impurity and grain boundary to predict the pinning force. We compare this to the measured optical force, taking into account the elastic force from the crystal and measure the grain boundary stiffness. Lastly, we find a surprisingly high depinning force, as a result of a newly created dislocation analogue at the position of the impurity.

In chapter 6, we examine the grain boundary fluctuations between two pinned impurities. We use optical tweezers to create different spacings along the same grain boundary. We find the correlation length and grain boundary stiffness to be consistent with the unpinned boundary, but find the shape of the grain boundary to be dominated by the mode with a wavelength twice the impurity spacing. We measure the grain boundary mobilities, finding a smaller spacings to increase the amount of drag per unit length. Finally, we examine the mean-squared displacements and again find a smaller spacing to have an impact, this time on the maximum displacement.

In chapter 7, we place a glass forming binary colloidal mixture on a tilt at different angles, leading to different gravitational forces parallel to the base of the cell. We find the system to reach sedimentation-diffusion equilibrium, with an increase in area fraction associated with a lower position in the sample. Examining the structure we find no order across the area fraction profile. Studying the dynamics, we find the system to show diffusive behaviour across the profile, with a decrease in the magnitude when the angle and force of gravity are increased. The speeding up of the dynamics we find is associated with an increase in the number of dynamic heterogeneities due to low density regions diffusing from low to high packing fractions.

Chapter 2

Theoretical background and experimental methods

Abstract

In this thesis, we study the structure and dynamics of doped colloidal polycrystals and binary fluids. Here, we provide an introduction to these systems, as well as the general methods pertaining to the experiments and simulations. We start by describing the properties of colloids and their phase behaviour, then binary systems. Next, the structure of crystals and grain boundaries, with the effect of doping is discussed, before we introduce supercooled fluids and the glass transition. In the next section, we examine the experimental colloidal model systems, video microscopy, image analysis and optical trapping. Finally, we discuss Brownian dynamics and Monte Carlo simulations.

2.1 Theoretical background

2.1.1 Colloidal model system

Brownian motion and the Langevin equation

In this thesis, we utilise suspensions of colloidal particles to study binary systems such as alloys and glasses. These particles are solid, typically made of plastic polymers, and have length-scales from ∼10 nm to ∼10 µm [50]. The particles are dispersed within a liquid solvent with thermally agitated molecules, which collide with the particles and impart some of their momentum. This buffeting from all sides will average to a net zero force vector over time, but instantaneously lead to a non-zero momentum due to thermal fluctuations. Therefore, the particles' motion is described as a random walk, which is known as Brownian motion [51].

To develop an equation of motion for colloidal particles we can consider the forces acting upon the particle. The first is the Brownian fluctuating random force, denoted by $\vec{f}(t)$. This is assumed to Gaussian white noise that is uncorrelated in time such that $\langle\vec{f}(t)\rangle = 0$, and $\langle\vec{f}(t)\vec{f}(t')\rangle = 2k_BT\xi\delta(t-t')$, where δ is a Dirac delta function [88]. Next, external perturbations such as gravitational and optical forces are incorporated as the external force $\vec{F}$. Finally there is a drag term; this force is proportional to the velocity with a friction coefficient, i.e. $\xi\vec{v}$. The friction of a single spherical colloidal particle in a solvent can be expressed using Stokes' formula: $\xi = 6\pi\eta a$ [50], where η is the viscosity of the solvent and a the radius of the colloid. This leads to the equation of motion, or the Langevin equation [88],

$$m\frac{d\vec{v}}{dt} = \vec{F} + \vec{f}(t) - \xi\vec{v}, \tag{2.1}$$

where m is the mass of the particle. From this we can describe the dynamics of our colloidal systems and build Brownian dynamics simulations to emulate our experiments. In our colloidal systems, the Reynolds number is small, on the order Re$\sim 10^{-5}$, meaning the viscous forces are greater than inertial forces [89]. Therefore, the system is in the over-damped limit, so there is no acceleration: $m.d\vec{v}/dt = 0$.

To characterise the particle dynamics, we can measure the mean squared displacement (MSD) $\langle\Delta r^2(t)\rangle$, where $\Delta r^2(t)$ is the square of the displacement of a particle at time t and $\langle ...\rangle$

denotes the ensemble average of the colloidal particles. For a spherical particle, this is given by the equation:

$$\langle \Delta r^2(t) \rangle = 2dDt, \tag{2.2}$$

where d is the dimension of the system (henceforth in this thesis taken to be $d = 2$). D refers the the diffusion constant, which at infinite dilution for a single sphere is the ratio of the thermal energy k_BT and the friction coefficient:

$$D = \frac{k_BT}{\xi}. \tag{2.3}$$

From this we can calculate the Brownian time, a characteristic timescale of a colloid, τ_B, which is the time taken for a particle to diffuse over its own diameter (σ):

$$\tau_B = \frac{\sigma^2}{4D}. \tag{2.4}$$

The particles used in this thesis are on the order of $1 - 10\mu m$, so τ_B is on the order of tens of seconds.

In addition to characterising timescales, the equilibrium height distribution at which particles sit relative to the bottom of a sample is also an important parameter in colloidal systems. The equilibrium is reached when the fluxes due to diffusion and sedimentation are equal. From this a height profile can be derived, with the form [90]

$$\phi(z) = \phi_0 \exp\left(-\frac{z}{h_g}\right), \tag{2.5}$$

where $\phi(z)$ is the area fraction (the fraction of the total area taken up by particles) at height z and ϕ_0 is the area fraction at the bottom of the profile. The parameter h_g is the gravitational height, given by the ratio of the gravitational potential and thermal energies:

$$h_g = \frac{6k_BT}{\pi g \Delta\rho \sigma^3}, \tag{2.6}$$

where g is the acceleration due to gravity and $\Delta\rho$ is the mass density difference between the colloid and solvent. Therefore the height distribution can be tuned by changing the size σ of the particles and also by changing either the solvent or material of the colloids to alter $\Delta\rho$.

Colloidal interactions

The interactions between pairs of colloidal particles are typically described by Derjaguin-Landau-Verwey-Overbeek (DLVO) theory [61, 62], which divides the terms into separate attractive Van der Waals, and repulsive electrostatic potentials:

$$U_{DLVO} = U_{vdW} + U_E. \tag{2.7}$$

The Van der Waals attraction is dominant at long distances, and is the result of dispersion forces between the two spherical colloids and the solvent medium. This is given by the equation

$$U_{vdW} = -\frac{\sigma A}{24R}, \tag{2.8}$$

where R is the distance between the particles' centres, and A is the Hamaker constant [91], which accounts for the strength of dispersive forces due to the material properties of the colloids and solvent.

The repulsive forces arise from the fact that the surfaces of the colloids are electrostatically charged. Clearly similarly charged surfaces will repel, but there is an additional effect due to the presence of ions in the solvent. Due to attraction to the charged surface, counterions have a higher than average concentration near the surface, which decays with distance. Conversely, due to repulsion, coions are distributed with a low concentration near the surface, which increases to the average with distance. The profile of counterions is given by an exponential relation: $\Phi = \Phi_0 \exp(-\kappa R)$, where Φ is the concentration of ions and κ^{-1} is the decay length, or the Debye length. This ion distribution is known as the electrical double layer, and when two double layers overlap the resultant osmotic pressure leads to an effective entropic repulsion between the particles.

The form of this repulsive term can be given by the Yukawa potential [92]:

$$U_E = \begin{cases} \infty & R < \sigma \\ Z^2 \lambda_B k_B T \left(\dfrac{\exp(\kappa\sigma)}{1+\kappa\sigma} \right)^2 \dfrac{\exp(-\kappa R)}{R} & R \geq \sigma \end{cases}, \tag{2.9}$$

where Z is the effective charge of the surface of the particle and λ_B is the Bjerrum length, which is the distance at which two charges have an interaction energy of $k_B T$. The potential is infinite

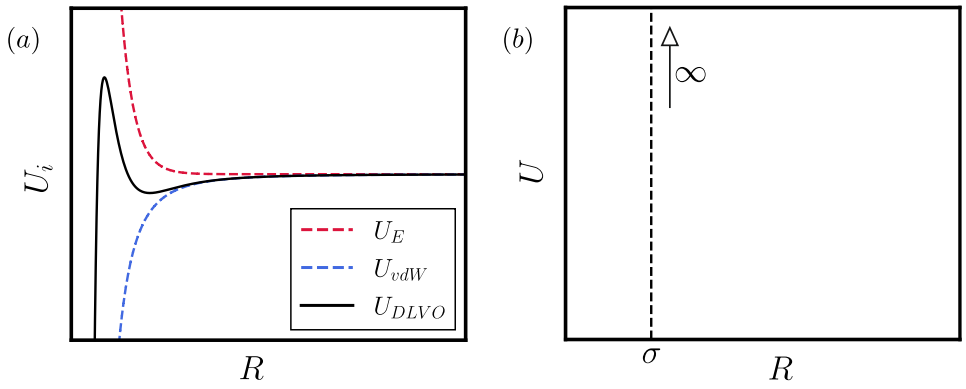


Figure 2.1: (a) the DLVO potential from the summation of Van der Waals and electrostatic repulsion terms. (b) the hard sphere potential, with diameter σ and infinite barrier labelled.

when $R < \sigma$ as the particles cannot overlap.

By taking both parts of eqn. 2.7, the form of the overall potential starts highly repulsive at short distances and electrostatic dominance, evolving to a potential minimum as the Van der Waals force dominates at longer distances, with $U_{DLVO} \to 0$ finally as $R \to \infty$. This can be seen in figure 2.1 (a). The form of this can be altered by modifying the experimental conditions. For example, decreasing the solvent-particle refractive index mismatch will decrease U_{vdW} and therefore the height of the minimum. Alternatively, the surface charge and ionic strength of the solvent can be altered to increase or decrease the Debye length and range of repulsive interaction. For instance, a hard-sphere-like potential can be achieved by minimising the Van der Waals forces and screening the charges by having a short κ^{-1}.

2.1.2 Hard spheres and disks

Colloidal hard-spheres are an important model system, due to the well documented and easy to describe phase behaviour [93]. The hard sphere potential has the form

$$U_{HS} = \begin{cases} \infty & R < \sigma \\ 0 & R \geq \sigma \end{cases}, \tag{2.10}$$

meaning that the only interactions will be when the particles make contact. This can be seen in figure 2.1 (b). The form of this potential leads to an equation of state that is dependent upon the volume fraction ϕ [94]. The volume fraction refers to the ratio of the volume of the system and the total volume encompassed by particles. In 2D this is the area fraction, given by the

equation

$$\phi = \frac{NA}{A_T}, \tag{2.11}$$

where A_T is the total area of the system, N is the total number of particles and A is the area of a particle.

The phase behaviour of hard spheres in 3D and 2D are quite different. In the case of a purely monodisperse 3D system there are two phases: fluid and crystal, at low and high volume fractions respectively [53]. These are physically differentiated by their structure and dynamics. The fluid phase exists below $\phi_{3D} = 0.49$ and is characterised by diffusive dynamics, i.e. where $\langle \Delta r^2 \rangle \propto t$, and an amorphous structure. There is a first order phase transition with a co-existence region within the range $0.49 \leq \phi_{3D} < 0.54$, after which only the crystal is thermodynamically stable [95, 96]. The crystalline phase is characterised by long-time arrested dynamics (i.e. where $\langle \Delta r^2 \rangle \propto t^\alpha$, $\alpha = 0$) and long range orientational and translational order. Here, orientational order refers to the orientation of neighbours relative to a reference axis and translational order refers to the position of particles with regards to a lattice.

Crystallisation is fully driven by entropy, due to the lack of an enthalpic term as a result of $U_{HS} = 0$. The entropy of the hard sphere system is the sum of two parts, configurational and vibrational or $S = S_{conf} + S_{vib}$. Below the crystallisation packing fraction, the value of S_{conf} is greater for an amorphous structure than a crystalline structure due to the total number of possible structural configurations. However, the vibrational component is even greater for the crystal due to the higher mean free volume in which each particle can occupy. This allows for particles to vibrate more freely around their lattice points, so S_{vib} has a greater contribution to total entropy, thereby favouring crystallinity at high ϕ.

For two-dimensional hard disk systems, the competition between S_{conf} and S_{vib} still governs the phase transitions, but in this case there are three separate phases. Similar to the 3D case, the lowest ϕ phase is the liquid and exists below $\phi_{2D} = 0.68$ and the most phase is the crystal and exists above $\phi_{2D} = 0.73$, as seen in figure 2.2 [72]. However, the differences between 2D and 3D are predicted by Kosterlitz-Thouless-Halperin-Nelson-Young (KTHNY) theory [97–99], which postulates the possibility of an intermediate phase, the hexatic. In simulations of hard disks and experiments with colloidal particles [63, 66, 72, 100–102], it has been found there are

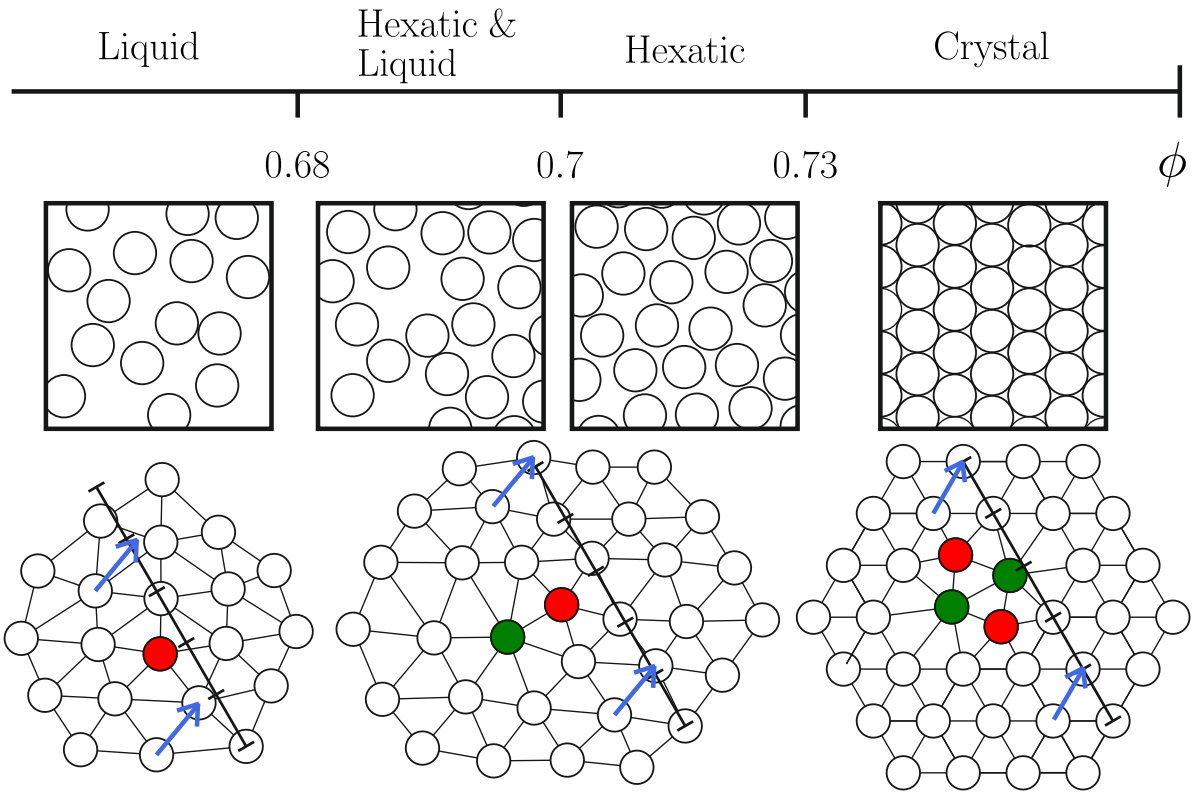


Figure 2.2: The phase diagram of 2D hard disks. The top line represents the area fraction, with the corresponding phases at the different values, with cartoons of each beneath. The values of the phase transitions are taken from the colloidal hard sphere experiments of Thorneywork *et al.* [72]. At the bottom are the defects found during the melting of the crystal phase. The blue arrows show the orientation, and the black line shows the translational order. In the left-most picture, a single 5-fold disclination in a liquid. There is no long-range translational or orientational order. The central picture shows a 5-7 dislocation in the hexatic phase. There is long-range orientational order, but not translational order. The right most picture shows a crystal. There is both long-range translational and orientational order.

two phase transitions, first order and continuous respectively, between the fluid and crystal. The reason for these transitions is that decreasing the area fraction starting from a crystal leads to a dissociation of the topological defects and a change in the correlations of bond-orientational and translational order.

The 2D crystal has hexagonal symmetry with each particle having six neighbours, with defect pairs consisting of neighbouring 5- and 7-coordinate particles called dislocations. In the crystal, the dislocations are bound in pairs, leading to continuity in both the bond-orientational and translational order. It is important to note however, that the translational order seen in 2D crystals is quasi-long range as a result of long-wavelength thermal phonons breaking this symmetry over large distances [103] [1]. At the transition between the crystal and hexatic phases, dislocation pairs unbind, leading to isolated dislocations. The result of this is that the hexatic

[1] This is not true for 3D systems as thermal fluctuations in these systems decay over a shorter distance.

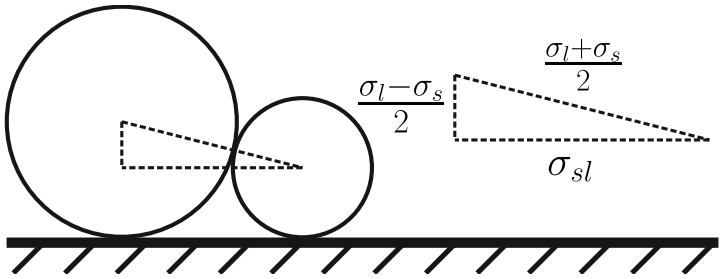


Figure 2.3: A diagram showing the in-plane size difference from the small and large particles. The dashed triangles correspond to one-another, showing the construction of the in-plane small-large diameter.

phase has long-range bond-orientational order but only short-range translational order, as seen in the bottom of figure 2.2. In the subsequent transition between hexatic and liquid, the 5- and 7- coordinate pair are unbound, leading to the fluid having no long-range bond-orientational or translational order.

2.1.3 Binary colloidal hard disk systems

Monodisperse hard disk systems in and of themselves are rich and complicated systems, however more complex behaviours can be studied through the introduction of a differently sized particle. The important parameters that control the behaviour of the system are related to the area fractions of the two disks. These are of the form of equation 2.11:

$$\phi_i = \frac{N_i A_i}{A_T}, \tag{2.12}$$

where i denotes the species of particle. For a 2D monolayer of hard spheres it is important to note that since the particles are sitting on a surface, the centres of the species are at different heights, as can be seen in figure 2.3. The 2D plane in which the system is analysed is the height of the centres of the smaller particle. Therefore, the in plane size of the larger particle is measured to be the distance between the central axis of the large particle and the surface of the smaller when both particles touch.

The key parameters that govern the system behaviour are the total area fraction, relative area fraction and relative sizes. The total area fraction is given by the expression

$$\phi_T = \phi_s + \phi_l. \tag{2.13}$$

The composition is characterised by

$$q = \frac{\phi_l}{\phi_s + \phi_l}. \tag{2.14}$$

Assuming high enough ϕ_T, in the monodisperse limits (i.e. $q \to 0$ and $q \to 1$) the system will crystallise. The species with the greater area fraction will form the crystal and the species with lower area fraction will exist as impurities within the crystal [24]. Conversely, as $q \to 0.5$ crystallisation is suppressed [104] and the particles will mix and the structure becomes amorphous to the extent that a glass may form [105]. Changing the size ratio also affects the phase behaviour of the system due to the non-additivity [106]. This is defined in the following equation:

$$\sigma_{sl} = \frac{\sigma_l + \sigma_s}{2}(1 + \Delta), \tag{2.15}$$

where σ_{sl} is the in-plane distance between the particles (shown in figure 2.3) and Δ is the non-additivity parameter. This determines the amount of free volume about each particle and whether hetero- or homo-coordination is preferred [107]. For positive Δ, homo-coordination is preferred and a demixing will occur [108]. For negative Δ, which is always the case for our colloidal hard sphere mixtures, particles maximise their free volume by clustering around the opposite species, thereby leading to short range preferential ordering and less demixing. A greater magnitude of Δ will lead to this phenomenon becoming more prevalent [109].

The amount of parameter space in binary systems leads to a great richness in their structure. For instance, near the aforementioned monodisperse limits, the system forms a crystal with dopants. The size ratio here is important, as the dopant can sit on lattice sites or interstitials, and be commensurate or incommensurate with the lattice [24]. These are important factors in the amount of strain in the crystal as is discussed in section 2.1.4 and will be relevant in chapters 3 and 5. With $q \to 0.5$, there are three possible arrangements all of which become relevant in chapter 7. The first is the glass, which is discussed in in section 2.1.5, but is not necessarily the most stable configuration depending on the exact composition and size ratio [34]. Instead, it is possible for the two species to completely fractionate, forming two separate crystals [110]. Given right conditions, such as vapour deposition [111], a binary crystal can even form, with many different possible unit cell configurations [112].

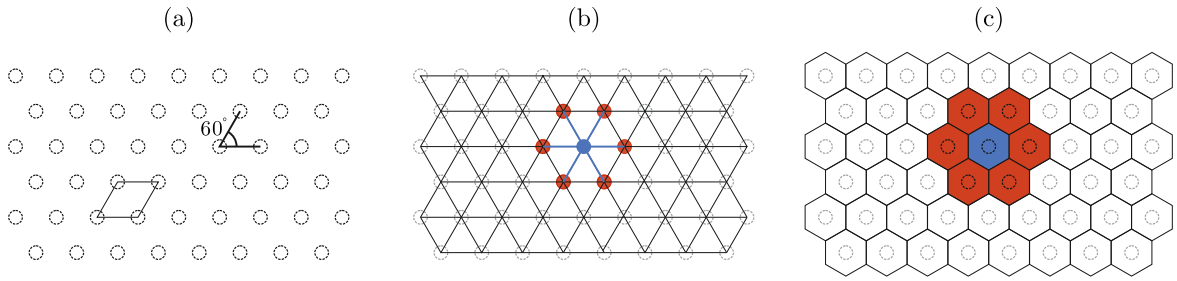


Figure 2.4: (a) Lattice points of a hexagonal lattice with the rhomboidal unit cell and the 60° angle highlighted. (b) A Delaunay triangulation of the lattice points, with blue central particle and its six neighbours. (c) A Voronoi diagram showing the space closest to each lattice point (bonded by each hexagon). The six neighbours of the central blue particle highlighted in red.

2.1.4 Crystals and grain boundaries

Two-dimensional lattices and crystals

A perfect two-dimensional crystal sits on an infinite lattice of points either seen as the centres of tessellated hexagons or vertices of tessellated equilateral triangles (see figures 2.4 (a), (b), (c) respectively). This results in a unit cell of a rhombus (fig. 2.4 (a)), whose height is $\frac{\sqrt{3}}{2}r$, where r is the distance between neighbouring points. Each lattice point itself has six neighbours evenly distanced and spaced angularly 60° apart. Therefore, when a rotation of less than 60° is performed, a new lattice is produced, said to have a different orientation. These orientations can be quantified as the angle of rotation relative to a fixed lattice, typically the x-axis of the reference frame.

For a real crystal, the lattice sites could be occupied by hard disks, for which the hexagonal lattice is the optimal packing, or the centres of the aromatic rings in graphene [113]. In such real crystals, the tessellation of triangles can be reverse engineered using a Delaunay triangulation, which creates a triangular mesh joining together closest neighbours, as seen in figure 2.4 (b). The hexagonal order can be similarly discerned with a Voronoi tessellation, producing interlocking cells whose areas comprise the region of points closest to the lattice point, shown in figure 2.4 (c). The edges of each cell are therefore equidistant between two lattice points, and the vertices are equidistant between three.

In this thesis, we measure crystallinity and orientation via the bond-orientational order

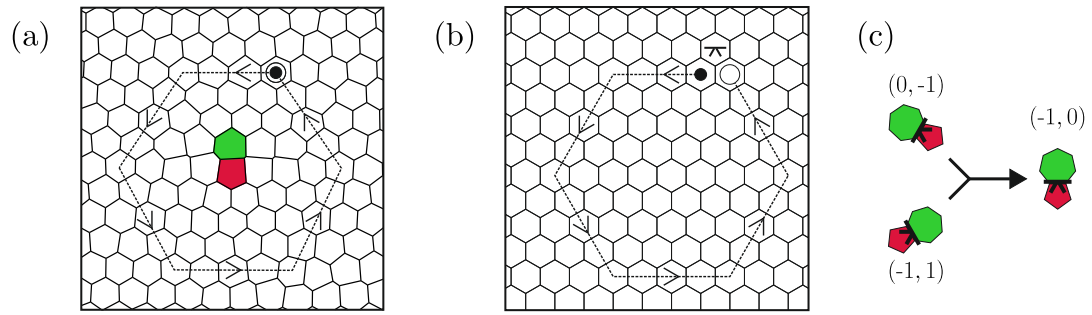


Figure 2.5: (a) A Voronoi diagram with a dislocation in the centre, taken from a real colloidal crystal. 7-Coordinate is coloured in green, 5-coordinate red. The dashed line represents a closed loop around the dislocation, with beginning of the path noted as the black dot, the end as the white. (b) A Voronoi diagram of a perfect lattice based on the lattice in (a). The path takes the same route, with the start and end denoted the similarly. The symbol above the start/end point represents the Burgers vector of this dislocation. (c) A reaction between dislocations showing the conservation of the numbers in the vector.

parameter [98]:

$$\psi_6(\vec{r}) = \frac{1}{N_j}\sum_{j=1}^{N_j}\exp(i6\theta_{jk}), \tag{2.16}$$

where the central particle k has N_j neighbours; joining the centre of k to each neighbour j forms a vector, which has the angle θ_{jk} between itself and an arbitrary axis. The result is a complex number with two-fold usefulness: firstly, from the argument $\theta_6 = \frac{1}{6}\arg(\psi_6(\vec{r}))$ we acquire a measure of the orientations of neighbours, allowing for the orientation of the lattice to be elucidated. Secondly, the modulus $|\psi_6(\vec{r})|$ is a measure of how close the arrangement of neighbours is to that of a perfect hexagonal lattice, for which $|\psi_6(\vec{r})| = 1$. This is therefore a good measure of local crystallinity, and particles are typically taken to be in a crystalline environment if $|\psi_6(\vec{r})| > 0.7$ [114].

Coordination and dislocations

Imperfect crystals, as all real systems are, have defects where some particles are coordinated to only 5 or 7 neighbours. Pairs of adjacent 5- and 7-coordinate particles are common and are known as dislocations [115,116]. These defects are topologically bound to six orientations, related to the hexagonal symmetry of the crystal, and move and react with one another. Dislocations are energetically costly to create, as to be accommodated, the surrounding crystal must deviate from the lattice, thus introducing strain. Therefore motion (or gliding) is energy neutral whereas annihilation reactions are energetically favourable and creation unfavourable.

An example of a dislocation can be seen in figure 2.5 (a), taken from a real colloidal crystal, (the 5-coordinate particle is coloured red and the 7-coordinate coloured green). The hexagons around the dislocation are distorted, indicating strain compared to the perfect lattice in figure 2.5 (b). To easily describe reactions and motion, we assign a Burgers vector to the dislocation [115]. To calculate this vector, we take a looped path around the dislocation (see the dashed line) and count how many cells are passed through in each direction. Next we take the same path in the analogous perfect crystal where there is no dislocation. Noting that the beginning and end of the path are denoted by the black and white circles respectively, for the perfect crystal there is a one cell difference between the start and end of the path, which is the Burgers vector. This vector from path end to beginning goes backwards one cell (-1) and does not go up or down a line of particles (0), hence is given the notation $(-1, 0)$. There are six possible orientations and six Burgers vectors for dislocations with a magnitude $|\vec{b}| = 1$, due to the symmetry of the crystal. One useful property of Burgers vectors is in describing the motion and reactions of these dislocations. There must be conservation of the numbers in the vector [117]:

$$\vec{b}_1 + \vec{b}_2 = \vec{b}_3, \tag{2.17}$$

with the elastic energy change:

$$b_1^2 + b_2^2 \geq b_3^2. \tag{2.18}$$

Dislocations can also glide, moving in the direction of their Burgers vector, but cannot change their orientation. A reaction is illustrated in figure 2.5 (c), where two dislocations glide together and react to produce a third. The reverse is also true [118], as a single dislocation can dissociate and form a pair dislocations such that:

$$\vec{b}_1 = \vec{b}_2 + \vec{b}_3, \tag{2.19}$$

where the total energy $b_2^2 + b_3^2 - b_1^2$ is minimised.

Grain boundaries and their properties

In addition to local defects, the other key difference between perfect crystals and those found in nature is that a crystal is often subdivided into regions of different orientations, i.e. the rotation

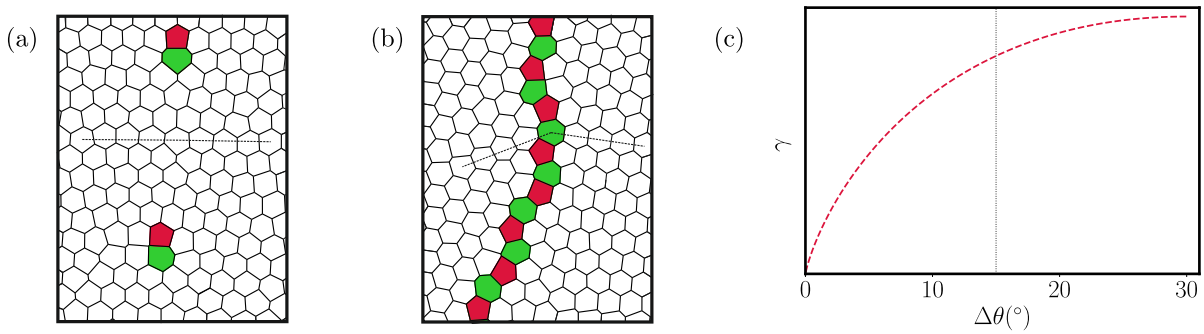


Figure 2.6: (a) A Voronoi diagram of a real colloidal grain boundary, where $\Delta\theta \approx 3°$ (i.e. a Small Angle Grain Boundary) with dislocations coloured. The dashed lines represent the planes of the crystal. (b) A Voronoi diagram of a Large Angle Grain Boundary from a colloidal crystal, where $\Delta\theta \approx 30°$. (c) A graph showing the form of the grain boundary energy, γ, as a function of misorientation. The vertical dotted line represents the approximate divide between SAGBs and LAGBs.

angle applied to the lattice in fig. 2.4 (a). The result is a polycrystal, and where each grain (domain) meets another, there is an interface known as a grain boundary (GB). Much like other interfaces, GBs are inherently less energetically favourable with respect to the bulk, and as such systems tend towards minimising the total GB length by increasing the average domain size. The properties of grain boundaries within a crystal therefore heavily dictate the texture of the system.

Possibly the most important property of a grain boundary is the misorientation, $\Delta\theta$. This is the difference between the orientations of the two adjacent grains that form the boundary ($\Delta\theta = |\theta_1 - \theta_2|$). Two such boundaries can be seen in figures 2.6 (a) and (b). Due to the hexagonal symmetry of the 2D crystal, positive and negative values are equivalent and the range is $0° < \Delta\theta \leq 30°$. This range is typically subdivided into small and large angle grain boundaries (S/LAGB), which have the ranges $0° < \Delta\theta \leq 15°$ and $15° < \Delta\theta \leq 30°$ respectively [26]. The reason for this divide is evident when examining both the structure and energies of GBs.

Firstly, the grain boundary structure consists of a line of dislocations. One such grain boundary can be seen in figure 2.6 (a), with a misorientation of approximately 3°. For such SAGBs, each dislocation has the same Burgers vector, b, and all are evenly spaced by a distance d; the misorientation is related by the simple formula: $\Delta\theta \approx b/d$ [28]. As this relationship implies, when the misorientation increases, the spacing of dislocations will decrease, as b is fixed. This can be seen in figure 2.6 (b), where the GB has a misorientation of $\sim 30°$, and the dislocations form a continuous line. Herein lies a key difference between S/LAGBs and a reason as for their separate classification: SAGBs have a clear structural dependence on $\Delta\theta$, whereas

LAGBs have a much more complex structure. Indeed, any relationship between the structure and misorientation for LAGBs is yet to be elucidated [26].

The structure of grain boundaries is directly related to the energy, as each dislocation means a greater distortion of the crystal and thereby a higher energy cost. Therefore GBs with high misorientations and more dislocations have a greater energy. This relationship is approximated by the expression [119]:

$$\gamma = \gamma_0 \, \Delta\theta(A - \ln \Delta\theta), \tag{2.20}$$

where γ is the GB energy, and γ_0 and A are constants. The form of this curve can be seen in figure 2.6 (c). Here, the differentiation between Small and Large Angle Grain boundaries becomes clear once again. Before the dotted line, there is a rapid change in γ with $\Delta\theta$, whereas the gradient is much reduced afterwards.

In our experiments, we typically measure the grain boundary stiffness, which has the form $\Gamma = \gamma + \gamma''$ [120], where γ'' is the second derivative of the energy with respect to inclination, the angle of the boundary with respect to the planes of the lattice.

Impurities in Grain Boundaries

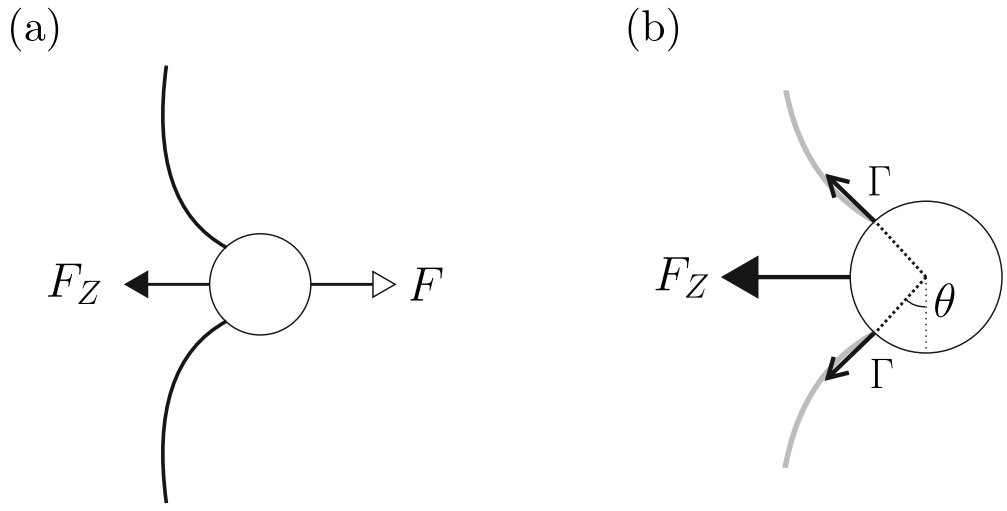


Figure 2.7: (a) A pinched grain boundary in 2D, where the embedded impurity is being pulled by force F with the resistive force F_Z. (b) Zooming in on (a), the Zener force F_Z is split into its two components due to the grain boundary stiffness Γ.

When introducing a second set of particles into polycrystals, the impurities tend to be adsorbed in grain boundaries rather than within grains, due to a greater free volume which allows for less deformation of the crystal [121]. This can also have a stabilising effect on the crystal, as impurities can reduce the grain boundary energy [122,123]. At equilibrium, there are typically a number of particles remaining in the grain, as the adsorption free energy is only a few units of k_BT [24].

Due to the stability of segregated impurities, if a boundary moves away from the particle, or vice versa, a restoring force acts on both entities, as can be seen in figure 2.7 (a). The grain boundary will begin to distort and become pinched, until the restoring force reaches a maximum and the particle will unpin as the boundary returns to its equilibrium position. As a result of this, grain growth in alloys is often slower due to the hindrance of solute particles dragging the grain boundaries [27].

The aforementioned restoring force, known as Zener pinning, is often modelled by assuming the force acting upon the particle is a result of the surface tension of the boundary. This force for a grain boundary is the stiffness Γ, and acts as a normal to the particle at the regions of intersection, which in two dimensions will be two points. As seen in figure 2.7 (b), the Zener pinning force F_Z is given by the sum of the GB tension components [124]:

$$F_Z = 2\Gamma \sin\theta, \tag{2.21}$$

where θ is the angle between the points of intersection and the axis parallel to the grain boundary.

2.1.5 Glasses and supercooled fluids

This section serves as an introduction to the concept of glasses and supercooled fluids and the associated dynamic slowdown, with relevance to chapter 7.

Supercooling and dynamic slowdown

A supercooled fluid is simply a liquid lowered to a temperature below its crystallisation point. For example, pure water can be slowly cooled below 0 °C, and despite the thermodynamic driving force, if there is no kinetic pathway towards solidification, the water remains liquid. Perform-

ing the same experiment on a polymer or SiO_2, as the liquid becomes more supercooled (the difference between T and T_m becomes more negative), the dynamics slow down. At a certain point, the rate of cooling outpaces the molecular cooling rate, and the structure no longer has the opportunity to rearrange [125]. At this point, for all intents and purposes the system has solidified. This is because the dynamics resemble a solid, but the structure actually retains the fluid's amorphousness. This is no longer a fluid, nor is it a crystal; this is a glass. This process is the 'glass transition', an apparent continuous phase transition [126]. This transition's associated temperature T_g is not fixed, and instead can happen within a range of temperatures, depending on the rate of cooling.

When approaching T_g, the dynamical processes rapidly slow down [127], with Arrhenius or super-Arrhenius behaviour. The system also becomes more dynamically heterogeneous [128] with regions becoming arrested or moving cooperatively in strings [129]. These structural rearrangements are thought of as local explorations of the energy landscape, regions that are not hindered by a kinetic barrier can search for a local thermodynamic minimum [130]. Whether an 'ideal' glass and a thermodynamic phase transition exist, is a long-standing and unresolved debate [131].

Colloidal supercooled fluids

Colloidal glasses have been studied extensively [132], owing to their length- and time-scales being well suited for experimental analysis. The dynamics of colloidal glasses align well with Brownian dynamics simulations [132] and the greater complexity in molecular systems appears not to cause much of a difference between the behaviours. Both two-dimensional and three-dimensional systems have been shown to have similar dynamics [133, 134]. In the case of three-dimensional hard sphere colloids, the system is a liquid below $\phi_{3D} = 0.49$ and crystalline above $\phi_{3D} = 0.54$ with a coexistence region in-between [53]. With correct preparation of the sample, in this coexistence region one can generate a supercooled phase, which is metastable relative to the crystal [132]. In two-dimensions however, one typically requires an amount of polydispersity to disrupt the crystalline structure [45]. Naturally, increased polydispersity also greatly aids three-dimensional glass formation too. Alternatively, a binary mixture can have the same effect [49, 135–137]; if sufficiently well mixed and with the right size ratio, neither particle can fractionate nor form a binary crystalline structure [34]. The control parameter for colloidal glasses instead

of temperature is packing fraction ϕ and to ensure vitrification, the system is often quenched in ϕ.

2.2 Experimental methods

2.2.1 Colloidal model systems

σ /µm	Polydispersity / %	Material	Supplier	Chapter(s)
2.79	2.2	MF	Microparticles GmbH	7
2.95	2.0	MF	Microparticles GmbH	3,4,5,6 and 7
6.20	1.9	MF	Microparticles GmbH	3 and 4
10.81	1.4	MF	Microparticles GmbH	5 and 6
3.87	5.8	TPM	Synthesis from [138]	7
3.77	2.9	PMMA	Microparticles GmbH	7

Table 2.1: σ is the diameter. MF = Melamine Formaldehyde, PMMA = Poly-methylmethacrylate and TPM = 3-(trimethoxysilyl)propyl methacrylate. The polydispersity values are either obtained from the manufacturer or through analysis of SEM images.

In this thesis, we mostly use spherical melamine formaldehyde (MF) particles which are carboxylic acid functionalised and when dispersed in aqueous solvent give the particle a negative surface charge to prevent clustering and sticking to the wall of the sample cell. MF has a mass density of $1.51\,\mathrm{g\,cm^{-3}}$ and a refractive index of 1.68, and those particles used in this thesis can be seen in table 2.1. The effective hard spheres diameters of all of the particles in this thesis have been measured from scaling experimental radial distribution functions (RDFs) to fit simulated hard sphere RDFs (using density functional theory, following Thorneywork *et al.* [65]).

Also used are spherical particles of 3-(trimethoxysilyl)propyl methacrylate (TPM), which were synthesised according to the method of Liu *et al.* [138]. Briefly, the particles were made by mixing 16 µL of NH_3 in 20 mL of deionised water (3.44×10^{-3}M, ∼pH 10) in a round bottom flask. The mixture was left with a stirrer bar set at 500rpm, with 0.6 mL of TPM oil added quickly in one go, and left to hydrolyse for 1hr, with the solution eventually appearing cloudy. At this point a few mg of azobisisobutyronitrile (AIBN) is added in excess as a radical initiator

to cross-link the TPM droplets. The solution is then kept in an 80 °C oven for 5hr, gently turning over every 1.5hr to re-disperse the sedimented reactants. The colloidal mixture is then left to cool and washed with deionised water. The resultant particles can be seen in table 2.1 and have a mass density of $1.29\,\mathrm{g\,cm^{-3}}$ and a refractive index of 1.49.

Finally we also use spherical poly-methylmethacrylate (PMMA) particles (Microparticles GmbH) also with carboxylic acid functionalised surfaces. These can be seen in table 2.1 and the material has a mass density of $1.18\,\mathrm{g\,cm^{-3}}$ and refractive index of 1.49.

To make up the dispersions used in the various experiments, colloidal particles are mixed with a 20/80 v/v% ethanol/deionised water mixture. The addition of ethanol is used to reduce surface tension allowing easier injection into the cell and to prevent the growth of bacteria. The cell in question is a quartz Hellma cell with internal dimensions 20 mm × 9 mm × 200 µm (l × w × h). The procedure for cleaning in between experiments is to place the cell into a bath of 2.5% Hellmanex surfactant v/v% deionised water heated to 55 °C for 1hr. The cell is then thoroughly washed with water and left to dry, before being placed into a plasma cleaner for 20 s to give the surface a negative charge. After this cleaning, 90 µL of the colloidal dispersion is injected into the cell with the inlets then being sealed with Blu-tack. The particles are then allowed to sediment to the bottom of the cell. By tuning the volume fraction and number ratios of the colloidal particles in the mixture we control the overall area fraction and composition of the resultant monolayer.

The system is quasi-two-dimensional as the high mass density of the particles means that the gravitational height h_g (equation 2.6) is much smaller than the diameter of the particles, meaning out of plane fluctuations are minimal. The plane here is defined as going through the centres of the smaller particles, as such the in-plane size of the larger particles must be accounted for when calculating the total area fraction (see figure 2.3). Where a polycrystalline monolayer is desired, a particle area fraction of $\phi_l > 0.73$ is prepared and left to equilibrate on a level surface, allowing for grains to grow for a week or so depending upon the required grain size.

2.2.2 Video microscopy

We image our colloidal systems using video microscopy. In this thesis three, different optical microscopes are used. Simply put, the sample is illuminated by an LED light source, and the

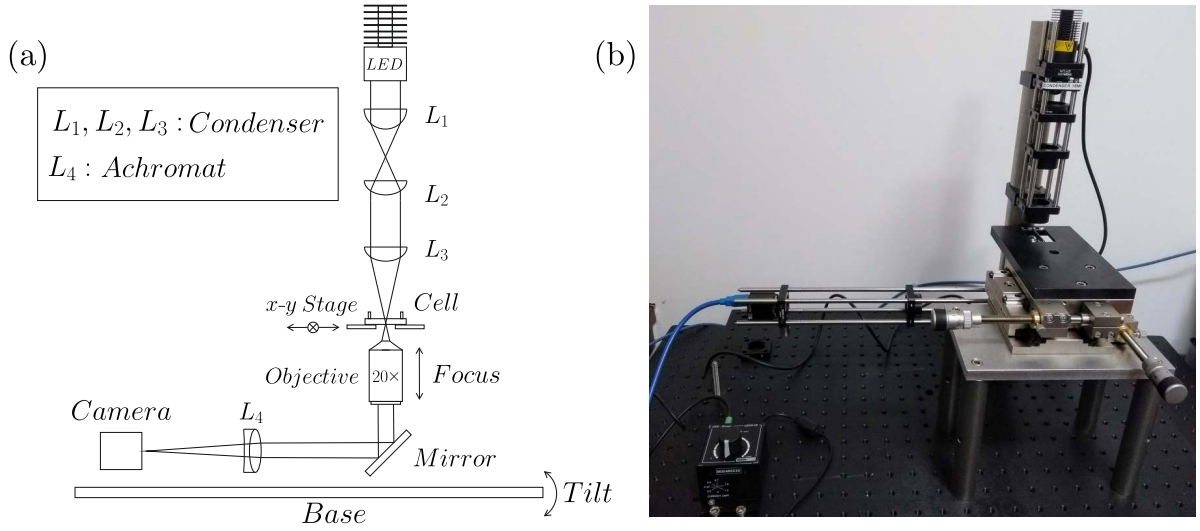


Figure 2.8: (a) A schematic of the optical and major components in the tilt set-up. (b) An image of the tilting microscope (when in use the horizontal arm is covered to minimise external light altering the image the camera collects).

image is focused down onto the camera chip by an objective. The camera used in all cases is a Ximea XiQ CMOS which has an image resolution of 2048 × 2048, and images are captured at rates between 20 Hz to 1/60Hz. The objectives (Olympus), have magnifications of 20×, 40×, and 50×; all are air objectives and have long working distances allowing for imaging through the relatively thick Hellma cell base.

The first of the three microscopes is an Olympus CKX41, used in chapters 3 and 4, for general imaging and in longer experiments in which the absence of gravitational drift is vital. This drift is avoided through the use of an actively damped Newport pneumatic optical table with adjustable legs. The table is levelled by changing the height of each of the legs until a dilute sample of colloidal particles shows negligible drift.

The second of the three microscopes, used in chapter 7, is a custom made inverted microscope with an adjustable base allowing for a tilt to be created in either x- or y-axes. Particles placed on the microscope will experience a low gravitational field parallel to the base of the cell and if left for enough time, a sedimentation-diffusion equilibrium will be reached. Altering the angle allows for a wide range of gravitational heights and thereby height profiles to be made. A diagram of the microscope can be seen in 2.8 (a). Lenses L_1-L_3 create a Köhler illumination to evenly light the sample. An x-y stage that holds the sample allows for precise movement of the cell such that a sequence of overlapping time series can be taken and re-stitched back together to probe an area larger than the field-of-view.

The third of the three microscopes, used in chapters 5 and 6, is also a custom made system, which incorporates an optical trapping set-up [139]. The microscopy part of this a standard microscope, with the lens set up identical to that of the tilt microscope in figure 2.8, but reversed with the illumination from below and imaging from above.

2.2.3 Optical Trapping

Optical trapping is the application of coherent laser light focused down and used to hold a microscopic dielectric object in place [140]. When a particle sits in a focused optical trap, there are two forces acting upon it: the gradient force, F_G, and scattering force, F_S. The origin of F_G is due to the difference in refractive index between the particle and the medium and the Gaussian profile of the laser. On the first count, laser light will be refracted when it enters and leaves the colloid, and doing so changes the photon's momentum. This can be seen in figure 2.9 (a), where two rays of light near the focus of the beam are refracted. To conserve momentum, a reactive force must act on the colloid. Due to the Gaussian profile of beam intensity, when the particle is offset from the focus the resultant forces from all the rays are unbalanced and lead to a total gradient force (seen in figure 2.9 (b)) towards the focus of the beam [141]. The scattering force pushes the particle in the same direction as the laser, due to radiation pressure caused by photons hitting the surface of the colloid [142]. In the case of the set-up used in this thesis, the sideways components of F_G are the most relevant, as the particles are pushed against the surface of the cell by the scattering and gravitational forces, outweighing the upwards component of the gradient force, as is shown in figure 2.9 (b).

In this thesis, we apply optical trapping using the set-up detailed in 2.9 (c) and pictured in 2.9 (d). In the schematic, the left-hand side shows the upright optical microscope section, with Köhler illumination from below, and a 50× objective above the sample with the image passing through dichroic mirror M_2 to reach the camera. The sample sits on a manual x-y stage, for finding suitable areas in the sample to investigate, and an automated translational piezo-electric stage that can be set to move at a constant velocity in steps of 0.4 nm and has a range of 200 µm in x- and y-directions. The optical trap is controlled on the right-hand side of the diagram. The infra-red 1064 nm laser first passes through a $\lambda/2$ waveplate, which rotates the polarisation of the light, thereby leading to a reduction in intensity after the polarising beam splitter (PBS). The beam is expanded by lenses L_7 and L_8 before hitting the acousto-optic deflector (AOD).

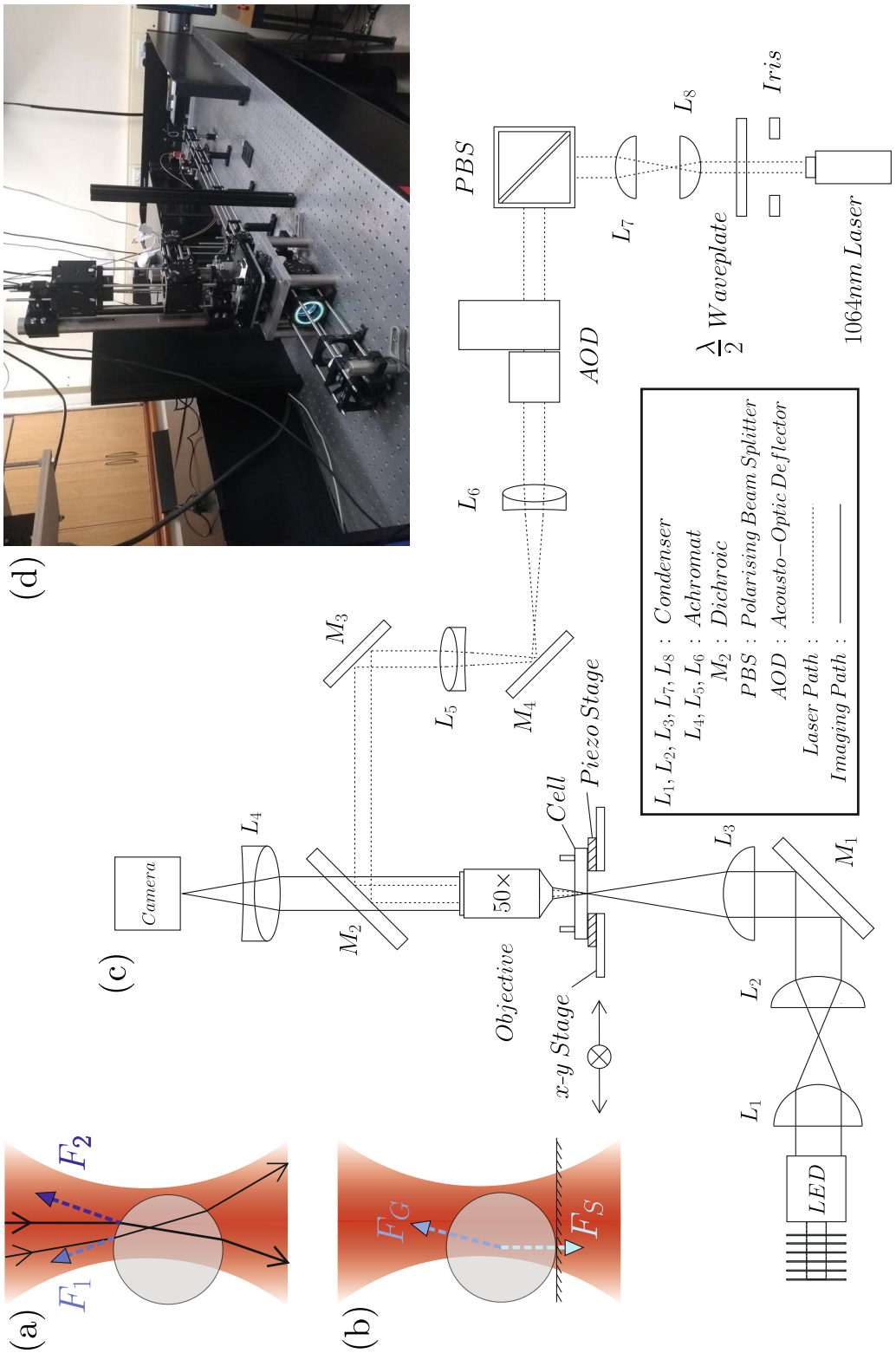


Figure 2.9: (a) A colloidal particle in an optical trap with two refracted rays, and the associated forces for each ray. (b) The total forces acting upon the particle, with the wall of the sample cell drawn in. (c) A schematic of the optical tweezing microscope. L_n is a lens and M_m is a mirror. For simplicity, the illumination path has not been drawn and relative distances are not to scale. (d) is an image of the constructed optical tweezing microscope.

The AOD utilises a TeO_2 crystal, and diffracts the beam and with the first-order peak being collected. The crystal is precisely vibrated by an acoustic wave using piezo-electric transducer, which creates a standing wave, with its wavelength controlling the position of this peak [143]. Therefore, the position of the beam once it reaches the sample can be remotely controlled. After the AOD, the beam makes its way to the back of the objective, where it is focused down to the same point as the focus of the image, thereby allowing for optical trapping.

2.2.4 Image Analysis

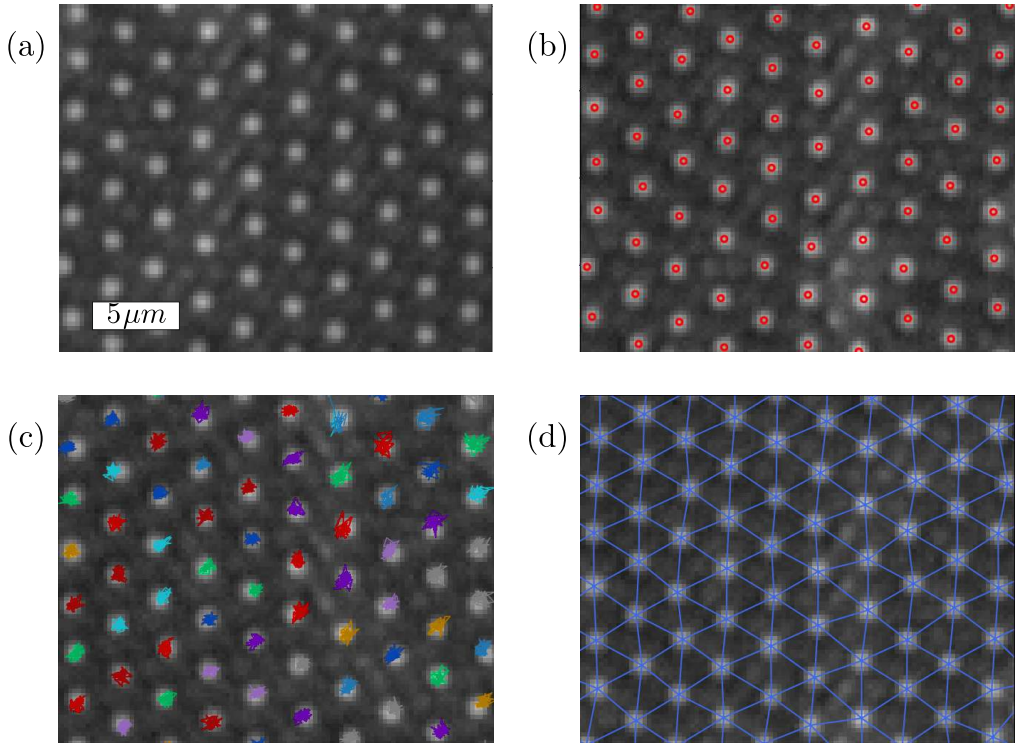


Figure 2.10: (a) The raw image before analysis. (b) Coordinates of found particles based on Gaussian fit. (c) Trajectories of particles after linking successive frames. (d) Delaunay triangulation for neighbour finding from the coordinates.

The images from video microscopy are relatively straightforward to analyse because each colloidal particle appears as a bright spot surrounded by a darker ring (see figure 2.10 (a)). Due to the angle of incidence of the rays of light onto the surface of the spherical particle, light nearer the central axis of the sphere is refracted towards the very centre whereas light further away is reflected off. Hence, light is concentrated at the centre of the particles and the dark ring appears due to less light being transmitted compared to the background.

Image analysis is completed using the Trackpy module of Python [144], which utilises algorithms written in IDL by Crocker and Weeks [145] developed from the paper of Crocker and Grier [146]. This method inputs an image of bright dots against a dark background and first applies a bandpass filter to smooth the image and subtract the background. Secondly, the method searches for 2D Gaussian bright spots, finding the centres of the dots. This is plotted in figure 2.10 (b). A time series of these coordinates can be made, with linking between frames allowing for the tracking of particles in time; examples of such trajectories are shown in 2.10 (c). Particles can be differentiated in size by the properties of the fitted Gaussian. Often noise or interstitials in the crystal may be accidentally found and must be filtered by size, eccentricity or brightness and even filtered by minimum trajectory length. In the case of dense systems, nearest neighbour finding is often of great importance for calculating crystallinity, tessellations or collective motion. To achieve this a Delaunay triangulation is performed to create a tessellation of adjacent triangles, see figure 2.10 (d). From the connectivity we can elucidate a particle's neighbours.

2.3 Computer simulations

2.3.1 Brownian dynamics simulations

In this thesis we use Brownian dynamics (BD) simulations to compliment our colloidal experiments. The advantage of BD simulations over Monte-Carlo simulations is that high density systems can be probed more easily [147]. The basic principle of BD is to apply the Langevin equation (equation 2.1) to a system of interacting particles (in this case mimicking our colloids). The system is considered overdamped, and as such the inertial term is ignored, leading to:

$$0 = \vec{F} + \vec{f}(t) - \xi\vec{v}(t). \tag{2.22}$$

Rearranging, the corresponding velocity is calculated:

$$\vec{v}(t) = \frac{1}{\xi}\left[-(\nabla\vec{U_p}(\vec{r}) + \nabla\vec{U_e}(\vec{r})) + \sqrt{2\xi k_B T}\vec{\eta}(t)\right], \tag{2.23}$$

where $\vec{U_p}(\vec{r})$ is the potential energy due to other particles, $\vec{U_e}(\vec{r})$ is the potential due to external forces such as gravity or optical traps, and $\vec{\eta}(t)$ is a Gaussian probability distribution function

which determines the Brownian motion. This function is defined such that the average value $\langle\vec{\eta}(t)\rangle = 0$ and the correlation function $\langle\vec{\eta}(t)\vec{\eta}(t')\rangle = \delta(t-t')$, i.e. the Kronecker delta [148]. For a small time-step Δt, $x(t+\Delta t) \approx x(t)+\frac{dx}{dt}\Delta t$, and in this discrete version $\langle\vec{\eta}(t)\vec{\eta}(t')\rangle = \delta(t-t')/\Delta t$ [147]. Hence:

$$\Delta\vec{r} = -\frac{D_0}{k_BT}(\nabla\vec{U_p}(\vec{r}) + \nabla\vec{U_e}(\vec{r}))\Delta t + \sqrt{2D_0\Delta t}\vec{\eta}, \tag{2.24}$$

with the diffusion constant at infinite dilution $D_0 = k_BT/\xi$ (equation 2.3). Therefore, knowing the equations of inter-particle and external potential, we can iterate over each frame and determine how each particle moves in the time-step Δt.

The BD simulations we use in this thesis are written in C, and other than varying the starting particle configurations and external potentials, all of the programmes have the same skeleton. As the forces cannot be infinite, we approximate hard spheres with a softer, but repulsive, pair-wise Weeks-Chandler-Andersen (WCA) potential [149]:

$$U_{WCA}(r)/k_BT = \begin{cases} 4(\epsilon/k_BT)\left[\left(\frac{\sigma_{ij}}{r}\right)^{12} - \left(\frac{\sigma_{ij}}{r}\right)^{6} + \frac{1}{4}\right] & r \leq 2^{1/6}\sigma_{ij} \\ 0 & r > 2^{1/6}\sigma_{ij} \end{cases}, \tag{2.25}$$

where σ_{ij} is the average particle diameter of the particles i and j, and ϵ is the energy scaling constant. This is a standard Lennard-Jones potential that is shifted upwards by ϵ such that the potential is entirely repulsive, only applying when particles are close enough that the repulsive $1/r^{12}$ term dominates. In all of our simulations, we always set the energy scale $\epsilon/k_BT = 40$, $D_0 = 1/\sigma$ and $\Delta t = 10^{-5} = 0.039\tau_B$ (where τ_B is the Brownian time of a particle for which $\sigma = 1$). The calculation of inter-particle potentials is simplified by dividing the simulation area into a grid of square cells, into which particles are sorted into based on their positions. To save on computation time, the pair-wise potential is only calculated between a particle and the particles in the 8 cells adjacent to the original particle's cell.

2.3.2 Monte Carlo simulations

In this thesis we use Monte Carlo (MC) simulations to examine systems under equilibrium and particles with hard disk potentials. Phase space is sampled randomly, and this method works by taking an initial configuration of the system and applying a Markov chain (a sequence of events

chosen by probability).

In the case of modelling our colloidal systems, this takes on the guise of particles exploring the space using the Metropolis method [150]. The simulation is started with the particles being given an initial configuration. After this, we randomly cycle through all of the particles. Each particle is given a random trial position within a box of side length $2\delta r_m$, where δr_m is the maximum permissible distance a particle can move. Whether a trial is accepted or not is dependent upon the relative energies of the initial, i, and trial, t state [147]. If there is a decrease in the total energy of the system, the move will be accepted. If there is an increase in energy, the probability of the move is based on the Boltzmann factor:

$$s_{it} = \min[1, \exp(-[U_i - U_t]/k_B T)]. \tag{2.26}$$

Essentially this means a number is randomly generated between 0 and 1. If this is less than the Boltzmann factor then the move is accepted and the uphill energy move is accepted, otherwise it is rejected and the particle retains its current position.

In the case of our simulations we also introduce a resizeable simulation box. Small MC alterations in the box size can allow for the total energy of the system to decrease and might also provide alternative pathways for the phase space to be explored and assist with equilibration [151]. As we aim to examine hard disks, the energetic requirement for trial moves becomes trivial; an overlap between particles will be rejected as the change in energy is infinite. The only energy that must be accounted for will be due to an external field.

Acknowledgements

Josh Abbott-Scott, Arran Curran, Taiki Yanagishima and Miranda Bell-Davies are thanked for practical assistance. Berend van der Meer is thanked for assistance with simulations.

Chapter 3

Crystallisation and grain growth in impurity-doped colloidal monolayers

Abstract

In this chapter, we examine how the dynamics of crystallisation and grain growth are affected by dopant concentration. We utilise a quenched monolayer of hard sphere colloidal particles, doped with larger impurities. We find experimental evidence that evolution of the characteristic length-scale with time is unaffected by the weakly quenched disorder, created by dopant area fractions up to 10%. We find that both initial crystallisation, subsequent grain growth and dependence on misorientation are frustrated by the presence of impurities. We finally derive a model combining the two mechanisms of domain growth to accurately describe the average grain size evolution.

3.1 Introduction

The inclusion of impurities into a growing crystal leads to a marked change in the dynamics of the system and can be a powerful means of controlling its microscopic structure, which is relevant to a wide variety of fields ranging from geological molten rocks [152], freezing ice in glaciology [153] and many types of manufactured materials. Doped materials with a wide variety in chemical composition have been the focus of many investigations [26, 31, 154–156], all aiming to tailor macroscopic properties such as strength, superplasticity, embrittlement, or thermal and electric conductivity [157–162]. While most materials have complex structures, often the dynamics of crystal growth can be generalised and show similar scaling and impurity pinning behaviour to other physical phenomena including phase transitions in spin glasses and ferromagnets, and spinodal decomposition [163–166].

To complete the whole picture of doped grain growth after a quench, both the primary and secondary steps of crystallisation should be accounted for [26]. Primary crystallisation consists of nuclei which grow out of the the melt until contact is made with another boundary. These could either be differently orientated domains or dopant particles. The resultant texture of the polycrystal is then driven to increase domain size in the secondary growth phase, minimising the total free energy by reducing the total length of the boundary network. Dopants segregate in the grain boundaries [24,167], which stabilises and reduces the mobility [168,169], slowing grain growth. While the growth of randomly bounded domains using Ising or Potts models is well established, it remains non-analytical [170–172] and the introduction of impurities complicates matters, due to pinning of domain walls [173–175], slowing the dynamics and obfuscating further any analytical growth law [172].

Colloidal systems have already been shown to provide a good entryway to investigating crystallisation whilst grain growth dynamics in undoped colloidal monolayers have been investigated [69,114,176], with [69] showing a strong dependence on the misorientation character of the grain boundary network. Colloidal monolayers have also been utilised to study the segregation of impurities [24, 168, 177, 178], so a pairing of the two should be greatly insightful into how dopants affect grain growth.

In this chapter we examine the effect of changing the dopant concentration on crystallisation and grain growth of a quenched monolayer of colloidal particles. We find that increasing

the concentration of impurities inhibits curvature driven grain growth and frustrates the amount of crystallisation. We extract a characteristic length-scale and find this is a good measure of average grain size, despite the introduction of disorder due to the impurities. We derive a simple growth law that describes the time evolution of this growing length scale by separately considering the contributions of crystallisation and grain growth. The rate of crystallisation is found to be independent of the impurity concentration and is very well described by the empirical JMAK equation, while grain growth is well described by a power law. The concentration of impurities is shown to have a large effect on the grain growth, reducing the growth exponent significantly. We find our growth law to describe the evolution of grain size very well for all impurity concentrations.

3.2 Theory

The formation and growth of grains after a quench occurs in two steps, formally: crystallisation and grain boundary induced grain growth. Taking a snapshot immediately after a quench, the particles are disordered with a liquid-like structure. Crystallisation is the organisation of the amorphous structure into regions of ordered, crystalline particles, i.e. grains [26].

3.2.1 Dynamic scaling

Dynamic scaling refers to the idea that if one were to take two images of a system in which a patchwork of domains are growing they could scale one of the images by a numeric factor and the resultant images would look similar. More fundamentally however, both images would have identical spatial correlation functions and domain size distributions. This scaling factor is a characteristic length-scale which, crucially, is the only aspect actually evolving in the system [170, 175]. For pure systems, i.e. without impurities, the scaled spatial correlation function is known to be described by Ohta-Jasnow-Kawasaki (OJK) theory [179], and has the form

$$C_{OJK} = \frac{2}{\pi} \arcsin\left(e^{-x^2/2}\right), \tag{3.1}$$

where x is the correlation distance scaled by the characteristic length-scale. This equation has been shown to hold true for grain growth in undoped polycrystalline colloidal systems [69].

However, the introduction of impurities changes the nature of the way in which domains grow. The impurities are distributed randomly, and if they are relatively stationary compared to the domains, they create a matrix of random obstacles the coarsening must develop around. The impurities will pin and slow the motion of the boundaries they come into contact with, As such, random domain walls will be pinned, and the growth of each grain will be radially anisotropic, depending on the amount and distribution of pinned impurities.

The "super-universality hypothesis" theorises that the dynamic scaling seen in pure systems is actually preserved in those with weakly-quenched disorder, i.e. the random matrix of static obstacles. Although this hypothesis has been confirmed in simulations [163, 172, 180], experimental proof of the preservation of dynamic scaling remains elusive.

3.3 Methods

3.3.1 Experimental system and set-up

The experiments in this chapter use a mixture of 2.95 and 6.20μm melamine formaldehyde particles (see table 2.1) in a solution of 20/80%v ethanol/water injected into a Hellma cell. The total concentration of colloids, $\phi_T = \phi_s + \phi_i$ (note we now use ϕ_i to represent the impurity area fraction), is kept constant across experiments at ~ 0.75, with the impurity particle concentration varied: $0 \leq \phi_i \leq 0.114$ and $0.6 \leq \phi_s \leq 0.75$ is changed accordingly to give $\phi_T = 0.75$.

Each experiment begins by tumbling the cell for 30 s to disperse the particles above the bottom of the cell and randomise their positions. The cell is then promptly placed on an Olympus CKX41 microscope with a 20× objective, sat on a levelled pneumatic table, to minimise drift. The sample is imaged at a random position near the centre of the cell, and image recording begins as soon as possible after tumbling, at a rate of 1/60Hz. This allows for the capturing of the point at which all of the particles finish sedimenting and crystallisation may begin. The process of crystallisation and grain growth is then followed for 1000 min (or $\sim 2000 t_B$, where t_B is the Brownian time of the smaller particles). This process was repeated seven times for each of the six values of ϕ_i.

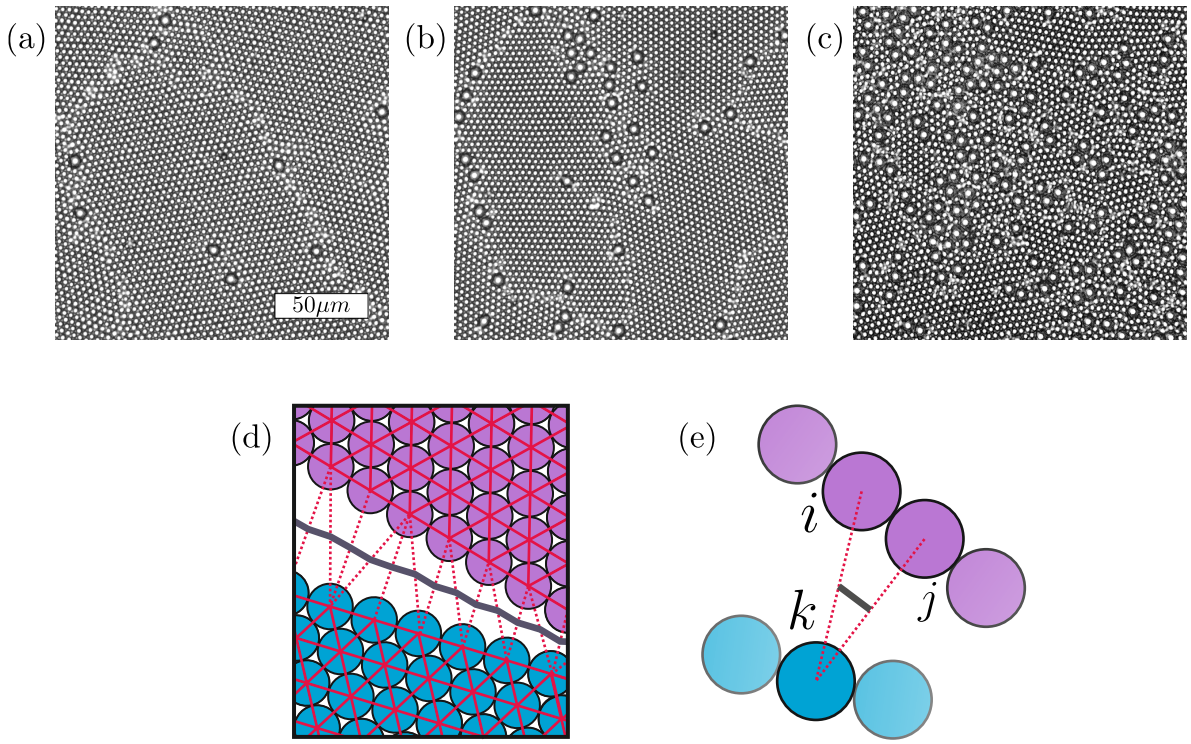


Figure 3.1: (a)-(c) Microscopy images of the impurity-doped colloidal polycrystals formed at $2000t_B$ for different impurity concentrations: (a) $\phi_l = 0.006$, (b) $\phi_l = 0.030$ and (c) $\phi_l = 0.108$. (d) is a visualisation of the process of drawing grain boundaries. The red lines show the Delaunay triangulation, with dashing indicating the connections between particles in different grains. The dark grey line joins the midpoints of the dashed lines and is the resultant grain boundary. (e) Is a zooming in on a single segment of the grain boundary.

3.3.2 Key parameters

The resultant images, examples of which can be seen in figure 3.1 (a)-(c), are then analysed using the methods noted in section 2.2.2, allowing us to examine different key parameters of the system. To examine local crystallinity and orientation, we use the method of averaging over secondary shells of neighbours from Lavergne *et al.* [69], to get a smoothed bond-orientational order parameter $\widetilde{\psi}_6(\vec{r}, t)$. To measure the total crystallinity of the system, x_c, we take the fraction of small particles where $|\widetilde{\psi}_6(\vec{r}, t)| > 0.7$:

$$x_c = \frac{N_s^c(t)}{N_s}, \tag{3.2}$$

where N_s^c is the number of small particles that are crystalline and N_s is the total number of small particles.

To quantify the local orientation of individual particles we again use $\widetilde{\psi}_6$, but this time

utilise its argument:

$$\widetilde{\theta}_{6,j} = \frac{1}{6}\arg(\widetilde{\psi}_{6,j}), \tag{3.3}$$

where $\widetilde{\theta}_{6,j}$ is the smoothed orientation of particle j. By performing a cluster algorithm on the particles based on crystallinity, position and orientation we can then group particles into grains. For a particle to be considered part of a grain it must have 3 neighbours within a distance of 2 particle diameters, where $|\widetilde{\theta}_{6,j} - \widetilde{\theta}_{6,k}| < 0.75°$. From the sorted particles, grain boundaries are drawn in the same manner as detailed in Lavergne *et al.* [69], as previously adapted from Dillmann *et al.* [114]. In short, a Delaunay triangulation is performed on all of the particles, and all but the connections between particles of different grains are excluded. From this 'zig-zag' of connections, the midpoints are joined together to draw the grain boundary. This can be seen in figure 3.1(d). Each connection of two midpoints has its own length l, and is assigned a misorientation, $\Delta\theta$, based on the orientation of the three relevant particles (as is seen in figure 3.1(e)):

$$\Delta\theta = \min\left(\left|\frac{\Delta\theta_{ik} + \Delta\theta_{kj}}{2}\right|, 60° - \left|\frac{\Delta\theta_{ik} + \Delta\theta_{kj}}{2}\right|\right), \tag{3.4}$$

where $\Delta\theta_{xy} = \min\left(\left|\widetilde{\theta}_{6,x} - \widetilde{\theta}_{6,y}\right|, 60° - \left|\widetilde{\theta}_{6,x} - \widetilde{\theta}_{6,y}\right|\right)$.

The grain boundaries form a network which has a total length within the field-of-view of Λ_I. As grain growth is affected by the misorientation of these boundaries, it use useful to subdivide this into the sum of segments of different misorientations:

$$\Lambda_k(t) = \int_k l(\Delta\theta, t)d\Delta\theta, \tag{3.5}$$

where $l(\Delta\theta, t)$ is the total length of segments with a misorientation of $\Delta\theta$, and k is the domain of misorientations under investigation, $I = [0°; 30°]$. To assess how misorientation affects grain growth, we use the grain boundary character distribution (GBCD) to examine the evolution of the structure of the grain boundary network:

$$P(\Delta\theta_k, t) = \frac{\Lambda_k}{\Lambda_I}. \tag{3.6}$$

Articulated, this is the fraction of the total grain boundary length that is reserved by a particular

misorientation. With regards to our experiment, if misorientation does indeed affect grain growth then there will be time evolution of the GBCD, due to certain grain boundaries being eliminated at different rates, owing to higher or lower stabilities.

Finally, we employ the bond-orientational order correlation function:

$$g_6(r,t) = \mathrm{Re}\left(\langle \widetilde{\psi}_6^*(\vec{r}-\vec{r}_0,t)\widetilde{\psi}_6(\vec{r}_0,t)\rangle\right), \tag{3.7}$$

to probe the pairwise correlation of orientations in space, averaged radially and over the ensemble at time t. The decay of this function is a measure of the long-range bond-orientational order. In a polycrystalline system, this can be taken as a measure of average grain size, as pairwise orientational correlations are lost after crossing a grain boundary. To quantify the decay, and therefore grain size, we use the parameter $R_6(t)$ defined such that:

$$g_6(R_6,t) = \frac{1}{2}. \tag{3.8}$$

3.4 Results and discussion

3.4.1 Evolution of impurity-doped colloidal monolayers

Initially, we consider the evolution of the grain structure for the lowest and highest impurity concentrations, with the corresponding images seen in figure 3.2 in the series (a)(i-iii) and (b)(i-iii) representing $\phi_i = 0.005$ and $\phi_i = 0.114$ respectively. The images are divided into coloured and white regions, where a coloured region represents a grain, and white represents a non-crystallised region. The different colours show the orientation of each particle, as seen in the colour bar, while the black lines represent the grain boundaries. In both cases the coloured regions grow into each other, and white regions shrink, indicating simultaneous grain growth and crystallisation. Strikingly, at the higher ϕ_i, the grain size is significantly smaller and grain growth is clearly suppressed. Furthermore, the presence of impurities also clearly affects the crystallisation, which can be inferred from the fact that the amount of non-crystalline area nearly disappears at low ϕ_i (figure 3.2(a)), in contrast to the system at high ϕ_i (figure 3.2(b)), where crystallisation has been frustrated by the high concentration of impurities. We therefore find that impurity doped polycrystals exhibit both crystallisation and grain growth, which are

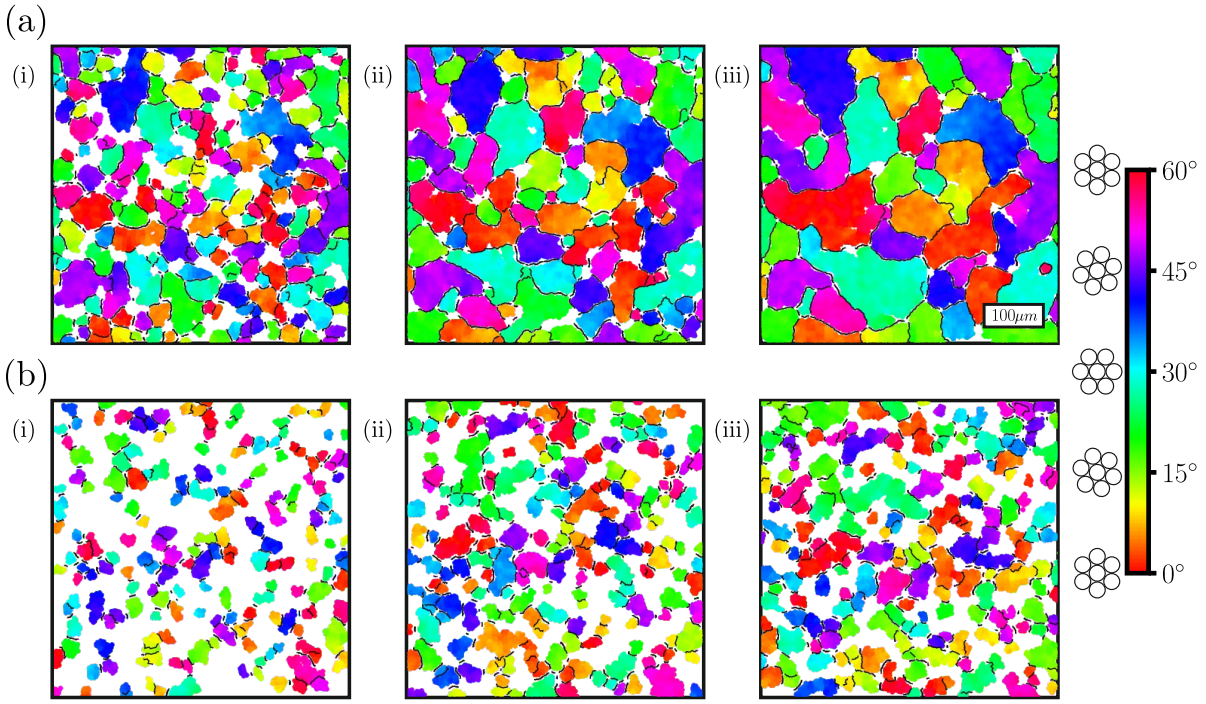


Figure 3.2: Images showing all of the grains in the microscope's field of view, colour-coded by their smoothed orientation field ($\widetilde{\theta}_6$) with drawn grain boundaries. The white areas represent non-crystalline regions, and tend to have high local concentrations of impurities. (a)(i-iii) are images for $\phi_i = 0.005$ at times (i) $20t_B$, (ii) $200t_B$ and (iii) $2000t_B$. (b)(i-iii) are images of $\phi_i = 0.114$ at the same times.

frustrated and slowed respectively by increasing the concentration of impurities.

3.4.2 Dynamic scaling

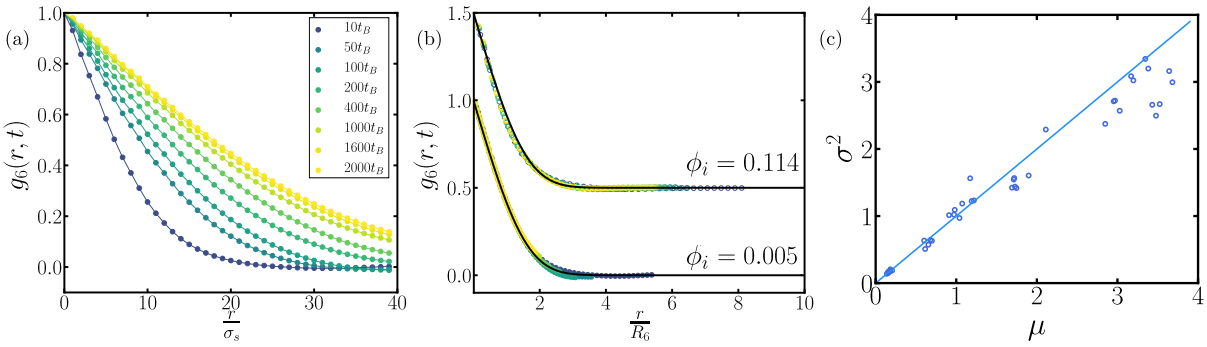


Figure 3.3: (a) Shows a representative decay of the bond orientational order parameter, $g_6(r,t)$, with distance (scaled by the small particle's diameter) and its evolution with time. The parameter R_6 is the value of r at the point at which scaled the correlation function is equal to one half. (b) Shows $g_6(r,t)$, with r scaled by R_6 for two different impurity concentrations, the higher being shifted up the y-axis. The black lines correspond to the theoretical OJK equation for dynamic scaling. (c) From the number of impurity particles per box in a grid of boxes: the mean μ plotted against the variance σ^2. The straight line is $y = x$.

Next, we examine whether the presence of impurities affects the dynamic scaling of the spa-

tial bond-orientational order parameter, $g_6(r,t)$, from equation 3.7. Figure 3.3 (a) shows $g_6(r,t)$ for a single set of experiments ($\phi_i = 0.005$) at different time stamps, denoted by the colour. From this we see the decay length increases with time, indicating the grain size and thereby characteristic length-scale are increasing. To test if dynamic scaling applies, we take $R_6(t)$ as the characteristic length and scale r by this, for the lowest and highest impurity concentrations, as seen in figure 3.3 (b). Clearly for both sets of experiments, all of the curves collapse and fit to the black line representing OJK theory, equation 3.1. Therefore, dynamic scaling still holds to remarkably high ϕ_i, and thereby a large amount of disorder.

To confirm the super-universality hypothesis we next characterise if the introduction of our impurities creates weakly-quenched disorder. Firstly, to be quenched the dopants must be relatively stationary; examining the dynamics of our impurities, on average the total displacement is $\sim 0.5\sigma_l$ or $\sim 3\mu m$ over the course of the entire experimental time-frame. As the length-scale corresponding to grain size is two orders of magnitude larger, we can assume the quenched nature of the disorder. Secondly, we can examine the randomness of the impurity positions, by creating a lattice of finite boxes and counting the number of impurity particles in each. When sequentially placing a number of random points in an area, if each point is allowed to overlap with others, the decision of where to place the next will be independent of the prior decisions. The resultant distribution of particles will follow the Poisson distribution, for which, the mean μ and variance σ^2 are equal. We can therefore check the randomness of the placements of our particles by comparing to this relation, which is shown in figure 3.3 (c), for boxes of dimensions $69.5 \times 69.5\mu$m. We find good agreement with the Poisson distribution at small ϕ_i (where the number of impurity particles per box is low), but at high ϕ_i there is a deviation. This is expected however: the assumption of overlapping points becomes less valid, as the total excluded area already taken up by impurities is higher and the approximation of the independent nature of particle placements breaks down. Therefore, we can affirm that the distribution and dynamics of impurities fits weakly-quenched disorder and we importantly can confirm experimentally that the super-universality hypothesis holds up to impurity concentrations of $\phi_i \sim 0.1$.

3.4.3 Crystallisation and grain growth

Next, we consider the time-evolution of $R_6(t)$ for all impurity concentrations also shown in figure 3.4 (a). Consistent with the qualitative observations made from figure 3.2, at all ϕ_i,

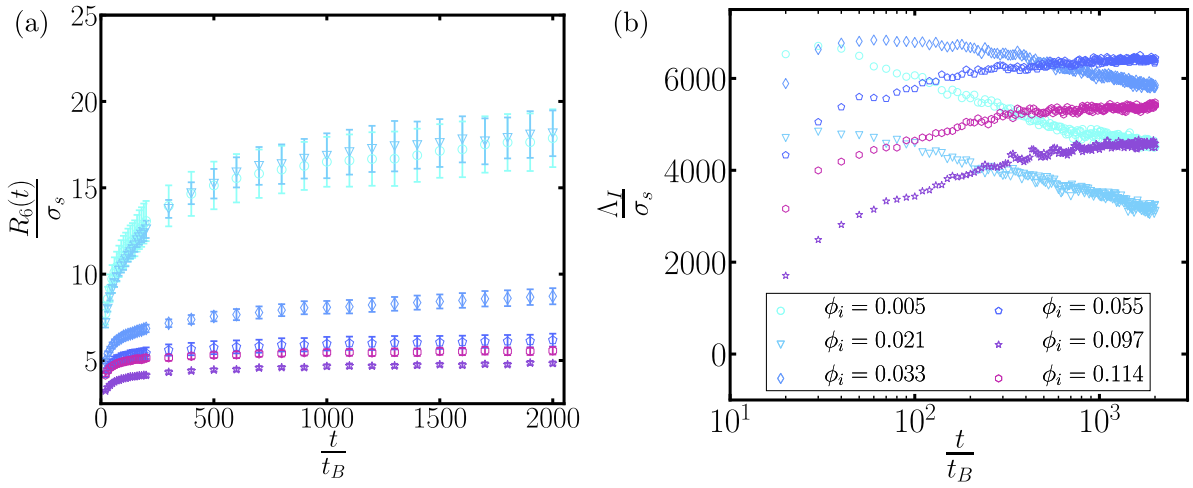


Figure 3.4: (a) shows the evolution of R_6 and therefore a measure of average grain size with time. The different markers represent different impurity concentrations as noted in the key in (b). The error bars represent the standard deviation from the seven runs of each experiment. (b) shows the evolution of the total grain boundary length in the field-of-view, Λ_I with time.

an overall increase in R_6 is observed, with a fast initial growth rate that slows down after $\sim 200t_B$. This is due to the fact that at earlier times fast crystallisation dominates, while at later times slower grain growth becomes dominant. The similar timescale for all ϕ_i, over which this transition occurs, suggests that the rates of crystallisation are unaffected by impurities. However, the magnitude of the average grain size reached in the crystallisation-dominated initial stage is clearly affected, with $R_6(t)$ reaching significantly lower values for higher ϕ_i at $\sim 200t_B$. Moreover, at longer times where crystallisation ceases to be dominant, the grain size plateaus for the highest three impurity concentrations ($\phi_i = 0.055, 0.097, 0.114$), indicating that grain growth is arrested. For the lower impurity concentrations ($\phi_i = 0.005, 0.021, 0.033$), the average grain size keeps increasing with time, indicating that grain growth is not arrested. Therefore the presence of impurities in the grain boundaries impedes grain growth significantly.

Because the time dependence of R_6 does not distinguish between crystallisation and grain growth, we also analyse the time evolution of the total grain boundary length, $\Lambda_I(t)$, which is shown in figure 3.4 (b) for the different impurity concentrations. Interestingly, quite differing and non-monotonic behaviour for the various impurity concentration is observed. In particular, we observe two regimes depending on the value of ϕ_i. For the lower impurity concentrations, there is initially a sharp increase followed by a clear and consistent decrease in the total grain boundary length as a function of time. This corroborates that at early times crystallisation dominates, as when new crystallites appear, they subsequently grow until their edges meet,

leading to an increase in the total grain boundary length. After this, grain growth dominates, which leads to annihilation of grain boundaries, and hence a decrease of Λ_I as a function of time. In contrast, for the higher impurity concentrations, Λ_I increases at all times, indicating that crystallisation dominates throughout and that grain growth is suppressed by the high impurity concentration. This can be rationalised by the fact that these impurities lead to pinning of grain boundaries, which is expected to depend on the total number of impurities within the grain boundary network [181]. Increasing the impurity concentration will increase the number of impurities in a grain boundary and therefore slow grain growth even more. Therefore, when ϕ_i is large enough, grain growth is suppressed and crystallisation dominates.

3.4.4 Grain boundary character distributions

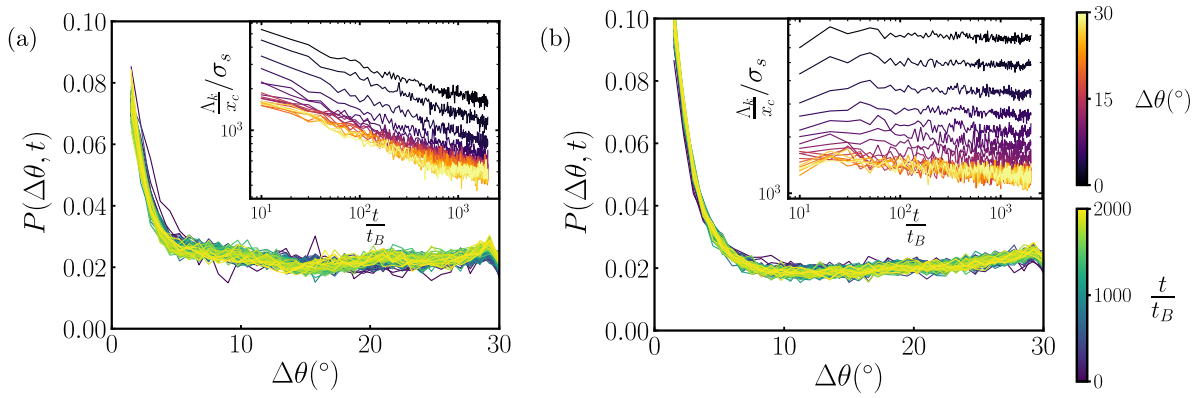


Figure 3.5: (a) shows the time evolution of the grain boundary character distribution (GBCD) averaged over the three lowest ϕ_i.(b) shows the GBCD averaged over the three highest high ϕ_i. The insets show the time evolution of the sum of the *absolute* grain boundary lengths binned by misorientation, for the respective set of ϕ_i.

Now, we consider the grain boundary character distribution (GBCD). Figures 3.5 (a) and (b) show the GBCDs averaged over the three lowest and three highest ϕ_i, respectively. In both cases there is little change over the whole experimental time-frame, which must mean the relative length of each misorientation in the GB network remains constant and the contribution to grain growth due to GBs is equal across all misorientations.

To show how the network evolves, we take the absolute total grain boundary length (Λ_I), and split it into bins of range k for different misorientations, giving lengths Λ_k (see equation 3.5). These are shown in the insets of figures 3.5 (a) and (b), but note that Λ_k is divided by the rate of crystallisation x_c, so only shows network evolution due to grain growth (this will be explained in section 3.4.7). In the inset of (a), the decrease in Λ_k for low ϕ_i shows that there is

grain growth, with all misorientations exhibiting a similar rate, shown by similar line gradients. In the inset of (b) for high ϕ_i, the system is arrested, as Λ_k is constant for all $\Delta\theta$. Hence, for the entire range of ϕ_i across these experiments, there is no dependence of the distribution of misorientations on the rate of grain growth.

The fact that in this impurity-doped system there is no misorientation dependence is in direct contrast with the monodisperse case [69]. In the pure system, the GBCD gradually skews towards small angle grain boundaries (SAGBs), where $\Delta\theta < 15°$, meaning grain growth is mostly driven by large angle grain boundaries (LAGBs), where $\Delta\theta \geq 15°$. This is because LAGBs have a greater grain boundary stiffness, Γ [26], leading to faster grain growth, as the curvature-based driving force of GB motion is proportional to Γ. The absence of this emerging skew in these experiments is due to impurities embedded in the GB, with these particles impeding grain boundary motion due to the drag force of Zener pinning. The magnitude of drag per GB is dependent on the boundary's misorientation; specifically, there is a proportionality between the pinning force and the grain boundary stiffness Γ [169, 181]. Therefore the oppositional forces of GB driving pressure, and drag due to impurities are *both* proportional to Γ, meaning LAGBs motion is more greatly resisted. Therefore the skew seen in the pure case is flattened out when impurities are added, hence the lack of evolution of the GBCD with time. Remarkably, this misorientation independence holds true for the lowest impurity concentration, indicating the Zener drag is always an important factor to consider.

3.4.5 Growth law

As we know that domain growth in this system is dependent upon both crystallisation and grain growth, we can develop a simple model to describe the evolution of $R_6(t)$. Conveniently, as shown in the previous section, there is no misorientation dependence of the grain growth, so we can treat all grain boundaries as equal.

We start by noting that the total area taken up by N circular grains, A, can be expressed in terms of of the average radius of a grain, R, as $A = N\pi R^2$. The crystallinity (see section 3.3.2) is quantified by the fraction of crystalline particles, x_c, which is related to the area via $A = A_T x_c$, where A_T is the total area of the field-of-view. Hence, x_c is given by

$$x_c = \frac{N\pi R^2}{A_T}. \tag{3.9}$$

Next, we have to account for the formation of grain boundaries, which form when two grains become adjacent. A grain can either be adjacent to regions of crystalline or amorphous particles. Parts of a grain adjoining to amorphous regions will tend to grow into this area via crystallisation. Parts of a grain adjacent to crystalline regions will grow due to grain growth. Therefore, splitting the perimeter of a grain, P, into a fraction beside amorphous regions and a fraction beside crystalline regions allows us to determine the relative potentials for crystallisation and grain growth. The fraction of the perimeter of a single grain that is taken up by grain boundaries is $x_g = P_{GB}/P$, where P_{GB} is the length of perimeter adjacent to another grain. Taking an average over all grains gives us the fraction of all grain perimeters that are adjacent to other grains, $\overline{x}_g$. In the case of a system that is fully polycrystalline and only grain growth occurs, $\overline{x}_g = 1$, while in the case of isolated grains (i.e. where no GB induced growth will occur) $\overline{x}_g = 0$.

The total grain boundary length, Λ_I, can now be written in terms of $\overline{x}_g$, as $\Lambda_I = \frac{1}{2}\overline{x}_g P_T$, with P_T being the summed perimeter of all of the grains, and the factor of $1/2$ is to prevent double counting. Assuming circular grains, $P_T = N2\pi R$, where again, R is the average radius of the grains and N the total number of grains. Hence,

$$\Lambda_I = \pi N \overline{x}_g R. \tag{3.10}$$

By eliminating N from equations 3.9 and 3.10, the average grain size can be written as:

$$R = \frac{A_T x_c}{\Lambda_I}\overline{x}_g. \tag{3.11}$$

Next, we need to find an expression for $\overline{x}_g$. Figure 3.6 (a) is a schematic of a grain and its environment and (b) shows a idealised version of this. The bold section of the perimeter is the amount adjacent to other grains. The fraction of this in the total perimeter is $\overline{x}_g$. The white sections of the ring are non-crystalline particles, the light-blue sections of the ring are the crystalline regions around the grain, whereas the dark-blue sections are the grain boundary particles. In this approximation we ignore the grain boundary particles, hence we only need to relate $\overline{x}_g$ to the fraction of light-blue regions within the ring. This is simply x_c, the bulk fraction of crystalline particles.

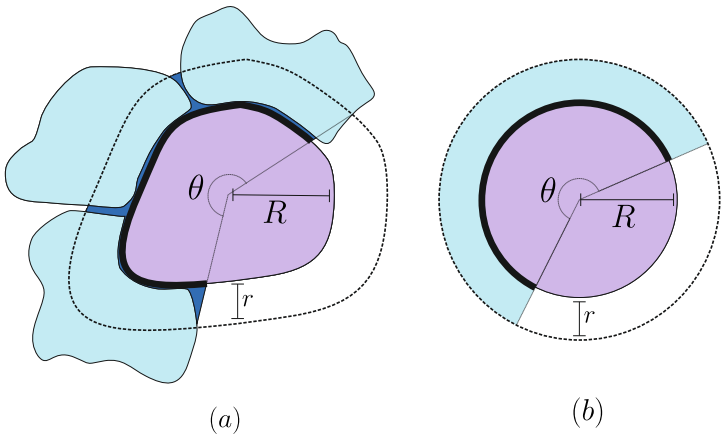


Figure 3.6: (a) A schematic of a grain and its environment. The fraction of the perimeter adjacent to other grains is in bold. R is the radius of the average grain, and r is the cut-off distance for which two grains are classed as adjacent, hence the dashed outer line bounds the region in which grain boundaries exist. (b) is an approximation of (a) as an idealised system, where the average grain is a circle, and the surrounding grains form a perfect ring around it. θ is the angle corresponding to the arc of the grain that forms the grain boundary. In the ring, the white regions represent non-crystalline particles, and light-blue the crystalline particles.

The length of an arc of a circle is $I = \theta R$, and the perimeter is $2\pi R$, hence:

$$\overline{x}_g = \frac{I}{2\pi R}. \tag{3.12}$$

The total area of the ring can be expressed: $A = \pi\left[(R+r)^2 - R^2\right]$. The area of a sector is $\frac{1}{2}\theta r^2$, so the area of the blue part of the ring is: $B = \frac{1}{2}\theta\left[(R+r)^2 - R^2\right]$. Hence the ratio of the blue sector to total ring area is:

$$\frac{B}{A} = \frac{1}{2\pi}\theta = \frac{I}{2\pi R}. \tag{3.13}$$

This is the ratio of crystalline to non-crystalline particles, meaning

$$\overline{x}_g \approx x_c. \tag{3.14}$$

The average grain size from equation 3.11 can now be rewritten:

$$R \approx A_T \frac{(x_c)^2}{\Lambda_I}, \tag{3.15}$$

meaning the growth of R is entirely described by the time-dependence of the fraction of crystalline particles x_c, which accounts for crystallisation, and the total grain boundary length Λ_I, which accounts for grain growth.

3.4.6 Crystallisation

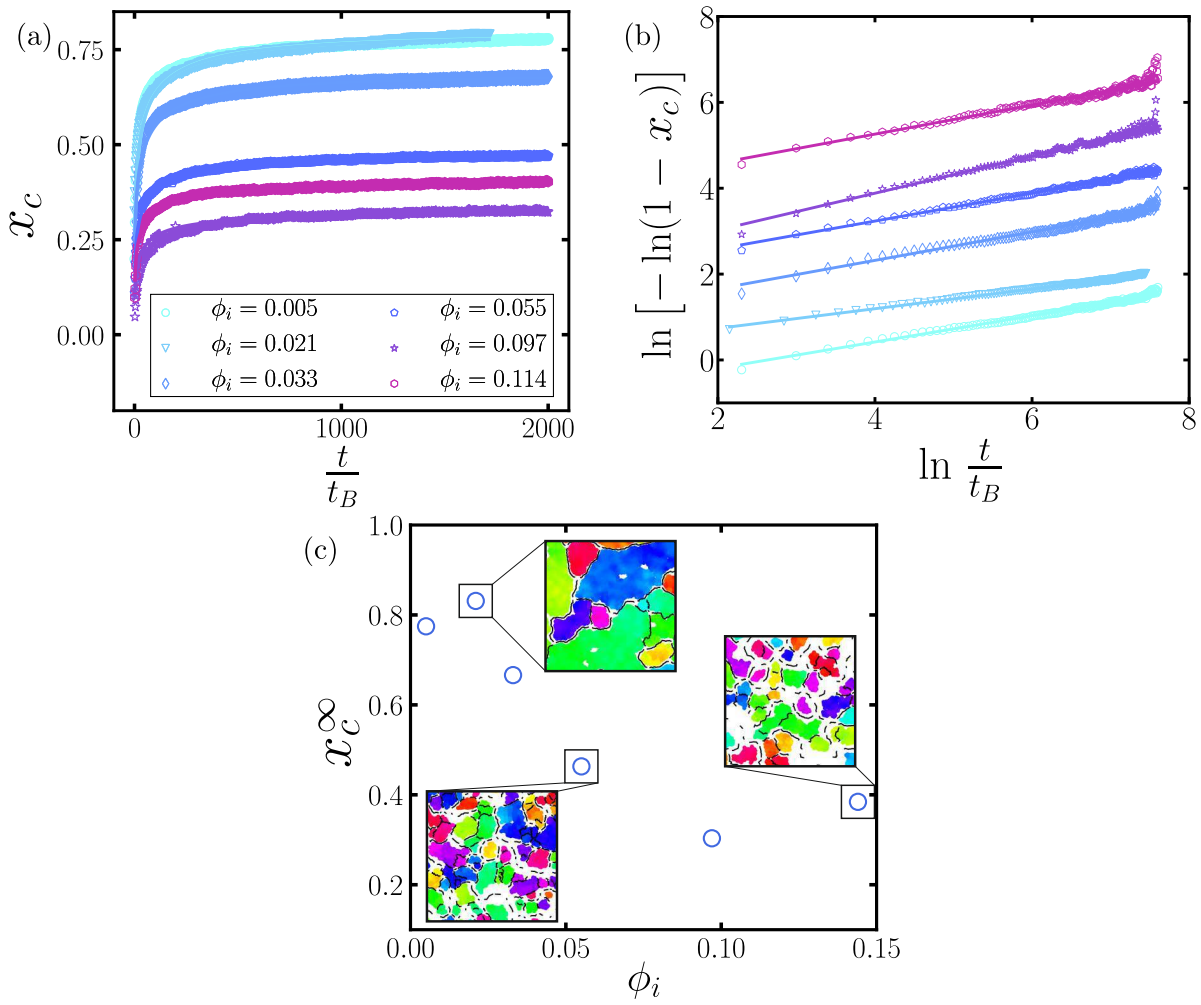


Figure 3.7: (a) shows the fraction of crystalline particles, x_c, over time. (b) shows the fit to JMAK, with curves moved up the y-axis for clarity. (c) shows the fraction of crystalline particles as $t \to \infty$, with inset images showing a representative patchwork of grains from the highlighted sets of experiments.

In this section we examine the evolution of crystallisation in each of our experiments. Firstly, the time-dependence of x_c is measured directly from our experiments, seen in figure 3.7 (a). This sharply increases with time before it reaches different plateaus for the different impurity concentrations. As shown in figure 3.7 (c), the final fraction of crystalline particles, x_c^∞, strongly decreases with increasing ϕ_i, which is a consequence of the frustration induced by the presence of impurities [104, 168]. We quantify these data by fitting them with the classical Johnson-Mehl-Avrami-Kolmogorov (JMAK) model [31]:

$$x_c = x_c^\infty[1 - \exp(-kt^n)], \tag{3.16}$$

with k and n the Avrami coefficient and exponent, respectively [31], and x_c^∞ the final fraction of crystallised particles. To find the parameters, we apply a double logarithm: $\ln[-\ln(1-x_c)] = n\ln t + \ln k$, which is plotted in figure 3.7 (b) for the different ϕ_i. Interestingly, the values of k and n are similar for all impurity concentrations, which suggests that the rate of crystal growth is independent of impurity concentration, consistent with the similar initial slopes in 3.4 (a).

The values of k and n are found to give an average over all impurity concentrations of 0.353 ± 0.017 and 0.327 ± 0.010 respectively. Though the value of the Avrami exponent in our case is much lower than the typical integer values found [31], similar values have been reported previously for a quasi two-dimensional (2D) system of monodisperse paramagnetic colloidal particles [176], 2D sheet growth in three-dimensional (3D) space [182], and atomistic alloys [31].

3.4.7 Measuring grain growth

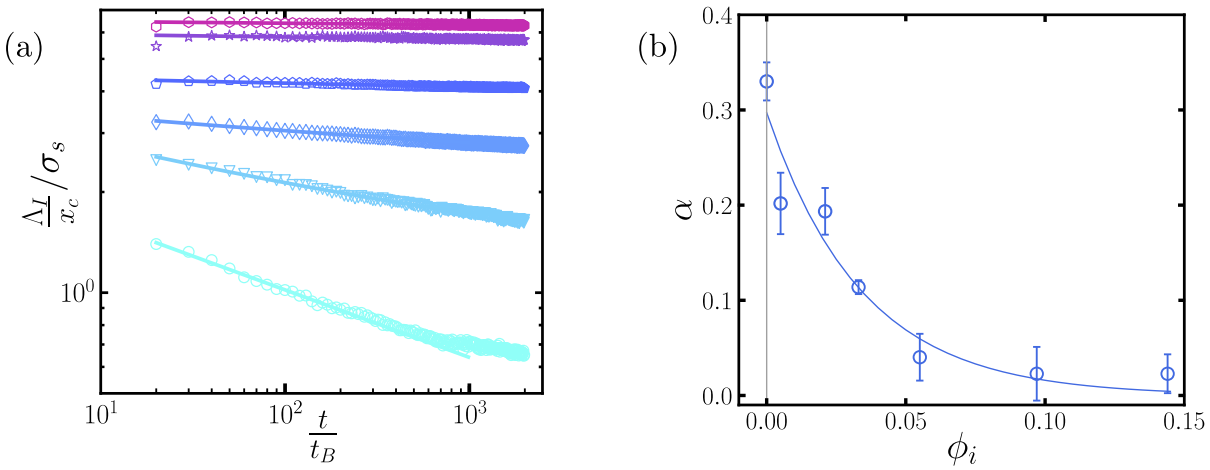


Figure 3.8: (a) shows a log-log plot of Λ_I/x_c against t. The different datasets are again moved up the y-axis for clarity and the markers correspond to the key in figure 3.7 (a). (b) shows the grain growth exponent α (from equation 3.20, measured from (a)), against the impurity particle concentration. The curve is an exponential fit and $\alpha(\phi_i = 0)$ is taken from Lavergne *et al.* [69].

Next, to find the time-dependence of the total grain boundary length, Λ_I, we first consider a fully polycrystalline system, where only grain growth contributes to the change of $R(t)$. In this case, the expression for $R(t)$ is typically given by a power law:

$$R^\star(t) \propto t^\alpha, \tag{3.17}$$

where the * refers to a fully polycrystalline system. From equation 3.15, the total grain boundary

length is then simply the ratio of the total area and the grain size $R^{\star}(t)$,

$$\Lambda_I^{\star}(t) = \frac{A_T}{R^{\star}(t)}. \tag{3.18}$$

In our current system, i.e. with impurities, we have a total grain boundary length $\Lambda_I(t)$ that is measured taking into account adjacent crystalline regions and ignores non-crystalline regions. Taking $\Lambda_I^{\star}(t)$ as the 'reference' total GB length in a perfect polycrystal, i.e. in the absence of any amorphous regions, then it follows that the ratio of this and $\Lambda_I(t)$ is simply the fraction of perimeters that form grain boundaries, i.e. the previously mentioned parameter $\overline{x}_g$:

$$\overline{x}_g = \frac{\Lambda_I(t)}{\Lambda_I^{\star}(t)} \approx x_c, \tag{3.19}$$

where $\overline{x}_g \approx x_c$ (see section 3.4.5).

Combining equations 3.17, 3.18 and 3.19, one then obtains the following relation for the evolution of the total grain boundary length

$$\Lambda_I(t) \propto x_c t^{-\alpha}. \tag{3.20}$$

Importantly, this means that the total grain boundary length is dependent on both crystallisation (the formation of GBs) and grain growth (the annihilation of GBs). Therefore there can be an increase or decrease in Λ_I depending on which mechanism is dominant, which is consistent with the findings in 3.4 (b).

Figure 3.8 (a) shows a log-log plot of Λ_I/x_c against time, from which it is clear the data sets follow a power law, with the gradient getting steeper for lower ϕ_i. We can measure this exponent and plot α against the impurity concentration ϕ_i, shown in figure 3.8 (b). From this, α clearly decreases with increasing impurity concentration. This implies that by increasing the amount of impurities in the system there is an overall decrease in the rate of grain growth, which is as expected due to the greater pinning force exerted by the impurities on the GBs.

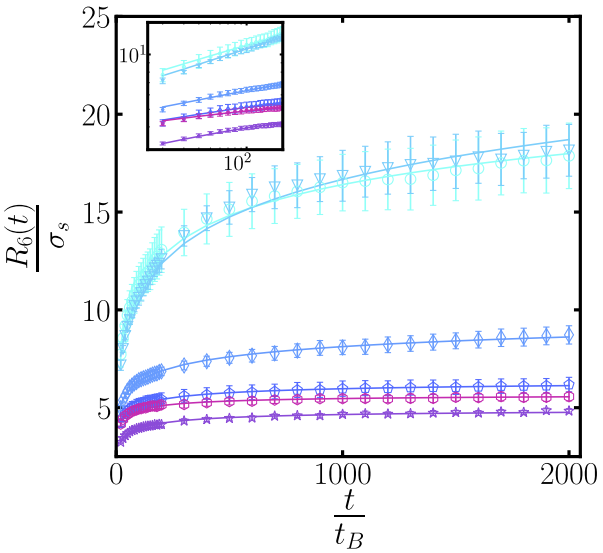


Figure 3.9: This graph shows the grain size evolution from figure 3.4 (a), with our growth law fitted to each experiment. The inset is a log-log plot of the early times (for $0t_B \leq t \leq 200t_B$), to highlight the suitability of the model for all times during evolution.

3.4.8 Grain evolution model

Finally, combining equation 3.11, with equations 3.16 and 3.20 for x_c and Λ_I, respectively, we obtain a growth law for the grain size $R_6(t)$, which is given by the following expression:

$$R_6(t) = A(1 - \exp(-kt^n))t^\alpha + R_6^0. \tag{3.21}$$

As we have found the constants k, n and α in the previous two sections for all of our experiments, the only two fitting parameters are A, which is a proportionality constant, and R_6^0, which is the average grain size at the start of the experiment. As seen in figure 3.9, our data are very well described by the growth law given by equation 3.21. This in turn shows that the time dependence of the grain size in impurity doped systems is dominated by the two phases of recrystallisation: crystallisation and grain growth, both of which exhibit their separate time-dependence and their combination explain the growth of the grain size in our impurity-doped colloidal polycrystal.

3.5 Conclusion

In conclusion, we have studied how crystallisation and grain growth contribute to the evolution of crystalline domains in colloidal monolayers with different impurity concentrations. We have

shown that crystallisation and grain growth are frustrated by the impurities, though the rate of crystallisation is relatively unaffected. The presence of impurities introduces weakly quenched disorder, and up to a relatively high packing fraction of impurities ($\phi_i \sim 0.1$), this does not affect the dynamic scaling of the correlation length $R_6(t)$, thereby confirming the super-universality hypothesis. Finally, we have developed a simple growth law for $R_6(t)$, thereby accounting for the separate contributions of crystallisation and grain growth to the evolution of the grain size. The crystallisation is well described by the JMAK model, while the grain growth follows a power law, with the exponent strongly dependent upon the impurity concentration due to the pinning of the grain boundaries. The growth law for the time evolution of the correlation length agrees very well with our experimental data for all considered impurity concentrations, which quantifies how crystallisation, grain growth and the presence of impurities affects the evolution of the grain size in impurity-doped polycrystalline systems.

Acknowledgements

This work was done in collaboration with François Lavergne, and Balkis Dohni is thanked for helpful discussions.

Chapter 4

Grain rotation in two-dimensional colloidal polycrystals

Abstract

In this chapter we examine the role of grain rotation during grain growth in a two-dimensional colloidal polycrystalline system. We follow single grains by tracking their centres of mass, average orientations, and their grain boundaries' average misorientations. An expression relating angular velocity with grain size and boundary misorientation within the theory of grain boundary sliding is found to describe the system well. Secondly, we examine the rate of grain growth due to rotation driven coalescence, finding the magnitude of rotation to be too small to make an appreciable difference. Finally, we visualise the trajectories of individual particles during grain rotation, and also examine the motion of dislocations in the grain boundaries.

4.1 Introduction

The rotational motion of domains is a feature of systems ranging from rotating superfluids with quantised vortices [183], to protein filaments under muscular contraction [184] to the formation of phases of black holes [185]. At the micro-scale, the torque that generates rotational motion is often the result of an energy gradient along the surface of the body, with examples being micromotors utilising interfacial tension gradients [186], cholesteric droplets rotating with a temperature gradient [187], and electrochemical gradients in motor proteins driving the rotation of bacterial flagella [188]. Grain growth combines rotating domains with micro-scale torque, as crystalline grains rotate due to an energy gradient - namely the grain boundary energy's orientational dependence [189].

Domain growth in polycrystals is typically driven by a reduction in the total interfacial energy in the system. In the case of the domain growth discussed in chapter 3, the reduction of curvature, and thereby grain boundary energy, drives the increase in grain size. However, the rotation of grains is also a means of decreasing the energy of boundaries, through a decrease in misorientation and a reduction in the density of dislocations. With a sufficient rotation, grains can coalesce without the translation of the grain boundary, this is known as grain rotation induced grain coalescence [189–191].

Grain rotations have been observed in atomic experimental systems such as annealing thin films [192, 193], materials under strain [194, 195], and in the coarsening of alloys [196, 197]. There have also been numerous simulations studying the rates and incidence of grain rotation during coarsening [189, 198–201]. In terms of colloidal crystals, grain rotation has also been observed in the coalescence of isolated crystallites [190], and in the shrinkage of grain boundary loops [117, 167]. However, these experiments are not necessarily representative of growth in polycrystals, owing to the contrivance of manipulating the grains via optical trapping. Therefore, we can examine rotation in colloidal polycrystals, which are much more exemplary of metallic structure.

In this chapter we measure and examine the role of grain rotation in a polycrystalline monolayer of colloidal particles undergoing grain growth. We first track grains via their centres of mass, and follow their average orientations, sizes and their grain boundaries' misorientations. We find accordance with the theory set out by Moldovan *et al.* [189], linking rotational velocity

with grain size and boundary energy, and find the result to be consistent with the mechanism of grain boundary sliding [202]. Secondly, we examine the effect that these grain rotations have on the total rate of grain growth and compare to curvature driven growth. Finally, we examine the particle and dislocation dynamics of grain rotation within a grain boundary network, examining the individual trajectories of particles and the motion of dislocations.

4.2 Theory

4.2.1 Angular velocity of rotating grains

In the previous work of Moldovan *et al.* [189], simulation techniques were used to examine the rate of grain rotation driven domain growth in a system with no curvature driven growth, i.e. no grain boundary translation. Firstly, they note that in order to rotate, the energy of the grain boundary (GB) must be anisotropic with respect to orientation, such that there is an overall energy gradient [189,190,192], and spontaneous rotation can reduce the energy of the boundary.

To quantify the amount of rotation in the system, we can examine the angular velocity of grains, ω, by looking at the rate of change of the grain's orientation, $\langle\theta\rangle$:

$$\omega = \frac{d\langle\theta\rangle}{dt}, \tag{4.1}$$

where $\langle\dots\rangle$, denotes the average over all of the particles in the grain. As Moldovan *et al.* [189] suggest, this angular velocity is proportional to a torque (τ):

$$\omega = M(R)\tau, \tag{4.2}$$

where $M(R)$ is a rotational mobility, dependent upon the size of the grain, R. This is suggested to have the form:

$$M(R) = C/R^p, \tag{4.3}$$

with p being an integer and C being a constant dependent upon the width of the GB, grain size and ratio of particle diffusion constants within the lattice and GB [203]. To find the torque driving rotation, we must look at the change in GB energy associated with a particular

change in misorientation of the grain boundary. In a polycrystal, each grain is likely to have multiple neighbouring grains, hence multiple grain boundaries. Each GB will favour a decrease in misorientation towards a lower energy, but this could be in either a clockwise or anti-clockwise direction. Each grain boundary will also generate a different magnitude of torque, due to the dependence of the GB energy on misorientation. We must therefore take the weighted sum of the torques from each GB segment along the perimeter:

$$\tau = \sum_j \Lambda_j \left(\frac{d\gamma}{d(\Delta\theta)} \right)_j , \tag{4.4}$$

where Λ_j is the length of grain boundary segment j, γ is its energy per unit length, and $\Delta\theta$ is its misorientation. It is important to note that the energy gradient has a sign, indicating the preference for clockwise or anti-clockwise rotation. Recalling equation 2.20, which gives us an expression for the GB energy in terms of misorientation ($\gamma = \gamma_0 \Delta\theta[A - \ln \Delta\theta]$, with γ_0 and A being constants), we can differentiate with respect to misorientation:

$$\gamma' = \gamma_0[(A-1) - \ln \Delta\theta]. \tag{4.5}$$

Putting this into equation 4.4 and setting the perimeter for that of a circular grain, $\sum_j |\Lambda_j| = 2\pi R$, we obtain the following expression for the torque τ:

$$\tau = 2\pi R \gamma_0 \left[A_W - \Theta_W \right]. \tag{4.6}$$

Here, we employ weighted averaging of the grain boundary energy gradient γ' and separate it into its two components, A_W and Θ_W, using equation 4.5:

$$\frac{\sum_j \gamma' \Lambda_j}{2\pi R} = \frac{\gamma_0 \sum_j (A-1)\Lambda_j}{2\pi R} - \frac{\gamma_0 \sum_j \ln \Delta\theta_j \Lambda_j}{2\pi R} = \gamma_0[A_W - \Theta_W]. \tag{4.7}$$

Note each individual torque has a sign for clockwise/anticlockwise directions, as will the total torque τ. We take the weighted averages to ensure a separation of the grain size and misorientation dependences, such that we can measure each separately. Thus, combining this equation and equations 4.2 and 4.3, the angular velocity of the grains should follow the expression:

$$\omega = 2\pi C \gamma_0 \frac{A_W - \Theta_W}{R^{p-1}}. \tag{4.8}$$

4.2.2 Grain boundary sliding of circular grains

To understand grain rotation on a particle level, we can use the approach of Moldovan *et al.*, [203], based on Raj and Ashby's work on grains sliding past one-another [202]. In the latter, Raj and Ashby examine the rate at which adjacent grains diffuse parallel to the direction of their planar boundary, due to an applied shear stress $\mathcal{T}$. This model assumes the two grains move at a constant relative velocity v, facilitated by a flux of particles, which is controlled by vacancy diffusion through the grain boundary and the lattice; quantified by the effective diffusion coefficient D [204].

Moldovan *et al.* [203] showed that the equations for linear grain sliding can be applied to grain sliding through the rotational motion of circular boundaries. Their method takes the shear stress $\mathcal{T}$ to be a result of the torque from equation 4.4, and converts the linear velocity to the angular velocity from equation 4.2. They relate the velocities via

$$v = \omega R, \tag{4.9}$$

and the stress to be the force per unit area,

$$\mathcal{T} = \tau / 2\pi R^2, \tag{4.10}$$

as the force is τ/R, with the torque given by equation 4.6.

4.2.3 Dislocations in rotating grains

To understand the emergence of rotation in terms of dislocations, we must examine the Frank formula, which relates the sum of Burgers vectors to a grain boundary and its misorientation. In the example GB shown in figure 4.1 ($\vec{r} = r\hat{t}$), the dislocations' directions, i.e. the Burgers vectors $\vec{b} = b\hat{n}$, where b is the magnitude and $\hat{n}$ is the unit vector normal to the GB, are topologically constrained by the misorientation of the boundary, $\Delta\theta$, and the tilt axis of the grains $\hat{l}$ [205,206]:

$$\sum_i b_i \hat{n}_i = r\Delta\theta(\hat{t} \times \hat{l}). \tag{4.11}$$

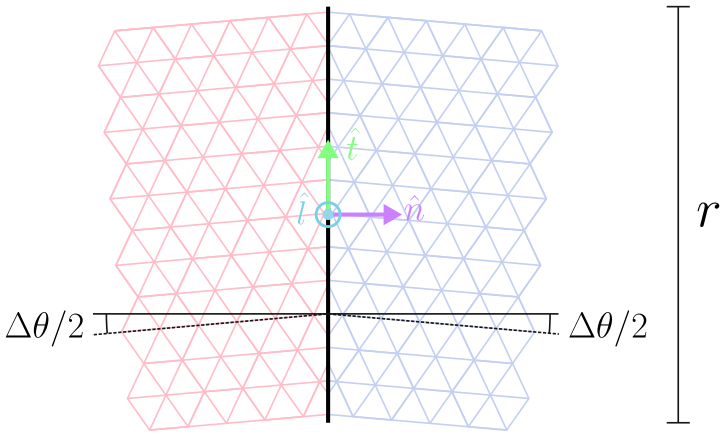


Figure 4.1: A symmetrical tilt grain boundary with $\Delta\theta = 10°$, noting the normal, parallel and tilt axes $\hat{n}$, $\hat{t}$ and $\hat{l}$ to the GB.

This can be simplified by considering a grain boundary made of N identical dislocations and a symmetric tilt axis, meaning $\hat{l}$ will be perpendicular to the GB, hence $\hat{t} \times \hat{l} = \hat{n}$, leading to $Nb\hat{n} = r\Delta\theta\hat{n}$. Considering that r/N is also the distance between each dislocation for a small misorientation [157]:

$$\frac{r}{N} = \frac{b}{\Delta\theta}. \tag{4.12}$$

In the experiments of Lavergne *et al.* [117], grain boundary loops, i.e. a circular grain encircled by one larger grain, were created in colloidal crystals. In these grain boundaries, b is a constant and, without dislocation reactions, N remains constant too. Therefore, as a grain shrinks and the length of GB, r, decreases, the misorientation must increase to preserve the ratio. Therefore, perhaps counter-intuitively, the grain rotates to a higher misorientation and GB energy per unit length. Eventually however, the dislocations react together and reduce N [207]. It is therefore entirely possible for grain rotations to arise in a polycrystalline system, provided dislocation reactions can occur. As Cahn and Taylor [208] speculate, and has been shown in simulations [206], rotation could be allowed via dislocations sited at the triple junctions acting as 'sinks' for adjacent GB dislocations.

4.3 Experimental system and analysis

The experiments in this chapter are the same as those detailed in section 3.3.1, in which solutions of 2.95 and 6.20μm diameter melamine formaldehyde particles (see table 2.1) are injected into a

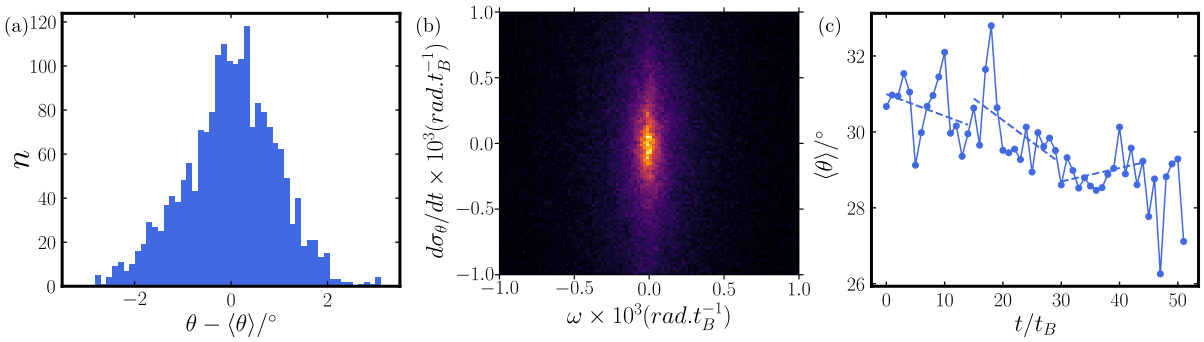


Figure 4.2: (a) shows a distribution of individual particles' orientations within a single grain, relative to the average. (b) is a 2D histogram of our measurement of rotational velocity against the rate of change of the standard deviation of the grain's orientation distribution. The colours of the cells indicate low prevalence (purple) to high prevalence (yellow-white). (c) is the orientation trajectory of a grain, with gradients at certain times plotted.

Hellma cell and imaged for $2000t_B$ to examine the coarsening of grains. The total colloidal particle area fraction is kept constant at $\phi_T \sim 0.75$, with the impurity particle concentration varied between $0 \leq \phi_i \leq 0.114$. The data in this chapter is averaged over a total of 42 experiments across the range of ϕ_i.

To examine the grain rotations, first we sort the particles into grains and draw their grain boundaries, using the methods described in section 3.3.2. From the drawn grain boundaries we have segments of each GB with an associated length and misorientation, allowing for a calculation of Θ_W by using the grain boundary segments' length Λ_j, and their associated misorientations, $\Delta\theta_j$, to find the weighted average of $\ln \Delta\theta$, Θ_W. We approximate the grain size as $R = \frac{1}{2}\sqrt{n}a_0$, where a_0 is the lattice spacing of the crystal, and n is the number of particles in the grain. The individual grains are tracked by applying the tracking procedure of Crocker and Grier [146] on the centre of mass of the particles in each grain. The grains at each snapshot have distributions of particles' orientations such as the one in figure 4.2 (a), and to track rotations we look at the evolution of the mean of this distribution for each of the tracked grains. The mean can shift either by the entire distribution moving, as would be the case for grain rotations, or a sudden skew in the distribution. In the case of the skew, we would expect our measured change in orientation to be accompanied by a change in the standard deviation, σ_θ, which is absent if the distribution is simply moving as one. We can therefore check for correlations between the rotational velocity ω (equation 4.1), i.e. the measured change in the mean $\langle\theta\rangle$, and the change in the standard deviation, $d\sigma_\theta/dt$ over the same period. A 2D histogram of the two is plotted in figure 4.2 (b), where the intensity indicates more measurements with a particular

$(\omega, d\sigma_\theta/dt)$. There is no positive or negative skew in the resultant pattern, indicating that ω and changes in σ_θ are uncorrelated. In addition, we find the value of the Pearson correlation coefficient $\rho_{X,Y} = \mathrm{cov}(X,Y)/\sigma_X\sigma_Y = 0.004$, i.e. the covariance divided by the two standard deviations. This is very close to zero, so there is no apparent correlation, indicating that our measure of $d\langle\theta\rangle/dt$ picks up a shifting of the centre of the distribution and is therefore a measure of rotational motion.

When measuring the angular velocity of grains, we take a linear fit of sections of the orientation trajectory, as can be seen in figure 4.2 (c). The timescale over which these fits are applied should be longer than the correlation time of rotational fluctuations, but short enough to ensure the grain size does not change significantly, which would affect the rate of rotation. As such, we want to minimise the bin length. From the auto-correlation function of the fluctuations, we find a correlation time of $10t_B$, and we therefore set our binning timescale slightly above this, to $15t_B$. From each of these bins we can therefore find ω, although it is important to note in this chapter we simply examine the magnitude, and ignore the sign. In each bin we also measure the grain size R, and components of the grain boundary energy gradient's weighted average, A_W and Θ_W (equation 4.7).

4.4 Results and discussion

4.4.1 Quantifying rotational motion in a polycrystal

In figure 4.3 (a), we plot the orientation of a grain, $\langle\theta\rangle$, as a function of time for a random selection of grains. We can see there are some obvious large changes in grain orientation over a short time period, but in other cases the orientation is mostly constant. From these trajectories, we determine the relationship between the absolute angular velocity and the grain size. As evidenced in figure 4.3, the relationship is almost reciprocal; the algebraic fit has an exponent of ~ -0.92. The inset shows the same graph on a log-log scale, with a reciprocal line in the dashed light blue. Intriguingly, this is in contrast to previous analytical and simulation approaches to grain rotation in polycrystalline networks [192, 196, 209], where the exponent has been predicted or found to be all integers from -5 to 0, *excluding* -1.

To explain our exponent, we take the simplest of Raj and Ashby's equations for sliding

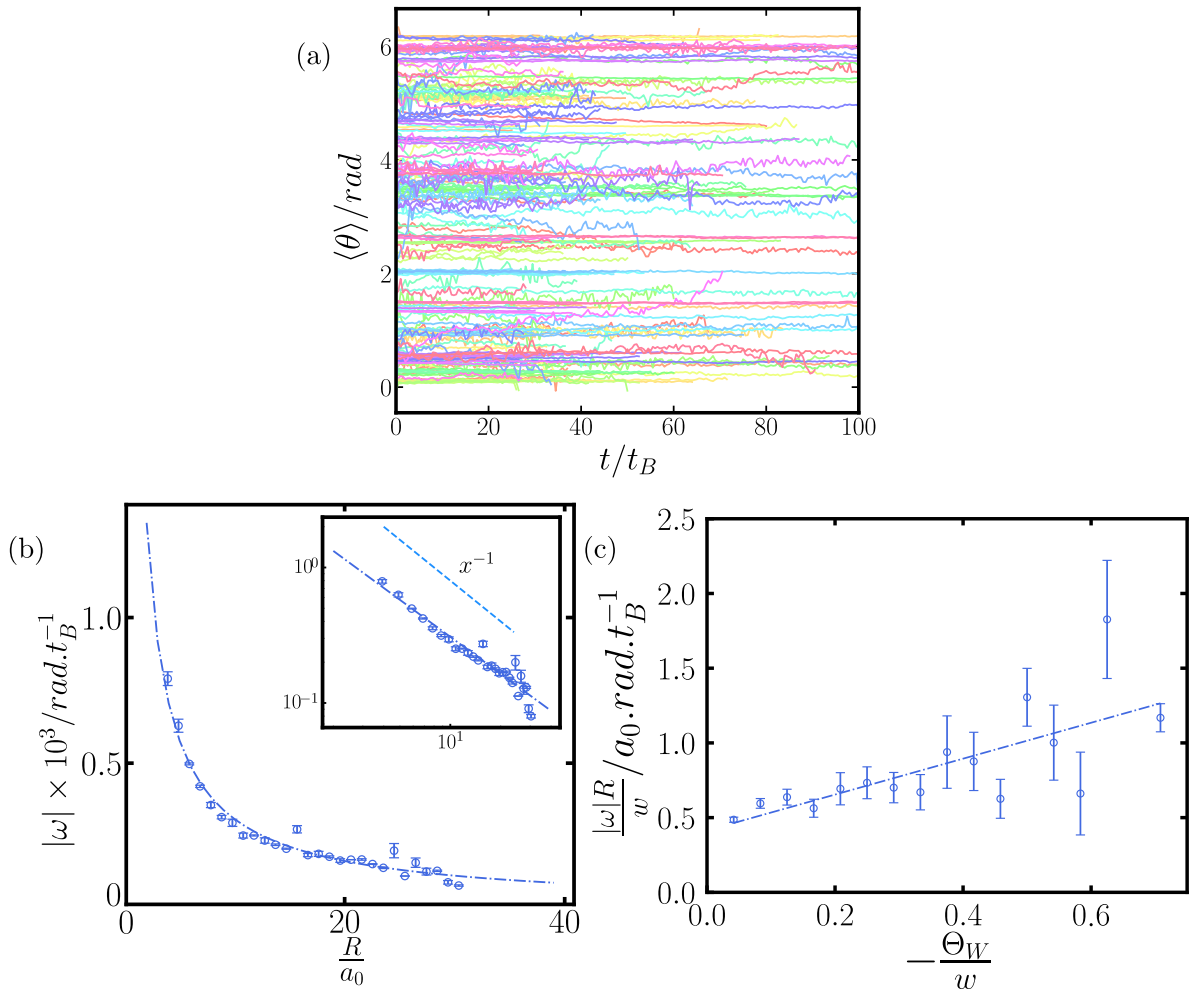


Figure 4.3: (a) shows a sample of orientation trajectories from a single experiment. (b) is a plot of the grain size R against the absolute rotational velocity $|\omega|$. The dashed line is an algebraic fit and the inset is the same graph on a log-log scale. (c) is a plot of the weighted mean of a grains' misorientations Θ_W, and the product of the grains' angular velocity and size. The dashed line is a linear fit and confirms the relationship in equation 4.8. The error bars in both graphs represent the standard error of each measurement.

periodic grain boundaries (equation 11 in [202]) and, applying the expressions for v and $\mathcal{T}$ from equations 4.9 and 4.10 we find:

$$\omega = \frac{\tau}{\pi k_B T R^3} \frac{a_0^2 \lambda}{h^2} D, \tag{4.13}$$

where a_0 is the lattice spacing, and λ and h are related to the roughness of the grain boundary. In [202], the grain boundary roughness is modelled as a sinusoidal wave, with λ as its wavelength and h as its amplitude. For a circular grain boundary, the lowest order oscillation will have a wavelength of $2\pi R$, and the amplitude of colloidal grain boundaries' fluctuations is on the order of a lattice spacing [71], hence $h \approx a_0$. Therefore, the angular velocity of a rotating grain

becomes:

$$\omega \approx \frac{2\tau}{k_B T R^2} D. \tag{4.14}$$

Comparing this to equations 4.2 and 4.3, which state that $\omega = C\tau/R^p$, and we find that $p = 2$ and $C = 2D/k_BT$. This is consistent with our measurement of $\omega \propto 1/R$, since $\tau \propto R$. This can be understood physically: the mechanism of rotation is via particle diffusion, evidenced by the diffusion coefficient D, so the rate at which the entire grain can rotate will be inversely proportional to the number of particles, which is given by $n \propto R^2$.

As the size dependence has been established, we can now quantify A from the GB energy, equation 2.20, and the diffusion constant D. To achieve this, we substitute equation 4.6 into equation 4.14 and take into account that $A_W = w\{A - 1\}$, where w, the weighting, is:

$$w = \sum_j \Lambda_j, \tag{4.15}$$

taking into account the direction of torque from this section of grain boundary. Therefore,

$$\frac{\omega R}{w} = \frac{4\pi\gamma_0 D}{k_B T} \left(\{A - 1\} - \frac{\Theta_W}{w} \right). \tag{4.16}$$

We now plot $-\Theta_W/w$ against $\omega R/w$ in figure 4.3 (b). The data is reasonably well described by a linear fit, with more scatter in the points further to the right, which is to be expected as these bins have fewer data points to average over. From the gradient and intercept of the fit, we find $A = 0.656$, which when compared to the original suggestion of Read *et al.* [119] of 0.23 is quite reasonable. Furthermore, A is proposed to have the form [119]:

$$A = 1 + \ln \frac{a_0}{2\pi r_0}, \tag{4.17}$$

where r_0 is the dislocation core radius [210] and a_0 is the lattice spacing. This gives $a_0/r_0 = 4.40$, which is consistent with the values of 3 to 4 from previous studies in colloidal crystals [211, 212]. The fact that our data is fairly well described by equation 4.16 is perhaps somewhat surprising, given the expression for grain boundary energy is only accurate for small angle grain boundaries [26]. However, referring to the grain boundary character distribution in figure 3.5 in chapter 3, we can see the majority of grain boundaries are indeed small angle.

Now, we can find the effective diffusion constant D by examining the gradient, m, of the fit from figure 4.3 (c), and we find it to be $m = 1.202\,\sigma_s t_B^{-1}$. We can rewrite γ_0 in terms of elastic constants [119]:

$$\gamma_0 = \frac{Ea_0}{8\pi(1-\nu^2)}, \tag{4.18}$$

where E is Young's modulus and ν is Poisson's ratio. Putting these and our value for C together allows us to approximate the lattice diffusion constant in our system:

$$D = \frac{2k_BT(1-\nu^2)m}{Ea_0}. \tag{4.19}$$

Using the approximate value of $\nu = 1/3$ [202,213] and $E \sim 1800k_BT/a_0^2$ from our measurement in chapter 5, we find $D \approx 3\times10^{-5}\mu m^2 s^{-1}$. To understand the value of D, it is important to note that effective diffusion is accommodated via imperfections in the crystal, such as vacancies or minor polydispersity, which provide space for particles to diffuse [214]. Vacancy diffusion in hard sphere crystals has been found to be highly dependent upon the particle area fraction and thereby activation energy, E_a required for a particle to move around in the lattice [215]. Thus, we can similarly take an Arrhenius approach and assume $D = D_0\exp(-E_a/k_BT)$, ignoring any constant that will be dependent upon hole concentration, coordination number, area fraction etc. [214]. Using $E_a \sim 8k_BT$, in line with the values of vacancy diffusion in hard sphere crystals [215], leads to a value of $D_0 \approx 10^{-1}\mu m^2 s^{-1}$, which is close to the Stokes-Einstein diffusion coefficient for our colloidal particles: $D_{SE} = 1.4\times10^{-1}\mu m^2 s^{-1}$. This suggests that the basis for rotation is due to particle diffusion, which over time causes a change in the grain's orientation.

Testing the hypothesis of particle diffusion mediated rotation further, we can examine the impact of impurity concentration on the rate of rotation. In figure 4.4, we show the probability distributions of the rotational velocity of the grains for experiments of three different impurity concentrations. We take these velocities from a narrow range of grain sizes for each set of experiments to negate the dependence of the rotational velocity on the grain size. As the grain boundary character distributions and lattice constants are similar for each experiment, the only factor that could determine a difference in these probability distributions is the impurity concentration. However, all three impurity concentrations have very similar distributions of angular velocities, therefore ϕ_i does not affect the rotations. This is consistent with the picture of particle diffusion: as the impurities tend to segregate in the grain boundaries [24], particle

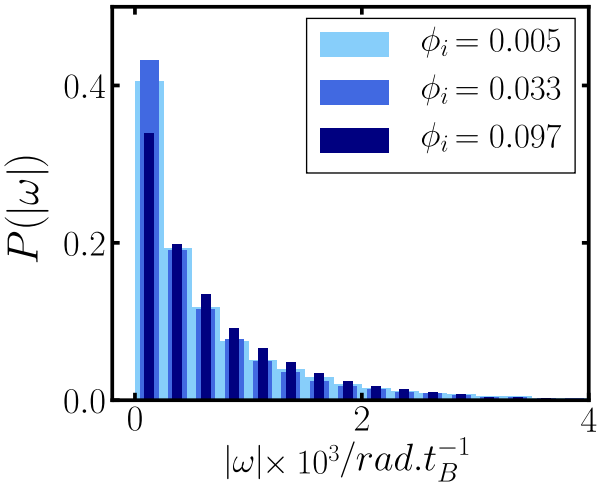


Figure 4.4: The distributions of grain angular velocities for three different impurity concentrations, all taken for a set grain size.

diffusion within grains will remain unobstructed and unaffected by an increase in ϕ_i.

4.4.2 Grain growth due to rotation driven coalescence

Previously, in chapter 3 we examined grain growth assuming purely curvature driven growth. In this chapter, we have established that grains rotate in a polycrystal, in order to reduce the energy of the grain boundary. Therefore, grains can rotate to coalesce, as another means of grain growth. As curvature driven growth is hindered by impurities via Zener pinning [26], but rotations are not, it is important to consider their relative rates when examining grain growth in doped systems.

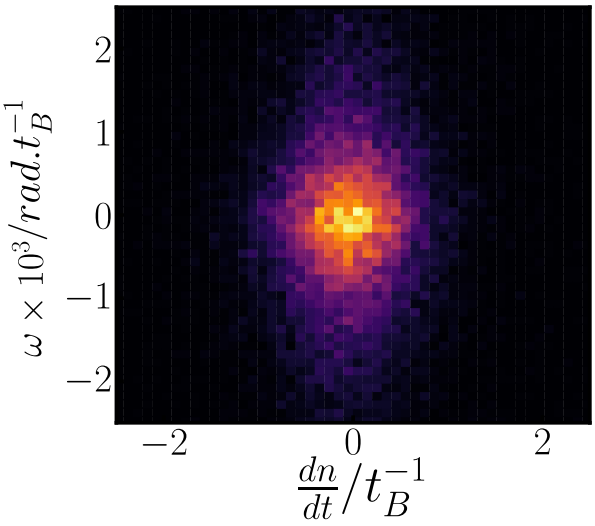


Figure 4.5: A two-dimensional histogram of the change in the number of particles in a grain against the rotational velocity.

Firstly, we must establish whether there is a coupling between curvature driven growth and growth from rotation driven coalescence. To achieve this, we plot a 2D histogram of the rate of change in the number of particles in the grain, dn/dt, against the angular velocity ω, in figure 4.5. These parameters are averaged over $10t_B$ to reduce noise. The resultant distribution is symmetric in both axes with no skew, and has a Pearson correlation coefficient of $\rho_{X,Y} = 0.018$. Therefore, there appears to be no correlation between the rotational velocity and change in grain size. As there is no significant coupling between rotation-mediated and curvature driven grain growth, we can separate the components:

$$\frac{dR}{dt} = \left(\frac{dR}{dt}\right)_C + \left(\frac{dR}{dt}\right)_R. \tag{4.20}$$

From figure 3.9 in chapter 3, we found curvature driven grain growth to be described by a power law $R_6 = At^{\alpha}$, where $0.025 \lesssim \alpha \lesssim 0.333$ for $0 \leq \phi_i \leq 0.114$. From the method of Moldovan *et al.* [216], and demonstrated in appendix A.1, the rotational component is given by the power law $\left(\frac{dR}{dt}\right)_R = Bt^q$, where B and q are constants. In appendix A.2, we measure the exponent to be $q = -0.176$, which should apply to all of our impurity concentrations, considering we found similar velocity distributions in figure 4.4. Therefore the total rate of grain growth can be expressed:

$$\frac{dR}{dt} = A\alpha t^{\alpha-1} + Bt^{-0.176}. \tag{4.21}$$

Given the range of exponent values for the curvature driven component: $-0.975 \lesssim (\alpha - 1) \lesssim -0.667$, we would expect curvature driven growth to dominate at short times, and lower ϕ_i. Conversely, we would expect to see rotation-mediated growth dominate at longer times and higher ϕ_i, when impurities pin the grain boundaries. However, in the grain size evolution curves from chapter 3, figure 3.9, we find experiments with high ϕ_i to quickly reach a plateau with no further growth. This indicates the amount of coalescence due to rotations, i.e. the value of B, is small in comparison to A, the rate of curvature driven growth.

To interpret this, we can examine the factors that govern the relative amounts of curvature and rotation-mediated grain growth. For curvature driven grain growth, the linear velocity of a grain boundary is given by the Herring relation $v = M\gamma\kappa$ [26]. This has a magnitude on the order of $10^{-1} - 10^{0}\mu m\, t_B^{-1}$ for colloidal polycrystals [71]. A grain expanding radially at

this velocity would increase its radius by a length on the order of a lattice spacing over one Brownian time. In contrast, grain growth via coalescence pays a greater return of $\Delta R \sim 10a_0$, the average grain size, in one event. The downside is that this is a single event and for a grain to grow via rotation over a single Brownian time, a number of criteria must be met. Firstly, the grain must have a small angle grain boundary, which provides the opportunity for a coalescence to occur. Secondly, the GB energy gradient must favour rotation in the direction of the possible coalescence. Thirdly, the magnitude of the rotational velocity must be great enough that coalescence could occur within a Brownian time. In the case of our experiments, there are many low-angle grain boundaries (seen in the grain boundary character distributions in figure 3.5), so the limiting factor must be the magnitude of the velocity. Referring to figure 4.3 (b), the smallest grains of radius $4a_0$ rotate with an average velocity of $\sim 8 \times 10^{-4}\,\mathrm{rad}.t_B^{-1}$, and would therefore coalesce with an adjacent grain across a grain boundary of $\Delta\theta = 1^\circ$ in $\sim 20t_B$. The time taken for the same grain to disappear via curvature driven shrinkage would be $4t_B$. Therefore, while we do measure rotations, for the effective diffusion constant D found in our experiments, ω is insufficient to have a significant contribution to grain growth.

Finally, we can compare our values to atomic systems. In a thin-layer gold system [192], a grain of radius $66nm$ ($\sim 5\sigma_{Au}$) was found to rotate on average of $2.4^\circ hr^{-1}$ at room temperature, which coincidentally is similar to the average rotation rate for a grain of $R = 5a_0$ in our system: $3.5^\circ hr^{-1}$. Importantly, this rate of rotation is very slow relative to the rate of curvature driven growth in atomic systems [154], consistent with our findings. Indeed, it is apparent that grain rotation only becomes significant under certain circumstances. First of these is high temperatures where curvature driven growth is impeded [196, 217–220], where particles may diffuse more quickly through the lattice as a result of the Arrhenius-like nature of the effective diffusion constant D. Second, and most studied, is with an applied deformation, such as shear strain [194, 195, 221, 222], as this applies an additional torque of a much larger magnitude compared to the grain boundary energy gradient.

4.4.3 Particle and dislocation dynamics during grain rotation

We have now found that grain rotation occurs in our polycrystals, quantified the rate of rotation, driving force, and examined the contribution towards grain growth. We also established in our derivation of equation 4.14 that the mechanism driving rotation is particle diffusion. In this

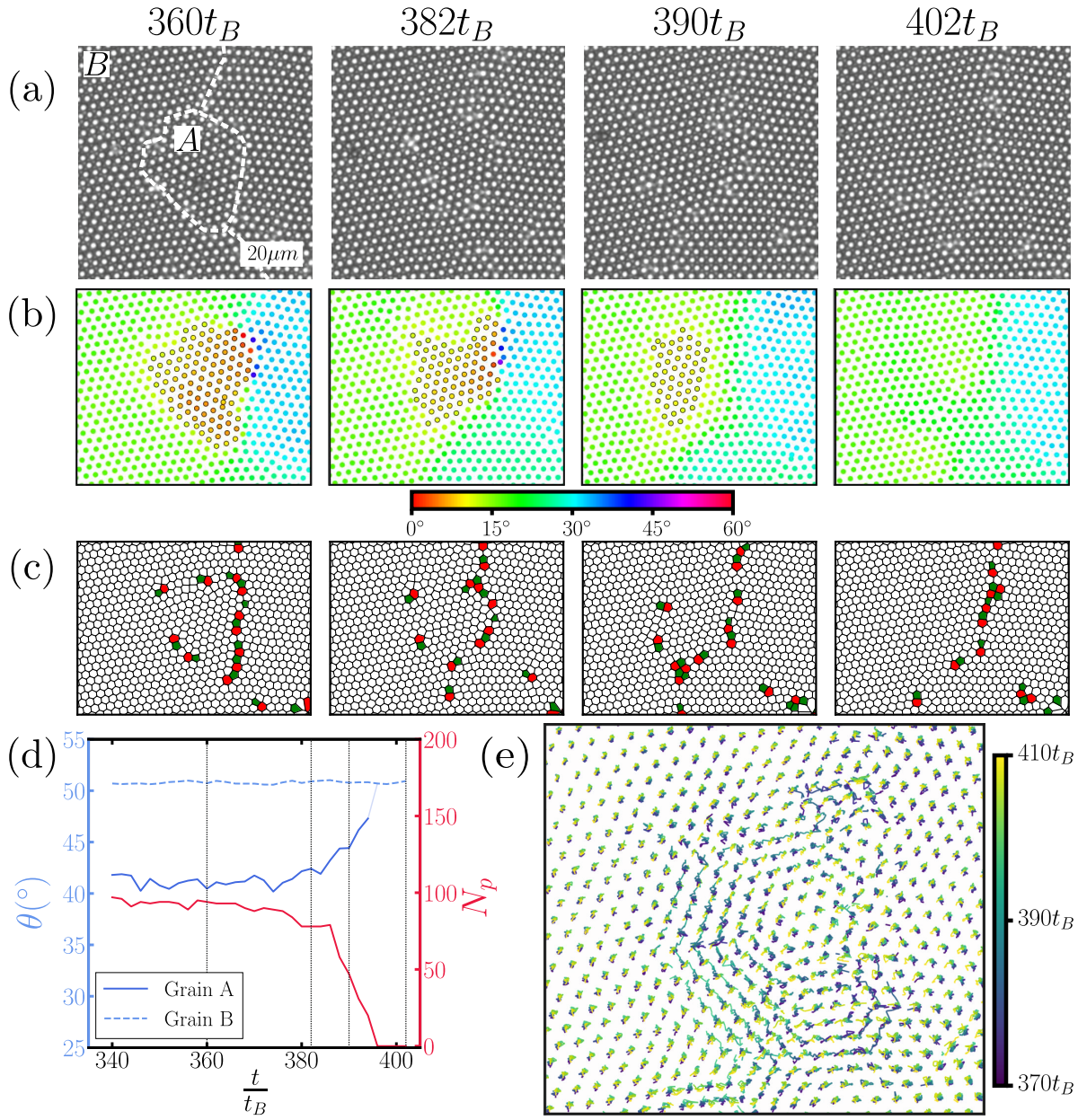


Figure 4.6: Aspects of a grain rotating to coalescence. (a)-(c) each have four images corresponding to the experimental time at the top of each column. (a) Microscopy images of the colloids, with a small grain, A, rotating to coalesce with the grain on the left, B. (b) The particle coordinates from (a) with colours representing their orientations. All of the particles contained in grain A have been given black outlines for clarity. (c) A Voronoi construction from the particle coordinates with each cell coloured by the coordination number. White = 6, green = 5 and red = 7. Pairs of 5-7 coordinate particles are dislocations and their locations indicate the position of the grain boundary. (d) is a graph showing the evolution of the orientations of grains A and B on the left-hand axis in blue, and the number of particles in grain A on the right-hand side. (e) Shows the trajectories of all of the particles over the entire time frame of the snapshots, with the position at a particular time indicated by the key, with initial positions being blue and final positions being in yellow.

section we directly examine the motion of the particles and dislocations during the rotation of a grain towards coalescence. It is important to acknowledge that the grain in question rotates at a velocity of $\sim 6 \times 10^{-3}\,\mathrm{rad} t_B^{-1}$, which is far faster than the average values in figure 4.3 (b) and

beyond the range of the distributions in figure 4.4. While the high rotational velocity of this grain is not representative of all grain rotation in our experiments, it does allow us to examine the particle and dislocation dynamics during grain rotation, within the experimental time scale.

Figure 4.6 (a), shows four snapshots of the colloids during a coarsening experiment ($\phi_i = 0.005$), in which small grain A in the centre rotates to coalesce with grain B on the left-hand side. As the presence of grains and grain boundaries is difficult to discern in these snapshots, figure 4.6 (b) shows the particle coordinates, where the colours indicate the orientation of their neighbours. The particles in the grain of interest are marked with black outlines. The graph in figure 4.6 (d) shows the orientations of grain A in bold and the grain B as a dashed line (left and blue), and the number of particles in the grain A over time (right and red).

The first frame is taken $360t_B$ after the experiment started, meaning the majority of the sample has crystallised. At this time, the grain sits with three neighbours, grain B to its left, and one to the right and below. There are fluctuations between this time and the next within the orientation but there is no particular trend. The size also remains more-or-less constant. The second snapshot is just after the coalescence begins, with the grain having changed shape, which may be the instigation that allows for rotation to begin. From here to the final time, as seen in 4.6 (d), the orientation of grain A gets closer to that of B, as the colours of the particles in 4.6 (b) change from orange to yellow to green as the two grains join in the final step. While this rotation occurs, the number of particles steadily decreases.

With grain rotation to a lower misorientation, the dislocations in the grain boundary are expected to be topologically constrained. Referring back to section 4.2.3, we noted that for a grain to rotate to a lower misorientation, either the distance between dislocations must increase or the number of dislocations must decrease. We can test this for grain A, by examining how the change in misorientation affects the number of dislocations in the grain boundary. Looking at figure 4.6 (c), we have a Voronoi construction from the particle coordinates, with 5- and 7-coordinate cells coloured green and red respectively. The dislocations can be used as a guide for locations of the grain boundaries: the four grains are easily visible and it is clear grain A always shares a boundary with the other grains.

Examining the dislocations directly, in the first frame there are four in the semicircular arc of the boundary between grains A and B. This progresses to three in the next frame, two in the next and none in the final. Clearly, by reducing the number of dislocations, the topological constraints

of equation 4.12 ($r/N = b/\Delta\theta$) are not being broken. We can check this by comparing r, N and $\Delta\theta$ between frames $360t_B$ and $390t_B$. The Burgers vector magnitude b is constant, but for the corresponding frames, the number of dislocations, N, are 4 and 2, and the misorientations, $\Delta\theta$, are 9° and 6°. We can approximate the grain boundary lengths by comparing the number of particles in the grain, as the circumference is related to the radius and $R \propto \sqrt{n}$, where n is the number of particles. Rearranging equation 4.12 gives us $N = \Delta\theta r/b$, and taking the ratio of both sides for each of our frames results in:

$$\frac{N_{360}}{N_{390}} = \frac{\Delta\theta_{360}\sqrt{n_{360}}}{\Delta\theta_{390}\sqrt{n_{390}}} \approx \frac{9^\circ\sqrt{90}}{6^\circ\sqrt{40}} = 2.25, \tag{4.22}$$

which is a good approximation of the ratio of the number of dislocations with the number reducing $4 \rightarrow 2$ between frames $360t_B$ and $390t_B$.

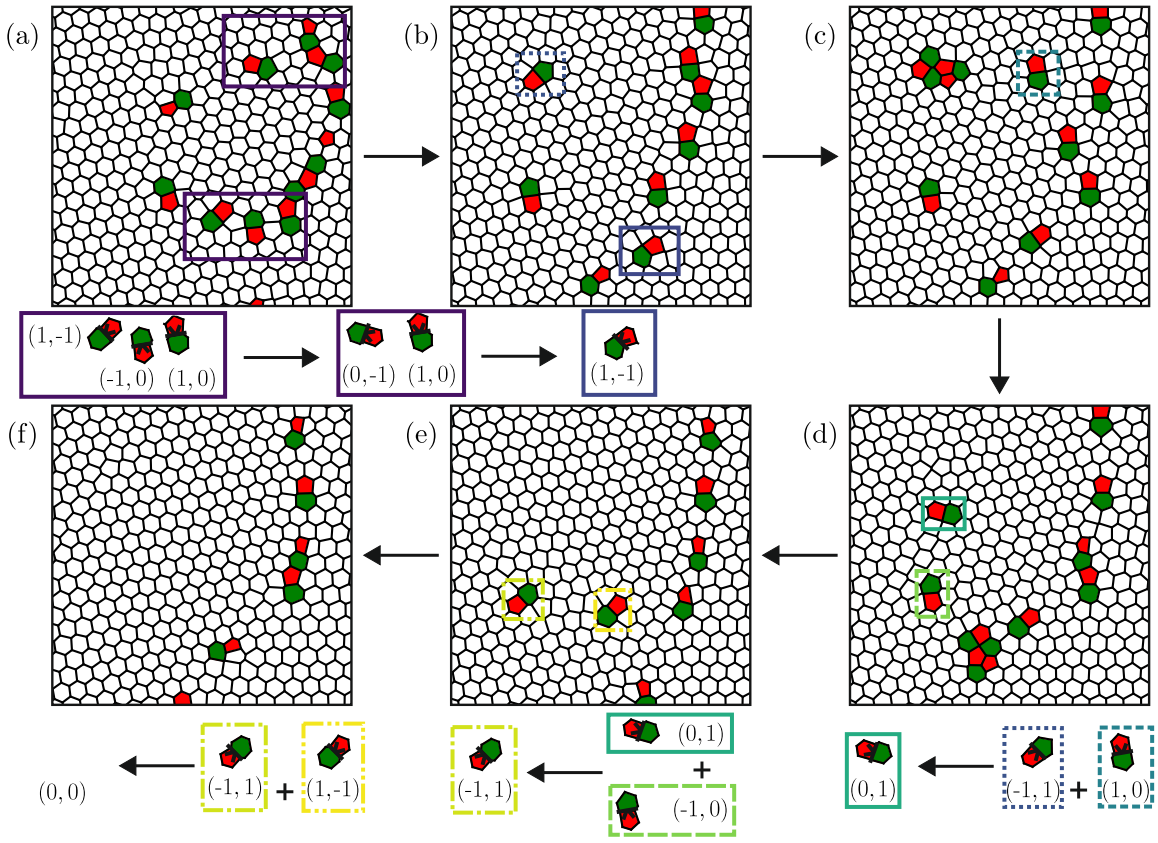


Figure 4.7: A timeline of the dislocation reactions that facilitate grain rotation. The reaction pathways corresponding to the result of each reaction in each frame are drawn below, with their Burgers vector values. Each dislocation is noted in their corresponding frame with a matching box colour and line type. (a) is the initial frame, with the dislocations closest to the triple-junctions highlighted. The proposed reaction pathway for the lower box is shown beneath this image. (b) shows the result of the first two dislocations being removed. (c)-(d) show the snapshots of the of the annihilation of the dislocations in the boundary between grains A and B.

The number of dislocations is reduced via dislocation reactions [208]. Examining the dislocation reactions of the grain rotation from this data is a little more difficult owing to the resolution of our experiments being $2t_B$ per frame. A more detailed sequence of images can be seen in figure 4.7, where the process of coalescence is followed through dislocation reactions. In (a), the highlighted boxes are the two dislocations closest to the ends of the disappearing boundary. While unfortunately our time resolution does not allow us to examine the reactions that occur in the top box, it is clear that these dislocations move towards the triple-junctions to be eliminated. This is in line with the prediction that triple-junctions act as dislocations 'sinks' to allow grain rotation [208]. In the lower box, the dislocation reactions are clearer, as can be seen in the reactions below (a) and (b). The left and centre dislocations join, and the resultant dislocation then reacts with the right, to give the $(1, -1)$ dislocation which sits in the grain boundary in (b).

The final process of rotation is much clearer, with the dislocations gliding around the grain boundary in the anti-clockwise direction; the opposite to the grain rotation direction. Firstly, the dislocation from the upper triple-junction glides towards the dislocation highlighted in figure (b), (the gliding can be seen highlighted in (c)). The result of this reaction is shown in (d) and the reaction shown beneath. The new dislocation now glides to the lower of the original dislocations, with this reaction and the result seen in (e). Finally, another dislocation from the lower of the triple-junctions glides out of the boundary and reacts with the final dislocation, resulting in an annihilation and the grain boundary between grains A and B disappears. This again shows the significance of the triple junctions as sinks, as they allow for rotation that would otherwise be disallowed for shrinking grains.

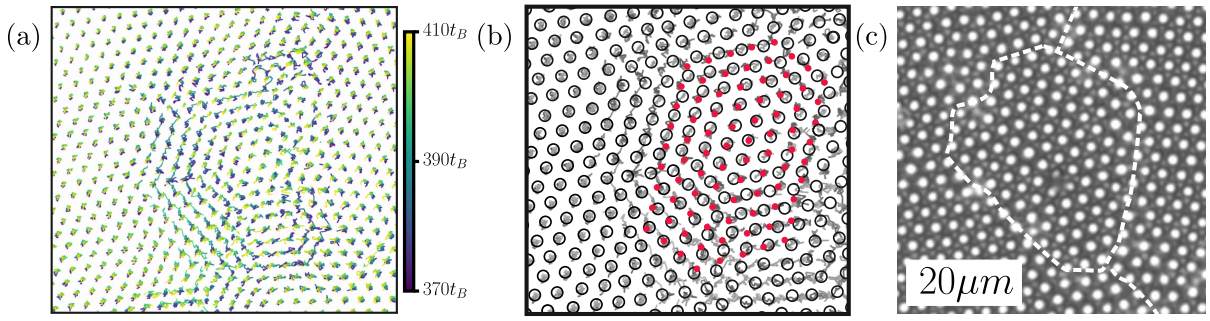


Figure 4.8: (a) The particle trajectories through the rotational motion of the grain. (b) The trajectories in the background in greyscale, with the lattice of grain B as black open circles and the lattice of grain A as red closed circles. (c) A zoomed in perspective of the grain.

Next we focus on the trajectories of the particles, which can be seen in figure 4.6 (e) and

4.8 (a), colour coded for their positions at each time during the grain rotation. From this there is clearly a case of rotational motion: there is a centre of rotation where there is no motion, and going radially out from here each hexagonal layer of particles has greater and greater amounts of displacement. Similar motion has been seen in the shrinkage of grain boundary loops [223], where this facilitates the motion of dislocations. A key difference here is that there is only one centre of rotation, and the number of coordination shells rotating is greater. In figure 4.8 (b), we show a zoomed in image of the trajectories in (a), with an overlay of the lattice of grain B (open black circles) and the lattice of grain A (closed red circles). As found with grain boundary loops [223], it is clear that the particle with the least motion at the centre of rotation is found to be at the coincident site lattice; where the two lattices have singular sites at exactly the same point. Comparing (a) and (b), the overlay of the lattices also predicts the final positions of the particles, and as such the trajectories of the particles. This can be seen by comparing the difference between the centres of the red and black circles.

The trajectories suggest that the rotation mechanism is governed by particle diffusion, which is consistent with our findings in section 4.4.1. The particles move collectively in chains towards their new lattice sites. However, looking at figure 4.8 (c), a zoomed in perspective of the grain shows there is a lack of vacancies which could facilitate fast diffusion. Given the unusual rapidity of the grain rotation, the motion of the grain boundary during shrinkage is likely to supply holes into which the particles can diffuse.

4.5 Conclusion

In this chapter we have examined the role of grain rotation in 2D colloidal polycrystals. We took the equation for grain rotation from Moldovan *et al.* [189], and found an unusual reciprocal relationship between rotation rate and grain size. We then modelled the torque using the equation of Read *et al.* [119] for grain boundary energy, and found it to describe our data well, meaning the grain rotations are a means to reduce the boundary energy. We rationalised both the reciprocal relationship and the GB energy through the grain sliding mechanism of Raj *et al.* [202], mediated by particle diffusion. We found rotation to be invariant with impurity concentration and uncorrelated to grain growth, allowing a growth law to be found based on the equations of Moldovan *et al.* [216]. We rationalised the rate of rotation to be far slower than curvature driven

growth, consistent with our measured angular velocities and measurements in atomic systems. Finally we examined the particle and dislocation dynamics of a grain rotating to coalescence. The motion of the dislocations in the boundary made topological sense with consistent reactions and the triple junctions were shown to facilitate rotation by acting as 'sinks'. We lastly observed particles rotating around the coincident site lattice.

Acknowledgements

François Lavergne, Berend van der Meer and Miranda Bell-Davies are thanked for their useful discussions.

Chapter 5

Active deformation and depinning of grain boundaries in colloidal polycrystals

Abstract

In this chapter, we study the depinning of an impurity particle from a grain boundary in a colloidal polycrystal. We use optical tweezing and a translation stage to measure the forces via constant velocity active microrheology. Firstly, we measure the elastic deformation of the crystal in front of the impurity to obtain the Young's modulus. Next, we perform experiments pulling the impurity from the grain boundary. We examine the position of the grain boundary, with respect to the impurity, and find that the force increases when the contact angle between the boundary and particle also increases. Another maximum is reached when the impurity has just depinned. We use our crystal deformation measurements to find the pinning force of the boundary on the impurity and correlate this to the boundary deformation to obtain the grain boundary stiffness. Finally, we find the large depinning force, which is related to the energy required to create a dislocation.

5.1 Introduction

Grain boundary pinning and depinning by impurities have long been known to control the microstructure of materials [224]. In the extensive literature on this phenomenon, the majority has focused on the impact of concentration [169,224,225], as more impurities lead to more pinned boundaries. Far less focus, however, has been placed on the nature of the force itself. Impurities impart this force on moving grain boundaries [169], the nature of which is restorative, i.e. trying to minimise the length of the grain boundary [224]. This force depends on the points of contact between the impurity and grain boundary and is therefore different in two- and three-dimensions, due to the respective line and planar boundaries [226]. Owing to the length-scales of atomic systems, direct measurement of the pinning force is experimentally difficult and many different models have been proposed [169]. These models have, as yet, only been tested experimentally via grain size analysis [124,225,227,228], or through simulations [229–232]. Direct measurement of depinning forces in an experimental system is therefore an open challenge.

Typically, rheology entails the measurement of deformation, flow and elastic response from macroscopically applied strains on materials [233]. To achieve this, sufficient material is required with a finely calibrated rheometer. In this chapter however, we are interested in the microscopic forces and flow with deformation on the same length-scale as our particles, rather than the bulk response. This calls for microrheology, where the 'rheometer' is a probe/tracer particle [234]. Microrheology is used widely for measuring the elastic properties of complex fluids [235–237] and in biological systems, e.g. in measuring live cell cytoskeletons [238] or the forces of motor proteins [239]. For colloidal systems, optical trapping provides an excellent method for measuring forces [86, 240, 241], and can be used for so-called 'active microrheology'. For grain boundary pinning, the probe is moved relative to the crystal. Assuming the interaction between the probe and trap follows Hooke's law [235], the forces can be measured based on the displacement of the probe from the centre of the trap.

In this chapter we use an impurity doped colloidal polycrystal and optical trapping to measure the forces acting on an impurity during depinning from a grain boundary. Firstly, we measure the elastic deformation and strain in front of the dragged impurity, from which we measure the Young's modulus of the crystal. We then measure the forces on a particle dragged from inside a grain boundary until depinning. We find the magnitude of the force is

related to the contact angle between the impurity and grain boundary. The highest force on the particle occurs when the particle has depinned and is no longer intersected by the boundary. We then use our measured elastic deformation of the crystal to find the elastic reaction force acting on the probe, and remove this from our trap force, such that the force measurement is only dependent upon the grain boundary pinning force. Using a model based on the measured grain boundary deformation and contact angles, we estimate the pinning force from the grain boundary on the impurity. Comparing this theoretical pinning force to the measured one, we extract the grain boundary stiffness. Finally, we elucidate why the depinning force is independent of misorientation and verify this with Brownian dynamics simulations. We find depinning is accompanied by a creation of a new dislocation which has an associated elastic energy, thus generating the large depinning force.

5.2 Theory

5.2.1 Microrheology of colloidal crystals using optical tweezers

Examining the diffusion of a tracer particle embedded in a crystal when unaided except for thermal motion is *passive* microrheology. In this chapter however, we study *active* microrheology, where the tracer is driven through the sample by optical or magnetic forces, allowing for non-linear responses of the medium [242]. Driven magnetic colloids have a constant force, but in our case of using optical tweezers, the probe has a constant velocity and a variable force. As the colloidal particle is dragged, there will be hydrodynamic interactions between the particles in the medium but these become less important as the Péclet number (Pe the ratio of directed and diffusive transport rates) tends to 0 [234, 242]. The dragging of a probe through a two-dimensional colloidal crystal has been examined in Brownian dynamics simulations [243, 244], and experiments probing velocity effects on the crystal [86]. Both the experiment and simulations find low velocities (thus low Pe) to minimise the 'wake' of melted crystal behind the tracer and the number of defects propagating into the crystal.

Optical trapping is described in section 2.2.3, but essentially a focussed beam creates a potential for colloidal particles as a result of gradient and scattering forces [140]. The depth of the potential depends on the laser power, and the shape of the potential (assuming small

displacements) is parabolic [234]:

$$U_T = \frac{1}{2}k\Delta x^2, \tag{5.1}$$

where k is the trap stiffness and Δx is the particle's displacement from the trap centre. The trap stiffness can be measured by using the Boltzmann factor: $P(x) \sim \exp(-U/k_BT) = \exp(-k\Delta x^2/k_BT)$, found by fitting a Gaussian to a histogram of Δx.

When dragging a particle through a crystal we can apply a one-dimensional Langevin equation:

$$m\frac{dv}{dt} = F + f(t) - \xi v, \tag{5.2}$$

where m is the mass of the particle, v is the velocity, F contains the external forces, $f(t)$ is the fluctuating Brownian force, and ξ is the drag. In the absence of a grain boundary, we can split the external force term, F, in two: the optical force from the trap $F_T = -k\Delta x$, and the elastic reaction force from deforming the crystal F_C (ignoring hydrodynamics). As the system is overdamped, i.e. $dv/dt = 0$, we find:

$$F_T = k\Delta x = F_C + f(t) - \xi v, \tag{5.3}$$

which gives us an expression for the force balance of a probe being dragged through a crystal.

5.2.2 Elastic response of the crystal

By dragging a particle through the crystal, we are applying a stress. In a two-dimensional system, this is simply the force per unit length that is being applied: $\varsigma = F/L$. When a stress is applied to a material, the response is a deformation, which when linear we can classify as strain. Normal strain is the change in length per unit length, or $\varepsilon = \Delta l/l$. A positive value indicates extension and negative indicates compression.

In two dimensions, there are three unique components of strain, in the x and y directions but also shear (of which there are two equal components in the strain tensor). These can be seen in figure 5.1 (a), where the initial square is deformed by linear strain in the y direction (the upper dashed line) and sheared as a function of y position (the dotted line). The two

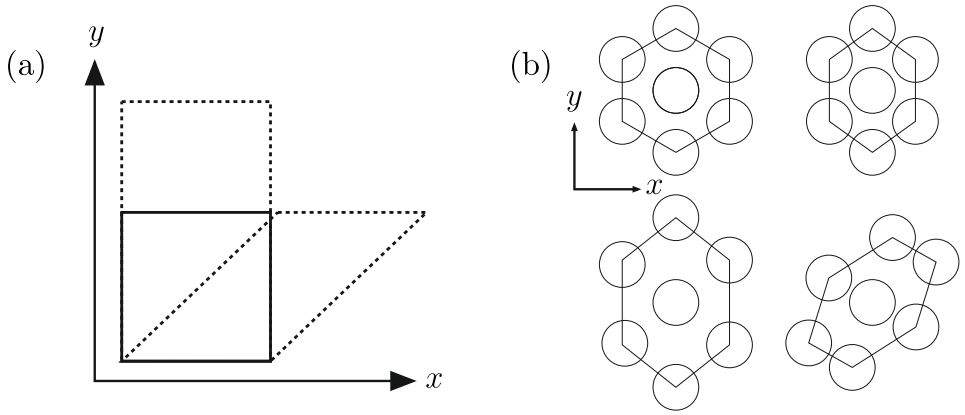


Figure 5.1: (a) shows a square that has been extended (dashed line) and sheared (dotted line). (b) shows the nearest neighbours of a particle in our system in the top left, with compressive strain in x ($\varepsilon_{xx} < 0$) in the top right, extensive strain in y in the bottom left ($\varepsilon_{yy} > 0$) and a shear strain the bottom right.

dimensional strain is expressed as a tensor:

$$\overline{\overline{\varepsilon}} = \begin{pmatrix} \varepsilon_{xx} & \varepsilon_{xy} \\ \varepsilon_{yx} & \varepsilon_{yy} \end{pmatrix}, \tag{5.4}$$

with $\varepsilon_{xy} = \varepsilon_{yx}$. Strain can be applied to any shape, and as such we can apply it in our colloidal crystal. Each particle has six neighbours in a regular hexagon, but the application of stress, such as from our probe particle, can deform the local shape of the crystal. Therefore, if we take a particle's neighbours and map that shape onto the perfect hexagon we should be able to measure the amount of strain around this particle. Examples of what this might look like can be seen in figure 5.1 (b). Our method to find the strain in our colloidal crystal is detailed in appendix B; in short we use an algorithm to best fit a point set registration of the two shapes' vertices and then a method to find the optimal affine transformation and thereby approximate the strain.

When applying small stresses, we will be in the elastic regime, where all strains and changes in structure will be reversible and there will be a linear relationship between stress, ς, and strain, ε: $E = \varsigma/\varepsilon$. The parameter E relating the two is the Young's modulus [82].

5.2.3 Dislocations and impurities

While a three dimensional crystal can have multiple types of dislocations, our two-dimensional system will only have edge dislocations, where the 'edge' refers to an additional line of the crystal

ending at the dislocation. The elastic energy per unit length of such a dislocation is [210]:

$$E_{el} = \frac{Eb^2}{8\pi(1-\nu^2)} \ln \frac{R}{r_0}, \tag{5.5}$$

where E is Young's modulus, b is the length of the Burgers vector, and ν is Poisson's ratio. Inside the logarithm we have the dislocation's core radius r_0, describing the circle within which the continuum elastic theory, modelling stress and strain fields, breaks down [245]. The final term R, is the distance from the centre of the dislocation. Therefore, a single dislocation in an otherwise perfect infinite crystal will lead to an infinite elastic energy, as the logarithmic term diverges. In real crystals however, the stress and strain fields can interact with those from other dislocations and orientate themselves to minimise the total elastic energy. Therefore, to find a dislocation's energy we can approximate R as the distance to the nearest dislocation with an oppositely signed Burgers vector [210].

Impurity atoms can sit either on lattice or interstitial sites. It is possible for impurities to be commensurate with the lattice [24], but when they are incommensurate, the particles around the impurity will be disturbed from their lattice points, inducing stress [246] and leading to a resultant elastic energy. The impurity is therefore a source of a stress field, which will interact with other stress fields in the crystal. As a means of minimising the total elastic energy in the crystal, an impurity atom and dislocation can superimpose [247]; hence the segregation of impurities in grain boundaries [248].

5.2.4 Boundary pinning and deformation

Due to the stabilising presence of impurities in grain boundaries (GBs), deviations of the impurity centre from the grain boundary lead to effective attractive interactions. Classical Zener pinning models this as tension from the boundary's stiffness acting from the boundaries points of contact with the impurity (as detailed in section 2.1.4). For boundaries with asymmetric points of contact relative to the direction of drag, the Zener equation is [124]:

$$F_Z = \Gamma[\sin\theta_a + \sin\theta_b], \tag{5.6}$$

where Γ is the grain boundary stiffness and θ_i is the contact angle of the GB on side i, shown in figure 5.2 (a). In our colloidal system, the boundary is easily distorted [71], and pulling on the

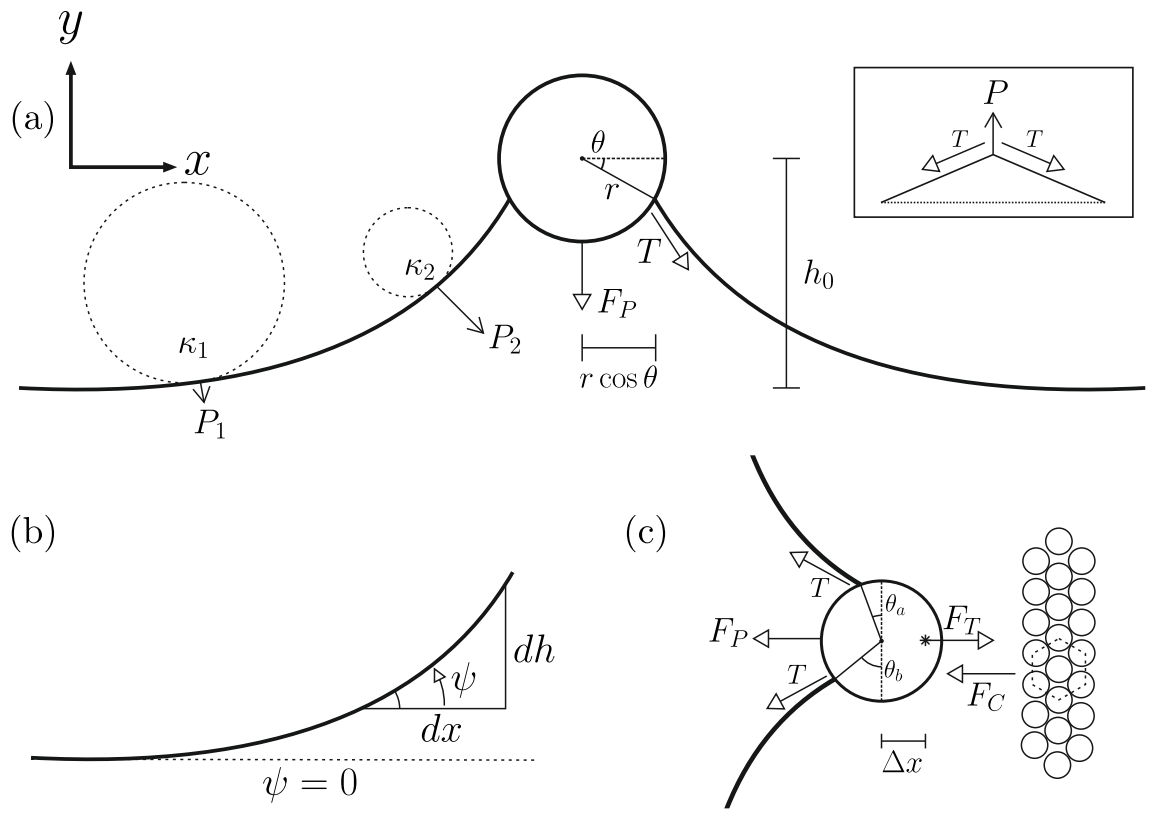


Figure 5.2: (a) A diagram showing the forces acting on a pinned impurity with a deformed boundary. The impurity of radius r has a contact angle θ with the grain boundary and is a height h_0 from the relaxed grain boundary position. The grain boundary pinning force is F_P. The deformation of the boundary creates different grain boundary curvatures, κ_1 and κ_2, each generating a different pressure. The box in the top right is a schematic showing how this pressure induces tension, T, in the grain boundary. (b) A diagram showing how the gradient, dh/dx of the grain boundary is related to the inclination ψ. (c) A diagram showing the different forces acting on the probe and their origins. The pinning force F_P results from the tension T, and contact angles θ_a and θ_b, from (a). The trap force F_T originates from the displacement, Δx of the particle centre from the trap centre marked with the star. The crystal reaction force F_C arises from the deformation of the crystal in front of the probe.

boundary changes its shape, adding curvature, which induces a restoring pressure. The Zener model can therefore be expanded upon by taking into account this added pressure, $P = \Gamma\kappa$, where κ is the curvature and Γ is the grain boundary stiffness [26]. Shown in figure 5.2, this curvature, κ, varies along the length of the boundary. When this pressure pulls the grain boundary, a tension is created along the line, shown in the top right of figure 5.2, similar to a mass placed on a taut string. When summed along the entire length, this gives the total tension, T, acting upon the impurity. The tension across an infinitesimal length is $dT = P(x,t)dx$, therefore the total tension is:

$$T(t) = \int_{r\cos\theta}^{\infty} \Gamma(x,t)\kappa(x,t)dx, \tag{5.7}$$

where the lower bound of integration is the $x-$coordinate of the contact point, shown in figure 5.2. Also shown in this figure, the total pinning force F_P will depend on the tensions T in each half of the grain boundary and the contact angles:

$$F_P = T[\sin\theta_a + \sin\theta_b]. \tag{5.8}$$

In modelling the GB deformation, we can take a similar approach to deformed liquid-gas interfaces [249]; from the fluctuation dissipation theorem and assuming a point force (F), the height profile takes the form:

$$h(x,t) = \frac{F(t)}{k_B T} g_h(x). \tag{5.9}$$

Here, $g_h(x)$ is the spatial height-height correlation function, as will be discussed in section 6.2.1. Using the equation for $g_h(x)$ for a grain boundary [71], the height profile has the form

$$h(x,t) = h_0(t)\exp(-x/\xi), \tag{5.10}$$

where ξ is the correlation length and $h_0(t) = F(t)\xi/2\Gamma$, which is shown in figure 5.2. Approximating the curvature of a function by the well known expression $\kappa = f''(x)/(1+f'(x)^2)^{3/2}$ [250], leads to

$$\kappa(x,t) = \frac{h_0}{\xi^2}\exp(-x/\xi). \tag{5.11}$$

The expanded form of the equation of Read *et al.* [119] for grain boundary stiffness is a function of misorientation ($\Delta\theta$) and inclination ($\psi(x,t)$):

$$\Gamma(x,t) = \frac{Ea_0}{8\pi(1-\nu^2)}\Delta\theta[A - \ln\Delta\theta](\cos\psi(x,t) + \sin\psi(x,t)), \tag{5.12}$$

and in this chapter we denote this as $\Gamma(x,t) = \Gamma_0(\cos\psi(x,t) + \sin\psi(x,t))$, where

$$\Gamma_0 = \frac{Ea_0}{8\pi(1-\nu^2)}\Delta\theta[A - \ln\Delta\theta]. \tag{5.13}$$

Now we must link the inclination to the height profile. For an infinitesimal section of the grain boundary, a right angled triangle is formed with base dx and height dh, as shown in figure 5.2. Assuming a grain boundary whose inclination $\psi = 0$ when relaxed, the inclination at a

point after deformation is the angle in the right-angled triangle such that $dh = \tan\psi(x,t)\,dx$. Therefore, the gradient of the boundary is $\dfrac{dh}{dx} = \tan\psi$. As we know the form of the height profile (equation 5.10), we can relate the inclination to x:

$$\frac{dh(x,t)}{dx} = \tan\psi(x,t) = -\frac{h_0(t)}{\xi}\exp(-x/\xi). \tag{5.14}$$

Using trigonometric identities, the grain boundary stiffness can be rewritten as $\Gamma(x,t) = \Gamma_0(1 - \tan\psi(x,t))/\sqrt{1+\tan^2\psi(x,t)}$. Substituting $\tan\psi(x,t)$ from equation 5.14:

$$\Gamma(x,t) = \Gamma_0 \frac{1 + \frac{h_0(t)}{\xi}\exp(-x/\xi)}{\sqrt{1 + \left(\frac{h_0(t)}{\xi}\right)^2 \exp(-2x/\xi)}}. \tag{5.15}$$

Now, using this and the curvature (equation 5.11) and placing both in the tension integral (equation 5.7), we find:

$$T(t) = \Gamma_0 \int_{r\cos\theta}^{\infty} \frac{1 + \frac{h_0}{\xi}\exp(-x/\xi)}{\sqrt{1 + \left(\frac{h_0}{\xi}\right)^2 \exp(-2x/\xi)}} \cdot \frac{h_0}{\xi^2}\exp(-x/\xi)dx. \tag{5.16}$$

Integrated by substitution ($u = \frac{h_0}{\xi}\exp(-x/\xi)$), the tension is

$$T(t) = \Gamma_0 \left[\sqrt{1+u^2} + \sinh^{-1} u^2\right]_{r_0}^{\frac{h_0}{\xi}}, \tag{5.17}$$

where $r_0 = \frac{h_0}{\xi}\exp(-r\cos\theta/\xi)$. Hence the pinning force from equation 5.8 is estimated:

$$F_P(t) = \Gamma_0 \left[\sqrt{1+u^2} + \sinh^{-1} u^2\right]_{r_0}^{\frac{h_0}{\xi}} [\sin\theta_a + \sin\theta_b], \tag{5.18}$$

where the profiles of the grain boundary on each side are averaged to find h_0. This expression is similar in form to the that of the well known depinning energy equation derived by Gladman [227]. For small deformations, $u \to 0$, so:

$$\lim_{u\to 0}[\sqrt{1+u^2} + \sinh^{-1} u^2] = 1. \tag{5.19}$$

From this, $F_P = \Gamma_0[\sin\theta_a + \sin\theta_b]$, which is the Zener equation (equation 5.6).

5.3 Experiment and simulations

5.3.1 Experiment

Our optical trapping set-up is detailed in section 2.2.3. Briefly, we have an inverted brightfield microscope with an infra-red laser focused from above. The sample cell sits on a manual x-y and a piezoelectric translation stage. This second stage is connected to the computer, with which we can control the position of the stage and move the sample at a fixed velocity. The acousto-optic deflector (AOD) is also connected to the computer, allowing us to control the position and power of the trap. Using our own software written in LabVIEW, we can use different experimental procedures with the stage, laser and camera.

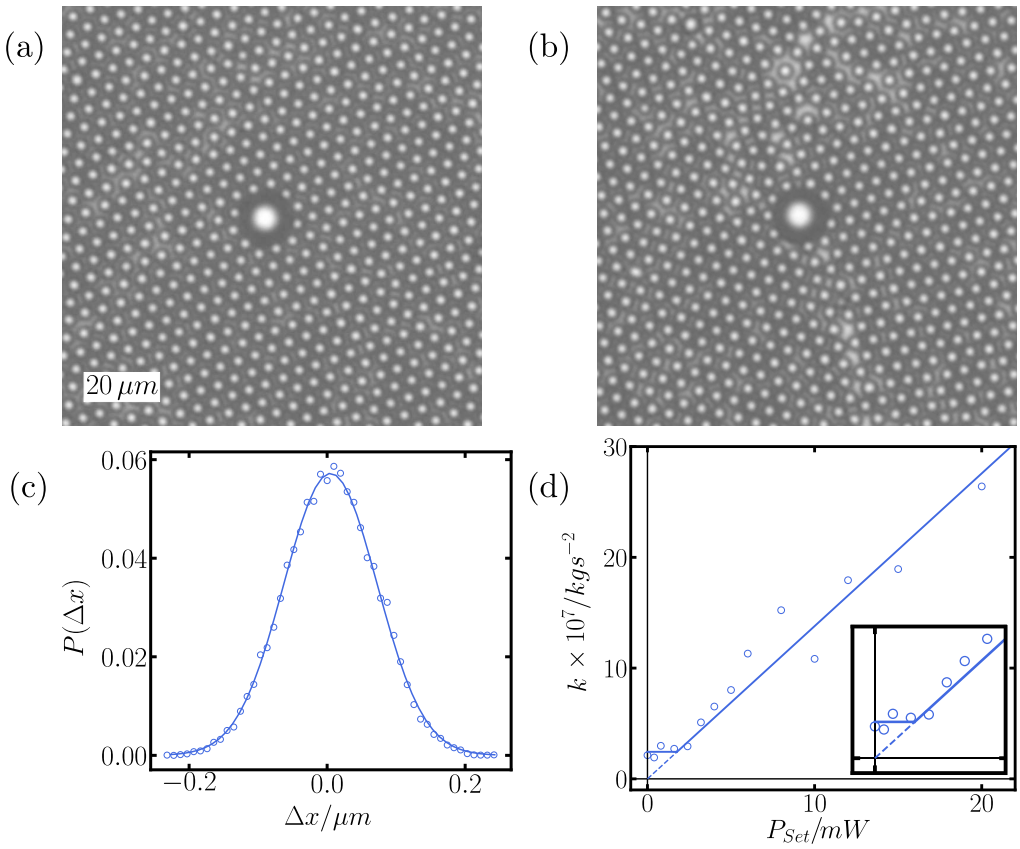


Figure 5.3: (a) shows a raw image of an impurity in the colloidal crystal. (b) shows a raw image of an impurity in a grain boundary. (c) shows the probability distribution of a trapped particle's displacement from the trap's centre. (d) shows the measured trap stiffness for different set powers from the laser. There is a linear relationship above $P_{Set} \sim 2mW$, and below this the stiffness of the crystal overrides the trap stiffness. The inset shows the region in which there is no power dependence on the measured stiffness.

Our colloidal system consists of 2.95 µm and 10.75 µm diameter melamine formaldehyde

spheres (see table 2.1) in a 20/80 v/v% ethanol/deionised water solution. This is injected into a Hellma cell, with volume fractions such that the small area fraction $\phi_s \sim 0.75$, and the impurity area fraction amounts to roughly one particle per field-of-view, $\phi_i \sim 0.001$. Therefore, the small particles will form a polycrystal with sparsely distributed impurities. After the cell is created, it is left to coarsen for roughly a week, to allow for large grains with straight grain boundaries to form. The results of the coarsening process can be seen in figures 5.3 (a) and (b), where we have raw images of an impurity particle sitting in the crystal and one sitting in a grain boundary respectively.

To measure the stiffness of the optical trap, we can apply the Boltzmann factor to the distribution of particle displacements of a trapped impurity and fit a Gaussian distribution. An example of this can be seen in figure 5.3 (c). When measuring this in our system, we must be mindful of the surrounding crystal also restricting the diffusive motion of the impurity particle. To find the stiffness of the trap, we vary the power and fit the displacement distributions. The measured stiffness for different set laser powers, P_{Set}, can be seen in figure 5.3 (d). Below $P_{Set} \sim 2mW$, the measured trap stiffness constant is roughly the same value. Above this, k increases with P_{Set}. With a weak laser, the size of the distribution will be larger than the restricted area from the crystal and we are measuring the potential due to the crystal, which does not depend on P_{Set}. At higher powers, the probe's displacement distribution from the trap's centre will be tighter and thereby undisturbed by the crystal, allowing for measurement of the trap stiffness. We expect a linear relationship between power and stiffness [139], and we see this above 2 mW.

Our experiments were split in two, dragging particles in the crystal and dragging particles in the grain boundary. The procedure of each experiment was the same. Firstly, we placed the laser and impurity at the centre of our field-of-view. The laser is set at a power of $\sim 4mW$, high enough that the particle will not fall out of the trap when being dragged, but low enough that we see relatively large displacements allowing for more accurate force measurements. The system is left for a few minutes to allow the structure to relax, and then the dragging measurement begins. Using our software, we set the stage to move in steps:

1. Move 1 µm at a rate of $0.02\,\mu\mathrm{m\,s^{-1}}$ (the slowest stage velocity)

2. Pause for 60 s

3. Repeat from step 1.

This moves the impurity particle at a quasi-constant rate with the wait time used to decrease the average velocity, allowing for the crystal and grain boundary to deform, but retain quasi-equilibrium conditions. For an average speed of $\sim 0.01\,\mu\mathrm{m\,s^{-1}}$ and with a Stokes' drag coefficient, $\xi \approx 1 \times 10^{-7}\,\mathrm{N\,s\,m^{-1}}$, the drag term from our Langevin equation (equation 5.3) is therefore $\xi v \approx 1 \times 10^{-15}\,\mathrm{N}$. The typical trapping force measured for a colloid dragged through a colloidal crystal is $\sim 1 \times 10^{-13}\,\mathrm{N}$ [86, 251]; this is much larger than the drag term, which we can therefore ignore. We continue these steps until we have enough data from dragging through the crystal, or the particle has snapped off the grain boundary and is clearly depinned.

5.3.2 Methods of analysis

In our analysis we require a quantitative measurement of strain generated by our impurity particle. As shown in figure 5.4 (a), we are interested in the deformation ahead of the dragged impurity and the easiest method is to draw a box and use the strain of the particles inside. However, deformation propagates through the crystal and we need to define a cut-off for our optimal box size. For this we must balance the greater number particles and therefore better statistics of a larger box with the 'dilution' of deformation further from the impurity. To this end, we looked at the decay of deformation for a representative experiment. To quantify deformation we use our parameter D^2, which is the squared difference between the points of a reference hexagonal structure and the real local structure (see appendix B). In figure 5.3 (b), we take an experiment in which we drag a probe and measure $\langle D^2(r)\rangle - \langle D^2\rangle$ averaged radially in a semi-circle, with the convex side facing the direction of motion of the impurity. From this decay we took the compromise of particle statistics and 'dilution' by using a box with 20 µm sides.

To examine grain boundary pinning, we must first find the grain boundary, divide the boundary on each side of the impurity, and fit equation 5.10 to find the deformation $h_0(t)$ and the contact angles from equation 5.18. To find the grain boundary we have large enough grains that only two will be visible in our field-of-view, as can be seen in figure 5.4 (c). As such we can divide our image into horizontal bins, take all of the particles in a single bin and plot their x-positions against their orientations. Such a graph can be seen in the inset of figure 5.4 (c). Following [71], we can fit a curve of the form $\theta = A\tanh(x - x_0) + C$, and define the x-coordinate

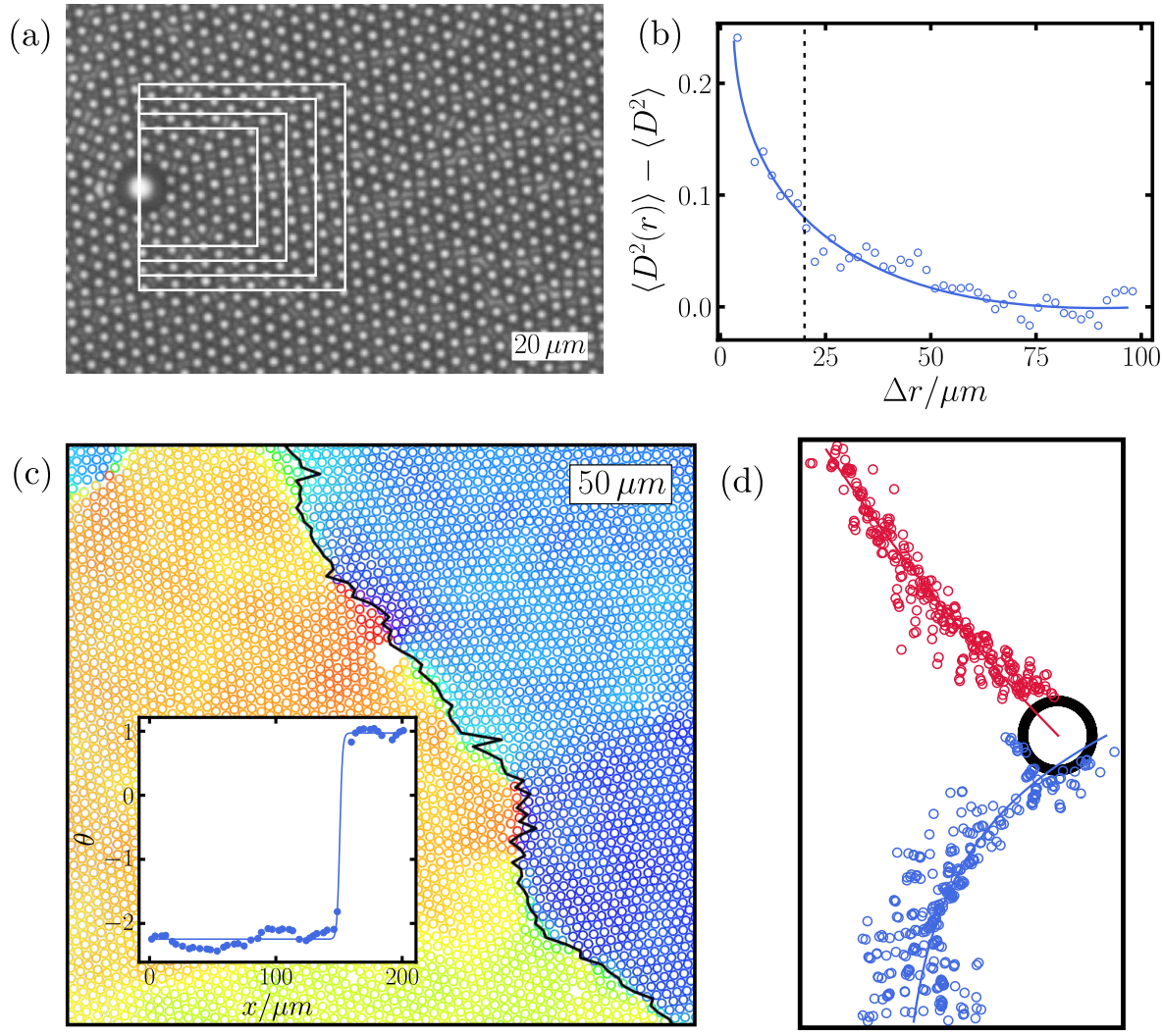


Figure 5.4: (a) A raw image of a dragged particle indicating the possible box sizes for measuring anterior strain. (b) We look at deformation (relative to a perfect crystal) in a system with a dragged impurity particle. The x-axis is the radial distance from the impurity and the y-axis is the deformation parameter for particles at this particular distance. Our chosen box size is represented by the dashed line. (c) Shows the drawn grain boundary with particles coloured by orientation. The inset shows an example tanh fitting. (d) We have an impurity (black circle) and the points from either sides of the grain boundary in red and blue. The points of the grain boundary are from 10 frames and the exponential fittings are shown as the solid lines.

of the grain boundary to be at x_0. The result is the black line in figure 5.4. To minimise the effect of thermal noise, we take an average over 10 s or 10 frames.

Our method of fitting the deformed boundary can be seen in figure 5.4 (d). The black circle is our impurity and the other points are from 10 frames' worth of grain boundary positions. These points are coloured and divided by their y-coordinate relative to the centre of the impurity. By dividing the grain boundary into two halves, we replicate the ideal model shown in figure 5.2, with two points of contact, each pulling the impurity with the grain boundary tension, with

their separate contact angles θ. For each of the halves of points, we can rotate the coordinates and fit equation 5.10:

$$h = h_0(t)\exp(-x/\xi) + C, \tag{5.20}$$

with a baseline C. From this fitting we find h_0, which we can put into our pinning force equation 5.18. Using the fitted lines, we then measure the points of intercept between the curve and the edge of the impurity to find the contact angles θ_a and θ_b.

5.3.3 Simulations

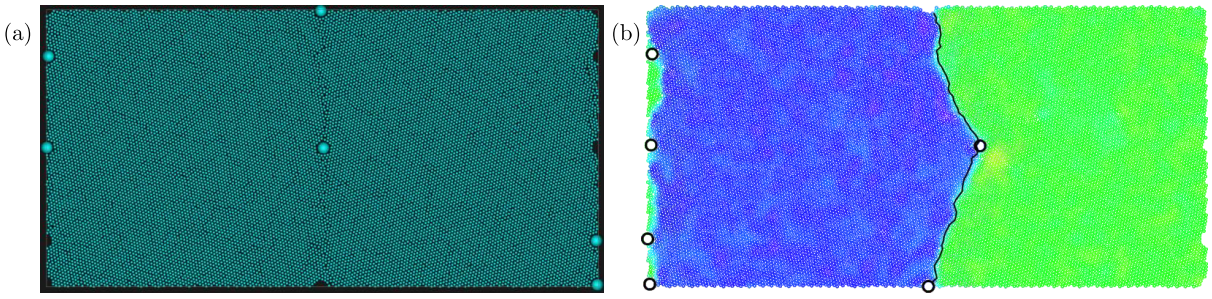


Figure 5.5: (a) The simulated system after a number of cycles to allow the structure to relax. (b) The simulated system after the probe has been pulled $\sim 5\,\sigma_l$. The GB is drawn in and the small particles are coloured by their orientation. The impurity particles have black outlines.

In this chapter, we use Brownian dynamics simulations to supplement our experiments, particularly to conveniently vary the grain boundary misorientation and impurity size. As discussed in section 2.1.1, we use a Weeks-Chandler-Andersen potential, which is much softer than our experimental colloidal particle pair potential. We generate an initial particle configuration of two adjacent grains. The grains initially have an orientation of 0° and are rotated in opposite directions to generate a symmetric grain boundary with the desired misorientation. Care is taken to ensure the box height exactly allows for continuity through the periodic boundaries. At the two grain boundaries (in the middle and at the left/right periodic boundary) we delete overlapping particles, and allow the structure to relax before taking data. Our probe particle is placed in the centre of the system and impurity particles are strategically placed in the boundaries to prevent boundary motion interfering with the experiment. This includes the single stationary impurity in the central boundary, which holds the boundary in place while the trapped particle snaps off.

The simulation procedure is the same as described in section 2.3, except that we add an external force mimicking the optical trap on our probe particle. This is simply a Hookian spring which moves linearly in the x-direction at a constant velocity. In this case we have simply changed the reference frame from the trap's to that of the crystal. The stiffness and velocity were set at $0.55\,k_BT\sigma_l^{-3}$ and $0.25\,\sigma_s t_B^{-1}$ respectively, compared to our experimental system's $0.15\,k_BT\sigma_l^{-3}$ and $0.20\,\sigma_s t_B^{-1}$. Note that we set the stiffness high relative to the experiment, as the softer pair potentials in the BD simulation meant the impurity could more rapidly change position and 'jumped' out of the grain boundary more easily. The simulation could then be carried out in the same manner as the experiment, stopping once the impurity snapped out of the boundary and the GB had relaxed.

5.4 Results and discussion

5.4.1 The crystal's elastic response to probe drag

To understand the process of depinning an impurity from the grain boundary, we first characterise the response from the crystal by dragging an impurity embedded in a grain and examining the strain of the crystal particles ahead. Figure 5.6 (a) shows the change in the different strain tensor components in front of the probe over 600 s, the approximate time taken for the probe to move over its radius. Note that we measure the difference from the initial static strain from of the impurity's inherent strain field. We focus on the comparison of the axial and transverse components; in the first $\sim 350s$, ε_{xx} decreases indicating compression and ε_{yy} increases indicating expansion. Beyond $\sim 350s$, both components of strain go to zero, which would indicate the crystal yields and there are plastic events beyond the limits of affine transformations and infinitesimal strain theory, thus our method of strain measurement from appendix B. Therefore, when comparing to the trap force on the impurity we should expect an elastic regime up to this point.

Figure 5.6 (b) plots the time evolution of the measured optical force from the trap ($F_T = k\Delta x$) in blue on the left-hand axis, and axial strain response $\langle \Delta\varepsilon_{xx} \rangle$ in red on the right-hand axis. When dragging a particle through the crystal, from our Langevin equation (eqn. 5.3), ignoring thermal noise, the measured optical force should be equal to the elastic reaction force, F_C, from the crystal. Examining the two curves in figure 5.6 (b), at approximately 100 s, the motion of

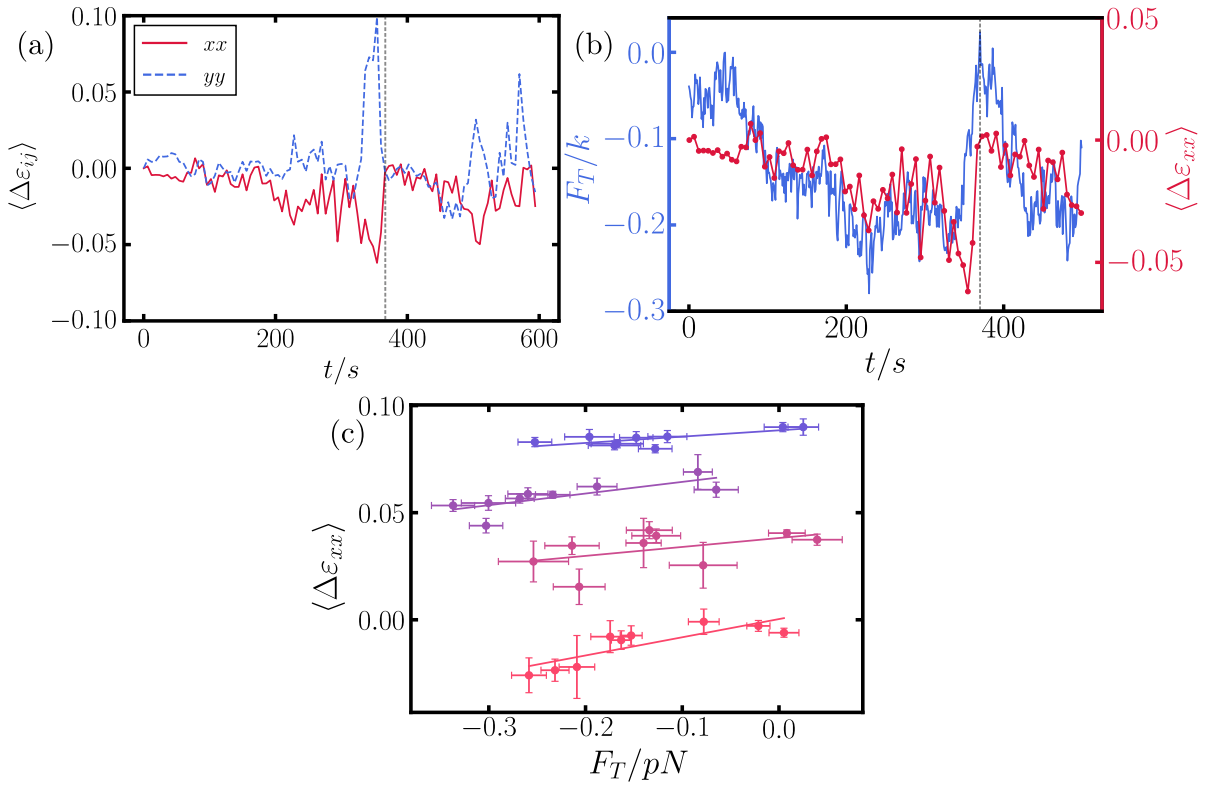


Figure 5.6: All plots are taken from experiments dragging a probe particle through a colloidal crystal. (a) The components of the strain tensor in the box ahead of the probe particle over a time frame of 600 s and the probe moving $\sim 0.5\sigma_l$. (b) An overlay of the fluctuations in measured optical force on the probe from the trap, and the axial component of strain relative to the direction of motion. The force is negative as the positive direction is that in the direction of driving and this allows for easy comparison to strain. (c) The measured trap force against the average strain for multiple experiments. The corresponding colour curves are linear fits of the data. Each subsequent data and curve is shifted up the y-axis for clarity.

the particle begins to affect the crystal and until approximately 350 s, F_T and $\langle \Delta\varepsilon_{xx} \rangle$ seem to be directly correlated. From this, we can measure the Young's modulus of the crystal, as we know the strain $\langle \Delta\varepsilon_{xx} \rangle$, and the force (and thereby stress) that causes this distortion. Beyond 350 s, we see that the force on the particle decreases rapidly and there is a slower response of the crystal which indicates a yielding of the crystalline structure.

In figure 5.6 (c) we have taken multiple experiments and compiled the trap force and axial strain at each time during the elastic regime. Due to thermal fluctuations, the data is fairly noisy, but there is clearly a linear relationship between the parameters and all the experiments have a similar gradient. The Young's modulus can be extracted from this gradient; this is defined $E = \varsigma/\varepsilon$, where the two-dimensional stress $\varsigma = F/L$, with L the length the force acts over. Therefore, $\langle \Delta\varepsilon_{xx} \rangle = -F_T/(EL)$ and we can find E by assuming L is the same as the box height we use to measure $\langle \Delta\varepsilon_{xx} \rangle$. We find the average Young's modulus to be $E \approx 1800 \pm 660\, k_B T/a_0^2$.

This is of a similar magnitude to previous measurements in colloidal crystals based on grain growth [252], local melting [86], lattice fluctuations [73] and macroscopically applied strain [74].

5.4.2 Visualising the depinning and the trapping force

Next we follow an example of an impurity depinning experiment and compare the trapping force trajectory with images showing the impurity and grain boundary. In figure 5.7 we track a representative experiment dragging a probe particle out of a grain boundary of misorientation 28°. In (a) we show the evolution of the trap force on the particle from the start of the experiment to shortly after depinning. The highlighted areas correspond to the snapshots in (b) with the same number and colour. Each snapshot plots the small particles with their colour indicating orientation, the black line showing the grain boundary and the probe as the black-outlined circle.

Between the first and second snapshots, the an increase in the force on the probe is mainly driven by the elastic response of the crystal, as the shape of the grain boundary and contact angle between it and the probe hardly change.

After this initial elastic regime, F_T fluctuates due to cycles between elastic deformation and yielding of the crystal. The force on the probe remains fluctuating about constant until a sharp negative peak in the force appears at $t \sim 12t_B$. Looking at the corresponding snapshot (iii), the GB has retreated slightly with a larger contact angle to the probe, which lead to a larger pinning force. From (iii) to (iv), the force has increased, and while the contact angle of the grain boundary is similar, the grain boundary has a greater amount of curvature and thereby a greater tension. From (iv) to (v), there is a decrease in the trap force back to the fluctuation region similar to (ii). Looking at the corresponding screenshots, the grain boundary has rebounded and the contact angle is small again, resulting in a smaller pinning force. From here to the end there is the largest increase yet, with the greatest force magnitude corresponding to snapshot (vi). Here, the probe has depinned from the boundary, but there is still a large force pulling the probe back. The magnitude of the force here is the greatest across the entire time series, however the cause of this cannot be the pinning force as the particle has left the grain boundary. There must therefore be a different force on the probe we have not accounted for.

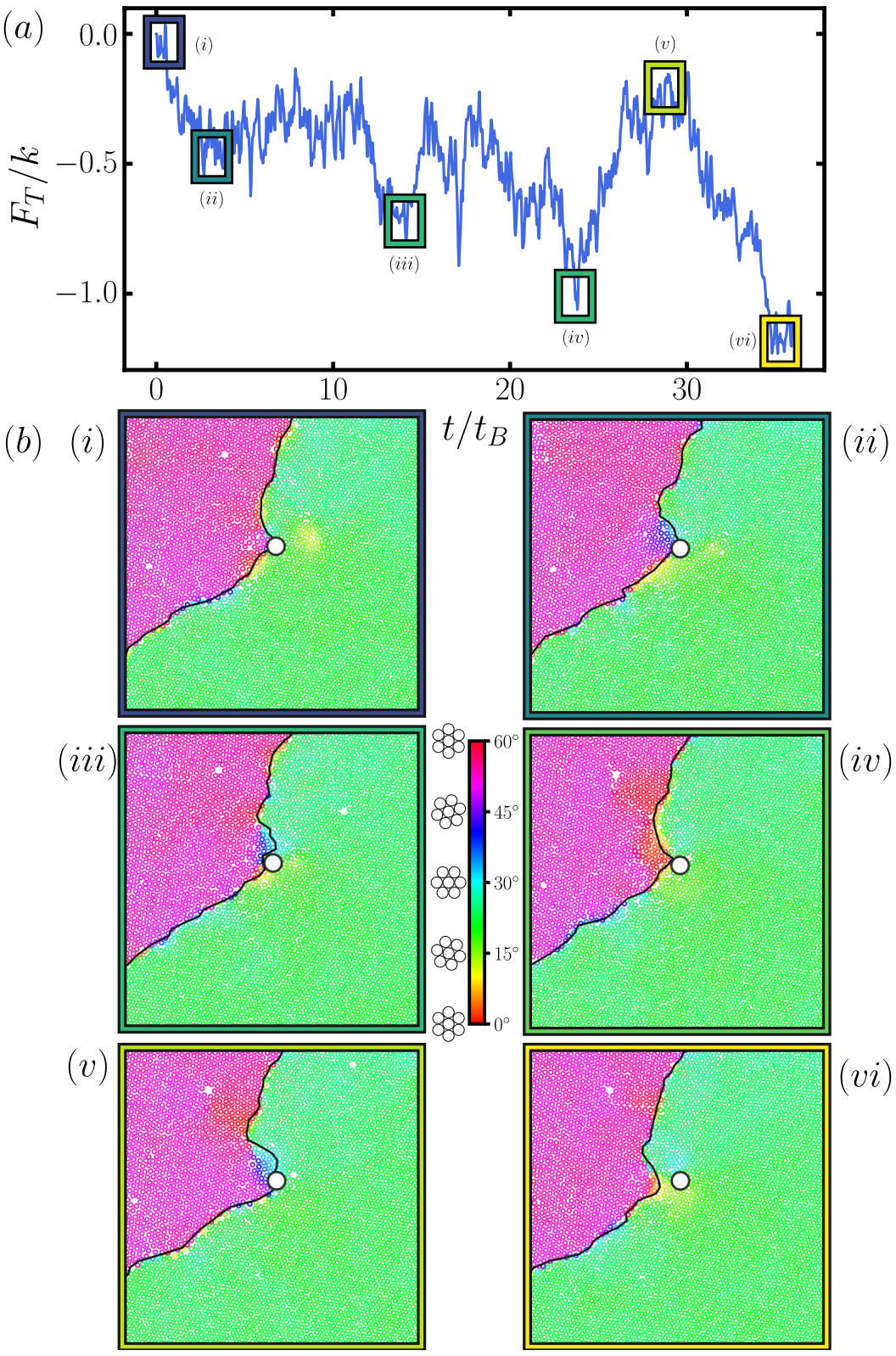


Figure 5.7: The process of dragging a probe from a grain boundary until the depinning. (a) The trap force on the probe particle over time from the initial point to when the particle and grain boundary depin. The highlighted areas correspond to the numbered snapshots in (b). In these images, the small particles are plotted and coloured by their orientation (see key), with the grain boundary drawn in black. The probe is the large black-outlined circle.

5.4.3 Measuring the pinning force

Now we have seen the evolution of the trap force on our probe particle with time, we can attempt to measure the pinning force between the grain boundary and probe. Firstly, we note that there are three forces acting on the probe: the trap force, F_T, crystal reaction force, F_C, and the pinning force, F_P. A schematic of these forces is shown in figure 5.2 (c). In the form of an equation, this is:

$$F_T = F_C + F_P. \tag{5.21}$$

In these depinning experiments, we can repeat the procedure from section 5.4.1 of using a box to measure $\langle \Delta\varepsilon_{xx} \rangle$, and therefore find F_C, allowing us to isolate F_P. Looking at figure 5.8 (a), we can see the trap force, F_T, on the impurity in red and the crystal's elastic reaction force, F_C, in blue. Clearly there is a correlation up until approximately $15t_B$, but afterwards it seems the amount of elastic force does not change, but there is a large change in F_T, a result of F_P. Returning to our expression for the pinning force in equation 5.18, we require the height of the grain boundary from the flat equilibrium position, h_0, and the contact angles on both sides of the boundary, as shown in figure 5.2. Figure 5.8 (b) shows the time evolution of both of these, with an amount of smoothing with a moving average. Both fluctuate, which aligns to the snapshots in figure 5.7 (b), where we see the grain boundary moving back and forth relative to the probe.

We predict the pinning force (from equation 5.18):

$$\frac{F_P}{\Gamma_0} = \left[\sqrt{1+u^2} + \sinh^{-1} u^2\right]_{r_0}^{\frac{h_0}{\xi}} \left[\sin\theta_a + \sin\theta_b\right] \tag{5.22}$$

from the values in figure 5.8 (b). We show the predicted pinning force F_P/Γ_0 in figure 5.8 (c) in red, and our measured pinning force, i.e. the trapping force on the probe minus the elastic reaction force $F_T - F_C$, in blue. The points are the raw data and the lines are smoothed data. Comparing these lines, there is a clear correlation with the positions of the peaks and troughs of each line, which suggests that equation 5.18 can be applied. It is pertinent to note that the final peak of F_P/Γ_0 coincides with a slight peak in $F_T - F_C$, and the final maximum in $F_T - F_C$ occurs when F_P/Γ_0 is at a minimum. This will be addressed in section 5.4.4. Using the correlation between our calculated (from equation 5.22) and measured pinning forces, we can get a measure of the grain boundary stiffness, Γ_0. Through binning the two lines of 5.8 (c) in

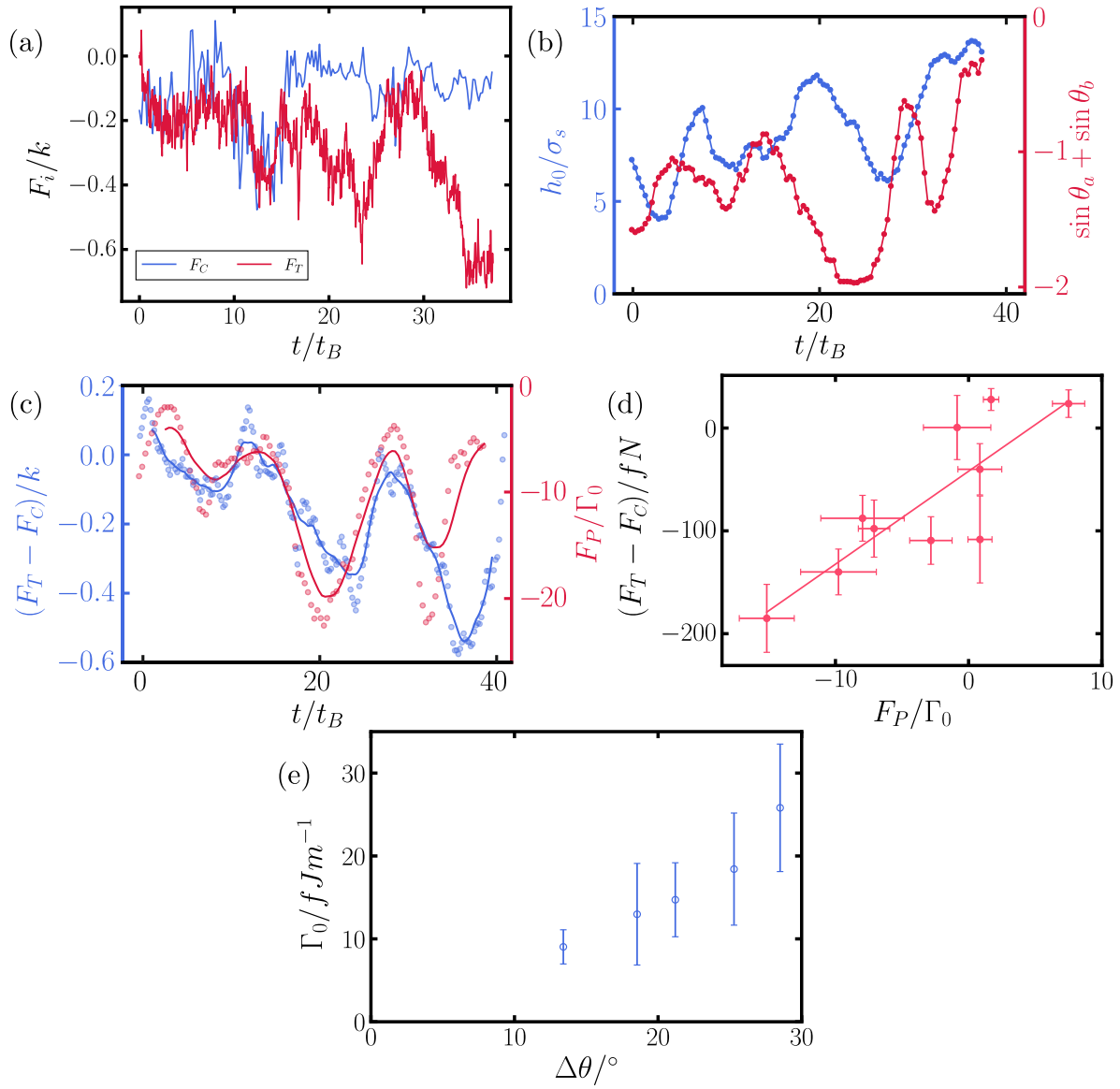


Figure 5.8: (a)-(c) correspond to a single grain boundary depinning experiment, (d) and (e) correspond to all of our depinning experiments. (a) is the time evolution of the measured trap force on the probe F_T in red and the predicted elastic force on the particle F_C in blue. (b) shows the time evolution of the measured height of the stretched grain boundary (scaled by small particle diameter) in blue, corresponding to the left-hand axis and the sines of the contact angles in red corresponding to the right-hand axis. (c) shows the time evolution of our measured pinning force (the trap force on the impurity minus the elastic force) in blue on the left-hand axis, and the predicted pinning force scaled by the grain boundary stiffness Γ_0. The solid lines are the smoothed averages of the points. (d) shows the linear scaling of the predicted pinning force against the measured pinning force, with the gradient being the grain boundary stiffness. (e) shows the change in the grain boundary stiffness measured from (d) against the misorientation of the grain boundary, for our five experiments.

time and comparing the mean values in each bin, we can examine the correlations between our measured pinning force, $F_T - F_C$ and our calculated pinning force, F_P/Γ_0, from equation 5.22. The latter is just $F_P = F_T - F_C$, scaled by the grain boundary stiffness Γ_0, therefore the gradient of a linear fit will be Γ_0. An example of a linear fit can be seen in figure 5.8 (d). The magnitudes

here are similar to those in the the unpublished experiments of Jones [251], who measured the mean pinning force through constant force microrheology, finding $F_P = 3.93 \times 10^{-13}\,\mathrm{N}$ from a GB of $\Delta\theta = 22.9°$.

We repeat this for five different grain boundaries and plot the resultant grain boundary stiffness in 5.8 (e), against the misorientation of each grain boundary. Notably, we have only plotted grain boundaries for which $\Delta\theta \gtrsim 12°$, as for boundaries below this threshold, the larger thermal fluctuations of the GB obstruct our analytical procedure of fitting the grain boundary profile and finding the contact angles. Nevertheless, the magnitudes are in line with previous measurements in colloidal crystals from grain boundary fluctuations [71, 253, 254], and indeed our own in chapter 6, which show Γ to have a magnitude of $10^{-15} - 10^{-14}\,\mathrm{J\,m^{-1}}$.
However, there is a clear trend in the stiffness, which increases with misorientation. This is not necessarily expected given simulations of colloidal polycrystals [167], suggest a plateau above $\Delta\theta \sim 20°$. The behaviour of large angle grain boundaries is dependent on the elastic properties of the crystal [26], and many two-dimensional [255, 256] and [257, 258] three-dimensional materials have different trends in the large angle grain boundary stiffness. We require more data to judge if this is truly a trend or whether there is a plateau among the noise.

5.4.4 Depinning and dislocation formation

As mentioned in the previous sections, the largest trapping force acting on the probe corresponds to the moment just after the impurity depins from the boundary. This is shown in figure 5.7 where the greatest trapping force, F_T, in (a) corresponds to the depinned snapshot (b)(vi). In figure 5.8 (c), the final measured trap force on the particle F_T is not accounted for by either the elastic response force F_C or pinning force F_P. Until depinning, $F_T - F_C$ and F_P are well correlated, and after depinning the probe is no longer in the grain boundary, so there cannot be a pinning force, and therefore there must be an additional force that arises at depinning, F_D:

$$F_T = F_C + F_P, \tag{5.23}$$

Forces during pinning

$$F_T = F_C + F_D. \tag{5.24}$$

Forces after depinning

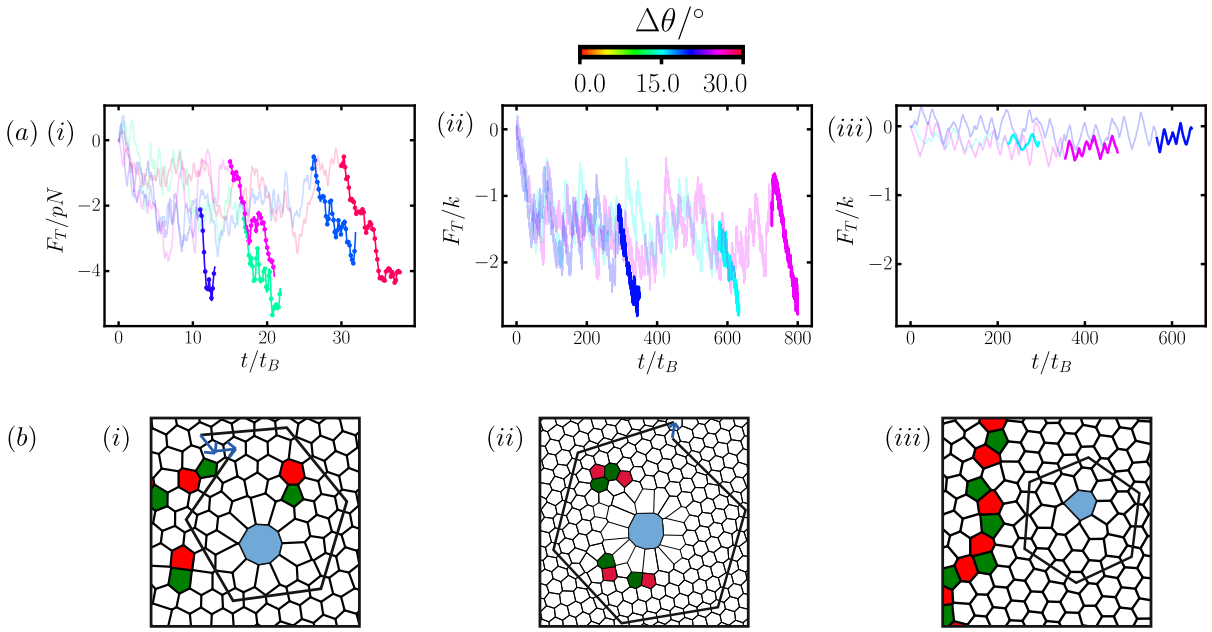


Figure 5.9: (a) (i) The force on the impurity for different experiments, colour coded by misorientation (see colour bar). The force at depinning is highlighted as opaque. (a) (ii) and (iii) show the force on the impurity for Brownian dynamics simulations with a large impurity and small impurity respectively. (b) (i), (ii) and (iii) show a Voronoi diagrams just after depinning with the impurity coloured light-blue and the dislocation 5,7-coordinate pairs coloured in green and red. A Burgers circuit is drawn around the impurity, with the Burgers vectors in blue arrows. Each diagram corresponds to the same numeral in (a).

We compare these final depinning forces, F_D, in figure 5.9 (a)(i), with the different experiments coloured by the misorientation of the boundary. The key areas where the particle becomes unpinned are highlighted with opacity. Examining the force maxima, there is a consistency in their values at the point of depinning across the experiments, irrespective of the misorientation. Therefore, the magnitude of this depinning force does not appear to be dependent on the nature of the grain boundary.

To test for a dependency on the size of the impurity instead we performed Brownian dynamics simulations, with a large ($4.5\sigma_s$) and small ($1.5\sigma_s$) sized probe. The force acting on the large probe can be seen in figure 5.9 (a) (ii) for multiple grain boundary misorientations. Note that the longer times required for depinning in these BD simulations is because the softer WCA potential leads to a less stiff and therefore more deformable grain boundary. Interestingly, the maximum force for each run of the simulation is the same, consistent with the experiments. In contrast, looking at figure 5.9 (a)(iii) for the small probe BD simulations, firstly the fluctuations are much smaller than compared to the larger probe simulations, which is because the elastic response from the crystal is less, due to this probe effectively pushing against less of the crystal. Secondly, there is no real change in the force on the probe during the depinning phase of the

simulation. Therefore, the nature of this depinning force is highly dependent on the nature of the impurity particle.

To investigate this, we look at the the Burgers vectors of each of the impurities just after depinning, shown in figure 5.9 (b) (i)-(iii), numbered to correspond to the graphs in (a). Each is a Voronoi diagram with the impurity coloured in blue and the dislocations coloured in green/red for the 5/7-coordinate particles. A Burgers circuit is drawn around each impurity with the resultant Burgers vectors as blue arrows. For (i), taken from one of the experiments, the Burgers vector is the sum of two lattice vectors. As the circuit contains a dislocation, one of the arrows is accounted for, but the only other feature is the impurity. Therefore the impurity, after leaving the boundary, creates a distortion of the lattice analogous to a dislocation. This is also noted for the impurity in (ii), where the impurity corresponds to a Burgers vector of length unity (the sum of the Burgers vectors of all of the dislocations is zero). In contrast however, for the small impurity in (iii), there is no Burgers vector from the circuit. This suggests that this depinning force is a result of the elastic energy required to create a dislocation-like distortion.

To test this, we look at the Burgers circuits around the impurity at different stages of the depinning procedure. In figure 5.10 (a) we show a circuit for a BD simulation of the large impurity size before the trap begins pulling the probe, i.e. when the system is at equilibrium. The corresponding circuit in the crystal is drawn to the right of the circuit around the impurity. Figure 5.10 (b) shows the system just before the impurity depins from the boundary. The magnitude of the resultant Burgers vector has not changed, indicating the extra dislocation analogue has not been created yet. This aligns with the notion that when the impurity is in the grain boundary, F_D is zero. In (c), the grain boundary has the same magnitude Burgers vector as in (a) and the impurity has a Burgers vector of length unity. This explains why the force F_D appears only after the particle depins; this dislocation-like distortion must have been created after depinning in (b). When the impurity is no longer adsorbed in the grain boundary, it is a separate entity analogous to a dislocation, which as established in section 5.2.3 has a corresponding elastic energy.

Using this knowledge, and from the measured forces in 5.9 (a) (i), we can estimate the elastic energy of the impurity, analogous to the elastic energy of a dislocation in equation 5.5. We assume this energy is equal to the work done on the particle over the depinning stage: $E_{el} = W = \int_{t_0}^{t} F_T \, v \, dt$, where v is the velocity of the stage and t and t_0 are the bounds of the opaque regions of figure 5.9 (a)(i). We find the elastic energy: $E_{el} = 14.0 \pm 3.3 \, k_B T$. This

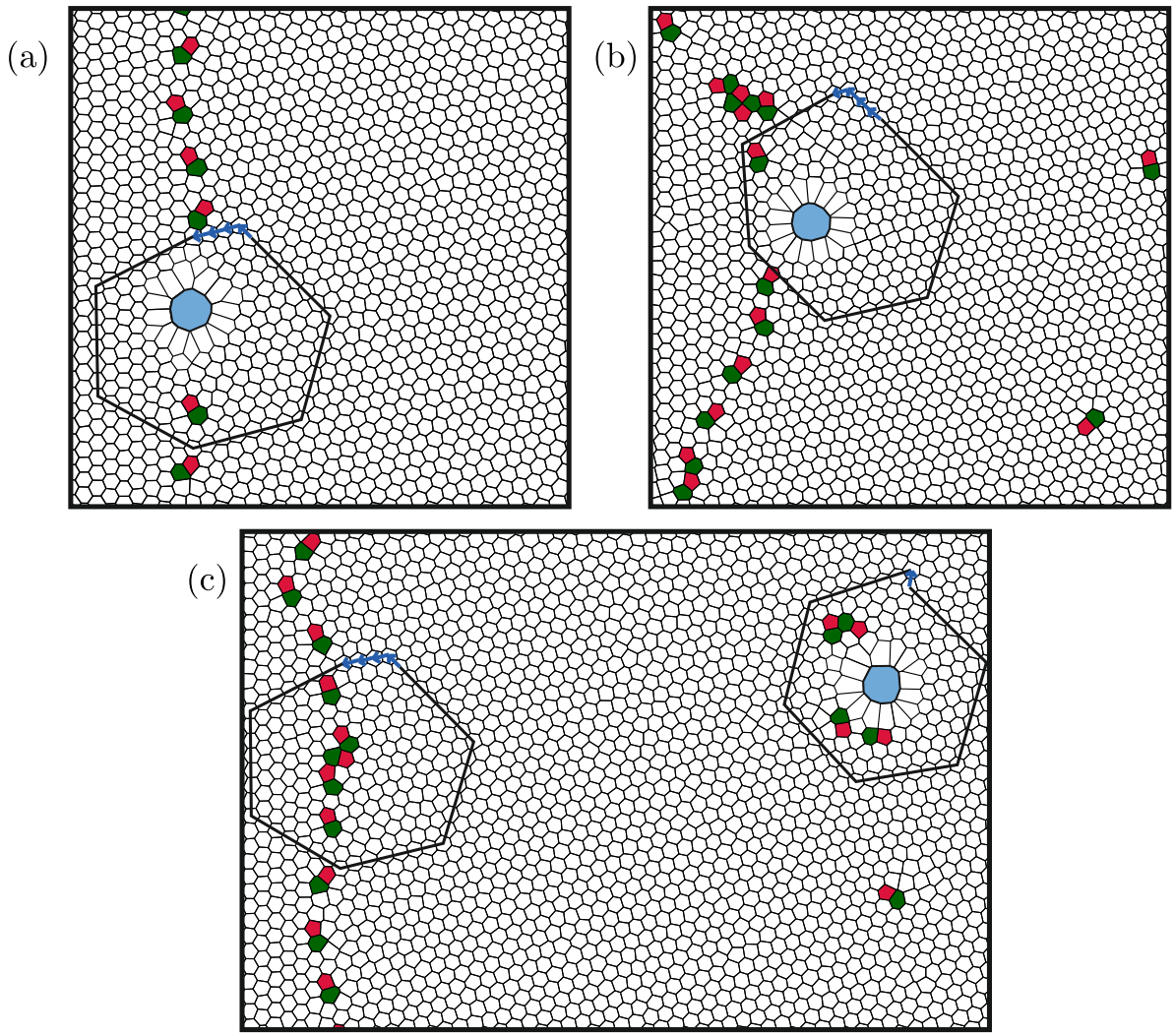


Figure 5.10: Voronoi diagrams and Burgers circuits around the impurities at three stages of depinning an impurity in a Brownian dynamics simulation with a large impurity. (a) The boundary at equilibrium, before dragging begins. (b) The system $\sim 5t_B$ before the particle depins. (c) The particle after depinning.

measurement lends credibility to our supposition of measuring the elastic energy, as it is very similar in magnitude to the energies of dislocations nucleated in colloidal crystals [212] and measured in hard-sphere Monte Carlo simulations [259].

5.5 Conclusion

In this chapter we use active microrheology in two-dimensional colloidal polycrystals to measure the forces acting on an impurity depinning from a grain boundary. Firstly, we designed an experimental procedure using our optical tweezing set-up to trap the impurity particle and image the system. Next, we dragged the impurity through a colloidal crystal to measure the elastic

deformation in front of the moving particle. We then examined the forces acting on a particle during depinning, which showed the force reached maxima when there was high deformation of the boundary and a high contact angle between the impurity and grain boundary. An additional, larger maximum is found just after the particle depins. We then use our model combining grain boundary deformation and contact angles to predict the pinning force on the particle and compare to our measured force, negating the elastic reaction force from the crystal, measured from the strain in front of the probe. We measure the grain boundary stiffness of multiple large angle grain boundaries, which all have the correct magnitude relative to previous experiments. Finally, we look at the final large depinning force, finding it to be consistent across experiments and simulations, regardless of the misorientation. Examining the Burgers circuit around the impurity, the magnitude increases at the same time as the final depinning force.

Acknowledgements

This work was performed in collaboration with Berend van der Meer, Miranda Bell-Davies and François Lavergne. Ivo Buttinoni and Nick Orr are thanked for their useful discussions. Arran Curran and Miranda are thanked for their experimental assistance and Berend is thanked for assistance with simulations.

Chapter 6

Grain boundary fluctuations between pinned impurities

Abstract

In this chapter we examine capillary wave fluctuations of a grain boundary between two impurities in a two-dimensional colloidal polycrystal. We take different spacings of the impurities and study the fluctuation spectrum, height-height correlation functions and mean-squared displacements (MSDs) of the grain boundary. We find impurities not to affect the amplitude of the modes, and the real-space form of the boundary to resemble the highest mode. We also report the impurity spacing to affect both the mobility of the grain boundary and the maximum range of the MSD. We then compare our MSDs to a previous simulation study, finding consistency between this and our experiment, and use our fluctuation spectrum to explain the behaviour.

6.1 Introduction

When asked to imagine a wave, ripples on the surface of water are likely to come to mind; from raindrops falling in a puddle to stones skipping on a lake. These are capillary waves [260], whose wavelength, wave speed and amplitude depend on the density difference, $\Delta\rho$, between air and water, surface tension, Γ, and energy E. Capillary waves are found on a variety of different phase interfaces: liquid-gas [261, 262], liquid-liquid [263, 264], solid-liquid [72, 265], and solid-solid [71, 266]. On the scale of nano- and micro-metres, these waves are instigated by thermal fluctuations [260]. In this case, the waves are like those on a stringed musical instrument [267]; the total oscillation is the sum of individual modes with different wavelengths, which can be separated by Fourier analysis. Each mode is equally excited by the thermal energy, with the distributed energy based on the wavelength, $\Delta\rho$ and Γ.

In polycrystalline systems the grain boundaries also exhibit thermal fluctuations; indeed, such fluctuations have been measured in atomic polycrystals [268, 269] and are thought to influence to their mobility [270, 271] by aiding migration of the boundary [272, 273]. The inclusion of impurities in grain boundaries is also known to greatly affect the mobility [26, 27], therefore understanding the interplay between the two is important for optimising grain growth. The time- and length-scales in atomic systems create difficulties in directly measuring the fluctuations; the aforementioned experiments can only qualitatively examine long time particle motion. Instead, grain boundary fluctuations have only been studied quantitatively through simulations [274–277] and colloidal polycrystals [71, 253].

Here, we use a doped colloidal polycrystal to examine the grain boundary fluctuations between two pinned impurities. We investigate the combined effects of grain boundary pinning on thermal grain boundary fluctuations, as has been performed in recent simulations [278, 279]. In this chapter, we use optical tweezing to create different spacings between pinned impurities in a two-dimensional colloidal polycrystal and subsequently directly image the grain boundary fluctuations. We look at the amplitude of individual fluctuation modes, finding consistency with the unpinned boundary in their scaling with $1/k^2$. Examining the spatial height-height correlation function, we find an anti-correlation at either end, consistent with the dominance of the mode with a wavelength twice the distance between the impurities. Next, we characterise the dynamic height-height correlations, finding the mobility to be highly dependent on the impurity

spacing. Finally, we examine the mean-squared displacements of the average grain boundary position at each impurity spacing, and we find a linear relationship between the area explored and the impurity spacing, which is understood by comparing the mean-squared displacements to the amplitudes of the highest wavelength modes.

6.2 Theory

6.2.1 Capillary wave theory

Power spectrum

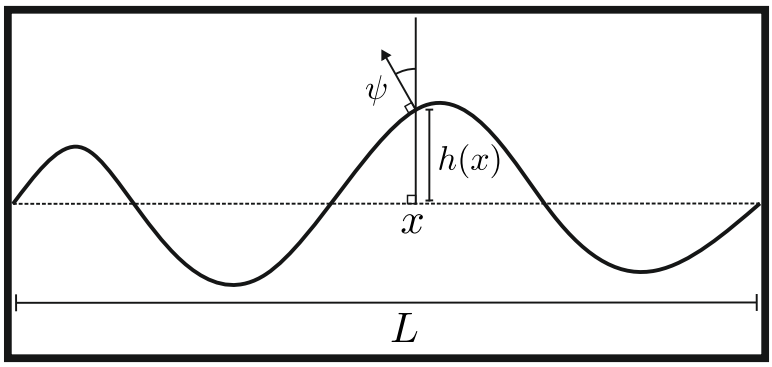


Figure 6.1: A diagram showing the fluctuations of a grain boundary from its flat position (dotted line). The boundary spans a box of length L with a point at position x having a height $h(x)$ and an angle ψ of the slope with respect to the flat boundary.

The derivations in this section are adapted from those of Skinner *et al.* [280]. Capillary waves in grain boundaries are the result of thermal fluctuations and are governed by the interfacial stiffness [281–283].

Increasing the length of a grain boundary has an associated energy cost $dE = \gamma(\psi)ds$, where γ is the GB energy per unit length, ψ is the angle of the slope, and ds is the change in length. Assuming the boundary is one dimensional at rest, when disturbed from equilibrium, the boundary at position x has a height $h(x)$ (see figure 6.1). Therefore, the extension length has the form $ds = \sqrt{1 + \left(\frac{dh}{dx}\right)^2}\,dx$, and the total energy of an interface of length L is

$$E = \int_0^L \gamma(\psi)\sqrt{1 + h'(x)^2}dx. \tag{6.1}$$

Assuming small fluctuations, $\sqrt{1+h'(x)^2} \approx 1 + \frac{h'(x)}{2}$, we can also expand the grain boundary energy:

$$\gamma(\psi) \approx \gamma + \gamma'\psi + \frac{\gamma''\psi^2}{2} + ... \tag{6.2}$$

with $'$ indicating a derivative with respect to ψ. With the supposition of small amplitude fluctuations, we can additionally approximate the slope angle in terms of h: $h'(x) = \tan\psi \approx \psi$. Therefore, with our expansions we can write the energy as:

$$E = \int_0^L \left(\gamma + \gamma' h'(x) + \frac{\gamma'' h'(x)^2}{2}\right)\left(1 + \frac{h'(x)^2}{2}\right) dx. \tag{6.3}$$

The magnitude of terms of a higher power than 2 is negligible, and the energy must be invariant with any coordinate transform: the sign of the gradient will change with a transform and therefore cannot contribute to the energy, and odd terms of $h'(x)$ can be ignored [274]. Therefore the energy reduces to

$$E = \int_0^L \left(\gamma + \frac{\gamma h'(x)^2}{2} + \frac{\gamma'' h'(x)^2}{2}\right) dx. \tag{6.4}$$

The integrated first term is $L\gamma$, the energy of the interface at rest. Therefore, the change in energy of a fluctuating boundary relative to the flat interface is $\Delta E = E - L\gamma$, hence

$$\Delta E = \frac{1}{2}\Gamma \int_0^L h'(x)^2 dx, \tag{6.5}$$

where $\Gamma = \gamma + \gamma''$ is the grain boundary stiffness.
Now, we can write the height of the boundary as the sum of normal modes:

$$h(x) = \sum_k A_k \exp(ikx), \tag{6.6}$$

with wave-vectors $k = 2\pi n/L$, and A_k is the amplitude of mode k. Taking the derivative and substituting into equation 6.5, we find

$$\begin{aligned}\Delta E &= \frac{1}{2}\Gamma \int_0^L \sum_{k_m} A_{k_m} \exp(ik_m x) \sum_{k_n} A^*_{k_n} \exp(-ik_n x) dx \\ &= \frac{1}{2}\Gamma \int_0^L \sum_{k_m}\sum_{k_n} A_{k_m} A^*_{k_n} \exp(i[k_m - k_n]x) dx\end{aligned} \tag{6.7}$$

Due to the orthogonality of Fourier transforms, the only non-zero terms in the integral are when $k_n = k_m$, therefore:

$$\Delta E = \frac{1}{2}\Gamma \sum_k L k^2 A_k A_k^*. \tag{6.8}$$

Using equipartition, where each Fourier mode is excited by $\frac{1}{2}k_B T$ and by finding the resultant wave amplitudes we can build a full model of the grain boundary fluctuations, according to the method of Hoyt *et al.* [274]. Assuming equipartition theory applies to each mode we find the static fluctuation spectrum of the grain boundary [266, 274, 275],

$$\langle |A_k|^2 \rangle = \frac{k_B T}{L\Gamma k^2}, \tag{6.9}$$

where $\langle ... \rangle$ indicates the ensemble average.

The corresponding dynamic correlation function for a particular wave-vector is found [274]:

$$\langle A_k(t_0) A_k(t + t_0) \rangle = \langle |A_k|^2 \rangle \exp(-M\Gamma k^2 t), \tag{6.10}$$

where t is the time lag and M is the mobility of the grain boundary; effectively the inverse of the friction coefficient [26].

Static correlation function

The static height-height correlation function, $g_h(x)$, is defined as

$$g_h(x) = \langle h(x_0) h(x + x_0) \rangle, \tag{6.11}$$

and measures the correlation of the height of two points on the grain boundary separated by a distance x. Given equations 6.6 and 6.9, we find the Fourier transform of the correlation function:

$$g_h(x) = \frac{k_B T}{L\Gamma} \sum_k \frac{1}{k^2} \exp(ikx). \tag{6.12}$$

The range of wave vectors has a maximum and minimum k_{max} and k_{min}. The minimum is defined by the length of the field-of-view, $k_{min} = 2\pi / L_{FoV}$, which we approximate $2\pi / L_{FoV} \to 0$. The

maximum will have the smallest possible wavelength, which will be on the order of the particle diameter: $k_{max} = 2\pi/\sigma$ which we approximate $2\pi/\sigma \to \infty$. We can convert equation 6.12 to an integral over the wave-vectors, which runs from $-k_{max}$ to k_{max}, as the waves have a direction:

$$g_h(x) = \frac{k_B T}{L\Gamma} \frac{L}{2\pi} \int_{-\infty}^{\infty} \frac{1}{k^2} \exp(ikx) dx. \tag{6.13}$$

The integral is symmetric about zero, so odd functions will cancel out. The complex part of the integral can be split up into $\cos(kx) + i\sin(kx)$, and the real and imaginary terms are even and odd respectively. Therefore, the integral is reduced to

$$g_h(x) = \frac{k_B T}{\pi\Gamma} \int_{0}^{\infty} \frac{1}{k^2} \cos(kx) dk. \tag{6.14}$$

The static correlation length ξ is introduced, to prevent divergence at small k [284, 285]. This is the length-scale over which the correlation of the heights between two points on the boundary decays. For fluctuations with wavelengths greater than ξ, their contribution to $g_h(x)$ is diminished as the correlations across the span of the wavelength become weaker.

$$g_h(x) = \frac{k_B T}{\pi\Gamma} \int_{0}^{\infty} \frac{1}{k^2 + \xi^{-2}} \cos(kx) dk. \tag{6.15}$$

This can be integrated analytically, leading to:

$$g_h(x) = \frac{k_B T}{2\Gamma} \xi \exp(-x/\xi), \tag{6.16}$$

which can be applied to real-space data to find Γ and ξ.

Dynamic correlation function

The dynamic correlation function, $g_h(t)$, is defined as

$$g_h(t) = \langle h(t_0) h(t + t_0) \rangle, \tag{6.17}$$

and measures the correlation in the height at a single point on the boundary at a time lag t. We have seen the inverse space equivalent of this in equation 6.10, which shows each Fourier mode

decays exponentially in time. Taking an inverse Fourier transform of equation 6.10 gives us:

$$g_h(t) = \frac{k_B T}{L\Gamma} \sum_k \frac{1}{k^2} \exp(-M\Gamma k^2 t) \exp(ikx). \tag{6.18}$$

By looking at $x = 0$ and following the same arguments as for $g_h(x)$, this can be made into an integral and we can introduce the correlation length, leading to [71]

$$g_h(t) = \frac{k_B T}{\pi\Gamma} \int_0^\infty \frac{\exp(-M\Gamma[k^2 + \xi^{-2}]t)}{k^2 + \xi^{-2}} dk. \tag{6.19}$$

This can be integrated analytically, leading to:

$$g_h(t) = \frac{k_B T \xi}{2\Gamma} \text{erfc}\left(\frac{\sqrt{\Gamma M t}}{\xi}\right), \tag{6.20}$$

where erfc is the complimentary error function. This can be fitted to our experimental data in conjunction with the static height-height correlation function to find the mobility M.

6.2.2 Grain boundary diffusion

We can also examine the dynamics of the fluctuations by studying the mean-squared displacement of each point on the boundary. These points can be assumed to be undergoing a one-dimensional random walk, with an average mean-squared displacement (MSD) $\langle \bar{h}^2 \rangle = 2Dt$, where $\langle ... \rangle$ indicates a time-lag average and $\bar{h}$ is the average height over the length of the boundary [209]. The diffusion constant has the form [276]:

$$D = \frac{M k_B T}{L}, \tag{6.21}$$

where M is the grain boundary mobility and L is the length of the interface.

The introduction of impurities into the grain boundary leads to a drag force on the boundary which impedes the random walk. For small displacements due to the fluctuations, the force from the impurities on the boundary can be approximated as a basic Hookean spring, with $F = L_C k_s h$, where L_C is the confinement length, i.e. the distance between the impurities, and k_s is a parameter that incorporates the amount of drag, dependent upon the particle size and spacing [279]. From the method of Chen *et al.* [279], this can be incorporated into the

mean-squared displacement. Firstly, they find the change in average height:

$$\frac{d\bar{h}(t)}{dt} = M[\bar{f}(t) - k_s h], \tag{6.22}$$

where $\bar{f}(t)$ is the mean thermal noise force across the length of boundary. They solve this equation, finding

$$\langle \bar{h}^2(t) \rangle = \frac{k_B T}{L_C k_s}[1 - \exp(-2Mk_s t)]. \tag{6.23}$$

In the small time limit of $t \ll 1/Mk_s$, $\langle \bar{h}^2(t) \rangle = \dfrac{2Mk_B T}{L_C}$ and the MSD is linear with respect to time. In the long time limit $t \gg 1/M\Gamma$: $\langle \bar{h}^2(t) \rangle = \dfrac{k_B T}{L_C k_s}$, and the MSD reaches a plateau.

6.2.3 Motion and forces of the pinned grain boundary

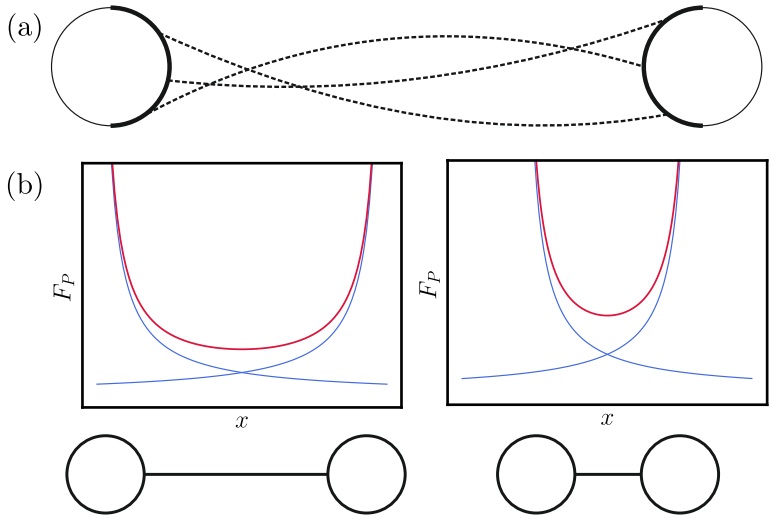


Figure 6.2: (a) Possible grain boundary positions relative to the impurities, with the possible contact points between the grain boundary and impurities highlighted. (b) The graphs show the pinning forces on the grain boundary from impurities in the blue lines, with the total pinning force in red. The two graphs are for different impurity spacings, indicated by the cartoons beneath.

It is important here to note that the ends of the grain boundary are not pinned in the sense of a vibrating string on a musical instrument, but instead the GB must maintain contact with the surface of the impurity. This could be at any point of the semi-circle on the same side as the GB, as shown in figure 6.2 (a). Therefore, the GB is akin to a vibrating string with free ends [286].

The impurities each also exert a pinning force on the boundary, and in chapter 5 the

deformation due to this force was shown to decay with distance along the boundary. Therefore, the GB between two impurities will have a total pinning force that is a sum of the two pinning forces. The magnitude of the total pinning force therefore varies across the bounded length and depends on the distance between the impurities, as shown in figure 6.2 (b).

6.3 Experimental

The experiments in this chapter consist of imaging the fluctuations of a single grain boundary bounded by two impurities in a two-dimensional colloidal polycrystal.
We use the same microscope and optical trapping set-up described in section 5.3.1, an inverted brightfield microscope with a 50× magnification objective. We also use the same colloidal system: 2.95 µm melamine formaldehyde spheres forming a polycrystal with a sparse scattering of 10.75 µm impurities of the same material (as shown in table 2.1).

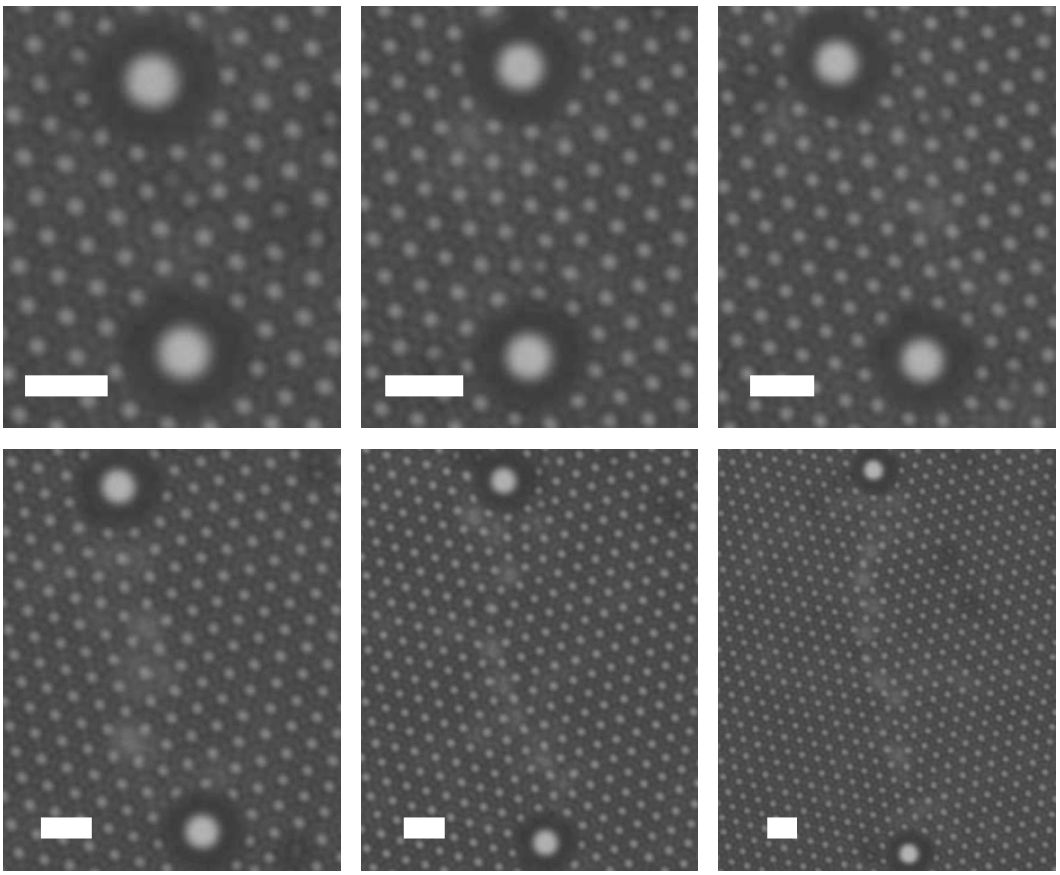


Figure 6.3: Images from an experiment showing different separations of the impurities in the boundary, $L = 29.4$, 36.3, 41.9, 60.3, 75.3 and 89.1 µm. The scale bar in each image represents 10 µm.

The experimental procedure was to find a long, straight grain boundary in the sample and to

use optical tweezers, as discussed in section 2.2.3, to place two impurities in the boundary, at a distance L_C apart. By moving the impurities slowly and in steps to allow for the crystal to relax, there was minimal disruption of the crystalline structure and that of the grain boundary. After the particles were in position and we allowed 10 min for the system to relax, we started recording the boundary at a frame rate of 2 Hz for 5 min. The experiment was repeated 3 times, before we used the optical tweezers to move one of the impurity particles further from the other, creating a longer impurity spacing. The optical trap is switched off before the experiment begins. Experimental images of these different distances can be seen in figure 6.3. The process of allowing relaxation and recording was then repeated. This grain boundary had a misorientation of 24.3°.

To analyse the data from the images, we performed our standard image analysis and bond-orientational order parameter, ψ_6, calculation as described in section 3.3.2. To find the grain boundary, we first reorientated the particle coordinates to account for the grain boundary being at an angle. To this end, we drew a vector between the centres of the impurities, and centred and rotated the coordinates about the middle of the line, such that the grain boundary was vertical. To then find the boundary, we employed the method described in section 5.3.2, of dividing the particle y-coordinates into bins of length $2\sigma_s$, and fitting a hyperbolic tangent function to the orientation. This method has successfully been used to measure the grain boundary fluctuations in non-doped colloidal crystals [71]. We calculate the height-height correlation functions by dividing the grain boundary into vertical bins with the length of two particle diameters. The height in each bin, $h(x)$, is relative to the average position of the grain boundary. We perform this procedure for both the unpinned and pinned boundaries, noting that, as is shown in figure 6.2, the pinned boundary is free to fluctuate at all points along its length and therefore we can average $g_h(x,t)$ across all bins. For the unpinned grain boundary, we use a length L of the boundary that covers the majority of our field of view, $L = 140\,\mu\text{m}$. Note that for the pinned boundaries, we have two lengths L_C and L. The first, L_C, is the distance between the impurities, whereas the second, L, is the length of grain boundary we divide into bins. The latter is taken from the edge of the impurities, therefore $L = L_C - \sigma_i$. Importantly, in this chapter, L_C is used when discussing the effect of pinning (for measuring the mobility and the MSD) and L is used when discussing the shape of the fluctuations and the individual modes.

6.4 Results and discussion

6.4.1 The unpinned grain boundary

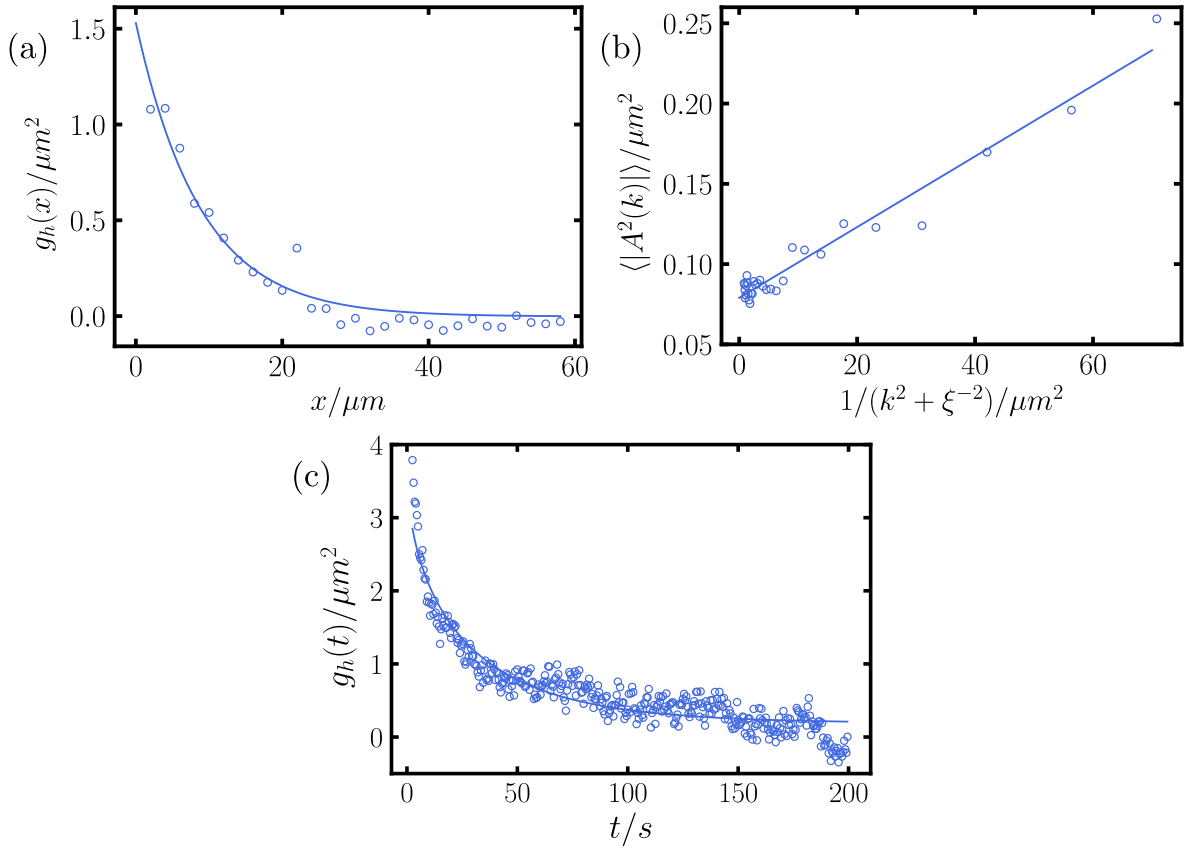


Figure 6.4: (a) The grain boundary's static height-height correlation function, $g_h(x)$ for an unpinned system. (b) The static power spectrum of the unpinned boundary. (c) The dynamic height-height correlation function $g_h(t)$ for an unpinned system.

Firstly, we examine the fluctuations of an unpinned grain boundary to find the stiffness, Γ, and correlation length, ξ. To this end, we use the static height-height correlation function and static power spectrum of the modes [71]. The analytical form of $g_h(x)$ is shown in equation 6.16, and we fit this to our data, as shown in figure 6.4 (a). From this, we find $\Gamma = 1.21 \times 10^{-14}\,\mathrm{J\,m^{-1}}$ and $\xi = 8.82\,\mu\mathrm{m}$, which are consistent with previous measures [71, 253, 254]. Introducing the correlation length into the power spectrum (equation 6.9), the square amplitude of each mode should follow the expression:

$$\langle |A_k|^2 \rangle = \frac{k_B T}{L\Gamma(k^2 + \xi^{-2})}. \tag{6.24}$$

Using the previous value of ξ, we find another measure of Γ from the gradient of the fit in figure 6.4 (b): $\Gamma = 1.04 \times 10^{-14}\,\mathrm{J\,m^{-1}}$, again consistent with previous measurements [71, 253, 254].

We can also examine the dynamic height-height correlation function. We use the analytical form of $g_h(t)$ in equation 6.20, to fit to the data plotted in figure 6.4 (c). From this we find $\Gamma = 1.02 \times 10^{-14}\,\mathrm{J\,m^{-1}}$, which is in good agreement with the static measurements.

6.4.2 Spatial aspects of the pinned boundary

Next, we study the fluctuations of a grain boundary pinned by two impurities. Here it is again important to note that we differentiate the different experiments with the impurity spacings L_C, e.g. in the key in figure 6.5 (b), but the length of the grain boundary, $L = L_C - \sigma_i$, is used to normalise the energy amplitude and to directly compare the static height-height correlation functions.

To examine the profile of the boundary between the impurities, first we examine the power spectrum, in line with equation 6.24, using $\xi = 8.82\,\mu\mathrm{m}$. We plot the power spectra for the different impurity spacings in figure 6.5 (a). These are all quite linear, as expected from equation 6.24, and there is a clear L dependence with shorter spacings having a higher gradient. Scaling the data sets by L, seen in figure 6.5 (a), the curves fall on top of one another. Therefore, the grain boundary stiffness Γ is unaffected by the impurities and can be extracted from linear fits. From averaging these fits, we find $\Gamma = 2.14 \pm 1.63 \times 10^{-14}\,\mathrm{J\,m^{-1}}$. This is close to our measured value in the previous section, further indicating the scaling with k is unaffected by the confinement.

The static height-height correlation function for the pinned boundaries is shown in figure 6.5 (c). The x-axis is scaled by the grain boundary length, L, and the functions have all nearly collapsed onto one another. The shape of each curve is an almost linear decrease from the mean-squared grain boundary width $g_h(x = 0) = \langle h^2 \rangle$, to the negative of this value, $g_h(x = L) = -\langle h^2 \rangle$. A further important aspect is that except for the highest impurity spacing experiment, $L = 78.4\,\mu\mathrm{m}$ ($L_C = 89.1\,\mu\mathrm{m}$), none of the curves pass through $(L/2, 0)$ either. This is vastly different compared to the shape of $g_h(x)$ for the unpinned boundary in figure 6.4 (a), which has an exponential decay that remains positive and the rate of decorrelation is determined by the correlation length ξ. When $g_h(x)$ for the unpinned boundary decays to zero, the positive

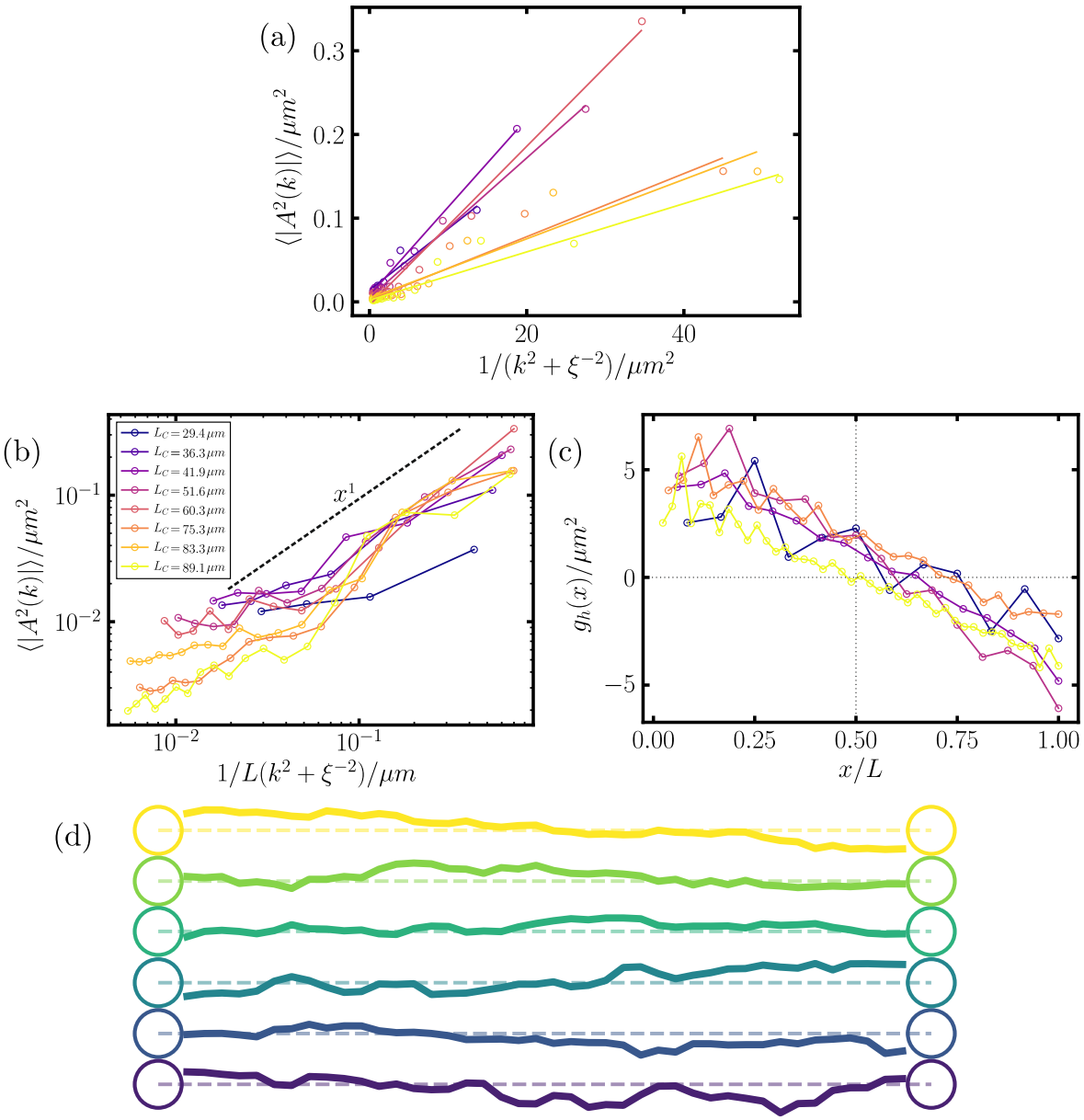


Figure 6.5: (a) The power spectra of the different impurity spacings, the colours corresponding to those in the key of (b). (b) The power spectra of pinned boundaries, scaled by the boundary length, L, on a log-log plot to resolve the different curves. (c) The static height-height correlation function of pinned boundaries, with the distance scaled by the length of the boundary. (d) A time series of a single pinned boundary. The line between each set of circles is the boundary's profile at this time, with the zero position marked as a dashed line. The spacing of each successive time is 50 s.

and negative correlations cancel out. In the case of the pinned boundaries, there must be a persistent negative correlation at opposite ends of the boundary: the total shape of the capillary wave should roughly be sinusoidal, with either end being in anti-phase.

To examine this further, in 6.5 (d), we plot the grain boundary profile at different times. In this figure, it is clear that the grain boundary is oscillating with a visually dominant mode

of wavelength $2L$, as is apparent in comparing the uppermost screenshot and fourth from the top. This mode dominating makes sense, considering the impurities act as barriers to modes, from which the capillary waves can either be reflected or transmitted through [287]. The modes we measure either must originate within the confinement, or penetrate through the impurities from the longer boundary, which has an energy cost to move the impurities themselves [286] and would likely greatly reduce their amplitude. It appears therefore, that modes must be excited within the confinement, and the wavelengths of these modes appear to have the form $2L/n$, where n is an integer, similar to the confined waves found in the capillary wave studies of Tan *et al.* [288] and Pigot *et al.* [289]. Therefore, the highest wavelength mode is the $2L$ wave seen in figure 6.5 (d), which we would expect to dominate, as the amplitude from equation 6.24 should be roughly double that of the next mode of wavelength L.

Finally, returning to the point that $g_h(x)$ does not pass through $(L/2, 0)$. For the unpinned boundary figure 6.4 (a), the function decays to zero, and becomes uncorrelated, at $\sim$30 µm. Therefore, for the $2L$ mode to be fully accommodated, the length of the boundary, L, must be at least double this length at $\sim$60 µm to permit a decay to zero at $(L/2, 0)$. In figure 6.5 (c), only the longest grain boundary, which does indeed pass through $(L/2, 0)$, meets this criterion.

6.4.3 The dynamic height-height correlation function of the pinned boundary

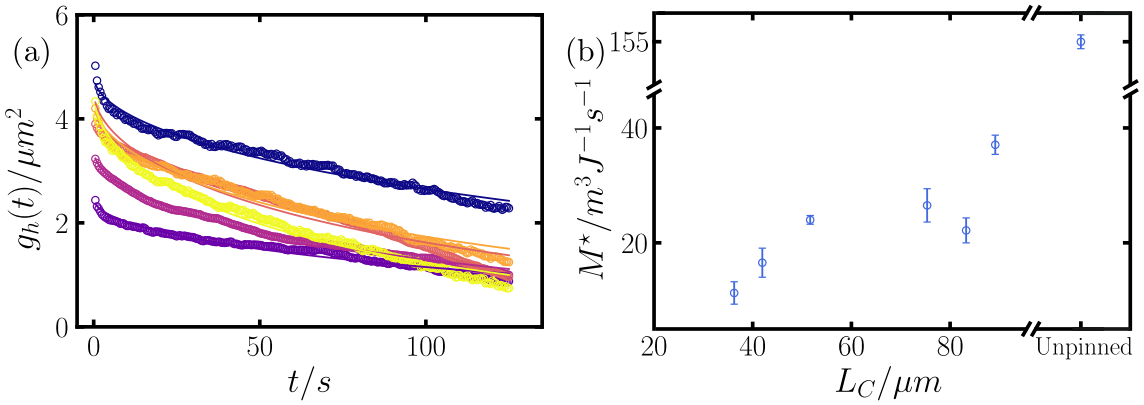


Figure 6.6: (a) The dynamic height-height correlation function, $g_h(t)$, for pinned boundaries, with the colours corresponding to the key in figure 6.5 (b). The fitted curves correspond to the solution to the integral for $g_h(t)$, shown in equation 6.20. (b) The effective mobility, $M^\star$, against the impurity confinement length L_C. The final point in the top right is the value of the mobility measured from the unpinned boundary, but the discontinuity in both axes means the position of this final point is not to scale.

Measuring the dynamic height-height correlation function, $h_g(t)$, for our pinned boundaries,

we find good fits for all impurity spacings, as seen in figure 6.6. There is no apparent trend in L_C, which is understandable as there is no length dependence in the solution for the integral of $g_h(t)$ in equation 6.20. This is also to be expected given the power spectrum in figure 6.5 (b), where the measured amplitudes of the dominant highest wavelength modes have similar values. The fitted curves correspond to the solution of the integral for $g_h(t)$, shown in equation 6.20. The magnitudes of the initial values, $g_h(t=0)$ or the mean squared width $\langle h^2 \rangle$, are similar to the unpinned boundary, however the decay rates are clearly different, as the unpinned boundary decays from $g_h(t) \approx 4$ to $g_h(t) \approx 1$ in approximately 30 s, whereas the pinned boundary with L_C = 29.4 µm decays from $g_h(t) \approx 5$ to $g_h(t) \approx 3$ in approximately 125 s. From equation 6.20, the data in figure 6.6 (a) will be fitted by the equation:

$$g_h(t) = \frac{k_B T \xi}{2\Gamma} \mathrm{erfc}\left(\frac{\sqrt{\Gamma M^\star t}}{\xi}\right). \tag{6.25}$$

The decay rate is governed by $\sqrt{\Gamma M^\star}/\xi$, and as we have established with our power spectra in figure 6.5 (b), both the grain boundary correlation length ξ and the grain boundary stiffness Γ are consistent with the unpinned boundary. Therefore, the difference in decay rate must be due to the effective grain boundary mobility, $M^\star$, being affected by pinning from the impurities. This is different from the mobility, M, of the unpinned boundary, as the value of M should be intrinsic to the GB, based on the misorientation and particle area fraction [253]. Conversely, $M^\star$ accounts for the pinning effect, and will be a function dependent on M and L_C.

We plot $M^\star$ against the impurity spacing L_C in figure 6.6 (b). Note that there is a discontinuity in both axes to show our measured value of the mobility for the unpinned grain boundary. We mark this 'Unpinned' on the x-axis, although this grain boundary will still be bounded by triple junctions beyond the field-of-view. Nevertheless, there is a clear trend: decreasing the impurity spacing leads to a decrease in the effective mobility. This trend is consistent with that measured from the mean-squared displacements of simulated pinned boundaries [279]. As shown in section 6.2.3, decreasing L_C leads to an increase of the total pinning force, therefore the resistance to motion, the inverse of mobility, will increase.

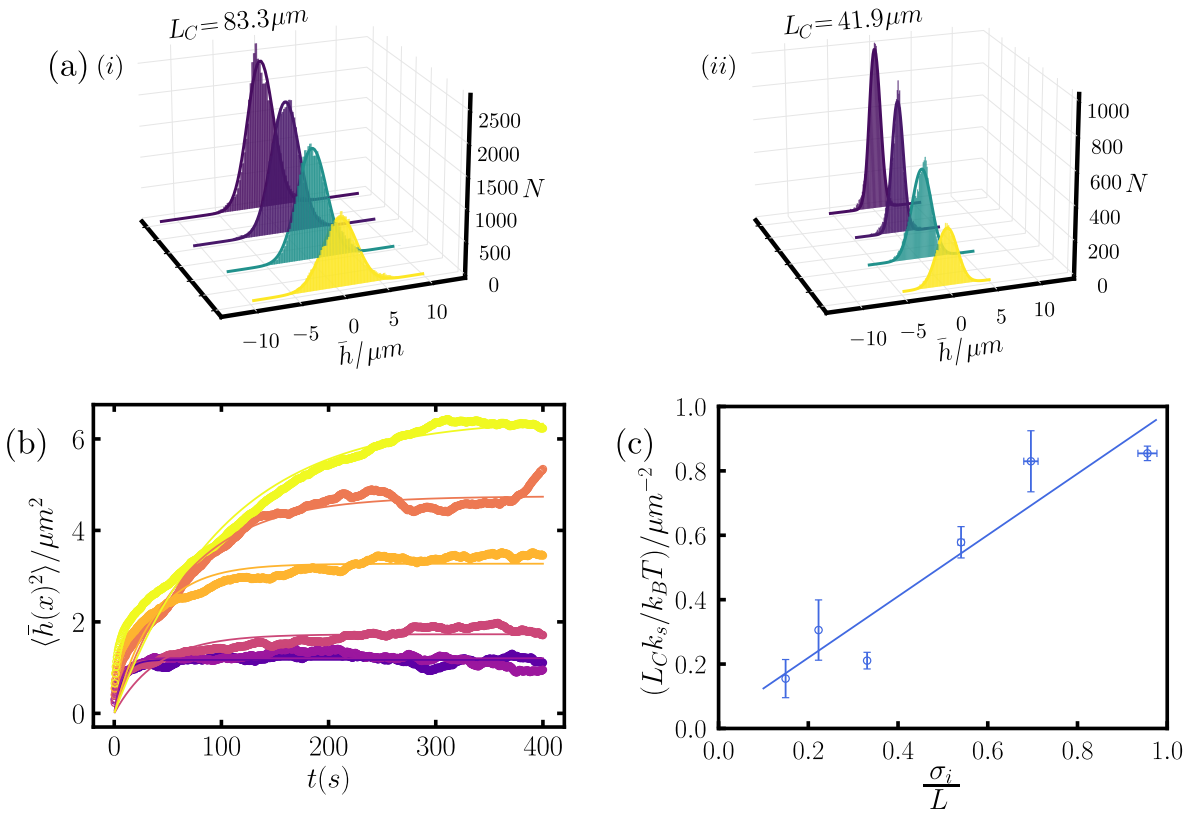


Figure 6.7: (a) (i) and (ii) are histograms showing the distributions of grain boundary displacements at different time lags: 25, 50, 200 and 400s in order for the distributions coming towards the viewer. (i) and (ii) are for impurity separations of 83.8 µm and 41.9 µm respectively. (b) is the mean-squared displacement of the grain boundary for different spacings (see key in figure 6.5 (a)). (c) a plot of the reciprocal of the grain boundary length against the plateau height from (b).

6.4.4 Mean-squared displacements of pinned boundaries

In this section, we compare our experimental results for the mean-squared displacements of pinned grain boundaries to those of the simulations of Chen *et al.* [279]. Firstly, figures 6.7 (a) (i) and (ii) show the distribution of displacements of the average grain boundary height $\bar{h}$ at certain time lags ($25, 50, 200$ and $400\,$s), with later times closer to the viewer. All distributions show a reasonable Gaussian fit with a broadening at longer times, as expected for a random walk. Comparing the two, the longer boundary shows broader distributions, which indicates motion is less restricted by the impurities. This is further supported by the mean-squared displacements from figure 6.7 (b), in which the plateau value indicates the limit on the motion from the impurities. The fits are from equation 6.23, which suggests the plateau value of $\langle h^2(t) \rangle$ is inversely proportional to $L_C k_s$, where k_s is a parameter quantifying pinning due to the impurities. This is further explored in figure 6.7 (c), in which the reciprocal of the grain

boundary length is plotted against the reciprocal of the plateau value. As shown in section 6.2.3, a shorter L_C corresponds to a greater pinning force, so the amount of drag per unit length also increases. With a greater amount of drag, the maximum distance the boundary can move decreases. With regard to the fit, Chen *et al.* [279] suggest a power law relationship with the power $1.5 - 1.8$. In contrast, our data is much more linear.

We can perhaps understand this linearity by providing an alternative explanation for the plateau and examining the individual modes that lead to the random walk. From equation 6.8, the energy of an individual mode is:

$$E_k = \frac{L\Gamma k^2 \langle A_k^2 \rangle}{2}, \tag{6.26}$$

with the wave vector $k = 2\pi/\lambda$, (λ being the wavelength), and A_k the amplitude of this mode. As shown in figure 6.5 (b), the modes that dominate the fluctuations are those with the highest wavelengths. We can make the approximation that the value of the MSD's plateau is reached as a result the highest wavelength mode, with $\lambda = 2L$, and the energy of this dominant mode is:

$$E_0 = \frac{2\pi^2 \Gamma \langle A_0^2 \rangle}{L}. \tag{6.27}$$

The actual value of the plateau is governed by $L_C k_s$, which has the units of an energy density Jm^{-2}. The energy density of the dominant mode can similarly be found by dividing both sides of equation 6.27 by $\langle A_0^2 \rangle$:

$$\frac{E_0}{\langle A_0^2 \rangle} = \frac{2\pi^2 \Gamma}{L}, \tag{6.28}$$

which also shows a reciprocal relationship between the grain boundary length L and the energy density. Testing this further, if $E_0/\langle A_0^2 \rangle \approx L_C k_s$, the gradient of the fitted curve in figure 6.7 (c) should be $2\pi^2\Gamma$. Inputting the gradient, we find $\Gamma \approx 5 \times 10^{-13}\,\mathrm{J\,m^{-1}}$, which is certainly the correct order of magnitude. Therefore, the value of the plateau in the MSD appears to be related to the energy density of the dominant modes. As each mode is given a quantised amount of energy, $\frac{1}{2}k_B T$, a lower energy density means the mode explores more area, hence leads to a greater $\langle \bar{h}(x)^2 \rangle$.

6.5 Conclusion

In this chapter we have performed experiments examining the thermally induced capillary waves between two impurities in two-dimensional colloidal grain boundaries. Comparing to an unpinned boundary, we examined different impurity spacings. Firstly, we examined the modes in each boundary, finding consistency with the unpinned boundary for the scaling of the amplitude with the wave vector. Next, we found an anti-correlation in the spatial height-height correlation function, indicating the highest wavelength mode dominated the profile. Secondly, we examined the dynamic height-height correlation function, finding the mobility of the grain boundary decreased with the impurity spacing. Finally, we examined the mean-squared displacements of the boundaries, finding the maximum value to scale linearly with the length, related to the energy density of the modes.

Acknowledgements

Berend van der Meer and Miranda Bell-Davies are thanked for useful discussions.

Chapter 7

Sedimentation-diffusion equilibrium of two-dimensional binary colloidal fluids

Abstract

In this chapter we study sedimentation-diffusion equilibrium of binary systems comprising differently sized colloids of different materials such that they possess the same gravitational height. When placed on a tilt with respect to gravity, they form a binary fluid up to area fractions of 0.9, without significant size fractionation. We equilibrate five tilt angles and examine the structures of the sedimentation-diffusion equilibrium, finding a lack of crystallinity and amorphous structure throughout. We characterise the dynamics in terms of the mean-squared displacements and self-intermediate scattering functions, finding transient subdiffusion at intermediate times and diffusion at long times at all packing fractions. Finally we find the magnitude of the dynamics decreases with an increased tilt angle, a result of structural rearrangements originating from the low density regions of the system.

7.1 Introduction

Considering the broadest picture, one creates a supercooled fluid by taking a liquid and cooling it past its freezing point, such that it is in a metastable, amorphous state [132]. Going further past this point leads to an Arrhenius, or even super-Arrhenius, [125] increase in the viscosity and eventually a glass forms. Alternatively, a glass is reached if the temperature is rapidly quenched, as the particles have no opportunity to rearrange [132]. The dynamics of the glass are typically arrested on any meaningful timescale, with the definition of 'meaningful' mostly set by to convention [82]. For example, an observer would see the famously viscous pitch drop experiment [290] drip a few times in their lifetime, whereas the glass bell jar encasing it would not have flowed appreciably over the lifetime of the universe [291]. Nevertheless, both would appear to be solids to the impatient experimentalist. Fortunately, understanding this dynamic slowdown is both accessible and relevant to studies of polymer glasses [292], metallic glasses [293] and even cryogenic freezing [294].

The structure and dynamics of glasses and supercooled fluids are inherently linked. Not only in the literal sense, as various theories of the glass transition assert [42,125,127,132], but also that both are complex and disordered. Disorder arises from the structure being amorphous, i.e. lacking order, and from dynamics being spatially and temporally heterogeneous. The complexity is embodied by the search for order and meaning in the structure [295, 296], and reasoning the dynamic slowdown approaching the glass transition [127, 297]. As such, supercooled fluids and glasses are one of the foremost unsolved topics in condensed matter physics [39].

Colloidal systems provide an excellent route to studying hard sphere glasses and supercooled fluids [42, 53, 82, 132, 298], due to their accessible time- and length-scales. In this case, cooling down the fluid is akin to increasing the packing fraction of colloids [299]. We can unite their utility with a previous experiment on the phase behaviour of two-dimensional monodisperse colloids [72], which put the system on a gravitational tilt. This experiment allowed for probing of the entire phase diagram under sedimentation-diffusion equilibrium. If we apply the same conditions to a binary colloidal system, we can potentially create a supercooled fluid or glass former with an equilibrated concentration gradient. As such, we can probe the dynamics throughout, examining how the continuous area fraction profile affects the dynamics. The behaviour of high area fractions would be of great interest as either the system will be arrested and

glassy, or deeply supercooled. The mechanisms of this arrest or supercooling should be studied, given the importance of dynamic length-scales in supercooling [42]. As the effect the Earth's gravitational field on the dynamics of 3D colloidal glasses has been shown [85] in comparison to microgravity [300], changing the tilt angle should also produce insights into vitrification.

In this chapter, we create a system of binary colloids that have equal gravitational height and, as such, when placed on a slope, both species of colloid will have overlapping sedimentation-diffusion profiles. By choosing the colloidal diameters and materials carefully, we prevent fractionation and create a concentration gradient with equal mixing throughout. We make sedimentation-diffusion profiles with area fractions $0 < \phi \lesssim 0.9$, for five different angles. In our analysis, we first check the sedimentation-diffusion profiles are consistent with one-another, and measure the gravitational heights using scaled particle theory. We next examine the structures across the density profile, finding the amorphous structure to hold throughout. We then look at the dynamics, finding a continuous slowing down of dynamics as the area fraction increases, along with two-step dynamics consisting of cage rattling motion and cage-breaking. Comparing the different tilt angles, we find the dynamics slow down with a decreased gravitational height. We finally examine the effect of gravitational height on the emergence, number and orientation of dynamic heterogeneities.

7.2 Theory

7.2.1 Sedimentation-diffusion equilibrium

A sedimentation-diffusion equilibrium is established when our colloids are placed in a gravitational field. In this case, we consider the two-dimensional system. There is a balance between the flux of colloids sedimenting due to gravity, J_s. and upward flux due to diffusing along the concentration gradient, J_d:

$$J_s = Nv_s, \tag{7.1a}$$

$$J_d = -\frac{k_B T}{\xi}\frac{dN}{dz}, \tag{7.1b}$$

where N is the number of particles, z is the height, and ξ is the drag constant. The terminal

sedimentation velocity, v_s, is reached when drag equals the gravitational force: $\xi v_s = k_B T/h_g$. Hence at equilibrium where $J_s = J_d$ we get the differential equation $dN/dz = -h_g N$, which when solved gives the area fraction distribution:

$$\phi(z) = \phi_0 \exp(-z/h_g). \tag{7.2}$$

Here $\phi(z) = Na/A$, where A is the total area, a is the particle area, and ϕ_0 is the area fraction at the bottom of the cell. At low densities we can assume an ideal gas: $\Pi = (N/A)k_B T = \phi k_B T/a$, with the osmotic pressure Π, which we can substitute into the density distribution to get the equation of state:

$$\frac{\Pi a}{k_B T} = \phi_0 \exp(-z/h_g), \tag{7.3}$$

or written in reduced units $\widetilde{\Pi} = \Pi a/k_B T$ and $\widetilde{z} = z/h_g$:

$$\widetilde{\Pi} = \phi_0 \exp(-\widetilde{z}). \tag{7.4}$$

Scaled particle theory

Scaled particle theory is highly useful for modelling hard sphere fluids due to the number of thermodynamic properties that can be derived [301]. While there is an extension of the theory to binary fluids, it has been shown experimentally that the simpler monodisperse theory is equally accurate for relatively small size ratios up to approximately 1.5 [65].
For our purposes, the expression relating pressure and total area fraction ($\phi_T = \phi_s + \phi_l$) is given by:

$$\frac{\Pi}{\rho k_B T} = \frac{1}{(1-\phi_T)^2}. \tag{7.5}$$

Multiplying both sides by the particle area a, we have the left hand side $\Pi a/\rho k_B T = \widetilde{\Pi}/\rho$ and, since $\phi_T = \rho a$, the expression simplifies to:

$$\widetilde{\Pi} = \frac{\phi_T}{(1-\phi_T)^2}. \tag{7.6}$$

We can unite this with the density profile by looking at the pressure at a point in the sample due to the weight of particles above. Starting at height z, if we move downwards by dz, the difference in pressure will be equal to the new weight supported from above:

$$\Pi(z) - \Pi(z + dz) = \rho(z)\frac{k_B T}{h_g}dz. \tag{7.7}$$

This can be written in integral form [302]:

$$\widetilde{\Pi}(z) = \frac{1}{h_g}\int_z^\infty \rho(z)dz, \tag{7.8}$$

and incorporating scaled particle theory leads to:

$$\frac{\phi_T}{(1-\phi_T)^2} = \frac{1}{h_g}\int_z^\infty \phi_T(z)dz. \tag{7.9}$$

This means we can find the pressure from our colloidal system by integrating the density profile. By fitting to scaled particle theory we can also find the gravitational height of our particles at the different tilt angles.

7.2.2 The structure of glasses and supercooled fluids

As discussed in section 2.1.5, both glasses and supercooled fluids have amorphous structures. To check our system is indeed amorphous and has no ordering due to binary crystallisation or fractionation, we first examine the structure of glasses and supercooled fluids using the radial distribution function (RDF) $g(r)$ [94]. The two-particle RDF is expressed as:

$$g(\vec{r}) = \frac{1}{\rho N}\left\langle \sum_{i=1}^{N}\sum_{j\neq i}^{N}\delta(\vec{r} - \vec{r}_i + \vec{r}_j)\right\rangle, \tag{7.10}$$

where r is a distance, N is the number of particles in the system, and ρ is the number density of the system. The Kronecker delta $\delta(\vec{r} - \vec{r}_i + \vec{r}_j)$ is 1 if $\vec{r}_i - \vec{r}_j = \vec{r}$, and 0 otherwise. To simplify, for our purposes we use a one dimensional RDF by taking a radial average across the system. The result is a function that describes the probability of finding a particle j at a scalar distance r away from particle i. When looking at binary systems, the total RDF is the sum of three

partial RDFs [65]:

$$g(r) = x_s^2 g_{ss}(r) + x_s x_l g_{sl}(r) + x_l^2 g_{ll}(r), \tag{7.11}$$

where x_i is the mole fraction of species i and $g_{ij}(r)$ indicates the partial RDF computed between species i and j. By examining the relative heights of the peaks of the partial RDFs ($g_{ss}(r)$, $g_{sl}(r)$ and $g_{ll}(r)$), we can characterise the amount of local ordering, fractionation and any long-range ordering that may be occurring throughout the sample.

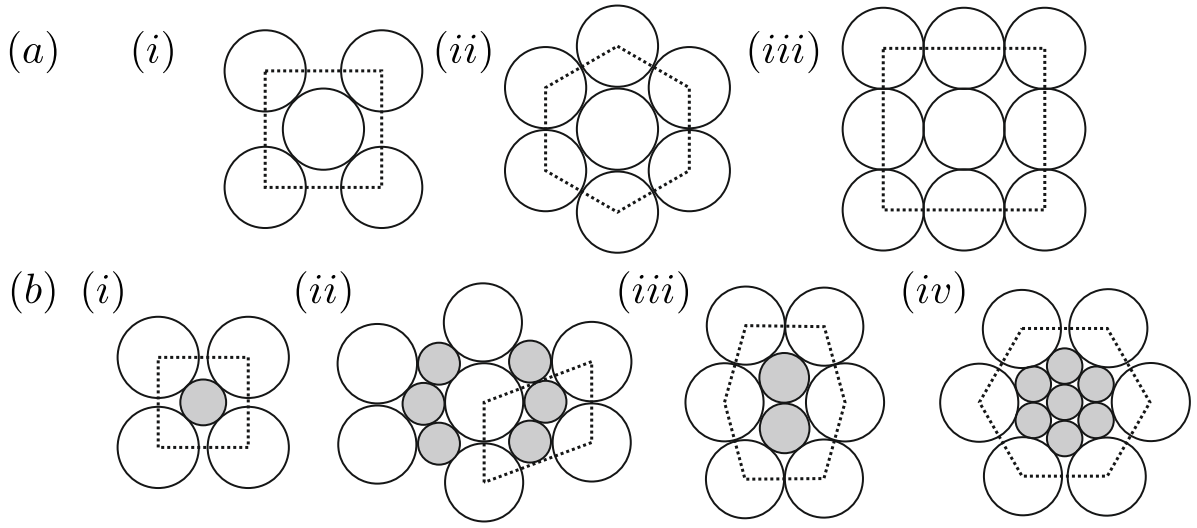


Figure 7.1: (a) shows unit cells of different monocrystalline structures. (b) shows unit cells of non-additive binary crystals that could occur with our size ratio at high pressures.

Next, we examine the prevalence of crystalline order in the structure. While an amorphous structure will have some local ordering [75], the cells should not form tessellated pattern as this would mean longer-range ordering. We can measure the crystallinity with the six-fold bond-orientational order parameter ψ_6 (see section 2.1.4). However, this alone is not sufficient, as monodisperse crystals can have non-close packed structures when formed under deposition [303, 304], as seen in figure 7.1(a) (i) and (iii). Both of these structures have square unit cells, which tessellate and therefore can lead to potential long-range order. We can detect these using a generalised bond-orientational order parameter:

$$\psi_n(\vec{r}) = \frac{1}{N_j} \sum_{j=1}^{N_j} \exp(in\theta_{jk}), \tag{7.12}$$

where n is the number of neighbours in the unit cell, with the crystallinity of a particle being

$|\psi_n(\vec{r})|$.

In addition to crystallisation due to fractionation [305], we can also examine binary crystallisation. Due to the non-additivity of the particles, as discussed in section 2.1.3, it is favourable for the small particles to cluster around the larger ones [107], which dictates the possible unit cells. The infinite pressure phase diagram of non-additive binary hard disks has been examined by Fayen *et al.* [112], from which we took the most probable binary unit cells based on our particles' size ratio and non-additivity. These four can be seen in figure 7.1. We can differentiate these unit cells based on the identity and ordering of the particles' neighbours.

Two-particle entropy

For supercooled fluids, there is a theorised connection between entropy and dynamics [306], which argues a greater number of microstates should increase the number of favourable local structural rearrangements, and therefore the likelihood of particles dynamically rearranging to these states. To test for such predispositions towards local rearrangements, we can examine the excess entropy. This is the entropy of the system relative to that of an ideal gas, and as such contains configurational and vibrational contributions to S [307]. Previous studies have shown a correlation between the excess entropy and the rate of dynamics in glasses [308–312].

We can approximate the excess entropy by calculating its first and most contributive term, the the two-particle entropy S_2, as previously utilised in experiments on colloidal monolayers [102,313]. This relates to the pair-wise correlations between particles [307]; for our binary system it is possible to derive an expression for this from the radial distribution functions [314],

$$S_2 = -\frac{\rho}{2}\sum_{i,j} x_i x_j \int_0^\infty [g_{ij}(r)\ln g_{ij}(r) - (g_{ij}(r)-1)]rdr, \tag{7.13}$$

where i and j refer to the small and large species, x is the mole fraction of a species and ρ is the density.

7.2.3 The dynamics of glasses and supercooled fluids

As discussed in section 2.1.5, decreasing temperature and more deeply supercooling an atomic glass former leads to slower dynamics. In the case of colloidal systems, the dynamics slow down

with an increase in total area fraction ϕ_T. The probability distribution of displacements by a vector $\vec{r}$ at a time interval t is given by the self-van Hove correlation function [94]:

$$G_s(\vec{r},t) = \left\langle \frac{1}{N}\sum_{i=1}^{N}\delta(\vec{r} - [\vec{r}_i(t+t_0) - \vec{r}_i(t_0)]) \right\rangle, \tag{7.14}$$

where $\langle ... \rangle$ indicates an average over different starting times t_0, and N is the number of particles. To gather more information on the dynamics of particles, we can examine the different moments of the self-van Hove function:

$$\langle \Delta r^n(t) \rangle = \int \vec{r}^{\,n}(t) G_s(\vec{r},t) d\vec{r}. \tag{7.15}$$

The most significant of these for our purposes is the second moment, the mean-squared displacement (MSD):

$$\langle \Delta r^2(t) \rangle = \frac{1}{N}\sum_{i=1}^{N}\langle [\vec{r}_i(t+t_0) - \vec{r}_i(t_0)]^2 \rangle, \tag{7.16}$$

which characterises the average area within which a particle moves in the time t. In the case of diffusive dynamics, as discussed in section 2.1.1, this area increases linearly with time, scaled by the diffusion constant. With an increase in particle density, this area is expected to decrease and eventually deviate from linearity, instead producing two regimes [132]. The initial regime at short times consists of intra-cage motion, where the particle's trajectory is bound by the positions of its neighbours. The MSD here appears diffusive ($\langle \Delta r^2(t) \rangle \propto t$), but quickly starts to flatten once the cage has been explored. This is β-relaxation, and is succeeded by α-relaxation, involving inter-cage motion. Here the sub-diffusive 'plateau' of the MSD transitions again into a diffusive regime, as the particle breaks out of its cage. With an increase in area fraction, one would expect both regimes to be affected. In the case of β-relaxation, the size of the cage will decrease and the value of the MSD will be lower. The length of the intermediate sub-diffusive phase should also increase as it will require more energy for a particle to break out, meaning this event is rarer, and the time for α-relaxation (τ_α) will increase. This behaviour is seen in binary colloidal systems [315], with the transition between a supercooled fluid and glass accompanied by a continuous slowing down of τ_α [76, 77, 298, 316, 317].

Often in standard mean-squared displacement measurements, measured α-relaxation can be obfuscated by either collective motion [78, 81, 318] or, in two-dimensions, long-wavelength

thermal Mermin-Wagner fluctuations [76, 81]. To filter these mechanisms, we can examine the displacement of a particle relative to all its neighbours' average displacements. This is the dynamic Lindemann parameter γ_L [319], which has the form:

$$\gamma_L(t) = \frac{\langle[\Delta r_i(t+t_0) - \Delta r_{NN}(t+t_0)]^2\rangle}{2a_0^2}, \tag{7.17}$$

where $\Delta r_i(t)$ is the displacement of particle i at time lag t, $\Delta r_{NN}(t+t_0) = \frac{1}{N_i}\sum_{n=1}^{N_i}\Delta r_n(t+t_0)$ is the sum of the displacements of all of the neighbours, at time t_0, of particle i, and a_0 is the lattice spacing (σ_s in the case of our binary system). The form of this curve should be similar to the MSD, but the τ_α in this case will truly only be related to cage breaking.

To further examine the relaxation time, we can look at the Fourier transform of the self-van Hove function, the self-intermediate scattering function (SISF):

$$F_s(k,t) = \left\langle \frac{1}{N}\sum_{j=1}^{N}\exp[i\vec{k}\cdot(\vec{r}_i(t+t_0) - \vec{r}_i(t_0))]\right\rangle, \tag{7.18}$$

where $\vec{k}$ is the wavevector. This function shows first β- then α-relaxation: starting at $F_s(k,t) = 1$, there is a decay then plateau, a result of the β-relaxation. After this, the function decays to zero, due to α-relaxation. We can extract the relaxation time by fitting a stretched exponential, $F_s(k,t) = \exp -(t/\tau_\alpha)^a$. Considering one dimension, $k = |\vec{k}|$, and at small values, the SISF can be expanded [320]:

$$\ln F_s(k,t) = -\frac{k^2\langle\Delta r^2(t)\rangle}{4} + \frac{1}{2}\alpha_2(t)\left(\frac{k^2\langle\Delta r^2(t)\rangle}{4}\right)^2 + \dots . \tag{7.19}$$

Retaining only the first term leads to the resultant expression for the SISF:

$$F_s(k,t) = \exp\left(-\frac{k^2\langle\Delta r^2(t)\rangle}{4}\right), \tag{7.20}$$

which is known as the Gaussian approximation [20,315]. This will hold only when the dynamics are diffusive, as this does not account for the α- and β-relaxation regimes. This approximation also holds in real space, as the self-van Hove correlation function can also be approximated as a Gaussian [94]:

$$G_s(r,t) = \left(\frac{1}{2\pi\langle\Delta r^2(t)\rangle}\right)^{1/2}\exp\left(\frac{-r^2}{2\langle\Delta r^2(t)\rangle}\right). \tag{7.21}$$

Comparing $G_s(r,t)$ to a Gaussian distribution should therefore give us an idea about the diffusive nature of the dynamics.

Dynamic heterogeneities and cooperative motion

When the dynamics are non-diffusive, the higher order terms of $\ln F_s(k,t)$ in equation 7.19 become relevant. Indeed, this can be quantified through the value of $\alpha_2(t)$, which is known as the non-Gaussian parameter [321] and is calculated in 2D as

$$\alpha_2(t) = \frac{1}{2}\frac{\langle \Delta r^4(t) \rangle}{\langle \Delta r^2(t) \rangle^2} - 1. \tag{7.22}$$

A greater value is indicative of greater deviation from diffusive dynamics. Furthermore, this parameter measures the kurtosis of the distribution of displacements, i.e. the weight of the tails [322]. Therefore, the value of $\alpha_2(t)$ also indicates the proportion of particles moving abnormally quickly with respect to the average rate of diffusion. This is useful because, as mentioned in section 2.1.4, in supercooled fluids, the motion of particles becomes more dynamically heterogeneous as the system is cooled further. With more heterogeneity, the tails of the self-van Hove distribution will become more prominent and $\alpha_2(t)$ increases in value [323]. Typically, for a supercooled fluid we would expect $\alpha_2(t)$ to evolve to reach a peak which then decays to zero [133]. The reason for this shape is due to the rearrangements having an associated average timescale; smaller rearrangements result in a peak at earlier times. Before the peak, the number of particles involved in rearrangements is increasing, therefore $\alpha_2(t)$ increases. After the peak, the width of the distribution increases due to single particle cage-breaking diffusion, and the distribution becomes more Gaussian, thus $\alpha_2(t)$ decreases.

The nature of these dynamic heterogeneities is cooperative [306], with particles moving in 'strings' [42]. If one particle were to find space in which to move, one of its neighbours could now move into the original particle's now vacated area. A precession of neighbours undergoing this process results in strings of moving particles. To measure these in our system we examine the positions of pairs of particles i and j after a time lag. The particles are defined to have moved cooperatively if the following condition is satisfied:

$$\min[|\vec{r}_i(t) - \vec{r}_j(0)|, |\vec{r}_i(0) - \vec{r}_j(t)|] < \delta = 0.6\sigma_s, \tag{7.23}$$

where the value of δ is chosen to match the original by Donati *et al.* [129]. For the pairs of particles that fulfil this condition, we can then join overlapping sets to formulate the strings. The presence of cooperative motion is thought to be indicative of a connection between the dynamic and spatial length scales, although the exact nature of this is unknown [42].

7.3 Methods

7.3.1 Experiments

For our aims in this experiment, we required both a microscope that could be permanently and stably set at a shallow angle, and a system of hard sphere-like binary colloids with equal gravitational heights.

Microscopy

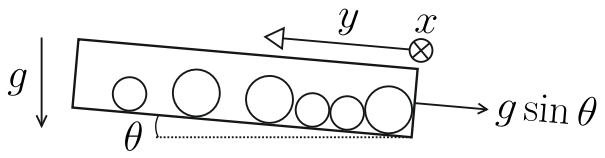


Figure 7.2: A schematic of the binary system in the cell placed on a tilt. We note the coordinate axes x and y, where x goes into the plane and perpendicular to gravity, and y is in the plane and parallel to gravity. The direction of gravity is denoted g and the tilt angle is θ. The acceleration due to gravity parallel to the base of the cell is given $g \sin\theta$.

Firstly, the microscope used is described in section 2.2.2. It is a bright-field optical microscope placed on a base with three height-adjustable legs allowing for the entire microscope to be set at an angle. The particle suspension was contained in a Hellma cell, which was placed on a machined flat plate affixed to the xy-stage. The cell was pushed against a fixed vertical block to ensure the position of the cell could be regained if knocked out of position. A hole underneath the Hellma cell allowed for imaging of the colloidal particles.

The diagram in figure 7.2 shows the cell placed at a tilt. The set angle, θ, leads to the colloidal particles sedimenting to the right hand side of the cell with an acceleration of $g \sin\theta$ and being confined to a monolayer with an acceleration of $g \cos\theta$. In this chapter, we set $\theta \lesssim 0.22°$, therefore the particles are still strongly confined in a monolayer. As a convention here we also refer to the axis parallel to the gravitational field $g \sin\theta$ as y, and perpendicular as x.

We used a digital spirit level to coarsely measure the angle, having calibrated the systematic error (due to the differences between the spirit level and cell's angle) by measuring sedimentation velocities of a dilute sample.

7.3.2 Colloidal particles

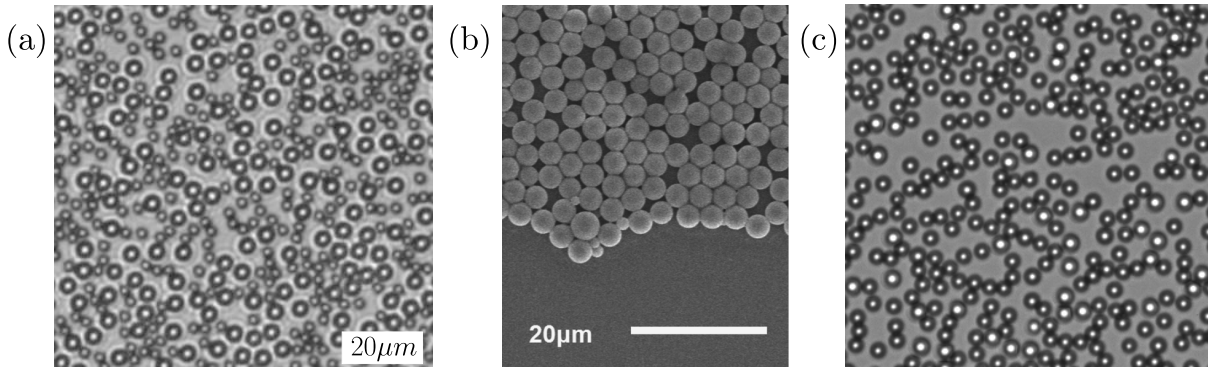


Figure 7.3: (a) shows a representative screenshot of the first system, with 2.79 µm MF and 3.77 µm PMMA in 20/80 v/v% EtOH/H_2O. (b) is an SEM image of our synthesised 3.85 µm TPM particles. (c) shows a representative screenshot of the second system with 3.85 µm TPM and 2.79 µm MF particles. The scale bar is the same as in (a).

For the particles, we used two different systems. The small particles in both cases were melamine formaldehyde (MF) spheres, chosen due to the stability in water and proven hard sphere nature [65]. These spheres have a mass density of $\rho_{MF} = 1.51\mathrm{g\,cm^{-3}}$. The constraints of our experiment required the criteria of similar gravitational heights, h_g, and a size ratio ≈ 1.4 to be fulfilled. The size ratio is complicated somewhat, due to the non-additivity [324]. As shown in figure 2.3, geometrically, the in plane size of the large particles is given as $\sigma_l' = 2\sqrt{\sigma_s\sigma_l} - \sigma_s$, therefore if $\sigma_l'/\sigma_s \approx 1.4$, then $\sigma_l/\sigma_s \approx 1.44$. With this and the gravitational heights fixed, we can estimate the mass density of the other type of particles. From the equation for the gravitational height (equation 2.6), we find the ideal large particle's mass density as:

$$\rho_l = \left(\frac{\sigma_s}{\sigma_l}\right)^3 [\rho_s - \rho] + \rho, \tag{7.24}$$

where ρ_i is the mass density of particle species i and ρ is the mass density of the solvent. In the case of the solvent being 20/80 v/v% ethanol/water as in our other experiments, $\rho = 0.971\mathrm{g\,cm^{-3}}$ [325, 326], hence the ideal large particle's material should have a density: $\rho_l = 1.15\mathrm{g\,cm^{-3}}$. The closest common material used for colloidal synthesis is polymethyl methacrylate (PMMA), which has a density of $\rho_{PMMA} = 1.18\mathrm{g\,cm^{-3}}$. Our first system therefore consisted of MF and PMMA

Experiment name	$\sigma_s/\mu m$	$\sigma_l/\mu m$	Large material
PMMA 0	2.79	3.77	PMMA
PMMA 1	2.79	3.77	PMMA
TPM 0	2.95	3.87	TPM
TPM 1	2.95	3.87	TPM
TPM 2	2.79	3.87	TPM

Table 7.1: σ is the diameter. PMMA = Poly-methylmethacrylate and TPM = 3-(trimethoxysilyl)propyl methacrylate.

particles of sizes 2.79 µm and 3.77µm respectively ($\sigma_l'/\sigma_s = 1.32$). A representative image of this system can be seen in figure 7.3 (a).

Due to the DLVO potential, a careful balance of electrostatic repulsion and van der Waals forces must be maintained to achieve the ideal hard-sphere potential. In this thesis we measure the particle diameter by fitting the radial distribution function of a monodisperse sample to a fundamental measure theory simulation from Thorneywork *et al.* [65]. Two of the tilt angles in this chapter use the PMMA particles, but from this fitting we found these to be highly charged, leading to a softer potential. Due to this, for the other three angles we use a different system with a harder potential.

By using the deuterated equivalent of the previous solvent: 20/80 v/v% CD_3CD_2OD/D_2O, the range of densities for the larger particle given by equation 7.24 changes. This new solvent has the same chemical properties, meaning the surface chemistry of the colloidal particles and thereby the pair potentials are unchanged, but with a greater density of $\rho = 1.08\mathrm{g\,cm^{-3}}$ [326]. The ideal large particle material mass density for this solvent is $\rho_l = 1.22\mathrm{g\,cm^{-3}}$, close to that of 3-(trimethoxysilyl)propyl methacrylate (TPM) which has a density of $\rho_{TPM} = 1.29\mathrm{g\,cm^{-3}}$. Using the synthesis of Liu *et al.* [138], we created particles of size 3.87 µm ($\sigma_l'/\sigma_s = 1.35$), which can be seen in an SEM image in figure 7.24 (b). These TPM colloids were found to be much more hard sphere in nature in their potentials compared to the PMMA particles. A representative image of this MF-TPM system is seen in figure 7.3 (c). The composition of the different experiments from this chapter are shown in table 7.1.

Imaging the sedimentation-diffusion profile

The experimental procedure for creating the sedimentation-diffusion profile is as follows. Firstly, a dilute suspension of both large and small particles was made, with concentrations adjusted for an equal area fraction of both. This was placed into a Hellma cell and sealed tightly with blu-tac. This was then placed on the tilting microscope, ensuring the cell was pushed against the block and the legs were secured tightly with the tilt set at a shallow angle. The entire set-up was then left for a minimum of six weeks to allow for sedimentation-diffusion equilibrium to be reached.

After this, to check equilibrium had been reached, the top of the density profile was imaged for 24hrs, ensuring there was no drift or change in the density profile over this time. At this point, data gathering began from the bottom of the density profile at the point at which the pressure became high enough that particles were forced out of the monolayer. This area was imaged for 3hrs at 1Hz, after which the field-of-view (FoV) was carefully moved higher up in the density profile, making sure there was overlap with the previous FoV and the same image gathering process was repeated. We took images following this procedure until the entire density profile had been imaged. After this, the angle was altered and then allowed to re-equilibrate before new data could be taken.

7.3.3 Brownian dynamics simulations

Brownian dynamics simulations (see section 2.3) are used to study the dynamics of the sedimentation. In this chapter, the simulations are performed by taking a starting configuration of small and large particles of sizes $\sigma_s = 1$ and $\sigma_l = 1.4$, ensuring the area fractions of each are equal. The box is configured such that there are periodic boundary conditions in the x-direction, but hard walls in y, which have the potential with particle i:

$$U(r)/k_BT = 4(\epsilon/k_BT)\left[\left(\frac{\sigma_i}{r}\right)^{12} - \left(\frac{\sigma_i}{r}\right)^{6} + \frac{1}{4}\right], \tag{7.25}$$

where σ_i is the diameter of the particle and r is the distance between the particle and the wall, with a cut-off of $r < 2^{1/6}\sigma_i$. The particle potentials are also described in section 2.3. For the entirety of the experiment, an external force of gravity is added to induce sedimentation. In this chapter, we examine two different regimes: one in which the gravitational heights are

representative of our experiments and one in which the sedimentation velocities are equal but the gravitational heights are not. For the former, we simply add an additional term of g to the y-force calculation step; the force due to gravity is equal for both particles. For the latter, we apply the same gravitational force prefactor to each particle.

7.4 Results and discussion

7.4.1 Density profiles

The resultant density profiles after equilibration for our five angles are shown in figure 7.4 (a). The x-axis is the height from the bottom of the first recorded field-of-view and is scaled by the diameter of the small particle, $\sigma_s = 2.79\,\mu\text{m}$. The y-axis is the total area fraction, $\phi_T = \phi_s + \phi_l$. It is clear that all five data sets have a similar shape: when descending from the top of the sample, there is at first a rapid increase in area fraction from $\phi_T \sim 0$ to $\phi_T \approx 0.7$. After this point, going deeper into the sample, there is a much slower increase in the total area fraction, going from $\phi_T \approx 0.7$ to $\phi_T \approx 0.85$ for all of the experiments. In this region, the sediment has the pressure due to the weight of the particles stacked above, thereby increasing ϕ_T. All of the experiments have a similar maximum area fraction; above this, the high osmotic pressure forces particles out of the monolayer, and note $y = 0$ was set where this multilayer began. A visual representation of the density profile is seen in figure 7.4 (c).

The five curves have the same shape, but the relative elongation is a result of the different tilt angles: the lower the angle the longer the distribution. In fact, the sedimentation-diffusion tail elongates with an increased gravitational height, as $\phi_T \propto \exp(-y/h_{g||})$. Neither of the two longest profiles reach $\phi_T = 0$, and instead tail off at $\phi_T \approx 0.1$. These are the experiments with the highly charged PMMA particles, as mentioned in section 7.3. This could be explained due to the charge: an elongation of the distribution has been found in the sedimentation-diffusion equilibrium of charged colloidal rods [327], the key to which was the absence of additional salt, a factor which our system also lacks. The length of the higher density parts of the profile, $0.7 \lesssim \phi_T \lesssim 0.9$, also increases with a shallower angle. This length should depend on the point at which the pressure from the weight above the particles is enough to form a multilayer. As a lower gravitational height means a smaller buoyant mass, more particles are required to reach this weight, hence the distribution is longer. As detailed in appendix C, we also find this

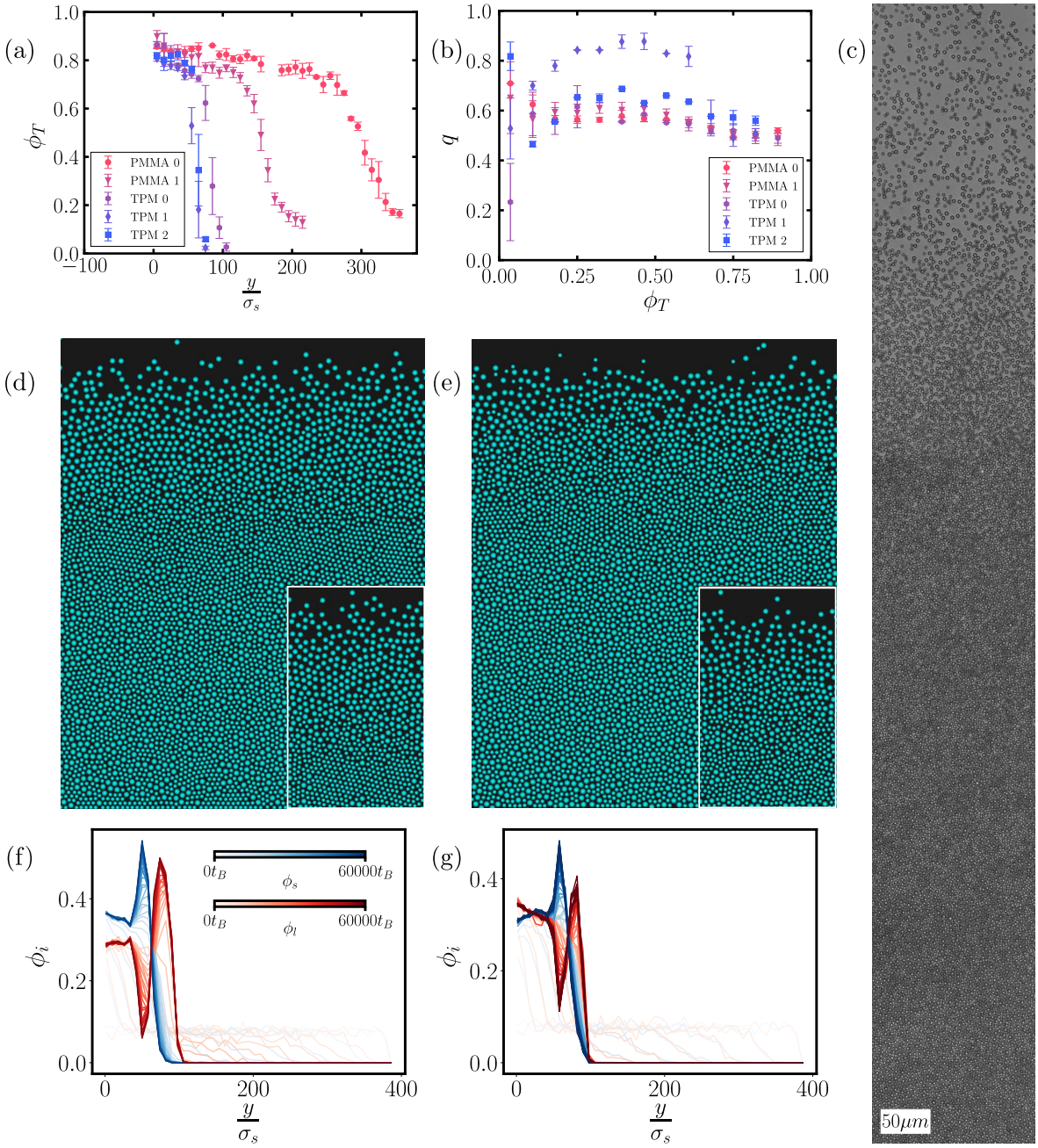


Figure 7.4: (a) The density profiles of area fraction for our five experiments. (b) The size fraction $q = \phi_l/(\phi_l + \phi_s)$ at different points in the density profile. (c) A stitched together image of the entire height of experiment *PMMA 0*. (d) The final particle configuration of the BD simulation with equal gravitational heights. Inset is the top of the sediment soon after all particles have finished sedimenting. (e) is the same as (d) but for the BD simulation where the particles have equal sedimentation velocity. (f) and (g) show, the area fractions at different heights in the sediment over the time-frame $6 \times 10^5 t_B$ for equal gravitational height and sedimentation velocity BD simulations respectively. The paler the colour, the earlier in time (see key).

behaviour in a dynamic Monte Carlo simulation of the experimental system.

Next, we quantify the composition throughout the density profile. Figure 7.4 (b) shows the fraction $q = \phi_l/(\phi_l + \phi_s)$ against the total area fraction in the sample, which is fairly consistent

across the entire density profile. For all but one set of experiments, $q \sim 0.5$ for the entire density profile. Therefore, the system has not fractionated. For TPM 1 however, there is a large increase in q until $\phi_T \sim 0.7$, meaning at lower densities there is a higher proportion of large particles. To investigate this, we turned to Brownian dynamics (BD) simulations to examine the process of sedimentation.

The first of the two BD simulations was representative of our experiment, in which the particles had the same gravitational height, thus experiencing the force due to gravity equally. However their sedimentation velocities differed due to different drag coefficients. In this simulation, the Péclet number, characterising the ratio of directed and diffusive transport rates, was set to be the same as in the tilt experiment with an angle of 0.05°. The final result of this simulation (after $6 \times 10^5\, t_B$) is seen in figure 7.4 (d), in which there is a clear fractionation of large particles at the top, a number of small particle crystallites beneath, and good mixing beneath this. The inset shows the top of the profile at an earlier time, $3 \times 10^5\, t_B$, which looks similar to the final result. Therefore, after sedimentation there is not much evolution of the profile. Figure 7.4 (f) shows the evolution of the density profile for large and small particles, with the different lines being the profile at different times. From this, the fractionation appears to occur during sedimentation, with the peaks appearing at early times, before all of the particles have settled. There is little change afterwards, implying the fractionation is entirely due to the sedimentation.

In the second of the BD simulations, the large and small particles were given the same sedimentation velocity, but had different gravitational lengths. The final result of this simulation, after $6 \times 10^5\, t_B$, is shown in 7.4 (e). Comparing to (d), there is much less fractionation, and comparing to the inset, what fractionation there is has occurred post-sedimentation. This is supported by figure 7.4 (g), in which after $3 \times 10^5\, t_B$, the large and small profiles are much more similar than in 7.4 (f), but go on to evolve and fractionate.

Therefore, the apparent fractionation in our experiments is arrived upon during the sedimentation process rather than a result of rearrangements of the denser sediment. This makes sense physically; the large particles experience more drag and therefore a lower terminal velocity. so separate from the faster small particles. In the case of experiment TPM 1 with a large amount of fractionation, this was initially set at a higher angle than the others, which exacerbated the difference in velocities and thereby the separation.

7.4.2 Equation of state

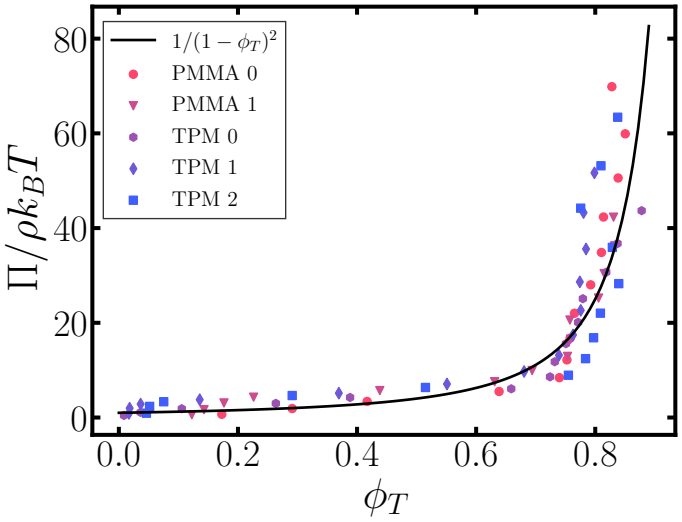


Figure 7.5: The equation of state for all of our experiments scaled by their fitted gravitational heights. The solid line shows the equation of state of scaled particle theory.

Experiment	$h_{g\|\|}$ /µm	$\theta/^\circ$
PMMA 0	82.7	0.047
PMMA 1	69.0	0.057
TPM 0	30.9	0.115
TPM 1	18.6	0.226
TPM 2	17.6	0.202

Table 7.2: A table showing the gravitational heights from each experiment and the corresponding tilt angles.

By integrating the density profiles in figure 7.4 (a), we can obtain the equation of state and we can use 7.9 to fit these to scaled particle theory (SPT). This is shown in figure 7.5, where the total area fraction is plotted against the pressure. All of the experiments fit SPT reasonably well, which further corroborates that the system is under equilibrium. The data also appears to be continuous; there are no observable discontinuities, which implies there is no first order phase transition. The fit by scaled particle theory starts to become less convincing around $\phi_T = 0.7$, which is to be expected as one of the assumptions required for SPT is a fluid. However, despite our binary system and charged PMMA particles, the fit to monodisperse hard sphere SPT is good.

From the fit by SPT, we can determine the gravitational heights $h_{g||}$ (see table 7.2) and the corresponding angle, given that $h_{g||} = h_g \sin\theta$, where h_g is the gravitational height of the small particle in the system. The narrow window of angles shows just how sensitive the density profile is to the gravitational height. Interestingly, experiments *TPM 1* and *TPM 2* have very similar $h_{g||}$ despite the difference in angle. This is due to the size of the small particles being different, as shown in table 7.1.

7.4.3 Structure

In this section we focus on the structural characterisation of the sedimentation-diffusion equilibrium profiles, the basis being the radial distribution functions at different area fractions, the amounts of local crystallinity and the tessellation of binary unit cells.

Radial distribution functions

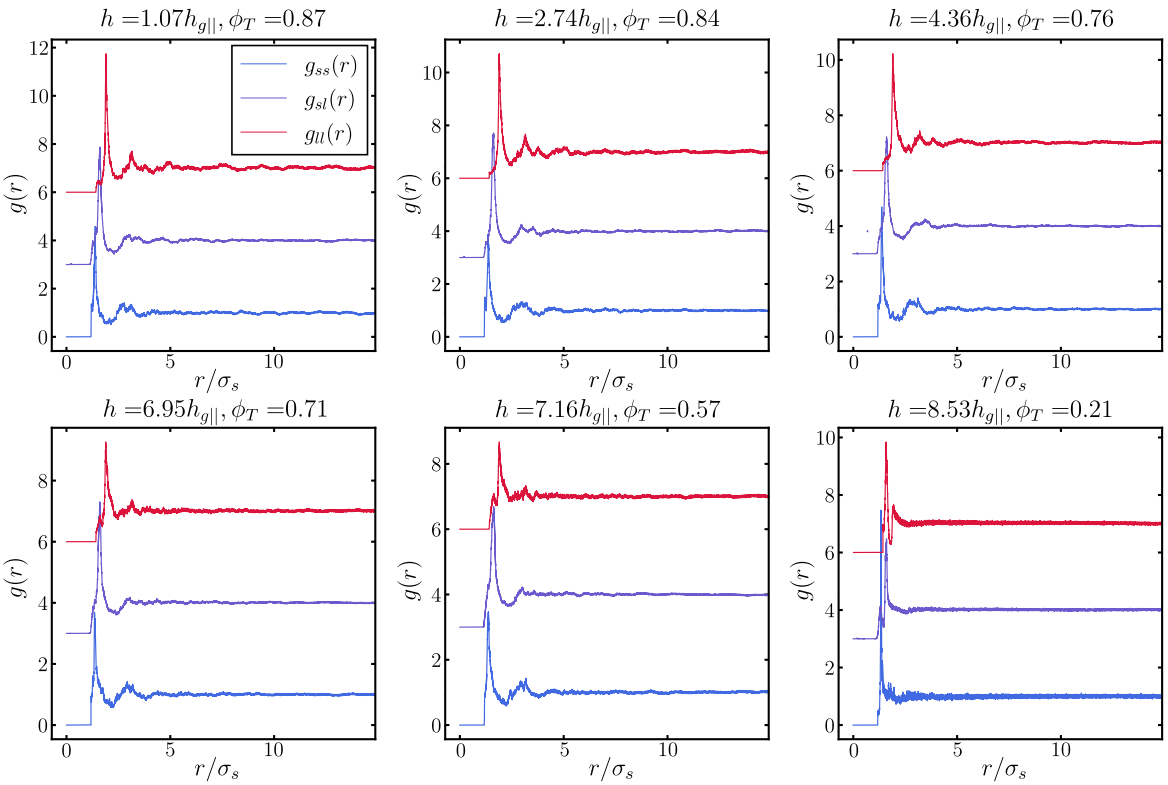


Figure 7.6: Radial distribution functions taken at different heights from the experiment $TPM\,0$ with $h_{g||} = 30.9\,\mu\text{m}$. The corresponding height and area fractions are above each graph. Each has the partial radial distribution functions of small-small, small-large and large-large pairs in blue, purple and red respectively. The second and third are shifted up the y-axis by 3 and 6 for clarity.

Figure 7.6 shows the partial radial distribution functions (RDFs) $g_{ss}(r)$, $g_{sl}(r)$ and $g_{ll}(r)$ for six different heights for the experiment where $h_{g||} = 30.9\,\mu\text{m}$, with these heights spanning the entire density distribution. Examining the general shapes of the curves, it is clear that there is no long-range order at any ϕ_T, even as the system gets denser, therefore the structure is amorphous throughout the density profile. There is also no real change in the relative heights of the first and second peaks for the different g_{ij} at each density, meaning the composition is likely to be consistent across the density profile too.

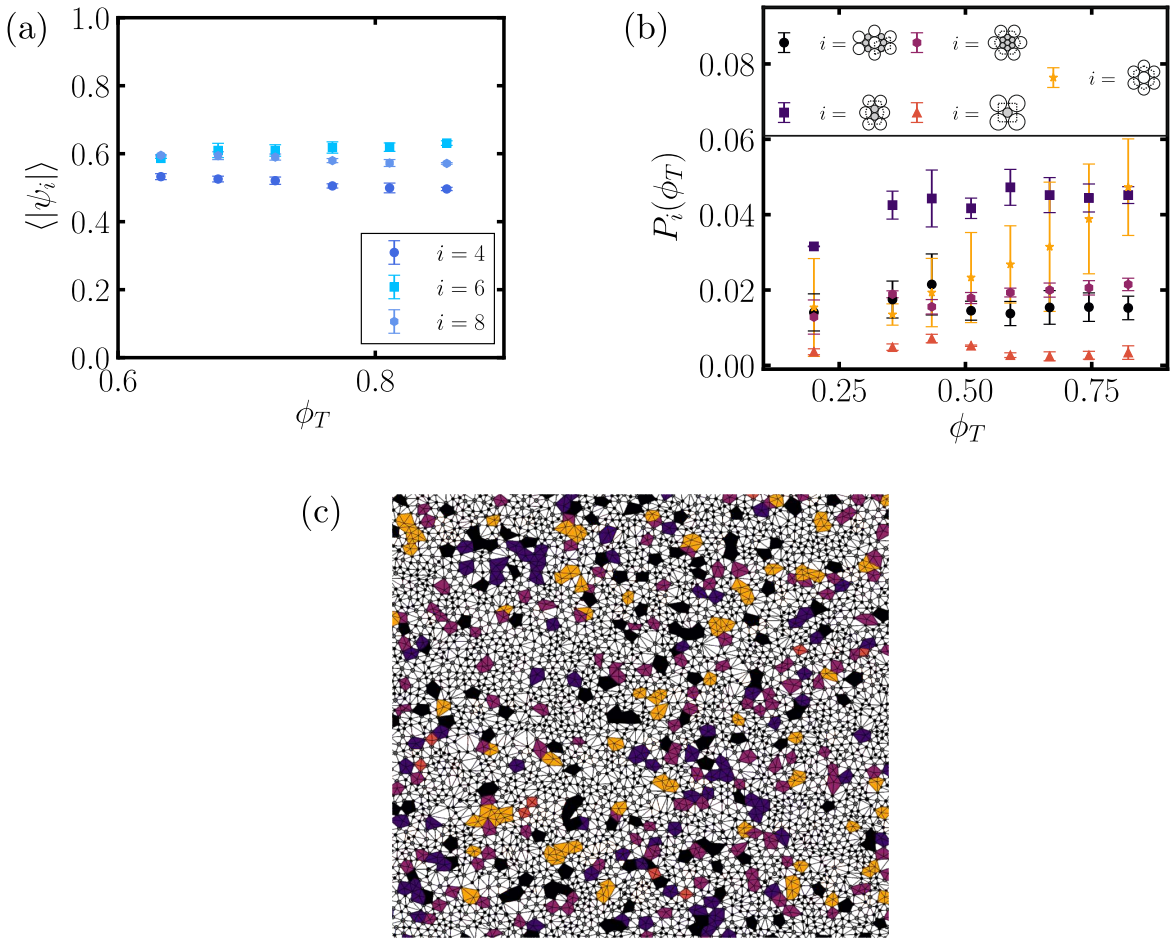


Figure 7.7: (a) The average crystallinity factor $\langle|\psi_i|\rangle$ for lattices with 4-,6- and 8-coordinate particles, against the total area fraction. (b) The probability to find a particular crystalline unit cell at different total area fractions in the system. The key shows an image of each of these unit cells. (c) A snapshot of a high area fraction field-of-view, with a Delaunay triangulation of the large (open circles) and small (closed circles) particles. Each particle found to be in one of the unit cells has the area between it and its neighbours filled in based on the colours from the key in (b).

Crystallinity

Next, we quantify the crystallinity in the system. The graph in figure 7.7 (a) shows the average crystallinity, $\langle|\psi_i|\rangle$, corresponding to the different bond-orientational order parameters for the three different coordination numbers ψ_4, ψ_6 and ψ_8. Note that we only checked for crystallinity where $\phi_T > 0.6$, as below this point we would expect a fluid. For all of the coordination numbers and across the density range $0.6 \leq \phi_T \leq 0.9$, the value of the average crystallinity is constant and below 0.6. Therefore, the system is not crystalline according to the 4, 6, or 8 coordination lattices and this is true across the density profile.

Studying the local order further, we can examine the fraction of particles found to be in

a unit cell for either the hexagonal lattice or one of the binary crystal cells discussed in section 7.2.2. Figure 7.7 (b), shows a graph of the probability a particle at a particular area fraction is in one of cells in the key. Firstly, the probabilities are all quite low, indicating most particles are not in a crystalline local region, consistent with the absence long-range ordering. Secondly, apart from the hexagonal packing, all of the binary unit cells seem to have equal probability at high and low area fractions. Figure 7.7 (c) shows a representative snapshot from a dense part of the experiment showing a Delaunay triangulation of all of the particles with those in particular unit cells coloured in. The different cells all appear to be scattered randomly with no clear tessellated patterns. Therefore, the structure here must be amorphous.

Excess entropy

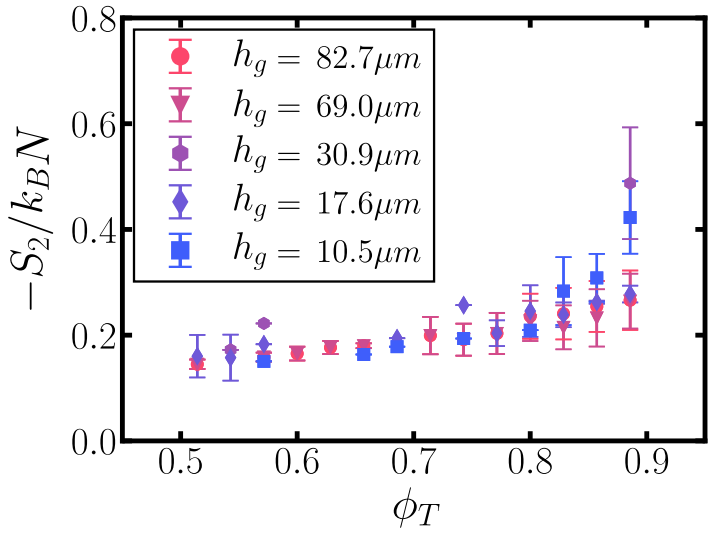


Figure 7.8: The two-point excess entropy per particle, S_2/N, against the total area fraction, for all four of our gravitational heights, and additionally the dynamic Monte Carlo simulation detailed in appendix C.

Here, we examine the excess entropy S_2. Recalling section 7.2.2, a more negative S_2 is expected to indicate a greater number of possible rearrangements and correlates with an increase in the rate of dynamics.

From figure 7.8, all of the data for our tilt angles and our dynamic Monte Carlo simulation lines up on-top of one-another, which indicates that based on the structure alone we would expect all angles to have a similar number of dynamic rearrangements. This is to be expected, considering the excess entropy is calculated from the radial distribution functions, and these are similar for all of the tilt angles.

7.4.4 Dynamics

Now, we analyse the dynamics of the sedimentation-diffusion profile, looking at the change in dynamics at different area fractions with the mean-squared displacements, and comparing different tilt angles with the self-intermediate scattering function and their relative relaxation times.

Mean-squared displacements

Figure 7.9 shows various mean-squared displacements (MSDs) from the experiment with $h_{g||} = 30.9\,\mu\text{m}$. Each graph has multiple curves with the colour representing the area fraction and thereby height in the sample. As shown in panels (a) and (b), the MSDs of the small and large particles show diffusive dynamics up to approximately $\phi_T = 0.5$, after which there is a slowing down of the rate of diffusion due to a growing ϕ_T. At higher densities, there is a transition between intra- and inter-cage motion, with the duration of the crossover increasing with area fraction. However, at long times, the MSD still shows diffusive dynamics after approximately $10^2 t_B$. Comparing (b) to (a), (the small and large particles), the curves are reasonably consistent with one another at high densities, but otherwise the small particles move faster, as is to be expected due to the small particles having a greater diffusion constant. Both the values of $\langle \Delta r^2 \rangle$ and the diffusivity times are consistent with previous measurements in two-dimensional colloidal glass formers without a concentration gradient [76, 316, 328].

Figures 7.9 (c) and (d) show the mean-squared displacements of the large particles in the x- and y-directions. There is no discernable difference between these, which suggests there is no influence of the concentration gradient on the rate of diffusion.

We also examine the dynamic Lindemann parameter, γ_L, to correct for long-wavelength fluctuations, in figure 7.9 (e). Looking at the highest area fractions, it is clear that there is much more of a plateau as compared to the MSD, indicating the apparent diffusiveness in the mean squared displacement at intermediate times could be due to long-wavelength thermal fluctuations. Even at the highest area fractions however, there is still an increase in the gradient of γ_L, indicating there is diffusive behaviour, albeit at a small magnitude.

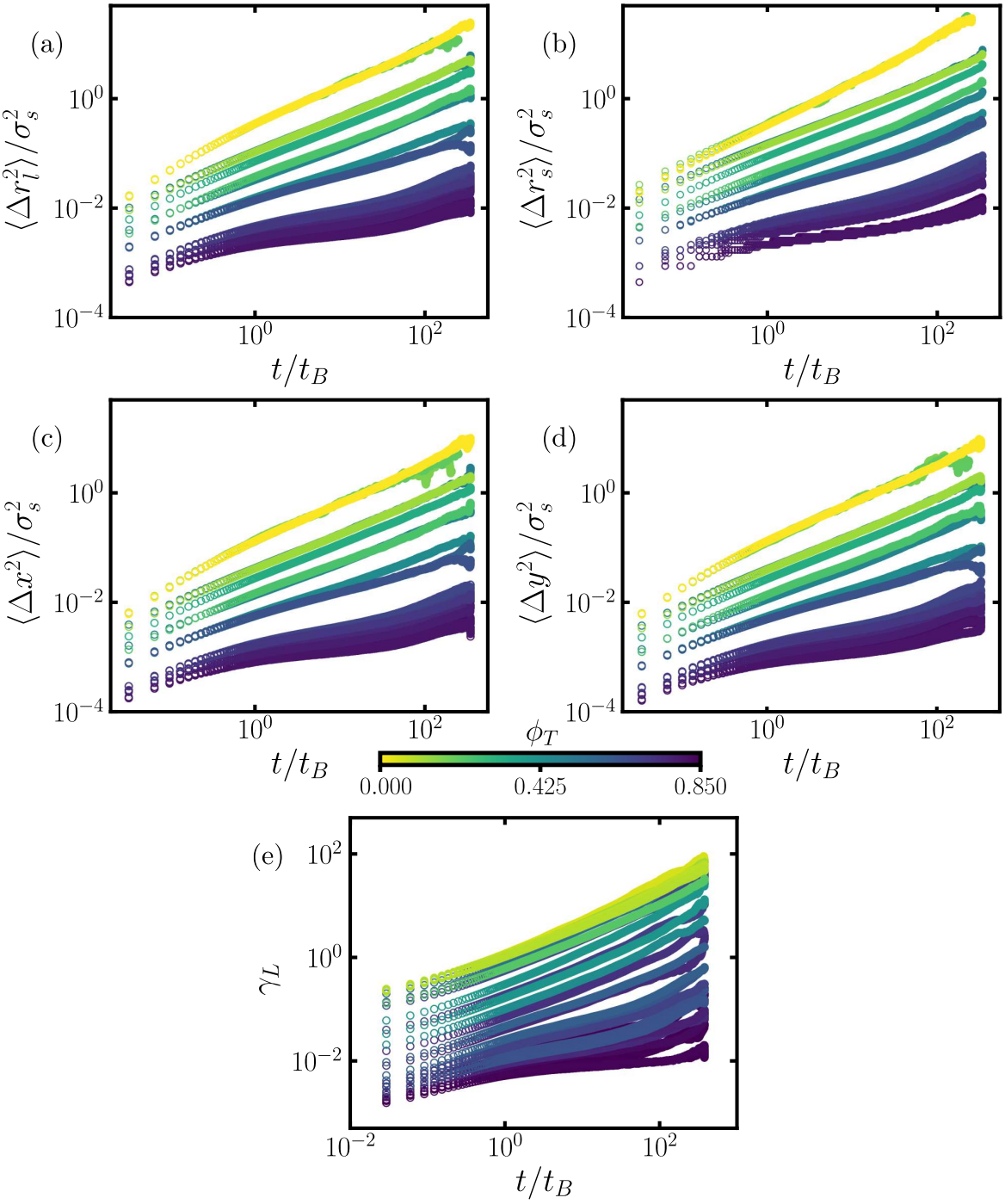


Figure 7.9: Mean-squared displacements (MSDs) of the experiment with $h_{g||} = 30.9\,\mu\text{m}$, binned by height, with colours representing the total area fraction ϕ_T (see colour bar). The times are scaled by the Brownian time of the small particles and the mean-squared displacement by the diameter of the small particles. (a) The MSDs of only the large particles. (b) The MSDs of only the small particles. (c) The MSDs of the large particles in the x-direction. (d) The MSDs of the large particles in the y-direction. (e) The Lindemann parameter of the particles.

Self-intermediate scattering functions

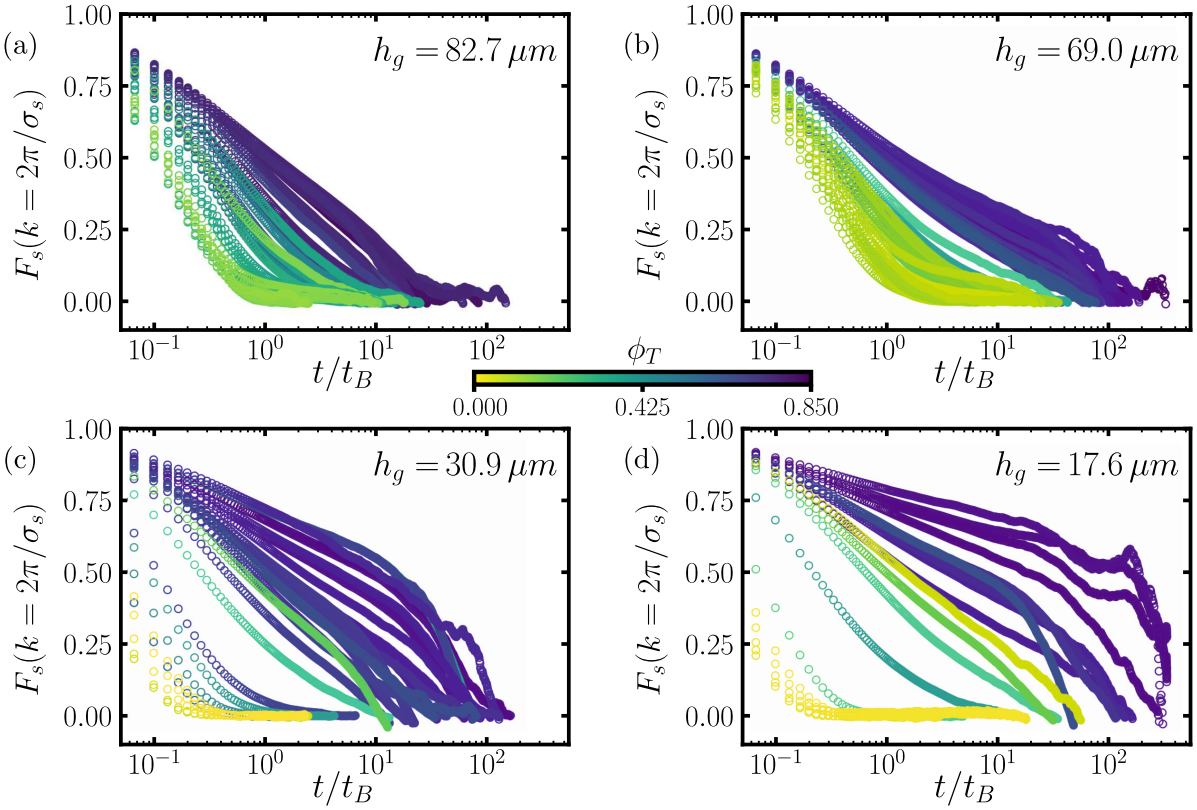


Figure 7.10: The self-intermediate scattering functions of small particles (with $k = 2\pi/\sigma_s$), binned by height and coloured by total area fraction, for four different tilt angles.

Next, we analyse the dynamics at each of the tilt angles by comparing the self-intermediate scattering functions $F_s(k, t)$. These can be seen in figure 7.10 for the small particles with a wave-vector $k = 2\pi/\sigma_s$. Looking at the trends while decreasing the gravitational height, there is little change at low area fractions but a large difference at high area fractions. All of the graphs decay to zero, meaning there is no arrest, but the magnitude of the time this takes increases with $h_{g||}$. This will not be due to an increase in Mermin-Wagner fluctuations, as the difference in system size in insufficient to lead to a difference of this magnitude [80].

Relaxation time

To quantify the slowing down of the dynamics, we can look at the α-relaxation time at the different tilt angles by fitting a stretched exponential, $F_s(k) \propto \exp -[t/\tau_\alpha]^a$, as shown illustratively in figure 7.11 (a), for the SISF for our dynamic Monte Carlo simulation detailed in appendix C. The resulting relaxation times are shown in figure 7.11 (b) for the four different $h_{g||}$ shown in

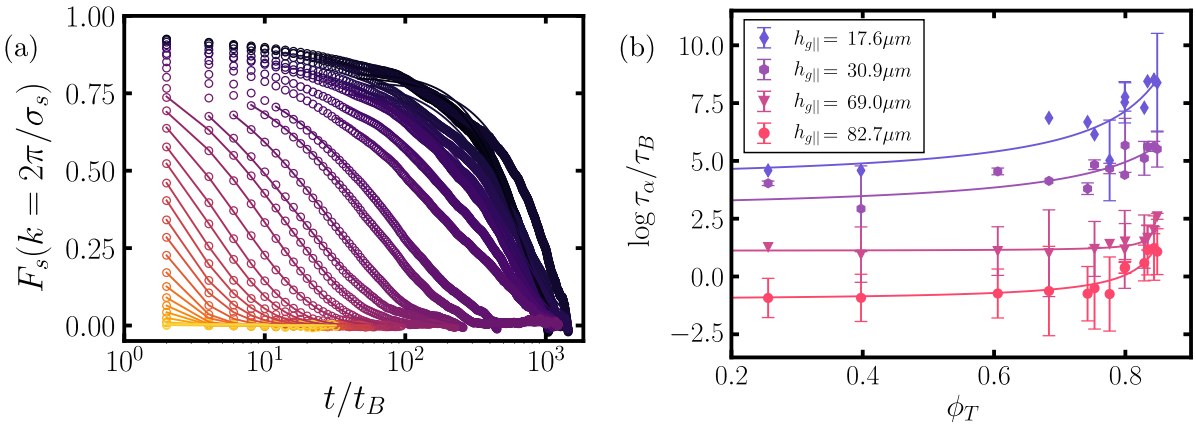


Figure 7.11: (a) is the self-intermediate scattering function of our dynamic Monte Carlo simulation detailed in appendix C, with lines fitted from an extended exponential. (b) shows the log of the α-relaxation time τ_α against the area fraction, for four $h_{g||}$. The curves are shifted up the y-axis for clarity.

figure 7.10.

From the graph, it is clear in all cases that there is a slowing down of the dynamics as ϕ_T increases, and on the time-scale of our experiment, the SISF always relaxes. Examining the behaviour of the different systems, there is a more rapid slowing down in the dynamics for those with a lower gravitational height. The systems become less 'fragile' as $h_{g||}$ decreases [132,292]. To quantify this, we can apply the Vogel-Fulcher-Tamman equation, which describes the change in a dynamic property (typically viscosity) with a control parameter (typically temperature) [127]. Our dynamic property is the relaxation time, and our control parameter is area fraction, which we can take as an inverse analogue of temperature [299]. The resultant VFT equation is [132]:

$$\tau_\alpha = \tau_0 \exp \frac{D_F \phi_T}{\phi_{T,v} - \phi_T}, \tag{7.26}$$

where τ_0 is the relaxation time at high pressures, $\phi_{T,v}$ is the glass transition area fraction, and D_F is the fragility index [292]. A greater D_F indicates a stronger glass former, and our measurements from fitting the data in figure 7.11 (b) are $D_F = 0.531$, 0.441 and 0.014 and 0.115 in ascending order of $h_{g||}$. Excluding the third, the fragility is indeed decreasing. A glass former being less fragile indicates a greater resilience to structural rearrangements [79,292], such as dynamic heterogeneities. However, it is important to note the values of $\phi_{T,v}$ are above the maximum ϕ_T in the system, and therefore comparisons to normal glass forming systems' fragility here are only to be taken as qualitative.

7.4.5 Dynamic heterogeneities and cooperative motion

In this section, we study dynamic heterogeneities and cooperative motion, by examining the non-Gaussian nature of the self-van Hove correlation function and look for evidence of string-like motion.

The self-van Hove and non-Gaussian parameter

Figures 7.12 (a)-(d) show the self-van Hove (SvH) correlation function (equation 7.14) for a single experiment ($h_{g||} = 17.6\,\mu m$) in various bins. At such low area fractions in (a), the distribution of displacements is very Gaussian, meaning the particles' behaviour is diffusive. At higher ϕ_T in (b) there is a marked difference from (a) as the shape of the curve is clearly non-Gaussian. In contrast, at even higher ϕ_T in (c), the SvH function is narrower, indicating far less motion, with particles at most moving one-tenth the distance. Most strikingly different however, is the change in the shape of the curves. As well as being non-Gaussian, there is asymmetry in the tails in the positive and negative directions. It is important to note that despite the asymmetry, the areas under the positive and negative sides are equal, and this is not therefore due to drift.

The same picture is painted by the data in (d): small distances moved, non-Gaussian behaviour, and tail asymmetry (again not a result of drift). One notable difference however, is the SvH in y is slightly broader, which indicates that there are more fast moving particles in the y-direction. This was not elucidated in the mean-squared displacements in figure 7.9 as these differences are only evident at the tails of the distribution, not enough to affect the overall averages too much.

To qualitatively examine the deviation from diffusivity, we can compute the non-Gaussian parameter α_2 (equation 7.22), which is shown for the highest and lowest experimental tilt angles in figures 7.12 (e) and (f). The location of the peaks seen in these graphs is the average time taken for the non-Gaussian motion to occur and the height represents the amount of non-Gaussian behaviour. Comparing the two, the largest difference is the position of the maxima; the lower angle peaks at later times. This indicates the rearrangements occurring for this angle take longer: more particles are involved and the time taken for repositioning is longer. Another key difference is seen when comparing the same ϕ_T in each system. For the low angle in (f), increasing ϕ_T leads to an increase in the peak height and in the amount of dynamic heterogeneity. For the

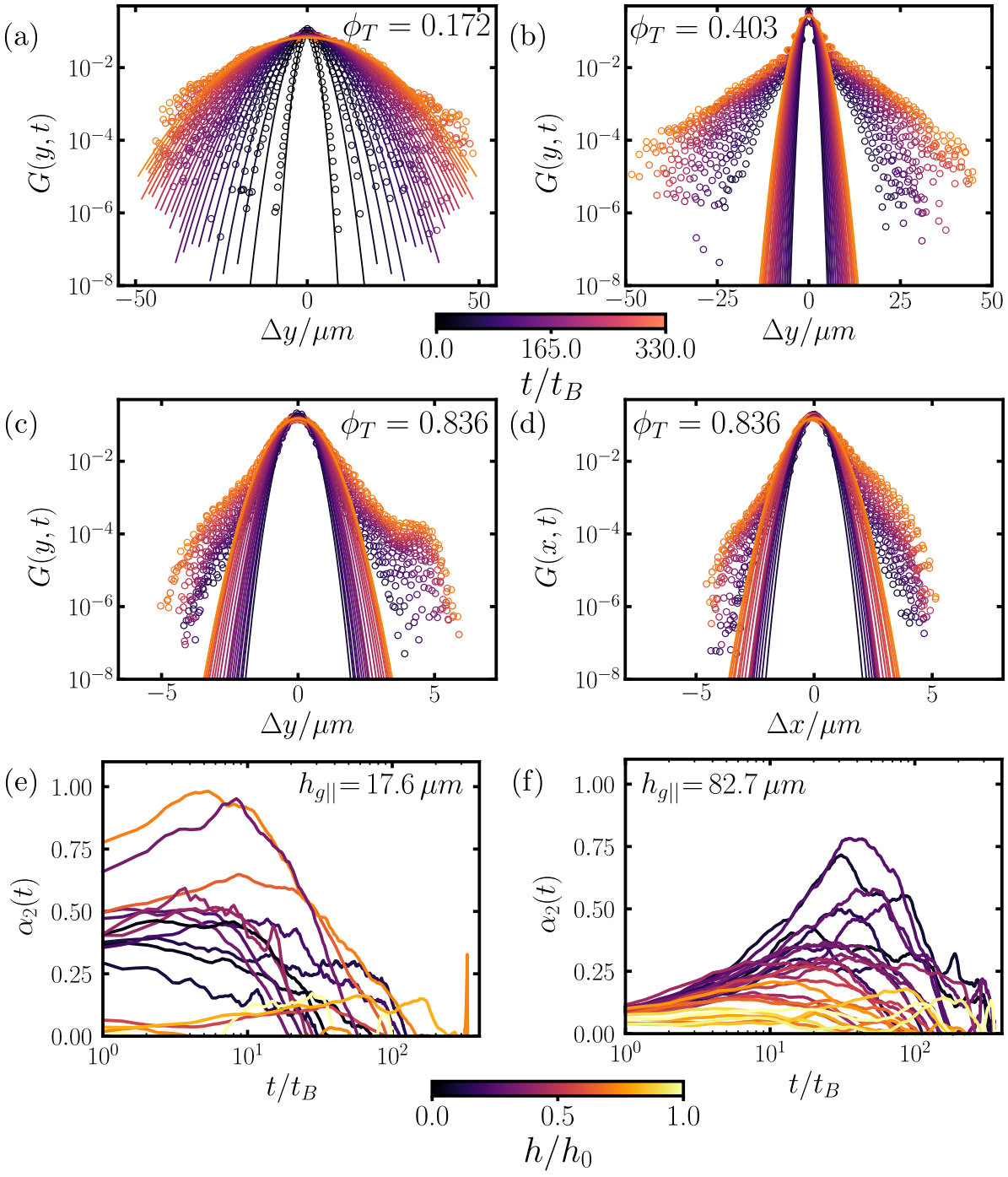


Figure 7.12: (a)-(d) Self-van Hove (SvH) correlation functions of the $h_{g||} = 17.6\,\mu m$ experiment, with different colours indicating the function at different times. The lines are the Gaussian fits. (a) and (b) show the SvH in the y direction in bins higher up in the experiment. (c) and (d) show the SvH in the y and x directions respectively, for a lower point in the system. (e) and (f) show the non-Gaussian parameter for the highest and lowest experimental angles, with the different lines representing bins of the height.

high angle in (e) however, increasing ϕ_T actually leads to a decrease in the amount of dynamic heterogeneity.

From these observations, it appears the system at the lower tilt angle shows slowly relaxing cooperative motion, and the amount of dynamic heterogeneity increases. The higher angle, on the other hand, has cooperatively moving regions that relax more quickly, indicating a shorter length, and dynamic heterogeneities decrease with ϕ_T. This is consistent with the relaxation times in figure 7.11, as a greater τ_α for the higher angle implies there is a lower amount of cooperative motion.

Cooperative motion

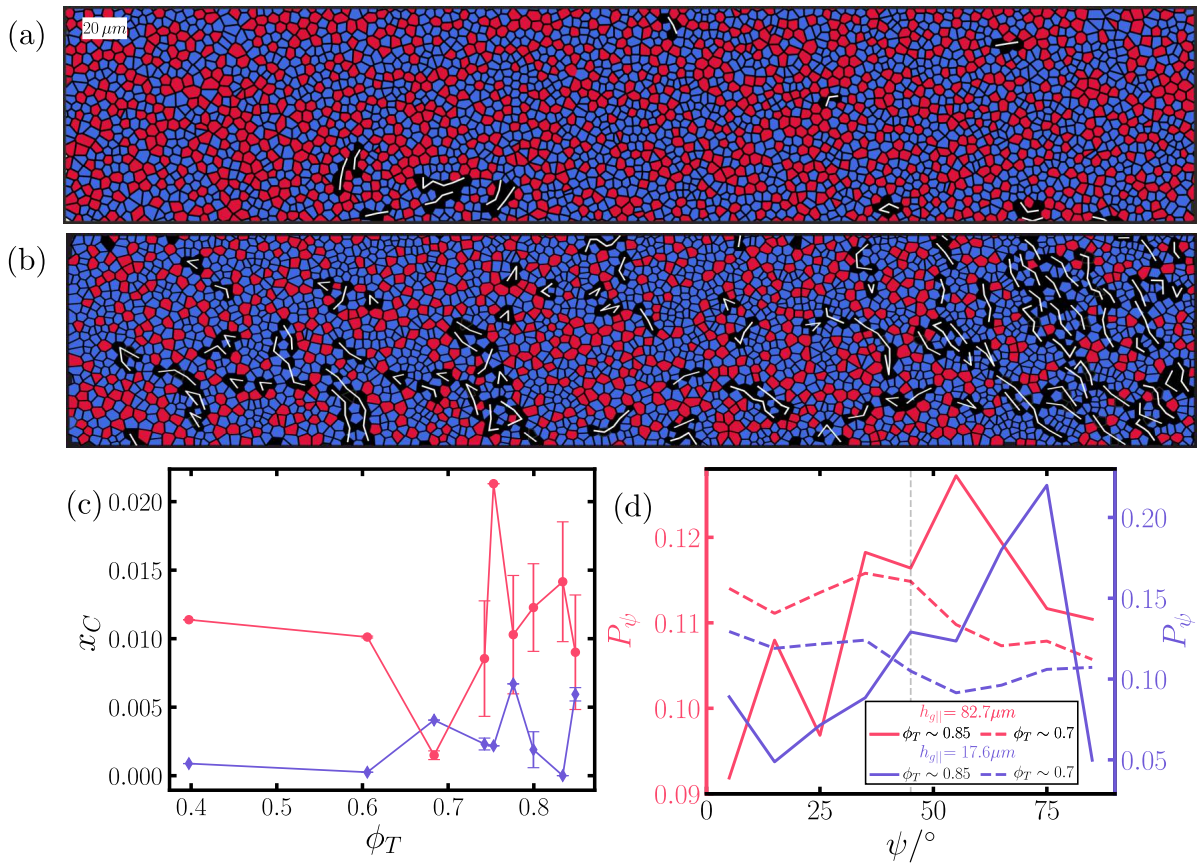


Figure 7.13: (a) and (b) are Voronoi diagrams with slow moving particles coloured in red/blue for large/small species. Those in black are involved with strings, with the white line drawing the string. Both are snapshots after the same lag time ($250t_B$) from the same area fraction ($\phi_T \sim 0.85$) in experiments with $h_{g||} = 17.6$ and $h_{g||} = 82.7$ for (a) and (b) respectively. (c) shows the fraction of particles involved in a string x_c at particular area fractions in the sample, for the highest and lowest angle. (d) shows the probability of a string having a certain orientation relative to the x-axis. The colours represent the two tilt experiments from (a) and (b) and the line style represents the area fraction (see key).

To look at cooperate motion we can qualitatively examine some screenshots of the system

at the lowest and highest angles. Figure 7.13 (a) and (b) show Voronoi diagrams from the two angles taken at the same area fraction and time. The cells with fills of red and blue are slow moving large and small particles respectively. The black filled cells are mobile particles, i.e. those found to be in strings using the method from equation 7.23. The strings have been plotted as the white lines, and panel (a) shows the higher angle and (b) the lower. Clearly, the lower angle has many more strings and particles involved in cooperative motion. To quantify this further, we can look at the fraction of particles involved in cooperative motion, x_C, for the different experiments. Figure 7.13 (c) shows the fraction at different ϕ_T for the two angles in (a) and (b). Clearly the trend here is a smaller gravitational height leads to fewer particles in strings.

Another notable feature in (a) and (b) is the strings appear to be more orientated along the y-axis, parallel to the concentration gradient. To test this point, we examine the orientations of all of the strings over a larger area. Using the particles' coordinates in each string, we can find the tangent of the corresponding cloud of points. This is achieved by taking the covariance matrix of the points,

$$\boldsymbol{C} = \begin{pmatrix} \mathrm{Cov}(\boldsymbol{x},\boldsymbol{x}) & \mathrm{Cov}(\boldsymbol{x},\boldsymbol{y}) \\ \\ \mathrm{Cov}(\boldsymbol{y},\boldsymbol{x}) & \mathrm{Cov}(\boldsymbol{y},\boldsymbol{y}) \end{pmatrix}, \tag{7.27}$$

where the cloud of n points form the vectors $\boldsymbol{x} = (x_1, x_2, ..., x_n)$ and $\boldsymbol{y} = (y_1, y_2, ..., y_n)$, and the covariance is $\mathrm{Cov}(\boldsymbol{x},\boldsymbol{y}) = 1/n \sum_{i=1}^{n}(x_i - \bar{x})(y_i - \bar{y})$. The tangent to the cloud of points (and direction of the string) is the eigenvector of $\boldsymbol{C}$ associated with the highest eigenvalue [329, 330]. From the angle of this vector we find the orientation of the string. Note that this method does not differentiate between positive and negative directions, and therefore the resultant orientation is in the range: $0° \leq \phi \leq 90°$.

Figure 7.13 (d) shows the probability distribution of the strings' orientations at $\phi_T \sim 0.85$ and $\phi_T \sim 0.7$ for both high and low tilt angles. Examining both of the experiments' solid lines, there is a clear trend for an increase in the strings orientated close to the vertical. In contrast, at $\phi_T \sim 0.7$, both experiments show far less of a difference in the preferred orientation. Therefore, the cooperative regions at higher ϕ_T are associated with greater orientational preference. The relative flatness of the dashed lines corresponding to lower ϕ_T parts of the system indicates a much more freely flowing fluid. This picture coincides with Goldstein's [331], of glass-forming

liquids transitioning from free-flow to activated motion (the activation in this case being related to the concentration gradient). This activation effect has also been observed in systems which speed the dynamics through added active particles [332] and swapping particle positions in Monte Carlo simulations [333].

We noted in section 7.4.3, based on the two-point excess entropy, none of the experiments are more predisposed to structural rearrangements. Key to our system, the contact between low and high ϕ_T provides a mechanism for rearrangements to occur. As demonstrated in previous experiments and simulations of polymer glass thin films [334–336], the dynamics of the bulk are enhanced due to percolating dynamic heterogeneities from the surface. In our experiments, the area fraction profile slowly increases after $\phi_T \sim 0.7$, which is the 'surface'. If a particle at the surface were to find space to move, this could be the beginning of a string, with the vacated area creating a free-volume packet; such packets have been observed in structural rearrangements during vapour deposition [337]. This packet would make its way down through the system to higher ϕ_T, allowing for structurally favoured rearrangements, otherwise kinetically forbidden due to high activation energies, to occur. Consequently, structural rearrangements that would be exceptionally energetically disfavoured in a system of uniform area fraction are now accessible in our sedimentation-diffusion profile. This mechanism therefore explains the diffusivity we find at long times for high ϕ_T, with cooperative motion leading to the cage breaking noted in our mean-squared displacements. The difference in dynamics between our tilt angles is also explained: a smaller gravitational height means particles have a greater buoyant mass, which will increase the gravitational force. The barrier to cooperative motion scales with the energy required to move the particles [338], therefore lower tilt angles have lower activation energies and therefore more rearrangements.

7.5 Conclusion

In this chapter we realised a system of binary two-dimensional colloids with a size ratio ~ 1.4 and equal gravitational height, h_g, such that we could form a sedimentation-diffusion equilibrium without size fractionation. We performed experiments on five different angles as well as Brownian dynamics simulations. We form sedimentation-diffusion equilibria and find a good mixing of large and small particles, except at low ϕ_T, which shows a slight fractionation of large

particles, but is consistent with the dynamics of sedimentation as we found in our BD simulation. We find all of the gravitational heights by fitting to the scaled particle theory equation of state. Examining the structure we find liquid-like ordering throughout the entire height profile and no signatures of mono- or binary-crystallisation, with no experiment more disposed to structural rearrangements.

Looking at the dynamics, we find the rate of diffusion to slow upon increasing ϕ_T, showing clear β- and α-relaxation even when accounting for long-wavelength thermal fluctuations. Comparing our multiple angles, we showed there was a slowing down of the dynamics as the gravitational height decreased. This was confirmed by the measured relaxation times, which showed the system becoming more fragile as $h_{g||}$ increased.

We find non-Gaussian diffusion at high ϕ_T, with higher angles showing smaller cooperative regions. Looking directly at the strings, their number increases with lower tilt angles, and they tend to be orientated along the concentration gradient. Finally, we note this implies the faster dynamics are due to strings diffusing downwards from the surface, allowing for structural rearrangements even at the most dense parts of the sample.

Acknowledgements

This work was performed in collaboration with Josh Abbott-Scott, Berend van der Meer, Arran Curran and Alice Thorneywork. Taiki Yanigishima is thanked for useful discussions. Arran, Josh and Taiki are thanked for practical assistance. Berend is also thanked for assistance with the simulations.

Appendix

A Grain size evolution due to rotations

A.1 Theoretical grain size evolution

According to the method of Moldovan *et al.* [189], in this section we show the derivation of the theoretical rate with which grains should grow in our quenched system, given the sole mechanism being coalescence via grain rotation.

Firstly, N grains are approximated to have an equal chance of decaying, with the decay constant λ being the rate with which this occurs:

$$\frac{dN}{dt} = -\lambda N. \tag{A.1}$$

The decay constant will be proportional to the mean rotational velocity:

$$\lambda = C_1 \langle \omega \rangle. \tag{A.2}$$

The average grain area A is related to the number of grains as thus:

$$NA = A_T, \tag{A.3}$$

where A_T is the total area of the system. Differentiating both sides with respect to t leads to:

$$\frac{1}{N}\frac{dN}{dt} = -\frac{1}{A}\frac{dA}{dt}. \tag{A.4}$$

The average grain size is related to the average grain area: $A = R^2$, as such $\frac{dA}{dt} = 2R\frac{dR}{dt}$ and $\frac{1}{N}\frac{dN}{dt} = -\frac{2}{R}\frac{dR}{dt}$. Now, this can be combined with equations A.1 and A.2 to give an expression for the rate of grain growth:

$$\frac{dR}{dt} = \frac{C_1 R\langle\omega\rangle}{2}. \tag{A.5}$$

In section 4.4.1 we find an expression for rotational velocity, which can be averaged for the whole system:

$$\langle\omega\rangle = \frac{M^\star}{R}\left\langle\frac{d\gamma}{d(\Delta\theta)}\right\rangle, \tag{A.6}$$

where $\langle d\gamma/d(\Delta\theta)\rangle$ is the average grain boundary energy gradient in the system. Moldovan *et al.* [189] posit this to scale with the average grain size:

$$\left\langle\frac{d\gamma}{d(\Delta\theta)}\right\rangle = C_2 R^q. \tag{A.7}$$

As such the grain size differential equation can be written entirely in terms of R:

$$\frac{dR}{dt} = BR^q, \tag{A.8}$$

where $B = (1/2)C_1C_2M^\star$.

A.2 Measuring the rate of coalescence

Using the equation of Read *et al.* [119] for grain boundary energy, we can find the average grain boundary energy gradient, $\langle d\gamma/d(\Delta\theta)\rangle$, in our experiments and thereby find a value for q. For a single grain, the weighted grain boundary energy gradient is given in equation 4.7:

$$\gamma'_W = \gamma_0[A_W - \Theta_W]. \tag{A.9}$$

Finding $\langle d\gamma/d(\Delta\theta)\rangle$ is a case of averaging γ'_W over the entire system:

$$\left\langle\frac{d\gamma}{d(\Delta\theta)}\right\rangle = \frac{1}{N}\sum_{i=1}^{N}[\gamma'_W]_i. \tag{A.10}$$

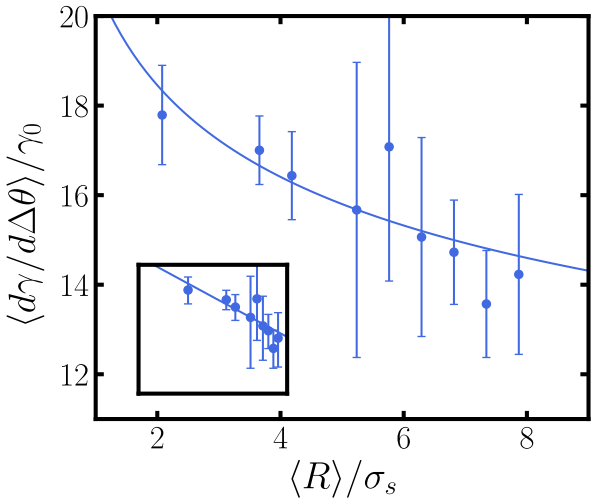


Figure A.1: A graph plotting the average grain boundary energy gradient, $\langle d\gamma/d(\Delta\theta)\rangle$, against the average grain size, $\langle R\rangle$. The inset is the same graph with the same axes, on a log-log scale. The curve is a power law fit in line with equation A.7.

In figure A.1, we plot the average grain boundary energy gradient $\langle d\gamma/d(\Delta\theta)\rangle$, against the average grain size $\langle R\rangle$. The data is well suited to a power law fit, and from this we find $q = -0.176$.

B Measuring strain in colloidal crystals on a single particle resolution

In this section we present our method of measuring strain in two-dimensional colloidal crystals, utilising the Kabsch algorithm [339]. Previous methods have utilised the overlaying of a reference lattice onto the crystal [63, 86], from relative x/y deformation [240, 340], from time dependent deformation of neighbours [341,342] and unit cell templating [343,344]. Our approach resembles the latter, where we use a template unit cell (the hexagonal neighbours of a particle). This has the advantage over these past methods of: single particle resolution; separating plastic and elastic deformation; ability to cope with defects, dislocations, impurities and thermal fluctuations; finding static strain; finding shear strain; and simplicity of a single template.

Firstly, we need to establish how we can get from a unit cell to two-dimensional strain. Looking at figure A.2, we start with a square in which each point undergoes a transformation:

$$\chi\left(\begin{bmatrix} x \\ y \end{bmatrix}\right) = \begin{bmatrix} X \\ Y \end{bmatrix}, \tag{B.1}$$

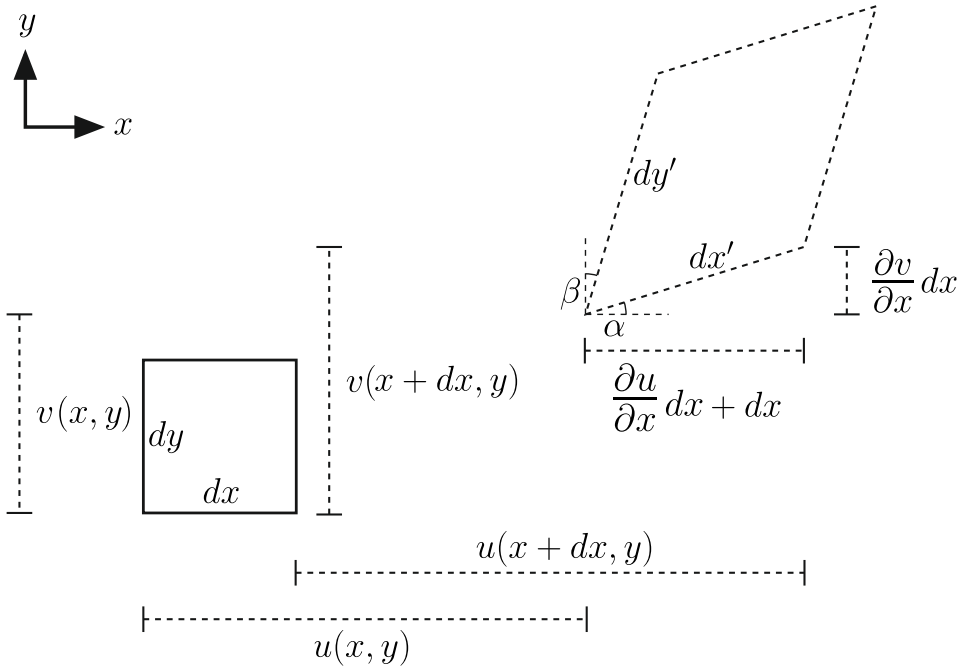


Figure A.2: A diagram showing a square with applied shear and x-strain and a translation. u is the function that shows the distance a point moves in the x direction after applying the transformation ($u(x, y) = x' - x$,). v is the same but in the y direction.

with $\chi(...)$ being the function defining the deformation, and we define $u(x, y) = X - x$ and $v(x, y) = Y - y$. The strain in x is $\varepsilon_{xx} = (dx' - dx)/dx$. This can be written in terms of x and u: [345]:

$$dx' = \sqrt{dx^2 \left[1 + \frac{\partial u}{\partial x}\right]^2 + dx^2 \left[\frac{\partial v}{\partial x}\right]^2} \tag{B.2}$$

$$\approx \left(1 + \frac{\partial u}{\partial x}\right) dx, \tag{B.3}$$

as $1 + \partial u/\partial x \gg \partial v/\partial x$; hence, the strain in x is given $\varepsilon_{xx} = \dfrac{\partial u}{\partial x}$. Similarly, the strain in y is: $\varepsilon_{yy} = \dfrac{\partial v}{\partial y}$. Shear strain is symmetric in x and y, and is defined: $\varepsilon_{xy} = \varepsilon_{yx} = \dfrac{1}{2}(\alpha + \beta)$ [345]. Due to the small angles, this can be approximated:

$$\varepsilon_{xy} \approx \frac{1}{2}(\tan\alpha + \tan\beta) \tag{B.4}$$

$$= \frac{1}{2}\left(\frac{\frac{\partial v}{\partial x}dx}{dx + \frac{\partial u}{\partial x}dx} + \frac{\frac{\partial u}{\partial y}dy}{dy + \frac{\partial v}{\partial y}dy}\right) \tag{B.5}$$

$$\approx \frac{1}{2}\left(\frac{\partial v}{\partial x} + \frac{\partial u}{\partial y}\right), \tag{B.6}$$

as for small deformations $\partial u/\partial x, \partial v/\partial y \ll 1$. Therefore, the strain tensor for small deformations

is:

$$\bar{\bar{\varepsilon}} = \begin{pmatrix} \varepsilon_{xx} & \varepsilon_{xy} \\ \varepsilon_{yx} & \varepsilon_{yy} \end{pmatrix} = \begin{pmatrix} \dfrac{\partial u}{\partial x} & \frac{1}{2}\left(\frac{\partial v}{\partial x} + \frac{\partial u}{\partial y}\right) \\ \frac{1}{2}\left(\frac{\partial v}{\partial x} + \frac{\partial u}{\partial y}\right) & \dfrac{\partial v}{\partial y} \end{pmatrix}. \tag{B.7}$$

To actually measure strain from our data we need to find the deformation gradient tensor $\mathbf{F}$. The deformation gradient describes how u and v vary based on their coordinates [346]. The afore mentioned function χ maps $\mathbf{x}$ to $\mathbf{X}$:

$$\mathbf{X} = \chi(\mathbf{x}), \tag{B.8}$$

and the gradient is $\mathbf{F} \equiv \dfrac{\partial \chi}{\partial \mathbf{x}} = \dfrac{\partial \mathbf{X}}{\partial \mathbf{x}}$ [347]. To find an expression for this, we can deform an infinitesimal segment: $d\mathbf{X} = \chi(\mathbf{x} + d\mathbf{x}) - \chi(\mathbf{x})$, which can be expanded via a Taylor series:

$$d\mathbf{X} = (\chi(x) + \nabla\chi(\mathbf{x}) \cdot d\mathbf{x} + ...) - \chi(\mathbf{x}) \approx \nabla\chi(\mathbf{x}) \cdot d\mathbf{x}. \tag{B.9}$$

As the gradient $\nabla\chi(\mathbf{x}) \equiv \mathbf{F}$, this means $d\mathbf{X} \approx \mathbf{F} \cdot d\mathbf{x}$, or for a set of coordinates:

$$\mathbf{F} \begin{bmatrix} x \\ y \end{bmatrix} = \begin{bmatrix} X \\ Y \end{bmatrix}. \tag{B.10}$$

Hence the components of $\mathbf{F}$ can be written in terms of $u = X - x$ and $v = Y - y$:

$$\mathbf{F} = \begin{pmatrix} \dfrac{\partial u}{\partial x} + 1 & \dfrac{\partial u}{\partial y} \\ \dfrac{\partial v}{\partial x} & \dfrac{\partial v}{\partial y} + 1 \end{pmatrix}. \tag{B.11}$$

Therefore the infinitesimal strain can be expressed $\bar{\bar{\varepsilon}} = \frac{1}{2}(\mathbf{F} + \mathbf{F}^T) - \mathbf{I}$, where $\mathbf{I}$ is the identity matrix.

However, this form of strain is not always desirable due to the incorporation of rotational transforms if present. We can instead use Lagrangian-Green strain [345]. This tensor is $\bar{\bar{\varepsilon}} = \frac{1}{2}(\mathbf{F}^T \cdot \mathbf{F} - \mathbf{I})$, which is the same as the infinitesimal strain but with additional quadratic terms [346]. This strain tensor is indeed independent of rotations: $\mathbf{F}^T \cdot \mathbf{F} = (\mathbf{R} \cdot \mathbf{G})^T \cdot (\mathbf{R} \cdot \mathbf{G}) = \mathbf{G}^T \cdot \mathbf{R}^T \cdot \mathbf{R} \cdot \mathbf{G} = \mathbf{G}^T \cdot \mathbf{G}$, where $\mathbf{R}$ is a rotation matrix and $\mathbf{G}$ is the rotation of $\mathbf{F}$.

In our system of two-dimensional crystals, we know the idealised state of a particle's

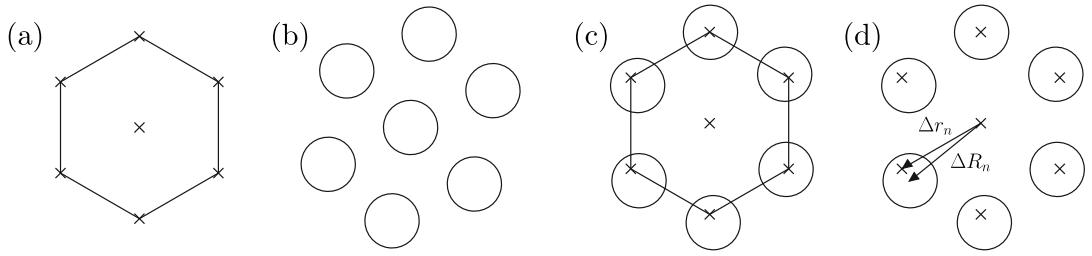


Figure A.3: (a) The idealised model hexagonal unit cell. (b) An specimen of a particle's nearest neighbours after applied strain. (c) The result of the Kabsch algorithm with each point in the model assigned to a neighbour and rotated to minimise the mean-squared distance. (d) The vectors used to construct the deformation gradient tensor.

neighbours: a hexagon with a radius of the lattice spacing. Deviation from this model will tell us the strain on the unit cell. An example of the process is shown in figure A.3. In (a) the model is generated, a regular hexagon from the average lattice spacing in the field-of-view. Figure (b) shows a specimen particle with its neighbours that have had a strain applied. In (c) we have applied the Kabsch algorithm. In its essence, we take the points from the model and points from (b) and find the optimal unique pairing of all of the points and rotational matrix as to minimise the mean-squared distance between the pair. In (c) it is clear the crosses denoting the points from the model have each been assigned corresponding pairs, with a rotation associated to assist. This method is useful as grain orientation is accounted for and this will work for particles with six or fewer neighbours. Now that each point in the model has a unique counterpart from the experimental data, we can find the optimal affine transformation that fits the model to the experiment.

Figure A.3 (d) shows two vectors, $\Delta\mathbf{r}_n$ and $\Delta\mathbf{R}_n$ which are the respective positions of the n^{th} pair of model-experimental points. These should be related via a deformation gradient $\Delta\mathbf{R}_n = \mathbf{F}_n \cdot \Delta\mathbf{r}_n$. Following the procedure of Gullett *et al.* [347], the total least squares error on the mapping of all of the pairs of points will be:

$$\varphi = \sum_{n=1}^{N} (\Delta\mathbf{R}_n - \mathbf{F}_n \cdot \Delta\mathbf{r}_n)^T (\Delta\mathbf{R}_n - \mathbf{F} \cdot \Delta\mathbf{r}_n). \tag{B.12}$$

To optimise the least squares error, they differentiate each matrix component by F_{ij} and set to zero, which leads to the result [347]:

$$\mathbf{F} \sum_{n=1}^{N} \Delta\mathbf{r}_n \cdot \Delta\mathbf{r}_n^T = \sum_{n=1}^{N} \Delta\mathbf{R}_n \cdot \Delta\mathbf{r}_n. \tag{B.13}$$

By rearranging they find an equation for the deformation gradient in terms of $\Delta\mathbf{r}_n$ and $\Delta\mathbf{R}_n$: $\mathbf{F} = \mathbf{A} \cdot \mathbf{D}^{-1}$, where

$$\mathbf{A} = \sum_{n=1}^{N} \Delta\mathbf{R}_n \cdot \Delta\mathbf{r}_n, \tag{B.14}$$

$$\mathbf{D} = \sum_{n=1}^{N} \Delta\mathbf{r}_n \cdot \Delta\mathbf{r}_n^T. \tag{B.15}$$

Finally, from this we can find the strain tensor $\bar{\bar{\varepsilon}} = \frac{1}{2}(\mathbf{F}^T \cdot \mathbf{F} - \mathbf{I})$.

C Dynamic Monte Carlo simulation of sedimentation-diffusion equilibrium for a binary hard disk system

C.1 Simulation set-up

To be able to study the dynamics of a binary hard-disk sedimentation-diffusion equilibrium at the highest area fraction areas of our data, we found BD simulations to be insufficient owing to difficulty removing drift and the soft interactions of the Weeks-Chandler-Andersen potential leading to quite different dynamics compared to our experiments. As such we chose to use a dynamic Monte Carlo (dMC) method, which is useful for probing systems with long relaxation times [348], including cooperative motion in liquid crystals [349, 350] and glasses [128, 351–353]. This algorithm takes the steps in a MC cycle, and makes the step length $\delta\xi_k$ in degree of freedom k, infinitesimally small. This means the acceptance rate of trial moves is maximised, and the motion is close to Brownian.

In our simulation, we first apply a normal MC method to form the sediment. We start from a random dilute configuration of large and small particles (equal in area fraction) in a box periodic in the x-direction, with a hard wall at the top and bottom. We use the no overlap condition to get hard disks with non-additivity and also make use of a gravitational field, meaning the probability for the trial conditions is dependent upon gravitational potential energy:

$$s_{it} = \min[1, \exp(-[m^\star g(y_i - y_t)]/k_B T)], \tag{C.1}$$

where y is the y-coordinate of the particle and $m^\star$, the buoyant mass, is equal for both small

and large particles. This is left to equilibrate, with box resizing to help in this.

Now we can apply the dMC algorithm. We take our configuration, reduce the step size, continue the MC cycles as before and begin recording.

C.2 Dynamic Monte Carlo sedimentation-diffusion profile

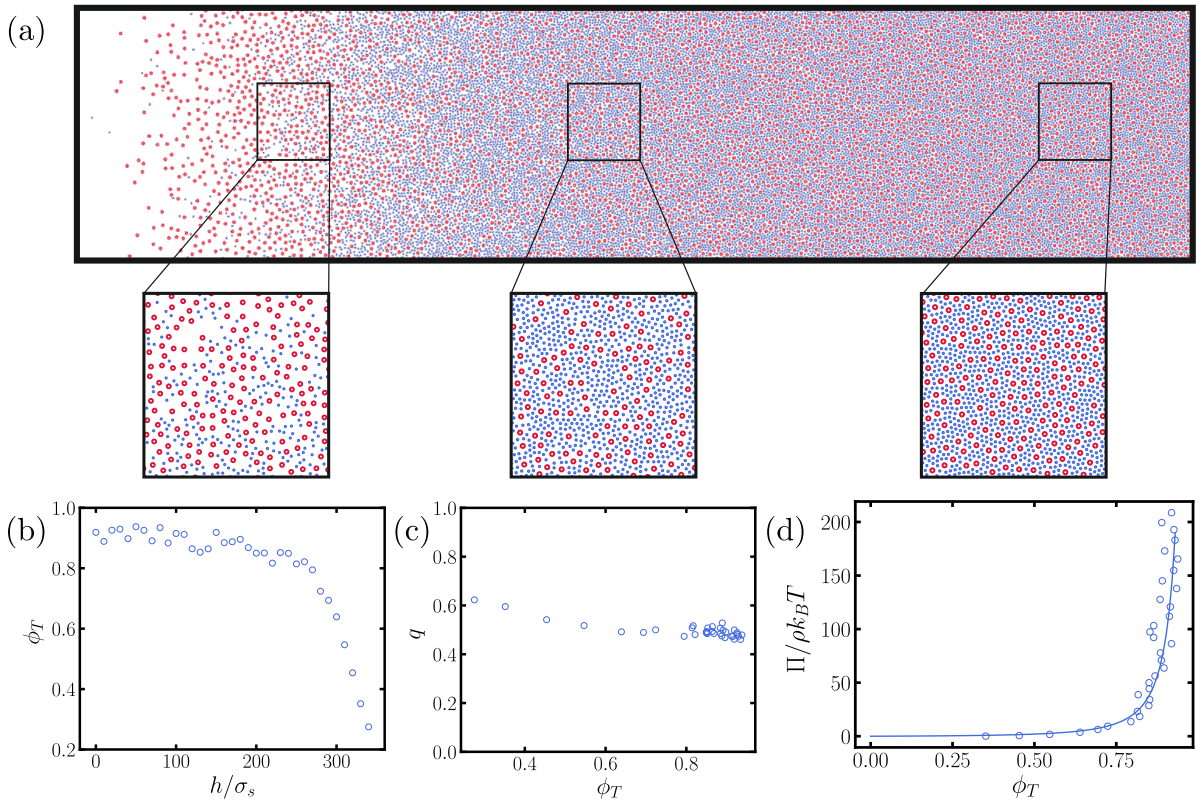


Figure A.4: (a) A screenshot of the particle coordinates from our Monte Carlo simulation, with large particles in red and small particles in blue. (b) The average height profile of the area fraction in the simulation. Three different parts of the profile have been highlighted and zoomed-in on. (c) The fraction of large particles for the different area fractions. (d) The osmotic pressure with the line representing scaled particle theory.

After sedimentation and equilibration we had a system that resembled our experiments. A snapshot of the entire height profile is seen in figure A.4 (a) with large and small particles in red and blue respectively. Qualitatively, the profile appears similar to that of our experiment in figure 7.4 (c), with a slight fractionation of large particles at the top and good mixing at dense areas. As can be seen in the magnified regions, the majority of large particles are surrounded by small particles as a result of the non-additivity [107]. The change in density is rapid at first (comparing the first and second magnified regions from the left), but then is slow (comparing second and third). This is corroborated quantitatively with A.4 (b), which shows a similar form

to the height profiles in figure 7.4 (a). Figure A.4 (c) also backs up the consistency of mixing throughout the system.

From the height profile we can additionally, as in section 7.4.2, find the osmotic pressure. This is plotted in A.4 (d), showing great consistency with scaled particle theory. From the fit we find the the gravitational height $h_g = 3.79\sigma_s$ or in experimental units, $h_g = 10.5\,\mu\text{m}$. Therefore this simulation is represents the highest angle of our collective data.

C.3 Simulation dynamics

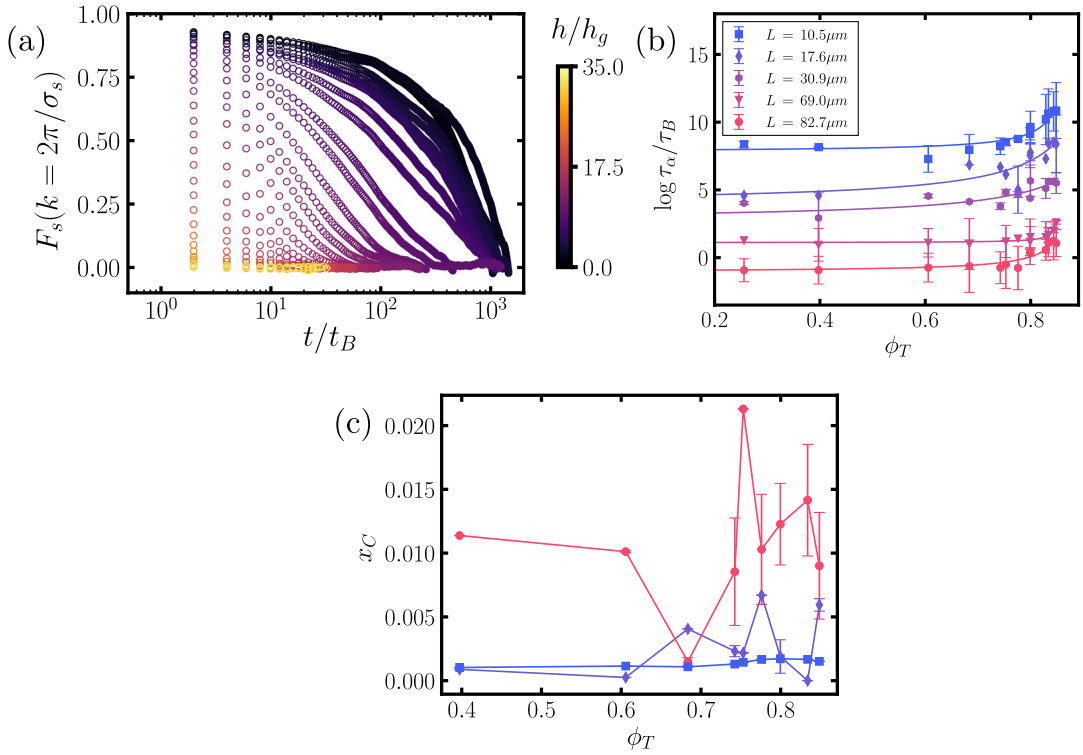


Figure A.5: (a) The self-intermediate scattering function for our dMC simulation. The lines are coloured by height to more clearly show the trend of slowing down. (b) The α-relaxation times of the experimental systems and the dMC simulation. (c) The fraction of particles involved in cooperative motion for the highest and lowest experimental angles and the dMC. The markers relate to the key in (b).

In this section we corroborate our dynamic results from our experiments with the dMC simulation. Figure A.5 (a) shows the self-intermediate scattering function, $F_s(k)$, for our dMC simulation. This is related to figure 7.10 in chapter 7. We have chosen the bins to be in height relative to the bottom rather than area fraction, as due to the narrow width of the simulation, the noise in ϕ_T slightly obfuscates the trend. The simulation replicates the behaviour of the experiments as this decays to zero at all points in the system, showing diffusivity. The magnitude of these dynamics is much lower, consistent with the higher h_g.

Figure A.5 (b) shows the relaxation times of all of the experiments and the dMC simulation. This relates to figure 7.11 (b). The fragility index D from the fitting of the dMC curve is 0.638, which continues the trend in the decrease in fragility with a decrease in h_g.

Figure A.5 (c) shows the fraction of particles involved in cooperative motion, with the highest and lowest experimental tilt angles and the dMC simulation. This relates to figure 7.13 (c), and continues the trend that an increase in h_g leads to a decrease in the number of cooperatively moving regions.

Bibliography

[1] X. Le Pichon, J. Francheteau, and J. Bonnin. *Plate tectonics*. Elsevier, 2013.

[2] H. Blatt, R. Tracy, and B. Owens. *Petrology: igneous, sedimentary and metamorphic*. Macmillan, 2006.

[3] P.Y. Julien. *Erosion and sedimentation*. Cambridge University Press, 2010.

[4] K. Bucher and M. Frey. *Petrogenesis of metamorphic rocks*. Springer, 2002.

[5] A.R. Philpotts and J.J. Ague. *Principles of igneous and metamorphic petrology*. Cambridge University Press, 2009.

[6] J.M. Schopf. Modes of fossil preservation. *Rev. Palaeobot. Palynol.*, 20(1):27, 1975.

[7] G.O. Poinar. *Life in amber*. Stanford University Press, 1992.

[8] T.A. Wertime. Man's first encounters with metallurgy. *Science*, 146(3649):1664, 1964.

[9] L.C. Lancaster. *Concrete vaulted construction in Imperial Rome: innovations in context*. Cambridge University Press, 2005.

[10] P.J. Lu and P.J. Steinhardt. Decagonal and quasi-crystalline tilings in medieval Islamic architecture. *Science*, 315(5815):1106, 2007.

[11] B.M. Fagan. *The Oxford companion to archaeology*. Oxford University Press, 1996.

[12] C.A. Berg. Process innovation and changes in industrial energy use. *Science*, 199(4329):608, 1978.

[13] L.A.B. Pilkington. The float glass process. *Proc. Math. Phys. Eng. Sci.*, 314(1516):1, 1969.

[14] Y. Taur. The incredible shrinking transistor. *IEEE Spectrum*, 36(7):25, 1999.

[15] J.M. Thomas. Centenary: The birth of X-ray crystallography. *Nature*, 491(7423):186, 2012.

[16] G. Binnig, H. Rohrer, C. Gerber, and E. Weibel. 7×7 reconstruction on Si(111) resolved in real space. *Nature*, 50(2):120, 1983.

[17] F.J. Giessibl. Advances in atomic force microscopy. *Rev. Mod. Phys.*, 75(3):949, 2003.

[18] K. Schmidt-Rohr and H.W. Spiess. Nature of non-exponential loss of correlation above the glass transition investigated by multidimensional NMR. *Phys. Rev. Lett.*, 66(23):3020, 1991.

[19] K. Ohno, K. Esfarjani, and Y. Kawazoe. *Computational materials science: from ab initio to Monte Carlo methods*. Springer, 2018.

[20] N. Hansen. Hall-Petch relation and boundary strengthening. *Scr. Mater.*, 51(8):801, 2004.

[21] Y.M. Tairov and V.F. Tsvetkov. General principles of growing large-size single crystals of various silicon carbide polytypes. *J. Cryst. Growth*, 52:146, 1981.

[22] J.S. Benjamin. Mechanical alloying. *Scientific American*, 234(5):40, 1976.

[23] N.N. Greenwood and A. Earnshaw. *Chemistry of the Elements*. Pergamon Press, 1984.

[24] F.A. Lavergne, S. Diana, D.G.A.L. Aarts, and R.P.A. Dullens. Equilibrium grain boundary segregation and clustering of impurities in colloidal polycrystalline monolayers. *Langmuir*, 32(48):12716, 2016.

[25] P.R. Bartlett, R.H. Ottewill, and P.N. Pusey. Freezing of binary mixtures of colloidal hard spheres. *J. Chem. Phys.*, 93(2):1299, 1990.

[26] A. Rollett, F. Humphreys, G.S. Rohrer, and M. Hatherly. *Recrystallzation and related annealing phenomena 2nd Ed.* Pergamon, 2004.

[27] G. Gottstein and L.S. Shvindlerman. *Grain boundary migration in metals: Thermodynamics, kinetics, applications 2nd Ed.* CRC Press, 2009.

[28] J.M. Howe. *Interfaces in materials: atomic structure, thermodynamics and kinetics of solid-vapour, solid-liquid and solid-solid interfaces*. Wiley-Interscience, 1997.

[29] H. Gleiter. Theory of grain boundary migration rate. *Acta Metall.*, 17(7):853, 1969.

[30] J. Nozawa, S. Uda, Y. Naradate, H. Koizumi, K. Fujiwara, A. Toyotama, and J. Yamanaka. Impurity partitioning during colloidal crystallization. *J. Phys. Chem. B*, 117(17):5289, 2013.

[31] J.W. Christian. *The theory of transformations in metals and alloys*. Pergamon, 2002.

[32] A.C. Wright. Neutron scattering from vitreous silica. v. The structure of vitreous silica: What have we learned from 60 years of diffraction studies? *J. Non-Cryst. Solids*, 179:84, 1994.

[33] W. Klement, R.H. Willens, and P.O.L. Duwez. Non-crystalline structure in solidified gold-silicon alloys. *Nature*, 187(4740):869, 1960.

[34] R.J. Speedy. Glass transition in hard disc mixtures. *J. Chem. Phys.*, 110(9):4559, 1999.

[35] D.N. Theodorou and U.W. Suter. Detailed molecular structure of a vinyl polymer glass. *Macromolecules*, 18(7):1467, 1985.

[36] E. Donth. *The glass transition: relaxation dynamics in liquids and disordered materials.* Springer, 2013.

[37] W.H. Zachariasen. The atomic arrangement in glass. *J. Am. Chem. Soc.*, 54(10):3841, 1932.

[38] H. Tanaka, H. Tong, R. Shi, and J. Russo. Revealing key structural features hidden in liquids and glasses. *Nat. Rev. Phys.*, 1(5):333, 2019.

[39] K. Chang. The nature of glass remains anything but clear. *The New York Times*, 29/06/2008.

[40] Y. Yang *et al.* Determining the three-dimensional atomic structure of an amorphous solid. *Nature*, 592(7852):60, 2021.

[41] K.L. Merkle and L.J. Thompson. Atomic-scale observation of grain boundary motion. *Mat. Lett.*, 48(34):188, 2001.

[42] L. Berthier, G. Biroli, J.-P. Bouchaud, L. Cipelletti, and W. van Saarloos. *Dynamical heterogeneities in glasses, colloids and granular media.* Oxford Science Publications, 2011.

[43] L. Bragg and J.F. Nye. A dynamical model of a crystal structure. *Proc. R. Soc. Lond. A*, 190(1023):474, 1947.

[44] A.S. Argon and H.Y. Kuo. Plastic flow in a disordered bubble raft (an analogue of a metallic glass). *Mater. Sci. Eng.*, 39(1):101, 1979.

[45] E.R. Weeks. *Soft jammed materials.* Tohoku University Press, 2007.

[46] S.N. Domenico. Elastic properties of unconsolidated porous sand reservoirs. *Geophysics*, 42(7):1339, 1977.

[47] J.B. Pieper, J. Goree, and R.A. Quinn. Three-dimensional structure in a crystallised dusty plasma. *Phys. Rev. E*, 54(5):5636, 1996.

[48] Y.-S. Su, C.-W. Io, and I. Lin. Transient slowing down relaxation dynamics of the supercooled dusty plasma liquid after quenching. *Phys. Rev. E*, 81(1):016405, 2012.

[49] J.M. Lynch, G.C. Cianci, and E.R. Weeks. Dynamics and structure of an ageing binary colloidal glass. *Phys. Rev. E*, 78(3):031410, 2008.

[50] D.F. Evans and H. Wennerström. *The colloidal domain: where physics, chemistry, biology and technology meet.* Wiley, 1999.

[51] A. Einstein. The theory of Brownian movement. *Ann. Phys. (Berl.)*, 17(549):371, 1905.

[52] J.B. Perrin. Mouvement Brownien et réalité moléculaire. *Ann. Chim. Phys*, 18:5, 1909.

[53] P.N. Pusey and W. Van Megen. Phase behaviour of concentrated suspensions of nearly hard colloidal spheres. *Nature*, 320(6060):340, 1986.

[54] W. Poon. Colloids as big atoms. *Science*, 304(5672):830, 2004.

[55] A. Kuijik, A. van Blaaderen, and A. Imhof. Synthesis of monodisperse, rodlike silica colloids with tunable aspect ratio. *J. Am. Chem. Soc.*, 113(8):822, 2011.

[56] F.M. van der Kooij and H.N.W. Lerkerkerker. Formation of nematic liquid crystals in suspensions of hard colloidal platelets. *J. Phys. Chem. B*, 102(40):7829, 1998.

[57] L. Rossi, S. Sacanna, W.T.M. Irvine, P.M. Chaikin, D.J. Pine, and A.P. Philipse. Cubic crystals from cubic colloids. *Soft Matter*, 7(9):4139, 2011.

[58] P.M. Johnson, C.M. van Kats, and A. van Blaaderen. Synthesis of colloidal silica dumbbells. *Langmuir*, 21(24):557, 2005.

[59] D. Frenkel, H.N.W. Lerkerkerker, and A. Stroobants. Thermodynamic stability of a smectic phase in a system of hard rods. *Nature*, 332(6167), 1988.

[60] P.F. Damasceno, M. Engel, and S.C. Glotzer. Predictive self-assembly of polyhedra into complex structures. *Science*, 337(6093):453, 2012.

[61] B.V. Derjaguin and L. Landau. Theory of the stability of strongly charged lyophobic sols and of the adhesion of strongly charged particles in solutions of electrolytes. *Acta Physicochim. URSS*, 14(3):30, 1941.

[62] E.J.W. Verwey. Theory of the stability of lyophobic colloids. *J. Phys. Colloid Chem.*, 51(3):631, 1947.

[63] K. Zahn, R. Lenke, and G. Maret. Two-stage melting of paramagnetic colloidal crystals in two-dimensions. *Phys. Rev. Lett.*, 82(13):2721, 1997.

[64] A. Vrij. Polymers at interfaces and the interactions in colloidal dispersions. *Pure Appl. Chem.*, 48(4):471, 1976.

[65] A.L. Thorneywork, R. Roth, D.G.A.L. Aarts, and R.P.A. Dullens. Radial distribution functions in a two-dimensional binary colloidal hard sphere system. *J. Chem. Phys.*, 140(16):161106, 2014.

[66] E.P. Bernard and W. Krauth. Two-step melting in two dimensions: First-order liquid-hexatic transition. *Phys. Rev. Lett.*, 107(15):155704, 2011.

[67] J.-T. Zhang, L. Wang, D.N. Lamont, S.S. Velankar, and S.A. Asher. Fabrication of large-area two-dimensional colloidal crystals. *Angew. Chem.*, 51(25):6221, 2012.

[68] T. Kawasaki and H. Tanaka. Structural signature of slow dynamics and dynamic heterogeneity in two-dimensional colloidal liquids: Glassy structural order. *J. Phys. Condens. Matter*, 23(19):194121, 2011.

[69] F.A. Lavergne, D.G.A.L. Aarts, and R.P.A. Dullens. Anomalous grain growth in a polycrystalline monolayer of colloidal hard spheres. *Phys. Rev. X*, 7(4):041064, 2017.

[70] C.D. Dushkin, H. Yoshimura, and K. Nagayama. Nucleation and growth of two-dimensional colloidal crystals. *Chem. Phys. Lett.*, 240(5):455, 1993.

[71] T.O.E. Skinner, D.G.A.L. Aarts, and R.P.A. Dullens. Grain-boundary fluctuations in two-dimensional colloidal crystals. *Phys. Rev. Lett.*, 105(16):168301, 2010.

[72] A.L. Thorneywork, J.L. Abbott, D.G.A.L. Aarts, and R.P.A. Dullens. Two-dimensional melting of colloidal hard spheres. *Phys. Rev. Lett.*, 118(15):158001, 2017.

[73] K. Zahn, A. Wille, G. Maret, S. Sengupta, and P. Nielaba. Elastic properties of 2D colloidal crystals from video microscopy. *Phys. Rev. Lett.*, 90(15):155506, 2003.

[74] K-Q. Zhang and X.Y. Liu. Determination of elastic constants of two-dimensional close packed colloidal crystals. *Langmuir*, 25(10):5432, 2009.

[75] F. Ebert, P. Keim, and G. Maret. Local crystalline order in a 2D colloidal glass former. *Eur. Phys. J. E*, 26(1):161, 2008.

[76] S. Vivek, C.P. Kelleher, P.M. Chaikin, and E.R. Weeks. Long-wavelength fluctuations and the glass transition in two dimensions and three dimension. *Proc. Natl. Acad. Sci. U.S.A.*, 114(8):1850, 2017.

[77] C.R. Nugent, K.V. Edmond, H.N. Patel, and E.R. Weeks. Colloidal glass transition observed in confinement. *Phys. Rev. Lett.*, 99(2):025702, 2007.

[78] S. Mazoyer, F. Ebert, G. Maret, and P. Keim. Dynamics of particles and cages in an experimental 2D glass former. *Eur. Phys. J. E*, 88(6):66004, 2010.

[79] T. Kawasaki, T. Araki, and H. Tanaka. Correlation between dynamic heterogeneous and medium-range order in two-dimensional glass-forming liquids. *Phys. Rev. Lett.*, 99(21):215701, 2007.

[80] H. Shiba, T. Kawasaki, and K. Kim. Local density fluctuation governs the divergence of viscosity underlying elastic and hydrodynamic anomalies in a 2D glass-forming liquid. *Phys. Rev. Lett.*, 123(26):265501, 2009.

[81] B. Illing, S. Fritschi, H. Kaiser, C.L. Klix, G. Maret, and P. Keim. Mermin–Wagner fluctuations in 2d amorphous solids. *Proc. Natl. Acad. Sci. U.S.A.*, 114(8):1856, 2016.

[82] H.M. Lindsay and P.M. Chaikin. Elastic properties of colloidal crystals and glasses. *J. Chem. Phys.*, 76(7):3774, 1982.

[83] L. Assoud, F. Ebert, P. Keim, R. Messina, G. Maret, and H.Löwen. Ultrafast quenching of binary colloidal suspensions in an external magnetic field. *Phys. Rev. Lett.*, 102(1):238301, 2009.

[84] A. Snezhko and I.S. Aranson. Magnetic manipulation of self-assembled colloidal asters. *Nat. Mater.*, 10(9):698, 2011.

[85] N.B. Simeonova and W.K. Kegel. Gravity-induced ageing in glasses of colloidal hard spheres. *Phys. Rev. Lett.*, 93(3):035701, 2004.

[86] R.P.A. Dullens and C. Bechinger. Shear thinning and local melting of colloidal crystals. *Phys. Rev. Lett.*, 107(13):138301, 2011.

[87] W.T.M. Irvine, A.D. Hollingsworth, D.G. Grier, and P.M. Chaikin. Dislocation reactions, grain boundaries, and irreversibility in two-dimensional lattices using topological tweezers. *Proc. Natl. Amer. Sci.*, 110(39):15544, 2014.

[88] K. Dill and S. Bromberg. *Molecular driving forces: statistical thermodynamics in biology, chemistry, physics, and nanoscience*. Garland Science, 2012.

[89] R.J. Hunter. *Foundations of colloid science*. Oxford University Press, 2001.

[90] J.K.G. Dhont. *An introduction to dynamics of colloids*. Elsevier, 1996.

[91] J.N. Israelachvili. *Intermolecular and surface forces*. Academic Press, 2015.

[92] S. Alexander, P.M. Chaikin, P. Grant, G.J. Morales, P. Pincus, and D. Hone. Charge renormalisation, osmotic pressure, and bulk modulus of colloidal crystals: Theory. *J. Chem. Phys.*, 80(11):5776, 1984.

[93] D. Frenkel. Entropy-driven phase transitions. *Physica A*, 263(1):26, 1999.

[94] J.P. Hansen and I.R. McDonald. *Theory of simple liquids*. Academic Press, 2006.

[95] B.J. Alder and T.E. Wainwright. Phase transition for a hard sphere system. *J. Chem. Phys.*, 27(5):1208, 1957.

[96] W.W. Wood and J.D. Jacobson. Preliminary results from a recalculation of the Monte Carlo equation of state of hard spheres. *J. Chem. Phys.*, 27(5):1207, 1957.

[97] J.M. Kosterlitz and D.J. Thouless. Ordering, metastability and phase transitions in two-dimensional systems. *J. Phys. C*, 6(7):1181, 1973.

[98] D.R. Nelson and B.I. Halperin. Dislocation-mediated melting in two dimensions. *Phys. Rev. B*, 19(5):2457, 1979.

[99] A.P. Young. Melting and the vector Coulomb gas in two dimensions. *Phys. Rev. B*, 19(4):1855, 1979.

[100] M. Engel, J.A. Anderson, S.C. Glotzer, M. Isobe, E.P. Bernard, and W. Krauth. Hard-disk equation of state: First-order liquid-hexatic transition in two dimensions with three simulation methods. *Phys. Rev. E*, 87(4):042134, 2013.

[101] U. Gasser, C. Eisenmann, G. Maret, and P. Keim. Melting of crystals in two dimensions. *ChemPhysChem*, 11(5):963, 2010.

[102] A.L. Thorneywork, J.L. Abbott, D.G.A.L. Aarts, P. Keim, and R.P.A. Dullens. Bond-orientational order and frank's constant in two-dimensional colloidal hard spheres. *J. Phys, Condens. Matter*, 30(10):104003, 2018.

[103] N.D. Mermin and H. Wagner. Absence of ferromagnetism or antiferromagnetism in one-or two-dimensional isotropic Heisenberg models. *Phys. Rev. Lett.*, 17(22):1133, 1966.

[104] V.W.A. de Villeneuve, R.P.A. Dullens, D.G.A.L. Aarts, E. Groeneveld, J.H. Scherff, W.K. Kegel, and H.N.W. Lekkerkerker. Colloidal hard-sphere crystal growth frustrated by large spherical impurities. *Science*, 309(5738):1231, 2005.

[105] H. Zhang and Y. Han. Compression-induced polycrystal-glass transition in binary crystals. *Phys. Rev. X*, 8(4):041023, 2018.

[106] T.W. Melynk and B.L. Sawford. Equation of state of a mixture of hard spheres with non-additive diameter. *Mol. Phys.*, 29(3):891, 1975.

[107] P. Ballone, G. Pastore, G Galli, and D. Gazzillo. Additive and non-additive hard sphere mixtures. *Mol. Phys.*, 59(2):275, 1975.

[108] P. Hopkins and M. Schmidt. Binary non-additive hard sphere mixtures: fluid demixing, asymptotic decay of correlations and free fluid interfaces. *J. Phys: Condens. Matter*, 22(32):325108, 2010.

[109] A. Santos, M. López de Haro, and S.B. Yuste. Equation of state of nonadditive d-dimensional hard-sphere mixtures. *J. Chem. Phys.*, 122(2):024514, 2005.

[110] T. Biben and J-P. Hansen. Phase separation of asymmetric binary hard-sphere fluids. *Phys. Rev. Lett.*, 66(17):2215, 1991.

[111] K.P. Velikov, C.G. Christova, R.P.A. Dullens, and A. von Blaaderen. Layer-by-layer growth of binary colloidal crystals. *Science*, 296(5565):106, 2002.

[112] E. Fayen, A. Jagannathan, G. Foffi, and F. Smallenburg. Infinite-pressure phase diagram of binary mixtures of (non)additive hard disks. *J. Chem. Phys.*, 152(20):204901, 2020.

[113] A.K. Geim and K.S. Novoselov. The rise of graphene. *Nature Mat.*, 6:183, 2007.

[114] P. Dillmann, G. Maret, and P. Keim. Polycrystalline solidification in a quenched 2d colloidal system. *J. Phys. Condes. Matter*, 20(40):404216, 2008.

[115] D.R. Nelson. *Defects and geometry in condensed matter physics*. Cambridge University Press, 2002.

[116] D. Hull and D.J. Bacon. *Introduction to dislocations*. Butterworth-Heinemann, 2001.

[117] F.A. Lavergne, A. Curran, D.G.A.L. Aarts, and R.P.A. Dullens. Dislocation-controlled formation and kinetics of grain boundary loops in two-dimensional crystals. *Proc. Natl. Acad. Sci. U.S.A.*, 115(27):6922, 2018.

[118] M-C. Chen, C. Yang, and L. I. Kinetic origin of grain boundary migration, grain coalescence and defect reduction in the crystallisation of quenched two-dimensional Yukawa liquids. *Phys. Rev. E*, 90(5):050401, 2014.

[119] W.T. Read and W. Shockley. Dislocation models of crystal grain boundaries. *Phys. Rev.*, 78(3):275, 1950.

[120] C. Herring. *The physics of power metallurgy: Surface tension as a motivation for sintering.* McGraw-Hill, New York, 1951.

[121] A.P. Sutton and R.W. Balluffi. *Interfaces in crystalline materials.* Oxford: Clarendon Press, 1995.

[122] J. Weissmüller. Alloy effects in nanostructures. *Nanostructured Mater.*, 3(1):261, 1993.

[123] S. Nam, K. Chang, W. Lee, M.J. Kim, J.Y. Hwang, and H. Choi. Structural effect of two-dimensional bnns on grain growth suppressing behaviours in Al-matrix nanocomposites. *Sci. Rep.*, 8(1614):1, 2008.

[124] E. Nes, N. Ryum, and O. Hunderi. On the zener drag. *Acta Metall.*, 33(1):11, 1984.

[125] P.G. Debenedetti and F.H. Stillinger. Supercooled liquids and the glass transition. *Nature*, 410(6825):259, 2001.

[126] J.H. Gibbs and E.A. DiMarzio. Nature of the glass transition and the glassy state. *J. Chem. Phys.*, 28(3):373, 1958.

[127] A. Cavagna. Supercooled liquids for pedestrians. *Phys. Rep.*, 476(4):51, 2009.

[128] L. Berthier and W. Kob. The Monte Carlo dynamics of a binary Lennard-Jones glass-forming mixture. *J. Phys.: Condens. Matter*, 19(20):205130, 2007.

[129] C. Donati, J.F. Douglas, W. Kob, S.J.Plimpton, P.H. Poole, and S.C. Glotzer. Stringlike cooperative motion in a supercooled liquid. *Phys. Rev. Lett.*, 80(11):2338, 1998.

[130] M.D. Ediger. Spatially heterogeneous dynamics in supercooled liquids. *Annu. Rev. Phys. Chem.*, 51(1):99, 2000.

[131] W. Kauzmann. The nature of the glassy state and the behaviour of liquids at low temperatures. *Chem. Rev.*, 43(2):219, 1948.

[132] G.L. Hunter and E.R. Weeks. The physics of the colloidal glass transition. *Rep. Prog. Phys.*, 75(6):066501, 2012.

[133] A.H. Marcus, J. Schofield, and S.A. Rice. Experimental observations of non-gaussian behavior and stringlike cooperative dynamics in concentrated quasi-two-dimensional colloidal liquids. *Phys. Rev. E*, 60(5):5725, 1999.

[134] W.K. Kegel and A. van Blaaderen. Direct observation of dynamical heterogeneities in colloidal hard-sphere suspensions. *Science*, 287(5451):290, 2000.

[135] A. Meller and J. Stavans. Glass transition and phase diagrams of strongly interacting colloidal mixtures. *Phys. Rev. Lett.*, 68(24):3646, 1992.

[136] T. Sentjabrskaja, E. Babaliari, J. Hendricks, M. Laurati, G. Petekidis, and S.U. Egelhaaf. Yielding of binary colloidal glasses. *Soft Matter*, 9(17):4524, 2013.

[137] A. Imhof and J.K.G. Dhont. Experimental phase diagram of a binary colloidal hard-sphere mixture with a large size ratio. *Phys. Rev. Lett.*, 75(8):1662, 1995.

[138] Y. Liu, T. Yanagishima, A. Curran, K.V. Edmond, S. Sacanna, and R.P.A. Dullens. Colloidal organosilica spheres for three-dimensional confocal microscopy. *Langmuir*, 35(24):7962, 2019.

[139] M.P.N. Juniper, R. Besseling, D.G.A.L. Aarts, and R.P.A. Dullens. Acousto-optically generated potential energy landscapes: Potential mapping using colloids under flow. *Opt. Express*, 20(27):28707, 2012.

[140] A. Ashkin, J.M. Dziedzic, J.E. Bjorkholm, and S. Chu. Observation of a single-beam gradient force optical trap for dielectric particles. *Opt. Lett.*, 11(5):288, 1986.

[141] A. Ashkin. Forces of a single-beam gradient laser trap on a dielectric sphere in the ray optics regime. *Biophys. J.*, 61(2):569, 1992.

[142] A. Ashkin. Acceleration and trapping of particles by radiation pressure. *Phys. Rev. Lett.*, 24(4):156, 1970.

[143] E.I. Gordon. A review of acoustooptical deflection and modulation devices. *Appl. Opt.*, 5(10):1629, 1966.

[144] D. Allan, C. van der Wel, and T.A. Caswell *et al.* soft-matter/trackpy: Trackpy v0.4.2. *https://doi.org/10.5281/zenodo.3492186*, October 2019.

[145] J.C. Crocker and E.R. Weeks. Particle tracking using IDL. *http://www.physics.emory.edu/faculty/weeks//idl/index.html*, 1997.

[146] J.C. Crocker and D.G. Grier. Methods of digital video microscopy for colloidal studies. *J. Colloid Interface Sci.*, 179(1):298, 1996.

[147] M.P. Allen and D.J. Tildesley. *Computer simulation of liquids: Second edition.* Oxford University Press, 2017.

[148] D.L. Ermak. A computer simulation of charged particles in solution. I. Technique and equilibrium properties. *J. Chem. Phys.*, 62(10):4189, 1974.

[149] J.D. Weeks, D. Chandler, and H.C. Andersen. Role of repulsive forces in determining the equilibrium structure of simple liquids. *J. Chem. Phys.*, 54(12):5237, 1971.

[150] N. Metropolis, A.W. Rosenbluth, M.N. Rosenbluth, A.H. Teller, and E. Teller. Equation of state calculations by fast computing machines. *J. Chem. Phys.*, 21(6):1087, 1953.

[151] D. Frenkel. Simulations: The dark side. *Eur. Phys. J. Phys. Plus*, 128(10):1, 2013.

[152] B. Evans, J. Renner, and G. Hirth. A few remarks on the kinetics of static grain growth in rocks. *Int. J. Earth*, 90(1):88, 2001.

[153] R.B. Alley, J.H. Perepezeko, and C.R. Bentley. Grain growth in polar ice: I. theory. *J. Glaciol.*, 32(112):415, 1984.

[154] C.V Thompson. Grain growth in thin films. *Annu. Rev. Mater. Sci.*, 20(1):245, 1990.

[155] A Zaleska. Doped-TiO_2: A review. *Recent Pat. Eng.*, 2(3):157, 2008.

[156] P-L. Chen and I-W. Chen. Grain growth in CeO_2: Dopant effects, defect mechanism and solute drag. *J. Am. Ceram. Soc.*, 79:1793, 1996.

[157] J.P. Hirth and J. Lothe. *Theory of dislocations 2nd Ed.* New York: Wiley, 1982.

[158] J. Schøtz, F.D. Di Tolla, and K.W. Jacobsen. Softening of nanocrystalline metals at very small grain sizes. *Nature*, 391(6667):561, 1998.

[159] R. Phillips. *Crystals, defects and microstructure.* Cambridge University Press, 2004.

[160] G. Duscher, M.F. Chisholm, U. Alber, and M. Rühle. Bismuth-induced embrittlement of copper. *Nat. Rev. Mater.*, 3(9):621, 2004.

[161] A. Tkach, J. Resende, K.V. Saravanan, M.E. Costa, P. Diaz-Chao, E. Guilmeau, O. Okhay, and P.M. Vilarinho. Abnormal grain growth as a method to enhance the thermoelectric performance of Nb-doped strontium titanate ceramics. *ACS Sustainable Chem. Eng.*, 6(12):15988, 2018.

[162] S. Yip. Nanocrystals: the strongest size. *Nature*, 391(6667):532, 1998.

[163] A.J. Bray and K. Humayun. Universality class for domain growth in random magnets. *J. Phys. A: Math. Gen*, 24(19):L1185, 1991.

[164] T. Hashimoto, M. Takenaka, and T. Izumitani. Spontaneous pinning of domain grain growth during spinodal decomposition of off-critical polymer mixtures. *J. Chem. Phys.*, 97(1):679, 1992.

[165] S.C. Glotzer, M.F. Gyure, F. Sciortino, A. Coniglio, and H.E. Stanley. Pinning in phase-separating systems. *Phys. Rev. E*, 49(1):247, 1994.

[166] G.S. Grest and D.J. Srolovitz. Impurity effects on domain-growth kinetics. i. ising model. *Phys. Rev. B*, 32(5):3014, 1985.

[167] Z. Guo and J.T. Kindt. Simulations of grain boundaries between ordered hard sphere monolayer domains: Orientation-dependent stiffness and its correlation with grain coarsening dynamics. *J. Chem. Phys.*, 149(4):044503, 2018.

[168] V.W.A de Villeneuve, L. Derendorp, D. Verboekend, E.C.M. Vermolen, W.K. Kegel, H.N.W Lekkerkerker, and R.P.A. Dullens. Grain boundary pinning in doped hard sphere crystals. *Soft Matter*, 5(12):2448, 2009.

[169] PA. Manohar, M. Ferry, and T. Chandra. Five decades of the Zener equation. *ISIJ International*, 38(9):913, 1998.

[170] A.J. Bray. Theory of phase-ordering kinetics. *Adv. Phys.*, 51(2):481, 2002.

[171] A. Onuki. *Phase transition dynamics*. Cambridge University Press, 2002.

[172] C. Aron, C. Chamon, L.F. Cugliandolo, and M. Picco. Scaling and super-universailty in the coarsening dynamics of the 3D random field Ising model. *J. Stat. Mech.*, 5:P05016, 2008.

[173] T. Nattermann, Y. Shapir, and I. Vilfan. Interface pinning and dynamics in random systems. *Phys. Rev. B*, 45(13):8577, 1990.

[174] D.A. Huse and C.L. Henley. Pinning and roughening of domain walls in ising systems due to random impurities. *Phys. Rev. Lett.*, 54(25):2708, 1985.

[175] L.F. Cugliandolo. Topics in coarsening phenomena. *Physica A*, 389(20):4360, 2010.

[176] P. Dillmann. *Nonequilibrium phase transition in a 2d colloidal system*. Doctoral Dissertation, University of Konstanz, 2012.

[177] N. Ghofraniha, E. Tamborini, J. Oberdisse, L. Cipelletti, and L. Ramos. Grain refinement and partitioning of impurities in the grain boundaries of a colloidal polycrystal. *Soft Matter*, 8(23):6214, 2012.

[178] K. Yoshizawa, T. Okuzono, T. JKoga, T. Taniji, and J. Yamanaka. Exclusion of impurity particles during grain growth in charged colloidal crystals. *Langmuir*, 27(22):13420, 2011.

[179] T. Ohta, D. Jasnow, and K. Kawasaki. Universal scaling in the motion of random interfaces. *Phys. Rev. Lett.*, 49(17):1223, 1982.

[180] S. Puri and N. Parekh. Non-algebraic domain growth for phase ordering dynamics in a random field. *J. Phys. A: Math. Gen*, 26(12):2777, 1993.

[181] L. Vanherpe, N. Moelans, B. Blanpain, and S. Vadewalle. Pinning effect of spheroid second-phase particles on grain growth studied by three-dimensional phase-field simulations. *Comput. Mater. Sci.*, 49(2):340, 2010.

[182] M.A. Etzold, P.J. McDonald, D.A. Faux, and A.F. Routh. Filling of three-dimensional space by two-dimensional sheet growth. *Phys. Rev. E*, 92(4):042106, 2015.

[183] R.P. Feynman. *Progress in low temperature physics.* Elsevier, 1955.

[184] J.E. Baker, I. Brust-Mascher, S. Ramachandran, L.E.W. LaConte, and D.D. Thomas. A large and distinct rotation of the myosin light chain domain occurs upon muscle contraction. *Proc. Natl. Acad. Sci. USA*, 95(6):2944, 1998.

[185] N. Altamirano, D. Kubiznák, and R.B. Mann. Reentrant phase transitions in rotating anti-de Sitter black holes. *Phys. Rev. D*, 88(10):101502, 2013.

[186] J.M. Catchmark, S. Subramanian, and A. Sen. Directed rotational motion of microscale objects using interfacial tension gradients continually generated via catalytic reactions. *Small*, 1(2):202, 2005.

[187] J. Yoshioka, F. Ito, Y. Suzuki, H. Takahashi, H. Takizawa, and Y. Tabe. Director/barycentric rotation in cholesteric droplets under temperature gradient. *Soft Matter*, 10(32):5869, 2014.

[188] H.C Berg. The rotary motor of bacterial flagella. *Annu. Rev. Biochem.*, 72(1):19, 2003.

[189] D. Moldovan, V. Yamakov, D. Wolf, and S.R. Phillpot. Scaling behaviour of grain-rotation-induced grain growth. *Phs. Rev. Lett.*, 89(20):206101, 2002.

[190] L.J. Moore, R.D. Dear, M.D. Summers, R.P.A. Dullens, and G.A.D. Ritchie. Direct observation of grain rotation-induced grain coalescence in two-dimensional colloidal crystals. *Nano Lett.*, 10(10):4266, 2010.

[191] E.R. Leite, T.R. Giraldi, F.M. Pontes, E. Longo, A. Beltrán, and J. Andrés. Crystal growth in colloidal tin oxide nanocrystals induced by coalescence at room temperature. *App. Phys. Lett.*, 83(8):1566, 2003.

[192] K.E. Harris, V.V. Singh, and A.G. King. Grain rotation in thin films of gold. *Acta Mater.*, 46(8):2623, 1998.

[193] C.S. Nichols, C.M. Mansuri, S.J. Townsend, and D.A. Smith. In situ studies of grain growth in thin metal films. *Acta Metall. Mater*, 41(6):1861, 1993.

[194] Y.B. Wang, B.Q. Li, and M.L. Sui. Deformation-induced grain rotation and growth in nanocrystalline Ni. *Appl. Phys. Lett.*, 92(1):011903, 2008.

[195] L. Margulies, G. Winther, and H.F. Poulsen. In situ mesasrement of grain rotation during deformation of polycrystals. *Science*, 291(5512):2392, 2008.

[196] J.C.M. Li. Possibility of subgrain rotation during recrystallization. *J. Appl. Phys.*, 33(10):2958, 1962.

[197] J.M. Dake, J. Oddershede, H.O. Sørensen, T. Werz, J.C. Shatto, K. Uesugi, S. Schmidt, and C.E. Krill III. Direct observation of grain rotations during coarsening of a semisolid Al-Cu alloy. *Proc. Natl. Acad. Sci. U.S.A.*, 113(41):E5998, 2016.

[198] R. Ahluwalia, T. Lookman, and A. Saxena. Elastic deformation of polycrystals. *Phys. Rev. Lett.*, 91(5):055501, 2003.

[199] S.V. Bobylev, N.F. Morozov, and I.A. Ovid'ko. Cooperative grain boundary sliding and migration process in nanocrystalline solids. *Phys. Rev. Lett.*, 105(5):055504, 2010.

[200] A. Adland, Y. Xu, and A. Karma. Unified theoretical framework for polycrystalline pattern evolution. *Phys. Rev. Lett.*, 110(26):265504, 2013.

[201] D.A. Vega, C.K. Harrison, D.E. Angelescu, M.L. Trawick, D.A. Huse, P.M. Chaikin, and R.A. Register. Ordering mechanisms in two-dimensional sphere-forming block copolymers. *Phys. Rev. E*, 71(6):061803, 2005.

[202] R. Raj and M.F. Ashby. On grain boundary sliding and diffusional creep. *Metall. Trans.*, 2(4):1113, 1971.

[203] D. Moldovan, D. Wolf, and S.R. Phillpot. Theory of diffusion-accommodated grain rotation in columnar polycrystalline microstructures. *Acta Mater.*, 49(17):3521, 2001.

[204] E. Arzt, M.F. Ashby, and R.A. Verrall. Interface controlled diffusional creep. *Acta Metall.*, 31(12):1977, 1983.

[205] F.C. Frank. Report of the symposium on the plastic deformation of crystalline solids. *Carnigie Institude of Technology, Pittsburgh*, page 150, 1950.

[206] K. Wu and P.W. Vorhees. Phase field crystal simulations of nanocrystalline grain growth in two dimensions. *Acta Mater.*, 60(1):407, 2011.

[207] F.A. Lavergne, A. Curran, D.G.A.L. Aarts, and R.P.A. Dullens. Shrinkage mechanisms of grain boundary loops in two-dimensional colloidal crystals. *Eur. Phys. J. B*, 92(7):1, 2019.

[208] J.W. Cahn and J.E. Taylor. A unified approach to motion of grain boundaries, relative tangential translation along grain boundaries, and grain rotation. *Acta Mater.*, 52(16):4887, 2004.

[209] M. Upmanyu, D.J. Srolovitz, A.E. Lobkovskyc, J.A. Warren, and W.C. Carter. Simultaneous grain boundary migration and grain rotation. *Acta Mater.*, 54(7):1707, 2006.

[210] P.M. Anderson, J.P. Hirth, and J. Lothe. *Theory of dislocations.* Cambridge University Press, 2017.

[211] M. Jorand, F. Rothen, and P. Pieranski. Dislocation motion in colloidal crystals. *J. Phys. (Paris)*, 46(C3):245, 1985.

[212] P. Schall, I. Cohen, D.A. Weitz, and F. Spaepen. Visualising dislocation nucleation by indenting colloidal crystals. *Nature*, 440(7082):319, 2006.

[213] D. Frenkel and A.J.C. Ladd. Elastic constants of hard-sphere crystals. *Phys. Rev. Lett.*, 59(10):1169, 1987.

[214] P. Heitjans and J. Kärger. *Diffusion in condensed matter. Methods, materials, models.* Springer, 2005.

[215] B. van der Meer, M. Dijkstra, and L. Filion. Diffusion and interactions of point defects in hard-sphere crystals. *J. Chem. Phys.*, 146(24):244905, 2017.

[216] D. Moldovan, D. Wolf, and S.R. Phillpot. Role of grain rotation during grain growth in a columnar microstructure by mesoscale simulation. *Acta Mater.*, 50(13):3397, 2002.

[217] C. Herring. Diffusional viscosity of a polycrystalline solid. *J. Appl. Phys.*, 21(5):437, 1950.

[218] Z.T. Trautt and Y. Mishin. Grain boundary migration and grain rotation studied by molecular dynamics. *Acta Mater.*, 60(5):2407, 1950.

[219] L. Wang, J. Teng, A. Hirata, E. Ma, Z. Zhang, M. Chen, and X. Han. Grain rotation mediated by grain boundary dislocations in nanocrystalline platinum. *Nature Commun.*, 5(1):1, 2014.

[220] R. Chaim. Grain coalescence by grain rotation in nano-ceramics. *Scrip. Mater.*, 66(5):269, 2012.

[221] T. Gorkaya, K.D. Molodov, D.A. Molodov, and G. Gottstein. Concurrent grain boundary motion and grain rotation under an applied stress. *Acta Mater.*, 59(14):5674, 1950.

[222] B. Chen, K. Lutker, J. Lei, J. Yan, S. Yang, and H. Mao. Detecting grain rotation at the nanoscale. *Proc. Natl. Acad. Sci. U.S.A.*, 111(9):3350, 2014.

[223] F.L. Lavergne. *Dynamics of grain boundaries in two-dimensional colloidal crystals.* University of Oxford, 2016.

[224] C.S. Smith. Introduction to grains, phases and interfaces- an interpretation of microstructure. *Trans. AIME*, 17(15):457, 1948.

[225] F.J. Humphreys and M.G. Ardakani. Grain boundary migration and zener pinning in particle-containing copper crystals. *Acta Mater.*, 44(7):2717, 1996.

[226] P.M. Hazzledine and R.D.J. Oldershaw. Computer simulation of Zener pinning. *Philos. Mag. A*, 61(4):579, 1990.

[227] T. Gladman. On the theory of the effect of precipitate particles on grain growth in metals. *Proc. R. Soc.*, 294(1438):298, 1966.

[228] P.R. Rios. A theory for grain boundary pinning by particles. *Acta Metall.*, 35(12):2805, 1987.

[229] J. Gao, R.G. Thompson, and B.R. Patterson. Computer simulation of grain growth with second phase particle pinning. *Acta Mater.*, 45(9):3653, 1997.

[230] A. Harun, E.A. Holm, M.P. Clode, and M.A. Miodownik. On computer simulation methods to model Zener pinning. *Acta Mater.*, 54(12):3261, 2006.

[231] H. Hallberg. Approaches to modelling of recrystallisation. *Metals*, 1(1):16, 2011.

[232] D. Raabe and L. Hantcherli. 2D cellular automaton simulation of the recrystallisation texture of an if sheet steel under consideration of Zener pinning. *Comp. Mat. Sci.*, 34(4):299, 2005.

[233] H.A. Barnes, J.F. Hutton, and K. Walters. *An introduction to rheology*. Elsevier, 1989.

[234] E.M. Furst and T.M. Squires. *Microrheology*. Oxford University Press, 2017.

[235] T.A. Waigh. Microrheology of complex fluids. *Rep. Prog. Phys.*, 68(3):685, 2005.

[236] T. Yanagishima, D. Frenkel, J. Kotar, and E. Eiser. Real-time monitoring of complex moduli from microrheology. *J. Phys.: Condens. Matter*, 23(19):194118, 2011.

[237] T.G. Mason, K. Ganesan, J.H. van Zanten, D. Wirtz, and S.C. Kuo. Particle tracking microrheology of complex fluids. *Phys. Rev. Lett.*, 79(17):3282, 1997.

[238] B. Fabry, G.N. Maksym, J.P. Butler, M. Glogauer, D. Navajas, and J.J. Fredberg. Scaling the microrheology of living cells. *Phys. Rev. Lett.*, 79(14):148102, 2001.

[239] M. Guo, A.J. Ehrlicher, M.H. Jensen, M. Renz, J.R. Moore, R.D. Goldman, J. Lippincott-Schwartz, F.C. Mackintosh, and D.A. Weitz. Probing the stochastic, motor-driven properties of the cytoplasm using force spectrum microscopy. *Cell*, 158(4):822, 2014.

[240] I. Buttinoni and R.P.A. Dullens. Mechanical properties of colloidal crystals at fluid interfaces. *J. Phys. Mater.*, 4(2):025001, 2021.

[241] J.M. van Doorn, R. Higler, R. Wegh, R. Fokkink, A. Zaccone, J. Sprakel, and J. van der Gucht. Propagation and attenuation of mechanical signals in ultrasoft 2D solids. *Sci. Adv.*, 6(37):eaba6601, 2020.

[242] R.N. Zia. Active and passive microrheology: Theory and simulation. *Annu. Rev. Fluid Mech.*, 50:371, 2018.

[243] I.C. Carpen and J.F. Brady. Microrheology of colloidal dispersions by Brownian dynamics simulations. *J. Rheol.*, 49(6):1483, 2005.

[244] C. Reichhardt and C.J. Olson Reichhardt. Local melting and drag for a particle driven through a colloidal crystal. *Phys. Rev. Lett.*, 92(10):108301, 2004.

[245] C.A. Sawyer, J.W. Morris Jr., and D.C. Chrzan. Dislocation core radii near elastic stability limits. *Phys. Rev. B*, 87(13):134106, 2013.

[246] A.H. Cottrell and B.A. Bilby. Dislocation theory of yielding snd strain ageing of iron. *Proc. Phys. Soc. A*, 62(1):49, 1949.

[247] B.A. Bilby. On the interactions of dislocations and solute atoms. *Proc. Phys. Soc. A*, 64(3):191, 1949.

[248] I. Medouni, A. Portavoce, P. Maugis, P. Eyméoud, M. Yescas, and K. Hoummada. Role of dislocation elastic field on impurity segregation in Fe-based alloys. *Sci. Rep.*, 11(1):1, 2021.

[249] A.A. Verhoeff, F.A. Lavergne, D. Bartolo, D.G.A.L. Aarts, and R.P.A. Dullens. Optical trapping of interfaces at ultra-low interfacial tension. *Soft Matter*, 11(16):3100, 2015.

[250] M. Kline. *Calculus: An intuitive and physical approach.* Dover, 1998.

[251] J. Jones. *Forced motion of an impurity through a two-dimensional polycrystalline colloidal system.* University of Oxford, 2014.

[252] Q.H. Wei and X.L. Wu. Grain boundary dynamics under mechanical annealing in two-dimensional colloids. *Phys. Rev. E*, 70(2):020401, 2004.

[253] M. Liao, X. Xiao, S.T. Chui, and Y. Han. Grain-boundary roughening in colloidal crystals. *Phys. Rev. X*, 8(2):021045, 2018.

[254] C.E. Cash, J. Wang, M.M. Martirossyan, B.K. Ludlow, A.E. Baptista, N.M. Brown, E.J. Weissler, J. Abacousnac, and S.J. Gerbode. Local melting attracts grain boundaries in colloidal polycrystals. *Phys. Rev. Lett.*, 120(1):018002, 2018.

[255] D. Taha, S.K. Mkhonta, K.R. Elder, and Z-F. Huang. Grain boundary structures and collective dynamics of inversion domains in binary two-dimensional materials. *Phys. Rev. Lett.*, 118(25):255501, 2017.

[256] Y. Liu, X. Zhou, and B.I. Yakobson. Dislocations and grain boundaries in two-dimensional boron nitride. *ACS Nano*, 6(8):7053, 2012.

[257] D. Wolf. A Read-Shockley model for high-angle grain boundaries. *Scrip. Metall.*, 23(10):1713, 1989.

[258] G.S. Rohrer. Grain boundary energy anisotropy: a review. *J. Mater. Sci.*, 45(18):5881, 2011.

[259] P.B. Bladon and D. Frenkel. Free energy and structure of dislocation cores in two-dimensional crystals. *J. Phys. Chem. B*, 108(21):6707, 2004.

[260] J. Rowlinson and B. Widom. *Molecular theory of Capillarity.* Clarendon, Oxford, 1982.

[261] H. Lamb. *Hydrodynamics.* Cambridge University Press, 1895.

[262] D.G.A.L. Aarts, M. Schmidt, and H.N.K. Lekkerkerker. Direct visual observation of thermal capillary waves. *Science*, 304(5672):847, 2004.

[263] F.P. Buff, R.A. Lovett, and F.H. Stillinger. Interfacial density profile for fluids in the critical region. *Phys. Rev. Lett.*, 15(15):621, 1965.

[264] S. Senapati and M.L. Berkowitz. Computer simulation study of the interface width of the liquid/liquid interface. *Phys. Rev. Lett.*, 87(17):176101, 2001.

[265] R.E. Rozas and J. Horbach. Capillary wave analysis of rough solid-liquid interfaces in nickel. *EPL*, 93(2):26006, 2011.

[266] S.M. Foiles and J.J. Hoyt. Computation of grain boundary stiffness and mobility from boundary fluctuations. *Acta Mater.*, 54(12):3351, 2006.

[267] T.D. Rossing and N.H. Fletcher. *Principles of vibration and sound*. Elsevier, 2004.

[268] K.L. Merkle, L.J. Thompson, and F. Phillipp. Collective effects in grain boundary migration. *Phys. Rev. Lett.*, 88(22):225501, 2002.

[269] M.L. Bowers, C. Orphus, A. Gautam, F. Lanc̈on, and U. Dahmen. Step coalescence by collective motion at an incommensurate grain boundary. *Phys. Rev. Lett.*, 116(10):106102, 2016.

[270] S.E. Babcock and R.W. Balluffi. Grain boundary kinetics-ii. in situ observations of the role of grain boundary dislocations in high-angle boundary migration. *Acta Metall.*, 37(9):2367, 1989.

[271] D.A. Molodov, J. Swiderski, G. Gottstein, W. Lojkowski, and L.S. Shvindlerman. Effect of pressure on grain boundary migration in aluminium bicrystals. *Acta Metall. Mater.*, 42(10):3397, 1994.

[272] H. Zhang, D.J. Srolovitz, J.F. Douglas, and J.A. Warren. Characterisation of atomic motion governing grain boundary migration. *Phys. Rev. B*, 74(11):115404, 2006.

[273] A. Rajabzadeh, F. Mompiou, M. Legros, and N. Combe. Elementary mechanisms of shear-coupled grain boundary migration. *Phys. Rev. Lett.*, 110(26):265507, 2013.

[274] J.J. Hoyt, Z.T. Trautt, and M. Upmanyu. Fluctuations in molecular dynamics simulations. *Math. Comput. Simul.*, 80(7):1382, 2010.

[275] Z.T. Trautt and M. Upmanyu. Direct two-dimensional calculations of grain boundary stiffness. *Scr. Mater.*, 52(11):1175, 2005.

[276] Z.T. Trautt, M. Upmanyu, and A. Karma. Interface mobility from interface random walk. *Science*, 314(5799):632, 2006.

[277] K.G.F. Janssens, D. Olmstead, E.A. Holm, S.M. Holm, S.J. Plimpton, and P.M. Derlet. Computing the mobility of grain boundaries. *Nat. Mat.*, 5(2):124, 2006.

[278] H. Sun and C. Deng. Direct quantification of solute effects on grain boundary motion by atomistic simulations. *Comp. Mat. Sci.*, 93:137, 2014.

[279] D. Chen, T. Ghoneim, and Y. Kulkarni. Effect of pinning particles on grain boundary motion from interface random walk. *Appl. Phys. Lett.*, 111(16):161606, 2017.

[280] T.O.E. Skinner. *Two-dimensional colloidal systems: grain boundaries and confinement.* University of Oxford, 2012.

[281] L. Mandelstam. Über die rauhigkeit freier flüssigkeitsoberflächen. *Ann. Phys. (Leipzig)*, 346(8):609, 2013.

[282] M.P.A. Fisher, D.S. Fisher, and J.D. Weeks. Agreement of capillary-wave theory with exact results for the interface profile of the two-dimensional Ising model. *Phys. Rev. Lett.*, 48(5):368, 1982.

[283] D. Bedeaux and J.D. Weeks. Correlation functions in the capillary wave model of the liquid-vapour interface. *J. Chem. Phys.*, 82(2):972, 1985.

[284] A. Werner, F. Schmid, M. Muller, and K. Binder. Anomalous size-dependence of interfacial profiles between coexisting phases of polymer mixtures in thin-film geometry: A Monte Carlo simulation. *J. Chem. Phys.*, 107(19):8175, 1997.

[285] K. Binder, M. Müller, F. Schmid, and A. Werner. Simulation of interfaces between coexisting phases in materials. *Comput.-Aided Mater Des.*, 4(3):137, 1998.

[286] D. Morin. *Waves (Draft).* Harvard University, 2021.

[287] L. Zhang and D.B. Thiessen. Capillary-wave scattering from an infinitesimal barrier and dissipation at dynamic contact lines. *J. Fluid Mech*, 719:295, 2013.

[288] M.K. Tan, J.R. Friend, O.K. Matar, and L.Y. Yeo. Capillary wave motion excited by high frequency surface acoustic waves. *Phys. Fluid*, 22(11):295, 2010.

[289] C. Pigot and A. Hibara. Surface tension measurement at the microscale by passive resonance of capillary waves. *Annal. Chem.*, 84(5):2557, 2012.

[290] R. Edgeworth, B.J. Dalton, and T. Parnell. The pitch drop experiment. *Eur. J. Phys.*, 5(4):198, 1984.

[291] E.D. Zanotto. Do cathedral glasses flow? *Am. J. Phys.*, 66(5):392, 1998.

[292] C.A. Angell. Formation of glasses from liquids and biopolymers. *Science*, 267(5206):1924, 1995.

[293] R. Busch, E. Bakke, and W.L. Johnson. Viscosity of the supercooled liquid and relaxation at the glass transition of the $Zr_4$6.75 Ti_8.25 Cu_7.5 $Ni_1$0 $Be_2$7.5 bulk metallic glass forming alloy. *Acta Mater.*, 46(13):4725, 1998.

[294] J.H. Crowe, J.F. Carpenter, and L.M. Crowe. The role of vitrification in anhydrobiosis. *Annu. Rev. Physiol.*, 63(1):73, 1998.

[295] H. Jónsson and H.C. Andersen. Icosahedral ordering in the Lennard-Jones liquid and glass. *Phys. Rev. Lett.*, 60(22):2295, 1988.

[296] H. Tanaka, T. Kawasaki, H. Shintani, and K. Watanabe. Critical-like behaviour of glass-forming liquid. *Nat. Mater.*, 9(4):324, 2010.

[297] G. Biroli, J.-P. Bouchaud, A. Cavagna, T.S. Grigera, and P. Verrocchio. Thermodynamic signature of growing amorphous order in glass-forming liquids. *Nat. Phys.*, 4(10):771, 2008.

[298] F. Sciortino and P. Tartaglia. Glassy colloidal systems. *Adv. Phys.*, 54(6):471, 2005.

[299] L. Berthier and T.A. Witten. Glass transition of dense fluids of hard and compressible spheres. *Phys. Rev. E*, 80(2):021502, 2009.

[300] J. Zhu, M. Li, R. Rogers, W. Meyer, R.H. Ottewill, Crew-Shuttle-Columbia, W.B. Russel, and P.M. Chaikin. Crystallization of hard-sphere colloids in microgravity. *Nature*, 387(6636):883, 1997.

[301] H. Reiss, H.L. Frisch, and J.L. Lebowitz. Statistical mechanics of rigid spheres. *J. Chem. Phys.*, 31(2):369, 1959.

[302] S. Buzzaccaro, R. Rusconi, and R. Piazza. Sticky hard spheres: Equation of state, phase diagram and metastable gels. *Phys. Rev. Lett*, 99(9):098301, 2007.

[303] P. Meakin and R. Jullien. Periodic disc packings generated by random deposition in narrow channels. *EPL*, 18(8):851, 1991.

[304] E. Kumacheva, P. Garstecki, H. Wu, and G.M. Whitesides. Two-dimensional colloid crystals obtained by coupling of flow and containment. *Phys. Rev. Lett.*, 91(12):128301, 2003.

[305] M. Fasolo and P. Sollich. Equilibrium phase behaviour of polydisperse hard spheres. *Phys. Rev. Lett.*, 91(6):068301, 2003.

[306] G. Adam and J.H. Gibbs. On the temperature dependence of cooperative relaxation properties in glass-forming liquids. *J. Chem. Phys.*, 43(1):139, 1965.

[307] A. Baranyai and D.J. Evans. Direct entropy calculation from computer simulation of liquids. *Phys. Rev. A*, 40(7):3817, 1989.

[308] Y. Rosenfeld. Relation between the transport coefficients and the internal entropy of simple systems. *Phys. Rev. A*, 15(6):2545, 1977.

[309] L.-M. Martinez and C.A. Angell. A thermodynamic connection to the fragility of glass-forming liquids. *Nature*, 410(6829):663, 2001.

[310] J.Mittall, J.R. Errington, and T.M. Truskett. Relationship between thermodynamics and dynamics of supercooled liquids. *J. Chem. Phys.*, 125(7):076102, 2006.

[311] T.S. Ingebrigtsen and H. Tanaka. Structural predictor for nonlinear sheared dynamics in the simple glass-forming liquids. *Proc. Natl. Acad. Sci. U.S.A.*, 115(1):87, 2018.

[312] K.L. Galloway, X. Ma, N.C. Keim, D.J. Jerolmack, A.G. Yodh, and P.E. Arratia. Scaling of relaxation and excess entropy in plastically deformed amorphous solids. *Proc. Natl. Acad. Sci. U.S.A.*, 117(22):11887, 2020.

[313] X. Ma, W. Chen, Z. Wang, Y. Peng, Y. Han, and P. Tong. Test of the universal scaling law of diffusion in colloidal monolayers. *Phys. Rev. Lett.*, 110(7):078302, 2013.

[314] B.B. Laird and A.D.J. Haymet. Calculation of the entropy of binary hard sphere mixtures from pair correlation functions. *J. Chem. Phys.*, 97(3):2153, 1992.

[315] A.L. Thorneywork, D.G.A.L. Aarts, J. Horbach, and R.P.A. Dullens. On the Gaussian approximation in colloidal hard sphere fluids. *Soft Matter*, 12(18):4129, 2016.

[316] Z. Zhang, P.J. Junker, P. Habdas, and A.G. Yodh. Cooperative rearrangement regions and dynamical heterogeneities in colloidal glasses with attractive versus repulsive interactions. *Phys. Rev. Lett.*, 107(20):208303, 2011.

[317] E.R. Weeks, J.C. Crocker, A.C. Levitt, A. Schofield, and D.A. Weitz. Three-dimensional direct imaging of structural relaxation near the colloidal glass transition. *Science*, 287(5453):627, 2000.

[318] S. Mazoyer, F. Ebert, G. Maret, and P. Keim. Correlation between dynamical heterogeneities, structure and potential-energy distribution in a 2D amorphous solid. *Eur. Phys. J. E*, 34(9):1, 2011.

[319] V.M. Bedanov and G.V. Gadiyak. On a modified Lindemann like criterion for 2D melting. *Phys. Lett. A*, 109(6):289, 1985.

[320] B.R.A. Nijboer and A. Rahman. Time expansion of correlation functions and the theory of slow neutron scattering. *Physica.*, 32(2):415, 1966.

[321] M.M. Hurley and P. Harrowell. Non-Gaussian behaviour and the dynamical complexity of particle motion in a dense two-dimensional liquid. *J. Chem. Phys.*, 105(23):10521, 1996.

[322] F. van Swol and D.N. Petsev. Molecular dynamics simulation of binary hard sphere colloids near the glass transition. *RSC Adv.*, 4(41):21631, 2014.

[323] A. Rahman. Correlations in the motion of atoms in liquid. *Phys. Rev.*, 136(2A):A405, 1964.

[324] N. Hoffmann, F. Ebert, C.N. Likos, H. Löwen, and G. Maret. Partial clustering in binary two-dimensional colloidal suspensions. *Phys. Rev. Lett.*, 97(7):078301, 2006.

[325] T.A. Scott Jr. Refractive index of ethanol-water mixtures and density and refractive index of ethanol-water ethyl ether mixtures. *J. Phys. Chem.*, 50(5):406, 1946.

[326] I.S. Khattab, F. Bandarkar, M.A.A. Fakhree, and A. Jouyban. Density, viscosity, and surface tension of water + ethanol mixtures from 293 to 323 K. *Korean J. Chem. Eng.*, 29(6):812, 2012.

[327] L.B.G. Cortes. *Colloidal liquid crystals: phase behaviour, dynamics and confinement.* University of Oxford, 2019.

[328] T. Narumi, S.V. Franklin, K.W. Desmond, M. Tokuyama, and E.R. Weeks. Spatial and temporal dynamical heterogeneities approaching the binary colloidal glass transition. *Soft Matter*, 7(4):1472, 2011.

[329] J. Berkmann and T. Caelli. Computation of surface geometry and segmentation using covariance techniques. *IEEE PAMI*, 16(11):1114, 1994.

[330] F.A. Lavergne, D.G.A.L. Aarts, and R.P.A. Dullens. Determining local geometrical features of grain boundaries from microscopy. *J. Phys: Condens. Matter.*, 27(19):194117, 2015.

[331] M. Goldstein. Viscous liquids and the glass transition: A potential energy barrier picture. *J. Chem. Phys.*, 51(9):3728, 1969.

[332] S.K. Nandi, R. Mandal, P.J. Bhuyan, C. Dasgupta, M. Rao, and N.S. Gov. A random first-order transition theory for an active glass. *Proc. Natl. Acad. Sci. U.S.A.*, 115(30):7688, 2018.

[333] L. Berthier, G. Biroli, J.-P. Bouchaud, and G. Tarjus. Can the glass transition be explained without a growing static length scale? *J. Chem. Phys.*, 150(9):094501, 2019.

[334] K. Fukao and Y. Miyamoto. Glass transitions and dynamics in thin polymer films: Dielectric relaxation of thin films of polystyrene. *Phys. Rev. E*, 61(2):1743, 2000.

[335] T.S. Jain and J.J. de Pablo. Investigation of transition states in bulk and freestanding film polymer glasses. *Phys. Rev. Lett.*, 92(15):155505, 2004.

[336] R.D. Priestley, C.J. Ellison, L.J. Broadbelt, and J.M. Torkelson. Structural relaxation of polymer glasses at surfaces, interfaces and in between. *Science*, 309(5733):456, 2005.

[337] X. Cao, H. Zhang, and Y. Han. Release of free-volume bubbles by cooperative-rearrangement regions during the deposition growth of a colloidal glass. *Nat. Commun.*, 8(1):1, 2017.

[338] T.R. Kirkpatrick, D. Thirumalai, and P.G. Wolynes. Scaling concepts for the dynamics of viscous liquids near an ideal glassy state. *Phys. Rev. A*, 40(2):1045, 1989.

[339] W. Kabsch. A solution for the best rotation to relate two sets of vectors. *Acta Cryst.*, 32(5):922, 1971.

[340] I. Buttinoni, J. Cha, W. Lin, S. Job, C. Daraio, and L. Isa. Direct observation of impact propagation and absorption in dense colloidal monolayers. *Proc. Natl. Acad. Sci. U.S.A.*, 114(46):12150, 2017.

[341] M.L. Falk and J.S. Langer. Dynamics of viscoplastic deformation in amorphous solids. *Phys. Rev. E*, 57(6):7192, 1998.

[342] L. Berthier and G. Biroli. Theoretical perspective on the glass transition and amorphous materials. *Rev. Mod. Phys.*, 83(2):587, 2011.

[343] A. Stukowski and A. Arsenlis. On the elastic-plastic decomposition of crystal deformation at the atomic scale. *Modelling Simul. Mater. Sci. Eng.*, 20(3):035012, 2012.

[344] B. VanSaders, J. Dschemuchadse, and S.C. Glotzer. Strain fields in repulsive colloidal crystals. *Phys. Rev. Mater.*, 2(6):063604, 2018.

[345] M.H. Sadd. *Elasticity. Theory, applications and numerics.* Elsevier, 2005.

[346] W.D. Means. *Stress and Strain.* Springer, 1976.

[347] P.M. Gullett, M.F. Horstemeyer, M.I. Baskes, and H. Fang. A deformation gradient tensor and strain tensors for atomistic simulations. *Modelling Simul. Mater. Sci. Eng.*, 16(1):015001, 2007.

[348] A. Cuetos and A. Patti. Equivalence of Brownian dynamics and dynamic monte carlo simulations in multicomponent colloidal suspensions. *Phys. Rev. E*, 92(2):022302, 2015.

[349] A. Patti, D. El Masri, R. van Roij, and M. Dijkstra. Stringlike clusters and cooperative interlayer permeation in smectic liquid crystals formed by colloidal rods. *Phys. Rev. Lett.*, 103(24):248304, 2009.

[350] S. Jabbari-Farouji and E. Trizac. Dynamic Monte Carlo simulations of anisotropic colloids. *J. Chem. Phys.*, 137(5):054107, 2012.

[351] P. Pfleiderer, M. Milinkovic, and T. Schilling. Glassy dynamics in monodisperse hard ellipsoids. *EPL*, 84(1):16003, 2008.

[352] G. Brambilla, D. El Masri, M. Pierno, L. Berthier, L. Cipelletti, G. Petekidis, and A.B. Schofield. Probing the equilibrium dynamics of colloidal hard spheres above the mode-coupling glass transition. *Phys. Rev. Lett.*, 102(8):085703, 2009.

[353] H.W. Cho, M.L. Mugnai, T.R. Kirkpatrick, and D. Thirumalai. Fragile-to-strong crossover, growing length scales, and dynamic heterogeneity in Wigner glasses. *Phys. Rev. E*, 101(3):032605, 2020.

List of Publications

To date the following publications based upon work in this thesis have been submitted or are in preparation:

Joseph D. Hutchinson, François A. Lavergne and Roel P.A. Dullens. *Crystallisation and grain growth in impurity-doped colloidal monolayers*, Submitted. (Chapter 3).

Joseph D. Hutchinson and Roel P.A. Dullens. *Grain rotation in two-dimensional colloidal polycrystals*, In preparation. (Chapter 4).

Joseph D. Hutchinson, Berend van der Meer, Miranda C.R. Bell-Davies, François A. Lavergne and Roel P.A. Dullens. *Active deformation and depinning of grain boundaries in colloidal polycrystals*, In preparation. (Chapter 5).

Joseph D. Hutchinson, Berend van der Meer and Roel P.A. Dullens. *Grain boundary fluctuations between pinned impurities*, In preparation. (Chapter 6).

Joseph D. Hutchinson, Berend van der Meer, Joshua L. Abbott, Arran Curran, Alice L. Thorneywork and Roel P.A. Dullens. *Sedimentation-diffusion equilibrium of two-dimensional binary colloidal fluids*, In preparation. (Chapter 7).

Acknowledgements

First off, I absolutely have to thank Roel for the support over the past eight years. I'm very thankful that you accepted me at Lincoln despite insulting your handwriting in the interview. You are by a long distance the best tutor I've had and really helped enthuse me for the more physical side of chemistry. Thanks for the fun parts of Chemistry dinners and helping organise great Christmas parties, but most of all you helped me do great (I hope) science while letting me do (mostly) my own thing, allowing me to grow and learn immensely. I'm forever grateful for your support.

Thanks too, those who have been so helpful get this thesis done. François and Berend especially, for their great knowledge and discussions about grains and grain boundaries. But also Arran and Taiki for helping me to overcome my sometimes immense frustration at experiments!

A massive thanks to those who have kept the group friendly, fun and alive. Josh for your enthusiasm about Pub Fridays and helping me get started, Mike, you're great but I'm still waiting for that chocolate train, Louis for being an accommodating, but crazy host, Siyu for your infinite friendliness and being up for anything, Ivo for being unpredictable and hilarious at the same time, Jack for your 'great' chat and many fun pub trips, Mariana for your warmth and enthusiasm, Balkis for listening and improving Anglo-French relations, Harriet for your frankly weird questions and sincerity, my co-conspirators Ruth and Caitlin, and all others who have made this the friendliest group I could imagine.

Miranda, you're the most dedicated about Pub Fridays, so clearly you deserve your own section. Firstly, thanks for being such a help with your set-up and for listening to my speculations with extreme scepticism. More generally, the lunches, teas and pub trips have been invaluable and you've been the best support and made the best company.

Thanks also to Paul, Josh and Miranda for proof reading this thesis. Any mistakes are on

you!

Finally I have to thank friends more generally for keeping me sane and also my family. Chris, I hope you enjoyed reading this! Paul, you're my favourite brother and a great one at that. Lastly my parents for being as supportive and loving as I could have asked for. Thank you.